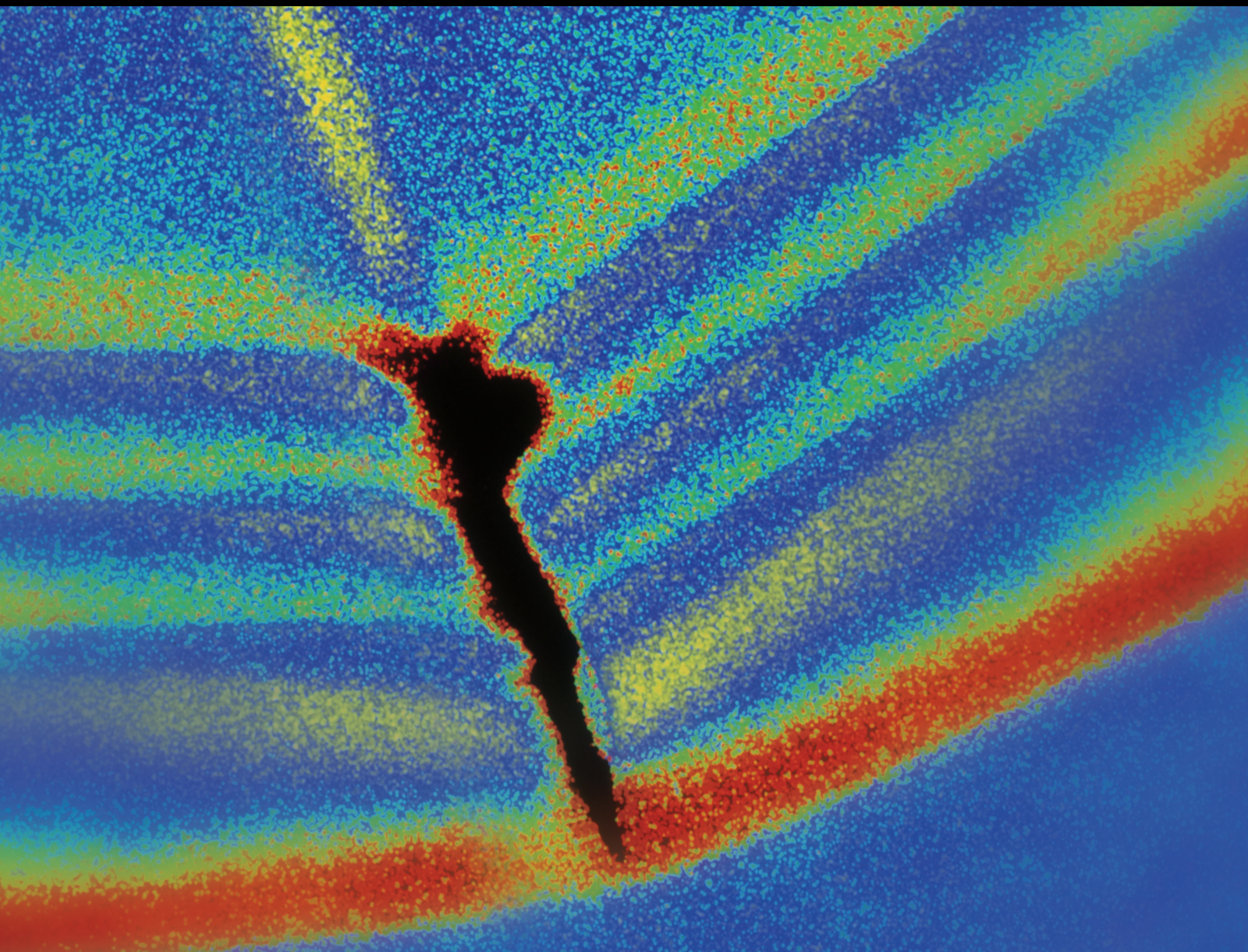


Shock and Vibration

# Reduced-Order Modeling, Testing, and Control of Nonlinear Mechanical and Structural Systems

Lead Guest Editor: José M. Balthazar

Guest Editors: Paulo B. Gonçalves, Angelo M. Tusset, Grzegorz Litak,  
and Livija Cveticanin





---

**Reduced-Order Modeling, Testing, and Control  
of Nonlinear Mechanical and Structural Systems**

Shock and Vibration

---

**Reduced-Order Modeling, Testing, and Control  
of Nonlinear Mechanical and Structural Systems**

Lead Guest Editor: José M. Balthazar

Guest Editors: Paulo B. Gonçalves, Grzegorz Litak,  
and Livija Cveticanin



---

Copyright © 2017 Hindawi. All rights reserved.

This is a special issue published in "Shock and Vibration." All articles are open access articles distributed under the Creative Commons Attribution License, which permits unrestricted use, distribution, and reproduction in any medium, provided the original work is properly cited.

## Editorial Board

Brij N. Agrawal, USA  
Marco Alfano, Italy  
Sumeet S. Aphale, UK  
Mariano Artés, Spain  
Hassan Askari, Canada  
Lutz Auersch, Germany  
Matteo Aureli, USA  
Mahmoud Bayat, Iran  
Marco Belloli, Italy  
Giosuè Boscato, Italy  
Francesco Braghin, Italy  
Ivo Caliò, Italy  
Antonio Carcaterra, Italy  
Dumitru I. Caruntu, USA  
Cristina Castejón, Spain  
Gabriele Cazzulani, Italy  
Noel Challamel, France  
A. Chasalevris, UK  
Simone Cinquemani, Italy  
Giorgio Dalpiaz, Italy  
Farhang Daneshmand, Canada  
Sergio De Rosa, Italy  
Dario Di Maio, UK  
Luigi Di Sarno, Italy  
Longjun Dong, China  
Lorenzo Dozio, Italy  
M. El Badaoui, France  
Mohammad Elahinia, USA

Fiorenzo A. Fazzolari, UK  
Matteo Filippi, Italy  
Francesco Franco, Italy  
Juan C. G. Prada, Spain  
Pedro Galvín, Spain  
Gianluca Gatti, Italy  
Anindya Ghoshal, USA  
Nere Gil-Negrete, Spain  
Hassan Haddadpour, Iran  
M.I. Herreros, Spain  
Hamid Hosseini, Japan  
Reza Jazar, Australia  
Sakdirat Kaewunruen, UK  
Yuri S. Karinski, Israel  
Jeong-Hoi Koo, USA  
G. Kouroussis, Belgium  
Mickaël Lallart, France  
Nuno M. Maia, Portugal  
Giuseppe C. Marano, Italy  
Laurent Mevel, France  
Emiliano Mucchi, Italy  
Sara Muggiasca, Italy  
Tony Murmu, UK  
Pedro Museros, Spain  
S. Natarajan, India  
Toshiaki Natsuki, Japan  
Miguel Neves, Portugal  
Francesco Pellicano, Italy

Evgeny Petrov, UK  
Giuseppe Piccardo, Italy  
Antonina Pirrotta, Italy  
Carlo Rainieri, Italy  
Didier Rémond, France  
Francesco Ripamonti, Italy  
Salvatore Russo, Italy  
Edoardo Sabbioni, Italy  
Onome E. Scott-Emuakpor, USA  
Vadim V. Silberschmidt, UK  
Kumar V. Singh, USA  
Isabelle Sochet, France  
Alba Sofi, Italy  
Jussi Sopanen, Finland  
Stefano Sorace, Italy  
Chao Tao, China  
Mario Terzo, Italy  
Tai Thai, Australia  
Marc Thomas, Canada  
Carlo Trigona, Italy  
Federica Tubino, Italy  
Nerio Tullini, Italy  
Jens Twiefel, Germany  
Filippo Ubertini, Italy  
Marcello Vanali, Italy  
Jörg Wallaschek, Germany  
Matthew J. Whelan, USA  
Enrico Zappino, Italy

# Contents

## **Reduced-Order Modeling, Testing, and Control of Nonlinear Mechanical and Structural Systems**

José Manoel Balthazar, Paulo Batista Gonçalves, Angelo Marcelo Tuset, Grzegorz Litak, and Livija Cveticanin

Volume 2017, Article ID 9232878, 2 pages

## **Bifurcation Analysis and Chaos Control of a Fractional Order Portal Frame with Nonideal Loading Using Adaptive Sliding Mode Control**

Karthikeyan Rajagopal, Anitha Karthikeyan, and Prakash Duraisamy

Volume 2017, Article ID 2321060, 14 pages

## **Drivability Improvement Control for Vehicle Start-Up Applied to an Automated Manual Transmission**

Danna Jiang, Ying Huang, Zhe Zuo, and Huan Li

Volume 2017, Article ID 5783527, 12 pages

## **Predicting the Pullout Capacity of Small Ground Anchors Using Nonlinear Integrated Computing Techniques**

Mosbeh R. Kaloop, Jong Wan Hu, and Emad Elbeltagi

Volume 2017, Article ID 2601063, 10 pages

## **Nonlinear Resonance Analysis of Slender Portal Frames under Base Excitation**

Luis Fernando Paullo Muñoz, Paulo B. Gonçalves, Ricardo A. M. Silveira, and Andréa Silva

Volume 2017, Article ID 5281237, 21 pages

## **Flexoelectric Effect on Vibration of Piezoelectric Microbeams Based on a Modified Couple Stress Theory**

Xingjia Li and Ying Luo

Volume 2017, Article ID 4157085, 7 pages

## **Longitudinal Seismic Behavior of a Single-Tower Cable-Stayed Bridge Subjected to Near-Field Earthquakes**

J. Yi and J. Li

Volume 2017, Article ID 1675982, 16 pages

## **Fatigue Properties of Plain Concrete under Triaxial Tension-Compression-Compression Cyclic Loading**

Dongfu Zhao, Haijing Gao, Huixuan Liu, Penghe Jia, and Jianhui Yang

Volume 2017, Article ID 9351820, 10 pages

## **A Spectrum Detection Approach for Bearing Fault Signal Based on Spectral Kurtosis**

Yunfeng Li, Liqin Wang, and Jian Guan

Volume 2017, Article ID 6106103, 9 pages

## **A Reduced-Order Controller Considering High-Order Modal Information of High-Rise Buildings for AMD Control System with Time-Delay**

Zuo-Hua Li, Chao-Jun Chen, Jun Teng, Wei-Hua Hu, Hou-Bing Xing, and Ying Wang

Volume 2017, Article ID 7435060, 16 pages

## **HOC Based Blind Identification of Hydroturbine Shaft Volterra System**

Bing Bai and Lixiang Zhang

Volume 2017, Article ID 6732704, 11 pages

## *Editorial*

# **Reduced-Order Modeling, Testing, and Control of Nonlinear Mechanical and Structural Systems**

**José Manoel Balthazar,<sup>1</sup> Paulo Batista Gonçalves,<sup>2</sup> Angelo Marcelo Tusset,<sup>3</sup> Grzegorz Litak,<sup>4</sup> and Livija Cveticanin<sup>5</sup>**

<sup>1</sup>*Aeronautics Technological Institute, São José dos Campos, SP, Brazil*

<sup>2</sup>*Pontifical Catholic University, Rio de Janeiro, RJ, Brazil*

<sup>3</sup>*Federal University of Technology-Parana, Ponta Grossa, PR, Brazil*

<sup>4</sup>*Lublin University of Technology, Lublin, Poland*

<sup>5</sup>*University of Novi Sad, Novi Sad, Serbia*

Correspondence should be addressed to José Manoel Balthazar; [jmbaltha@ita.br](mailto:jmbaltha@ita.br)

Received 9 July 2017; Accepted 16 July 2017; Published 16 August 2017

Copyright © 2017 José Manoel Balthazar et al. This is an open access article distributed under the Creative Commons Attribution License, which permits unrestricted use, distribution, and reproduction in any medium, provided the original work is properly cited.

This special issue addresses the general problem of model size reduction for describing nonlinear vibration of structural elements and systems. The aim is to provide and analyze tools that allow accurately capturing nonlinear dynamic behavior using a minimal number of degrees of freedom. It involves modeling and control of nonlinear dynamical phenomena in structural systems and other complex multibody mechanisms. The problems discussed involve identification and control of nonlinear systems as well as responses of the nonlinear system under cyclic excitations. The problem is related to the dimensionality of the nonlinear system which could be a measure of complexity. It is worth noticing that in nonlinear systems there are a variety of multiple solutions which, together with a synchronization phenomenon, play basic and many times competing roles. In some of the systems, for example, the systems showing stick and slip phenomenon, due to dry friction, the dimensionality varies in time. On the other hand, nonlinear systems with memory are characterized by long transients which strongly influence the dynamics identification control procedure. Such a memory effect is frequently observed as a hysteretic behavior based on appearing additional degrees of freedom and can be modeled with a fractional derivative. Finally, the material, structural, and multibody interaction nonlinearities can lead to localized effects which increase the system complexity

but the particular response of the dynamical system can be described by a size reduced model.

The authors of one of the papers study the chaotic oscillations in a fractional order model of a portal frame with nonideal loading. The bifurcation of the fractional order portal frame system for parameters and fractional orders are investigated. Adaptive sliding mode controllers are designed to suppress the chaotic oscillations with uncertain parameters. In another paper, the authors predict the pullout capacity of small ground anchors using nonlinear computing techniques. Results show that the developed prediction models enhance the precision of predicting the pullout capacity when compared with previous studies. In one of the papers, in order to investigate the seismic damage of cable-stayed bridges, a scaled model of a single-tower cable-stayed bridge with A-shaped tower was designed, constructed, and tested on shake tables. Experimental and simplified numerical analysis show the correspondence with fairly small error. One of the papers is dealing with dynamic nonlinear responses and stability of slender structures in the main resonance regions. In this paper, an incremental technique for direct calculation of the nonlinear response in frequency domain of plane frames subjected to base excitation was proposed. In another paper a control methodology is applied to an automated manual transmission vehicle for drivability enhancement

during vehicle start-up phase. Based on a piecewise model of powertrain, a multiple-model predictive controller (mMPC) is designed with the engine speed, clutch disc speed, and wheel speed as the measurable input variables and the engine torque reference and clutch friction torque reference as the controller's output variables. In another paper fatigue tests were performed on plain concrete under triaxial tension-compression-compression (T-C-C) cyclic loading with constant and variable amplitude using a large multiaxial machine. Experimental results show that, under constant amplitude fatigue loads, the development of residual strain in the fatigue loading direction depends mostly on the lateral compressive stress ratio and is nearly independent of stress level. In one of the papers, a new reduced-order controller based on the improved Balanced Truncation (BT) method is designed to reduce the calculation time and to retain the abandoned high-order modal information. In addition, a design method based on Guaranteed Cost Control (GCC) algorithms was presented to eliminate the adverse effects of data acquisition and actuator response time-delays in the design process of the reduced-order controller. A paper is devoted to a novel electric Gibbs function proposed for the piezoelectric microbeams (PMBs) by employing a modified couple stress theory. Based on the new Gibbs function and the Euler-Bernoulli beam theory, the governing equations that incorporate the effects of couple stress, flexoelectricity, and piezoelectricity were derived for the mechanics of PMBs. In another paper, the bearing fault signal was detected adaptively, and time-frequency characteristics of the fault signal can be extracted accurately. The validity of this method was verified by the identifications of simulated shock signal and test bearing fault signal. The method provides a new understanding of wavelet spectrum detection based on spectral kurtosis for rolling element bearing fault signal. Finally, in one of the papers, in order to identify the quadratic Volterra system simplified from the hydroturbine shaft system, a blind identification method based on the third-order cumulants and a reversely recursive method were proposed. The input sequence of the system under consideration is an unobservable independent identically distributed, zero-mean, and non-Gaussian stationary signal, and the observed signals are the superposition of the system output signal and Gaussian noise. The results show that the method is applicable to the blind identification of the hydroturbine shaft system and has strong universality.

*José Manoel Balthazar  
Paulo Batista Gonçalves  
Angelo Marcelo Tuset  
Grzegorz Litak  
Livija Cveticanin*

## Research Article

# Bifurcation Analysis and Chaos Control of a Fractional Order Portal Frame with Nonideal Loading Using Adaptive Sliding Mode Control

**Karthikeyan Rajagopal, Anitha Karthikeyan, and Prakash Duraisamy**

*Center for Nonlinear Dynamics, Defence University, Bishoftu, Ethiopia*

Correspondence should be addressed to Karthikeyan Rajagopal; [rkarthikeyan@gmail.com](mailto:rkarthikeyan@gmail.com)

Received 6 March 2017; Revised 11 April 2017; Accepted 3 May 2017; Published 20 July 2017

Academic Editor: Angelo Marcelo Tuset

Copyright © 2017 Karthikeyan Rajagopal et al. This is an open access article distributed under the Creative Commons Attribution License, which permits unrestricted use, distribution, and reproduction in any medium, provided the original work is properly cited.

We investigate the chaotic oscillations in a fractional order model of a portal frame with nonideal loading. The bifurcation of the fractional order portal frame system for parameters and fractional orders are investigated. Bicoherence analysis shows the existence of quadratic nonlinearities. Fractional order adaptive sliding mode controllers are designed to suppress the chaotic oscillations with uncertain parameters. Power efficiency analysis of the FPGA implemented control scheme shows the maximum power utilization in the fractional order showing the largest Lyapunov exponent.

## 1. Introduction

Many recent researches have been dealing with the study of nonideal vibration systems when the excitation has an influence from the system response. These kind of nonideal vibrations systems are considered as major challenge in engineering research [1, 2]. Chaotic vibrations of a portal frame system with nonideal loading and its control are presented by Tuset et al. [3]. Early researches on nonlinear vibration of frames under support motion do not consider the nonlinear elastic forces [4]. After two decades Brasil and Mazzilli studied the framed machine foundation considering both initial and elastic nonlinear effects including stiffness of columns and elastic deformations of the frames [5]. A simple portal frame structure with its nonlinear behavior under internal resonance conditions is analyzed for several energy levels [6].

Optimal linear feedback control for suppression chaotic oscillations was proposed by Rafikov et al., [7]. Nonlinear oscillations of a portal frame excited by a nonideal motor with limited power output are considered and, with slow increase of power levels, the possibilities of occurrence of Sommerfeld effect are investigated [8]. Dynamical behavior of an elastic

nonideal portal frame with fractional nonlinearities taken into account the full interactions of the vibration systems with an energy source of limited supply is investigated [9]. A nonlinear control method based on the saturation phenomenon of systems coupled with quadratic nonlinearities in a shear building portal frame is studied [10]. A portal frame structure based on energy harvesters with piezo electric coupling exhibiting chaotic behavior is investigated and an optimal control scheme to regulate the energy captured to a designed operating frequency is preferred [11].

Recently many researchers have discussed fractional order calculus and its applications [12–14]. Fractional order nonlinear systems with different control approaches are investigated [15–17]. Numerical analysis and methods for simulating fractional order nonlinear system are proposed by Petras [18] and MATLAB solutions for fractional order chaotic systems, discussed by Trzaska Zdzislaw [19]. A fractional order control based approach is proposed for piezo-actuated nanopositioning stage to suppress the vibration of the low-damped resonant mode and also to minimize the tracking error for nanopositioning applications and it is proposed [20]. A fractional order proportional-integral (FOPI) controller for a mass-spring-damper system which

is poorly damped is proposed and it is proved that FOPI controllers are effective compared to the classical PI controllers [21]. A fractional order (FO) controller is proposed for solving the vibration suppression problem in civil structures experimented on a laboratory scaled steel structure, with one floor, modeled as a single degree-of-freedom system proposed and investigated [22]. The comparisons of the step responses of the integer order and the three types of fractional order damping systems are studied and it is shown that the optimal fractional order damping systems achieve much better step responses than optimal integer order systems [23]. The stability of fractional order systems using Lyapunov stability theory has been investigated in the literature [24, 25]. A fractional order controller to stabilize the unstable fixed points of an unstable open-loop system was proposed by Tavazoei and Haeri [26]. A bifurcation diagram shows the long term qualitative changes (equilibria or periodic orbits) of a system as a function of a bifurcation parameters of the system. The complete dynamics of the system with the variation of the parameters can be studied with the help of bifurcation diagram [27–29]. Nonlinear dynamical system undergoes abrupt qualitative changes when crossing bifurcation points [30]. For a more exhaustive qualitative analysis of a nonlinear dynamic system, it is compulsory to identify both singularities of the parameter plane and singularities of the phase plane [31].

Implementation of chaotic and hyperchaotic system using Field Programmable Gate Arrays (FPGA) is widely investigated [32–34]. Chaotic random number generators are implemented in FPGA for applications in image cryptography [35]. FPGA implemented Duffing oscillator based signal detectors are proposed by Rashtchi and Nourazar [36]. Digital implementation of chaotic multiscroll attractors is extensively investigated [32, 37]. Memristor based chaotic system and its FPGA circuits are proposed by Xu et al. [38]. A FPGA implementation of fractional order chaotic system using approximation method is investigated by Rajagopal et al. [39, 40].

Motivated by the above, in this paper we investigate the fractional order model of a portal frame (FOPF) under a nonideal excitation. Bifurcation plots of the FOPF system are investigated. To study the quadratic nonlinearities in the FOPF system, bicoherence contours along with the higher dimension power spectrum are presented. An adaptive sliding mode controller is designed to suppress chaotic oscillations and finally the proposed controller is implemented in FPGA for real-time implementation.

## 2. Preliminaries and Problem Formulation

We consider the horizontal motion of a portal frame with nonideal excitation [3] as described in Figure 1(a). The portal frame shown in Figure 1(a) is approximated with coupled oscillators [3] as shown in Figure 1(b).

As described in [3], the parameters of this dynamical system consist of  $m_0, m_1$ , the mass and unbalanced mass,  $k_1, k_{nl}$ , linear and nonlinear stiffness,  $c_1$ , linear damping,  $x_1, \varphi$ , displacement and angular displacement,  $J$ , inertial moment, and  $r$ , eccentricity of the unbalanced mass.  $d$  is related to the

voltage applied across the armature of the DC motor and  $s$  is a constant for each model of the DC motor considered. The resulting mathematical model of the structure is given by

$$\begin{aligned} (m_1 + m_0) \ddot{x} + b\dot{x} - k_1x + k_{nl}x^3 \\ = m_0r (\ddot{\varphi} \sin \varphi + \dot{\varphi}^2 \cos \varphi), \\ (J + r^2m_0) \ddot{\varphi} - rm_0\ddot{x} \sin \varphi = L(\dot{\varphi}) = d - s\dot{\varphi}. \end{aligned} \quad (1)$$

Using  $\tau = \omega t$ ,  $x = x/x^*$ , and  $z = \varphi/\varphi^*$ , the dimensionless form of (1) can be derived as,

$$\begin{aligned} \dot{x} &= y, \\ \dot{y} &= -ay + bx - cx^3 + d\dot{w} \sin z + d\omega^2 \cos z, \\ \dot{z} &= w, \\ \dot{w} &= 0.05\dot{y} \sin z - 100w + 200, \\ a &= \frac{b}{(m_1 + m_0)\omega}, \\ \omega &= \sqrt{\frac{k_1}{m_1 + m_0}}, \\ b &= \frac{k_1}{(m_1 + m_0)\omega^2}, \\ c &= \frac{k_{nl}x^{*2}}{(m_1 + m_0)\omega^2}, \\ d &= \frac{m_0r\varphi^*}{(m_1 + m_0)x^*}, \\ \rho_2 &= \frac{d}{(J + r^2m_0)\omega^2\varphi^*} = 100, \\ \delta_2 &= \frac{m_0r\varphi^{*2}}{(m_1 + m_0)x^*}, \\ \rho_1 &= \frac{rm_0x^*}{(J + r^2m_0)\varphi^*} = 0.05, \\ \rho_3 &= \frac{s\omega\varphi^*}{(J + r^2m_0)\omega^2\varphi^*} = 200. \end{aligned} \quad (3)$$

System (2) shows chaotic oscillations when  $a = 0.1$ ,  $b = 1$ ,  $c = 2$ ,  $d = 8.473$  with initial conditions  $[0.1, 0.1, 0.1, 0.1]$ . Figure 2 shows the 3D phase portraits of system (2).

## 3. Fractional Order Portal Frame (FOPF)

In this section we derive the fractional order model of the portal frame (FOPF) from the integer order dimensionless model discussed in (2). There are three commonly used definitions of the fractional order differential operator, namely, Grunwald–Letnikov, Riemann–Liouville, and Caputo [12–14]. We use the fractional order system derived from the

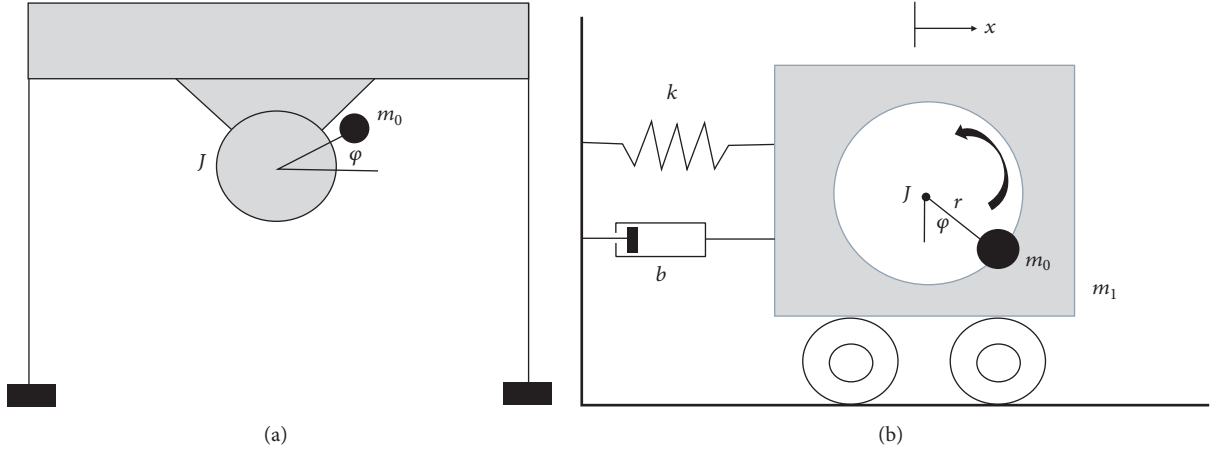


FIGURE 1: (a) Portal frame with nonideal excitation. (b) Coupled oscillator approximation.

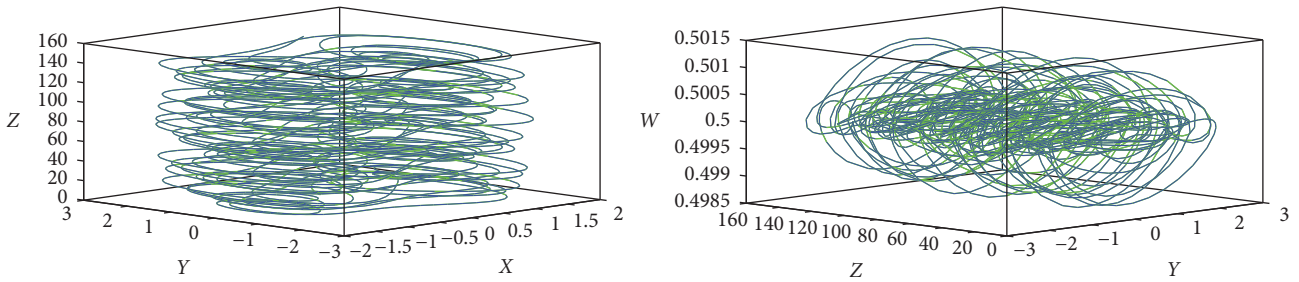


FIGURE 2: 3D phase portraits of the portal frame system (2).

portal frame system (1) with the Grunwald -Letnikov (GL) definition, which is defined as

$${}_a D_t^q f(t) = \lim_{h \rightarrow 0} \left\{ \frac{1}{h^q} \sum_{j=0}^{\lfloor (t-a)/h \rfloor} (-1)^j \binom{q}{j} f(t-jh) \right\} \quad (4)$$

$$= \lim_{h \rightarrow 0} \left\{ \frac{1}{h^q} \Delta_h^q f(t) \right\},$$

where  $a$  and  $t$  are limits of the fractional order equation,  $\Delta_h^q f(t)$  is generalized difference,  $h$  is the step size, and  $q$  is the fractional order of the differential equation.

For numerical calculations the above equation is modified as

$${}_{(t-L)} D_t^q f(t) = \lim_{h \rightarrow 0} \left\{ h^{-q} \sum_{j=0}^{N(t)} b_j f(t-jh) \right\}. \quad (5)$$

Theoretically fractional order differential equations use infinite memory. Hence when we want to numerically calculate or simulate the fractional order equations we have to use finite memory principal, where  $L$  is the memory length and  $h$  is the time sampling.

$$N(t) = \min \left\{ \left\lceil \frac{t}{h} \right\rceil, \left\lceil \frac{L}{h} \right\rceil \right\}. \quad (6)$$

The binomial coefficients required for the numerical simulation are calculated as

$$b_j = \left( 1 - \frac{a+q}{j} \right) b_{j-1}. \quad (7)$$

Using the relations (4) and (5), the fractional order portal frame dimensionless model can be derived as

$$\begin{aligned} D^{q_x} x &= y, \\ D^{q_y} y &= -ay + bx - cx^3 + d(D^{q_w} w) \sin z + dw^2 \cos z, \\ D^{q_z} z &= w, \\ D^{q_w} w &= 0.05(D^{q_y} y) \sin z - 100w + 200. \end{aligned} \quad (8)$$

The parameter values are  $a = 0.1$ ,  $b = 1$ ,  $c = 2$ ,  $d = 8.473$  and the initial conditions are  $[0.1, 0.1, 0.1, 0.1]$ . The system shows its largest Lyapunov exponent (0.08138) when  $q = 0.998$  against its integer order Lyapunov exponent of 0.075 [3], confirming that the chaotic oscillations are more in fractional order close to 1 compared to the integer order. Figure 3 shows the 3D phase portraits of the FOPF system.

## 4. Dynamic Analysis of FOPF System

**4.1. Bifurcation Analysis with Parameters.** The FOPF system described in (8) has four parameters  $a, b, c, d$  and to study the

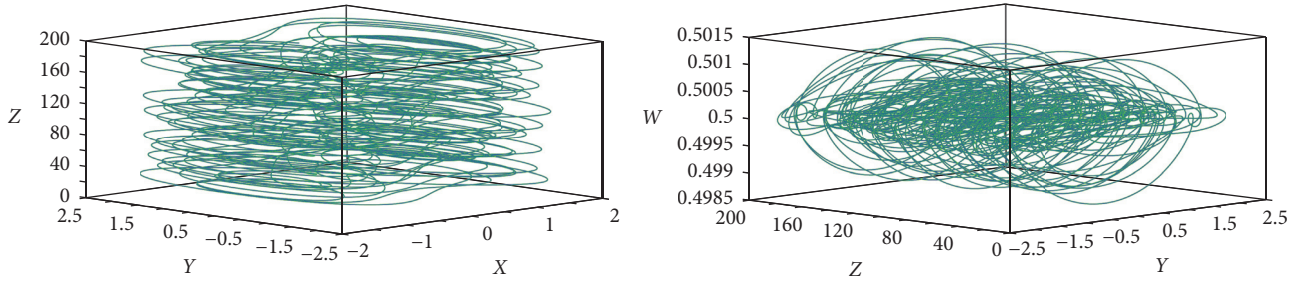
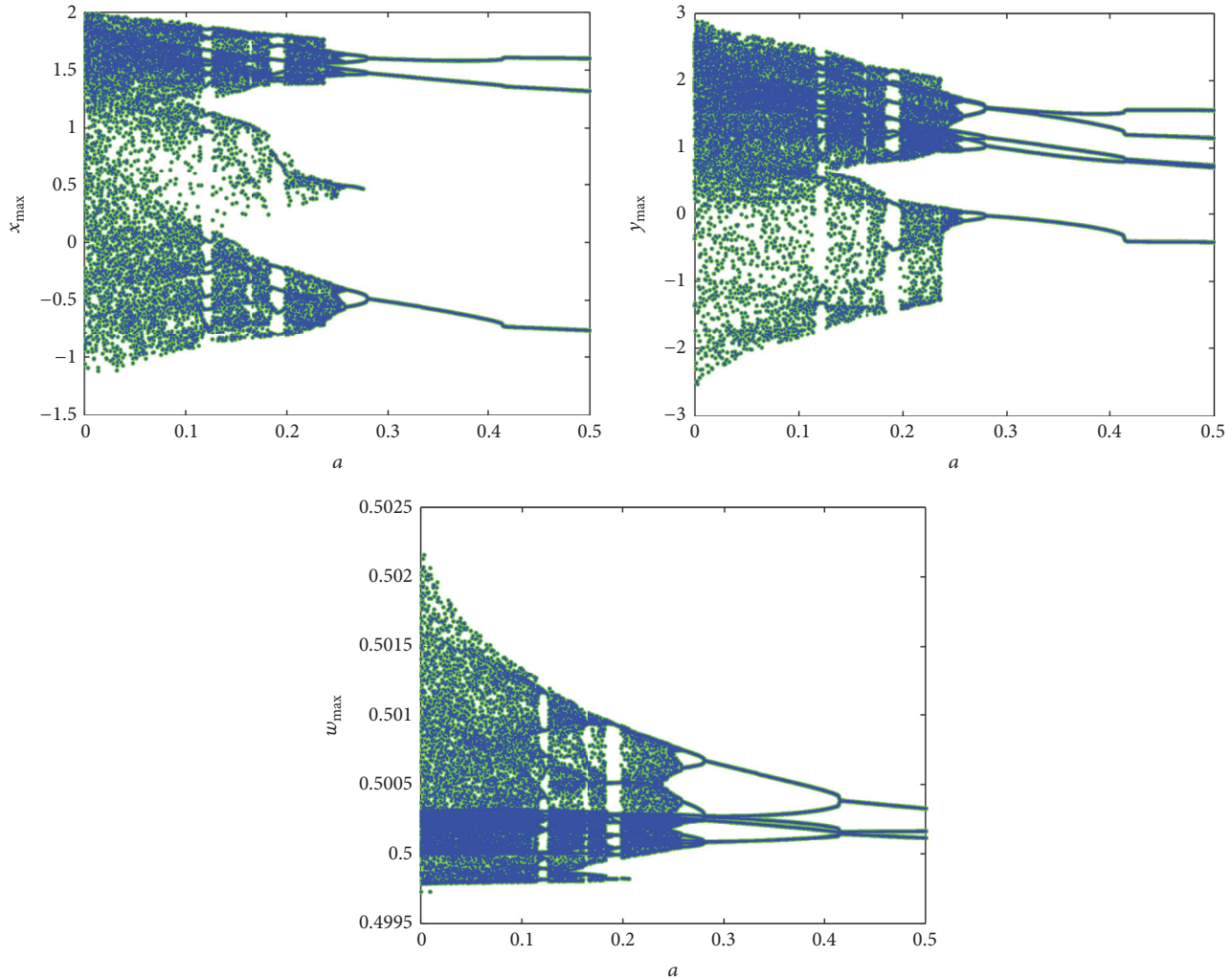


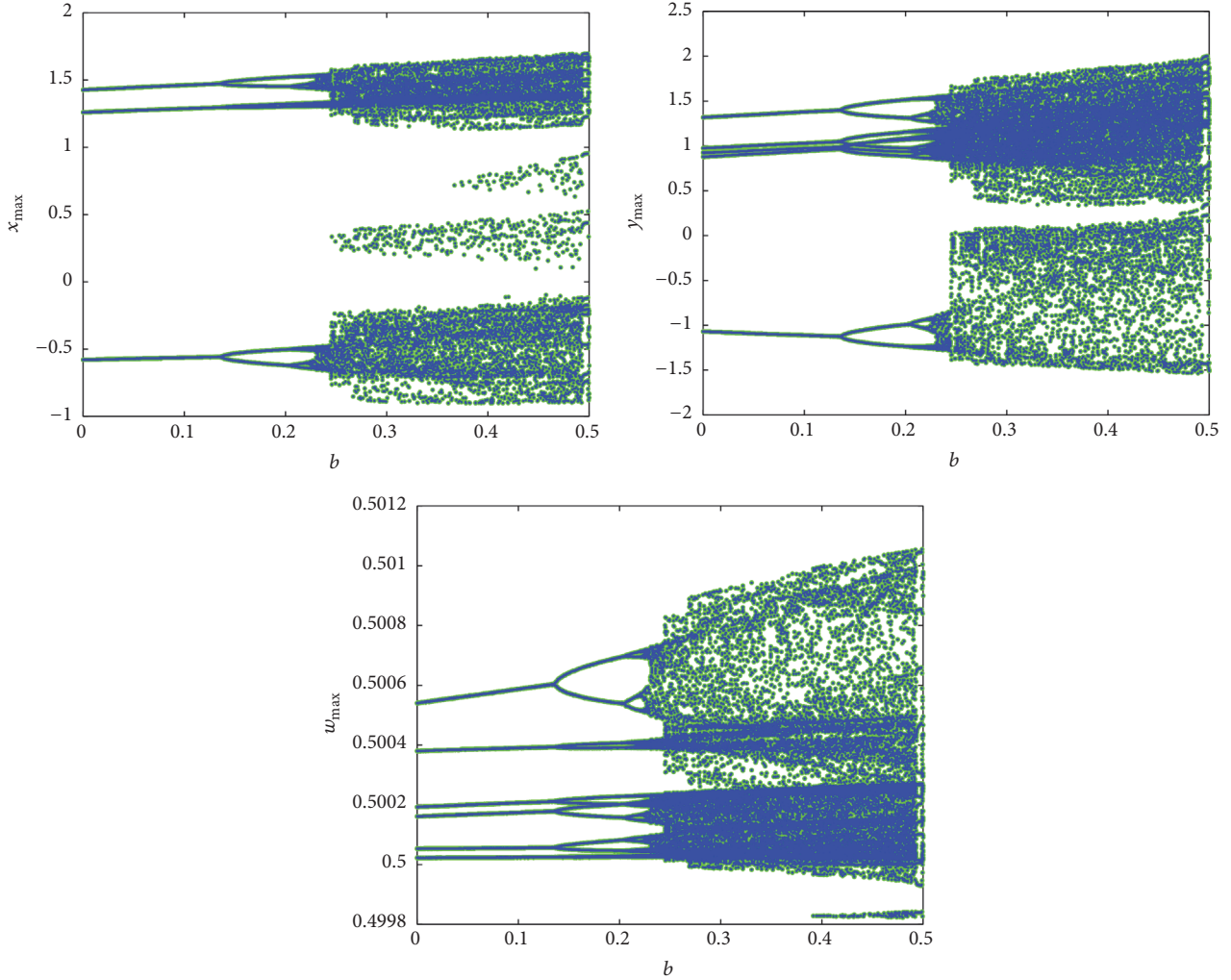
FIGURE 3: 3D phase portraits of the FOPF system.

FIGURE 4: Bifurcation of FOPF system with  $a$ .

impact of these parameters of the FOPF system, we derive the bifurcation plots. Figure 4 shows the bifurcation plots of FOPF system for the parameter  $a$ . As can be seen from Figure 4, the FOPF system shows multiple chaotic regions for  $a$ . There exists a wide band chaotic region for  $0 \leq a \leq 0.12$  and the systems maximum Lyapunov exponent (0.08138) is shown when  $a = 0.1$ . The system shows quasi-periodic state when positive Lyapunov exponent becomes zero for  $0.12 \leq a \leq 0.14$ . The second chaotic region of the FOPF system is

seen for  $0.14 \leq a \leq 0.18$  and the Lyapunov exponent of the system lies between  $[0.0317, 0.0453]$ . For a narrow band of  $0.18 \leq a \leq 0.19$  the FOPF systems show multiple stable limit cycles attracting the neighboring trajectories exhibiting self-sustained oscillations. There exists the third chaotic region for  $0.21 \leq a \leq 0.25$  and the FOPF system takes period halving route for  $0.25 \leq a \leq 0.27$  to exit chaotic oscillations.

Figure 5 shows the bifurcation of the FOPF system for  $b$ . The FOPF system takes a routine period doubling route

FIGURE 5: Bifurcation plots of FOPF system for  $b$ .

to chaos and shows multiple period doubling for  $0.15 \leq b \leq 0.25$ . Figure 6 shows the bifurcation of FOPF system with parameter  $c$ . The FOPF system shows multiple chaotic regions for  $c$ . For  $0.2 \leq c \leq 0.3$  the FOPF systems show a chaotic region. Stable and unstable limit cycles are seen for  $0.41 \leq c \leq 0.63$  and  $0.63 \leq c \leq 1.27$ , respectively. The system takes a routine period doubling route to chaos for  $1.35 \leq c \leq 1.57$  and  $1.63 \leq c \leq 1.94$ . A narrow band of quasi-chaotic state exists for  $1.94 \leq c \leq 1.97$  where the systems only positive Lyapunov exponent becomes zero. The third chaotic region is seen for  $1.97 \leq c \leq 2.4$  and the systems maximum Lyapunov exponent (0.08138) exists when  $c = 2$ .

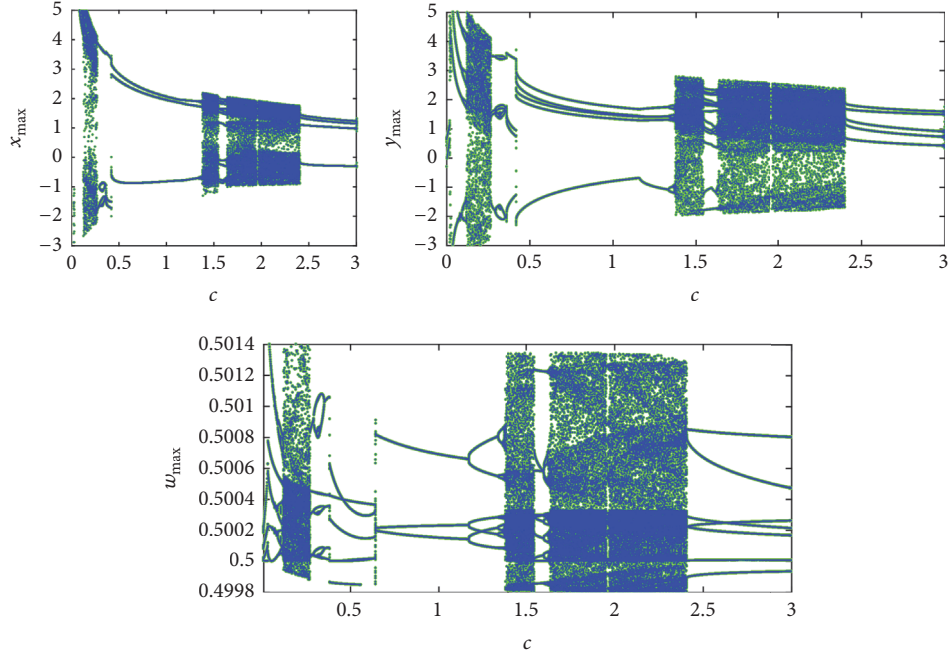
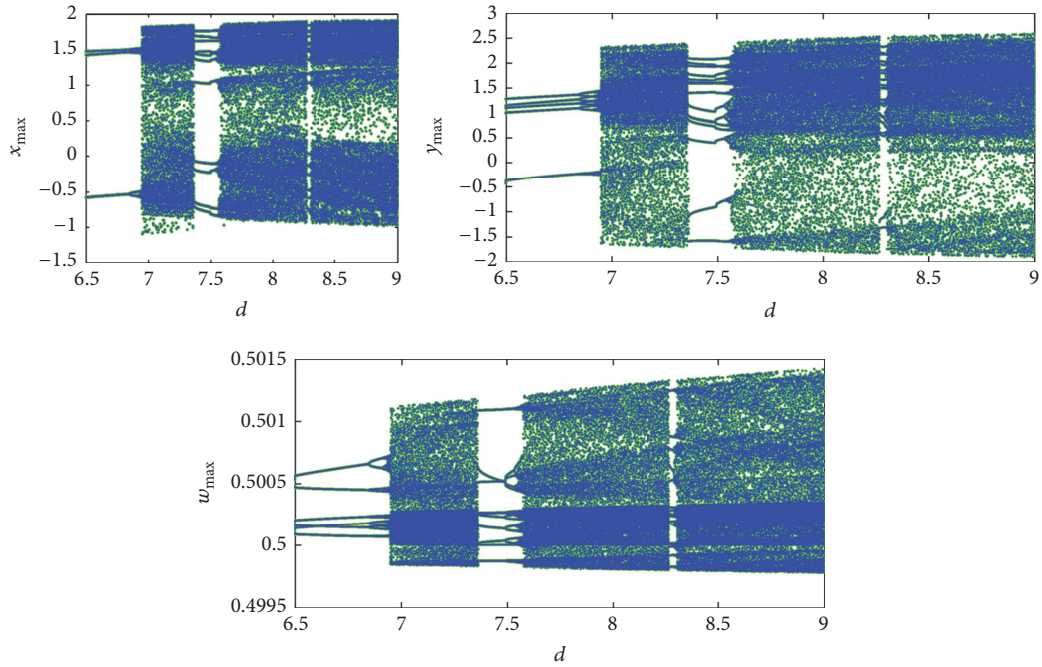
Figure 7 shows the bifurcation of FOPF system with  $d$ . The system enters in to chaos with period doubling for  $6.50 \leq d \leq 6.92$ . The first chaotic region exists for  $6.92 \leq d \leq 7.4$ . Then the system enters in to the second chaotic region ( $7.6 \leq d \leq 8.37$ ) through period doubling ( $7.4 \leq d \leq 7.6$ ). There exists a small band of quasi-chaotic region for  $8.37 \leq d \leq 8.39$  when the Lyapunov exponent goes to zero. The third chaotic

region exists for  $8.39 \leq d \leq 9$  and the FOPF systems largest Lyapunov exponent (0.08138) is seen when  $d = 8.473$ .

**4.2. Bifurcation Analysis with Fractional Order.** The bifurcation of the FOPF system with fractional orders is another important topic of investigation. Figure 8 shows the bifurcation plots of the FOPF system for various fractional orders. The FOPF system shows chaotic oscillations for the commensurate orders  $q_i > 0.99$  and the largest positive Lyapunov exponent (0.08138) of the nonideal portal frame system exists in the fractional order  $q = 0.998$  against the integer order Lyapunov exponent of 0.075 [3]. This clearly confirms that fractional order chaos control is effective compared to the integer order control as discussed in [23].

**4.3. Bicoherence.** Higher order spectra have been used to study the nonlinear interactions between frequency modes [41]. Let  $x(t)$  be a stationary random process defined as

$$x(t) = \sum_{n=1}^N A_n e^{j\omega_n t} + A_n^* e^{-j\omega_n t}, \quad (9)$$

FIGURE 6: Bifurcation of FOPF system for  $c$ .FIGURE 7: Bifurcation of FOPF system with  $d$ .

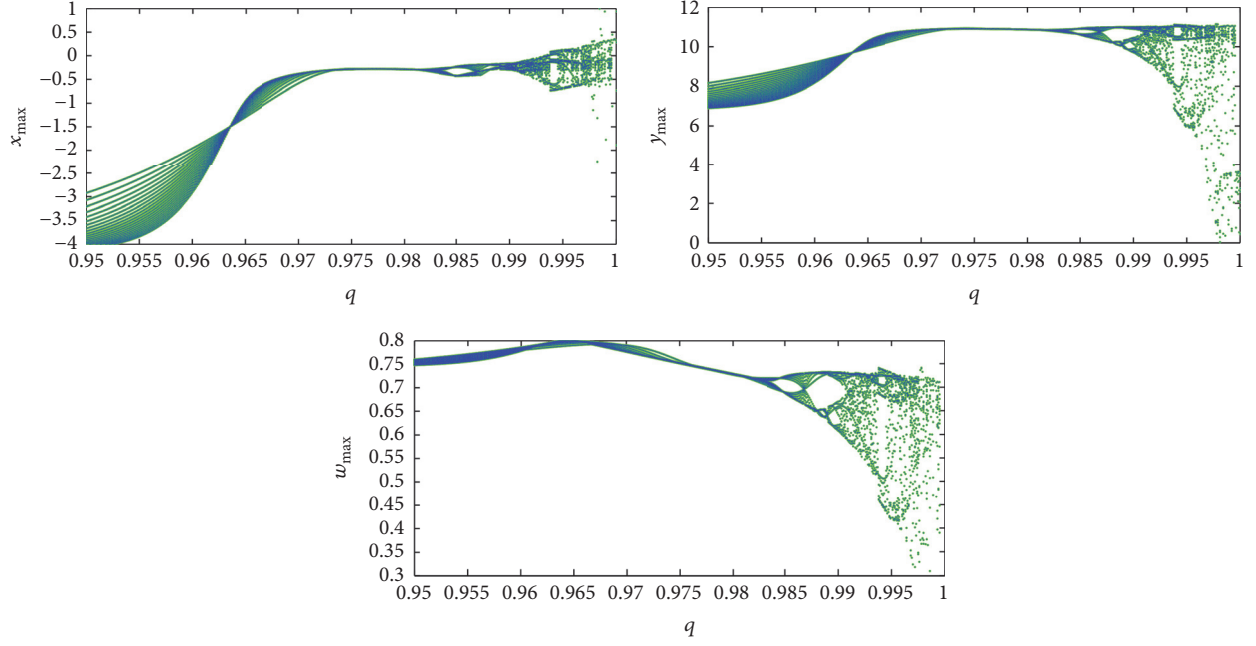
where  $\omega$  is the angular frequency,  $n$  is the frequency modal index, and  $A_n$  are the complex Fourier coefficients. The power spectrum can be defined as

$$P(\omega_k) = E[A_{\omega_k} A_{\omega_k}^*] \quad (10)$$

and discrete bispectrum can be defined as

$$B(\omega_k, \omega_j) = E[A_{\omega_k} A_{\omega_j} A_{\omega_k + \omega_j}^*]. \quad (11)$$

If the modes are independent then the average triple products of Fourier components are zero resulting in a zero bispectrum [41]. The study of bicoherence is to give an indication of the relative degree of phase coupling between triads of frequency components. The motivation to study the bicoherence is twofold. First, the bicoherence can be used to extract information due to deviations from Gaussianity and suppress additive (colored) Gaussian noise. Second, the

FIGURE 8: Bifurcation of FOPF system with fractional order  $q$ .

bicoherence can be used to detect and characterize asymmetric nonlinearity in signals via quadratic phase coupling or identify systems with quadratic nonlinearity. The bicoherence is the third-order spectrum. Whereas the power spectrum is second-order statistics, formed from  $X'(f) * X(f)$ , where  $X(f)$  is the Fourier transform of  $x(t)$ , the bispectrum is third-order statistics formed from  $X(f_j) * X(f_k) * X'(f_j + f_k)$ . The bispectrum is therefore a function of a pair of frequencies  $(f_j, f_k)$ . It is also a complex-valued function. The (normalized) square amplitude is called the bicoherence (by analogy with the coherence from the cross-spectrum). The bispectrum is calculated by dividing the time series into  $M$  segments of length  $N_{\text{seg}}$ , calculating their Fourier transforms and biperiodogram and then averaging over the ensemble. Although the bicoherence is a function of two frequencies the default output of this function is a one-dimensional output, the bicoherence refined as a function of only the sum of the two frequencies. The autobispectrum of a chaotic system is given by Pezeshki [42]. He derived the autobispectrum with the Fourier coefficients.

$$B(\omega_1, \omega_2) = E[A(\omega_1)A(\omega_2)A^*(\omega_1 + \omega_2)], \quad (12)$$

where  $\omega_i$  is the radian frequency and  $A$  are the Fourier coefficients of the time series. The normalized magnitude spectrum of the bispectrum known as the squared bicoherence is given by

$$b(\omega_1, \omega_2) = \frac{|B(\omega_1, \omega_2)|^2}{P(\omega_1)P(\omega_2)P(\omega_1 + \omega_2)}, \quad (13)$$

where  $P(\omega_1)$  and  $P(\omega_2)$  are the power spectra at  $f_1$  and  $f_2$ .

Figures 9(a) and 9(b) show the bicoherence contours of the FOPF system for state  $x$  and all states together, respectively. Shades in yellow represent the multifrequency

components contributing to the power spectrum. From Figures 9(a) and 9(b) the cross-bicoherence is significantly nonzero and nonconstant, indicating a nonlinear relationship between the states. As can be seen from Figure 9(a), the spectral power is very low as compared to the spectral power of all states together (Figure 9(b)) indicating the existence of multifrequency nodes. Also Figure 9(b) shows the nonlinear coupling (straight lines connecting multiple frequency terms) between the states. The yellow shades/lines and nonsharpness of the peaks, as well as the presence of structure around the origin in figures (cross-bicoherence), indicate that the nonlinearity between the states  $x, y, z, w$  is not of the quadratic nonlinearity and hence may be because of nonlinearity of higher dimensions. The most two dominant frequencies  $(f_1, f_2)$  are taken for deriving the contour of bicoherence. The sampling frequency  $(f_s)$  is taken as the reference frequency. Direct FFT is used to derive the power spectrum for individual frequencies and Hankel operator is used as the frequency mask. Hanning window is used as the FIR filter to separate the frequencies [40].

## 5. Fractional Order Adaptive Sliding Mode Control (FOASMC)

In this section we derive the fractional order adaptive sliding mode controllers for suppressing the chaotic oscillations in the FOPF system. As discussed in [3], it is sufficient to control states  $x$  and  $y$ ; hence we include two controllers  $u_x$  and  $u_y$ . To include uncertainties, we assume the system parameters  $(a, b, c, d)$  are unknown. We redefine the FOPF system with the FOASMC controllers as

$$\begin{aligned} \dot{x} &= y + u_x, \\ \dot{y} &= -ay + bx - cx^3 + d\omega \sin z + d\omega^2 \cos z + u_y, \end{aligned}$$

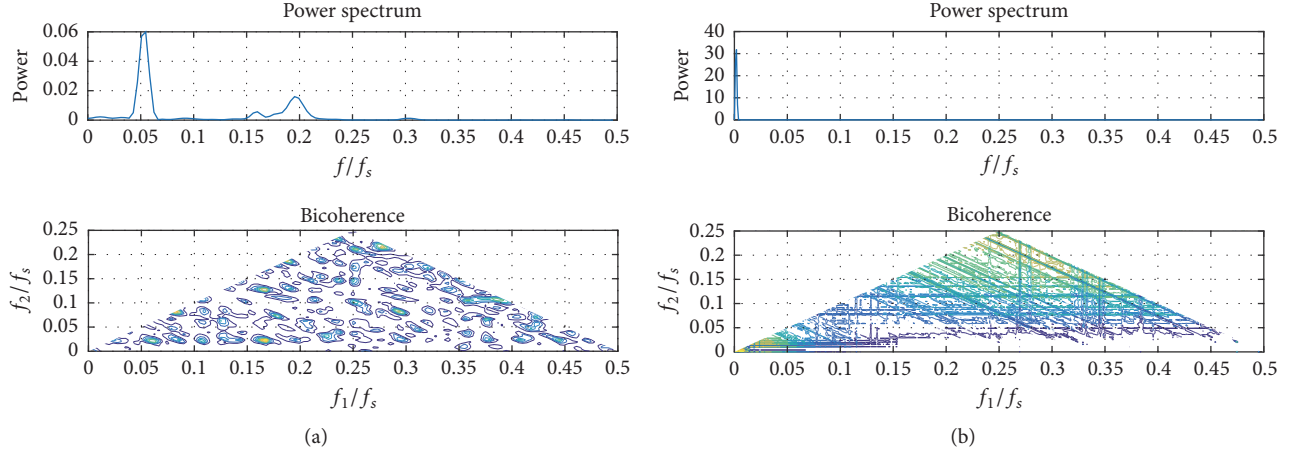


FIGURE 9: (a) Bicoherence of state  $x$ . (b) Bicoherence of all states of FOPF system.

$$\begin{aligned} \dot{z} &= w, \\ \dot{w} &= 0.05 \dot{y} \sin z - 100w + 200, \end{aligned} \quad (14)$$

where  $u_i$  is the adaptive sliding mode controller with  $i = x, y$ . The sliding surfaces [39, 40, 43] are defined as

$$\begin{aligned} s_x &= x + k_x \int_0^t x(\tau) d\tau, \\ s_y &= y + k_y \int_0^t y(\tau) d\tau. \end{aligned} \quad (15)$$

The Fractional derivative of sliding surfaces (15) is given by

$$\begin{aligned} D^{q_x} s_x &= D^{q_x} x + k_x x, \\ D^{q_y} s_y &= D^{q_y} y + k_y y. \end{aligned} \quad (16)$$

To include uncertainties in the FOPF system, the parameters  $a, b, c, d$  are assumed unknown and hence the parameter estimation errors are defined as

$$\begin{aligned} e_a &= \hat{a} - a, \\ e_b &= \hat{b} - b, \\ e_c &= \hat{c} - c, \\ e_d &= \hat{d} - d. \end{aligned} \quad (17)$$

The fractional derivative of the parameter estimation errors (17) is

$$\begin{aligned} D^{q_y} e_a &= D^{q_y} \hat{a}, \\ D^{q_y} e_b &= D^{q_y} \hat{b}, \\ D^{q_y} e_c &= D^{q_y} \hat{c}, \\ D^{q_y} e_d &= D^{q_y} \hat{d}. \end{aligned} \quad (18)$$

We define the Lyapunov candidate function

$$V = \frac{1}{2} [s_x^2 + s_y^2 + e_a^2 + e_b^2 + e_c^2 + e_d^2]. \quad (19)$$

The first derivative of (19) is

$$\begin{aligned} \dot{V} &= s_x \cdot \dot{s}_x + s_y \cdot \dot{s}_y + e_a \cdot \dot{e}_a + e_b \cdot \dot{e}_b + e_c \cdot \dot{e}_c + e_d \\ &\quad \cdot \dot{e}_d. \end{aligned} \quad (20)$$

By definition of fractional calculus [12–14],

$$\dot{x}(t) = D_t^{1-q} \cdot D_t^q x(t). \quad (21)$$

Using (21) in (20),

$$\begin{aligned} \dot{V} &= s_i \cdot D_t^{1-q} \cdot D_t^q s_i - (b - \hat{b}) (D_t^{1-q} \cdot D_t^q \hat{b}) \\ &\quad - (a - \hat{a}) (D_t^{1-q} \cdot D_t^q \hat{a}) - (c - \hat{c}) (D_t^{1-q} \cdot D_t^q \hat{c}) \\ &\quad - (d - \hat{d}) (D_t^{1-q} \cdot D_t^q \hat{d}), \end{aligned} \quad (22)$$

where  $i = x, y$  and  $q$  is the commensurate order of the system. Finding the sign of the Lyapunov first derivative using (22) seems difficult and hence we use the modified fractional order Lyapunov method defined by Rajagopal et al. [39, 40, 44] as

$$\frac{1}{2} D_t^q x^2(t) \leq x(t) \frac{1}{2} D_t^q x(t), \quad q \in (0, 1). \quad (23)$$

Using (14), (16), (18), and (23) in (20)

$$\begin{aligned} \dot{V} &\leq s_x [y + u_x + k_x x] + s_y [-ay + bx - cx^3 \\ &\quad + d \dot{w} \sin z + d w^2 \cos z + u_y + k_y y] + e_a D^{q_y} \hat{a} \\ &\quad + e_b D^{q_y} \hat{b} + e_c D^{q_y} \hat{c} + e_d D^{q_y} \hat{d}. \end{aligned} \quad (24)$$

The adaptive sliding mode controllers are defined as

$$\begin{aligned} u_x &= -y - k_x x - \eta_x \operatorname{sgn}(s_x) - \rho_x s_x, \\ u_y &= \hat{a} y - \hat{b} x + \hat{c} x^3 - \hat{d} \dot{w} \sin z - \hat{d} w^2 \cos z - k_y y \\ &\quad - \eta_y \operatorname{sgn}(s_y) - \rho_y s_y, \end{aligned} \quad (25)$$

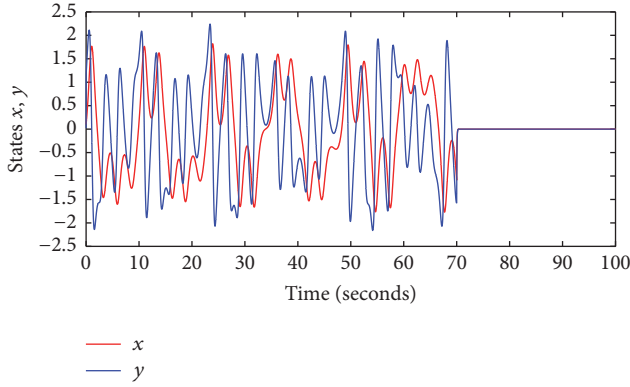


FIGURE 10: Time history of FOPF states (controller in action at  $t = 70$  s).

where  $\eta_i$ ,  $\rho_i$ , and  $k_i$  are positive constants for  $i = x, y$ . The parameter estimation laws are derived as

$$\begin{aligned} D^{q_y} \hat{a} &= -s_y y, \\ D^{q_y} \hat{b} &= s_y x, \\ D^{q_y} \hat{c} &= s_y x^3, \\ D^{q_y} \hat{d} &= s_y [w^2 \cos z + \dot{w} \sin z]. \end{aligned} \quad (26)$$

Using (25) and (26) in (24), we simplify the Lyapunov candidate function as

$$\dot{V} \leq -\eta_x |s_x| - \eta_y |s_y| - \rho_x s_x^2 - \rho_y s_y^2 \quad (27)$$

as  $\eta_i$  and  $\rho_i$  are all positive for  $i = x, y$ ;  $\dot{V}$  is negative definite. Using Barbalat's lemma [45], we conclude that  $e_i(t) \rightarrow 0$  as  $t \rightarrow \infty$ . Figures 10 and 11 show the time history of the states ( $x, y$ ) and parameter estimates, respectively. The controller is switched on at time  $t = 70$  s and the initial conditions of the FOPF system are taken as  $[0.1, 0.02, 0.3, 0.04]$  and parameter estimates as  $[1, 4, 5, 6]$ .

## 6. FPGA Implementation of the FOPF System

For numerically simulating the FOPF control scheme, we first implement the FOPF model in FPGA [39, 40] using the Xilinx (Vivado) System Generator toolbox in Simulink. Firstly we configure the available built in blocks of the System Generator toolbox. The Add/Sub blocks are configured with zero latency and 32/16 bit fixed point settings. The output of the block is configured to rounded quantization in order to reduce the bit latency. For the multiplier block a latency of 1 is configured and the other settings are same as in Add/Sub block. Next we will have to design the fractional order integrator which is not a readily available block in the System Generator [39, 40]. Hence we implement the integrators using the mathematical relation discussed in Section 3 and the value of  $h$  is taken as 0.001 and the initial conditions are fed in to the forward register with fractional order taken as  $q = 0.998$  for FOPF system. Figure 12 shows the Xilinx RTL schematics of the

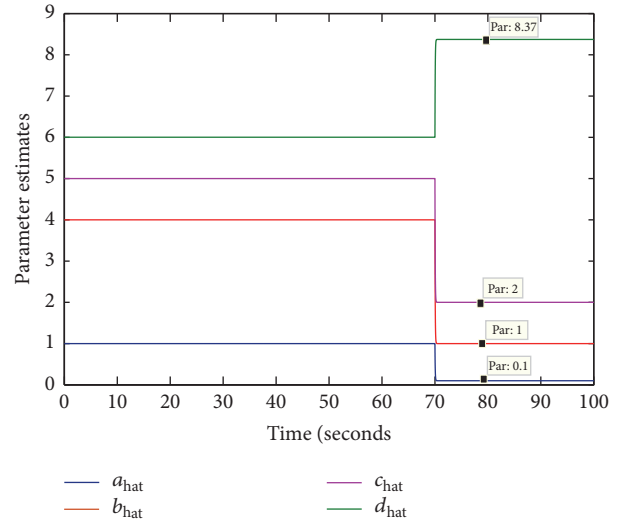


FIGURE 11: Time history of FOPF parameter estimates (controller in action at  $t = 70$  s).

FOPF system implemented in Kintex 7 (Device = 7kl60t Package = fbg484 S) and Figure 13 shows the 3D phase portraits of the FOPF system implemented in FPGA. Here we used a sampling period of 0.01 s. Increasing the sampling time period in some implementation may lead to a clock frequency mismatch and hence plays a critical role in implementation. Also negative time slack may also create problems while implementing the design and hence choosing constraints may also be critical in cases where the number of logical operations is more. Avoiding DDR clocks help in reducing the route delays. Table 1 shows the resources consumed and for analyzing the power consumed by the controllers, we use the approximation methodology discussed in [39, 40]. Figures 14(a) and 14(b) show the power utilization for fractional order  $q = 0.998$  and power utilization for various fractional orders. It confirms that larger power will be consumed by the system when the FOPF system shows the largest Lyapunov exponents (FOPF  $q = 0.998$ ) as shown in Figure 14(b).

**6.1. FPGA Implementation of FOASMC Synchronisation.** For real-time implementation of the proposed control scheme, the FOASMC controller can be implemented in FPGA and the output voltages from the respective control pins can be configured with an active magnetorheological damper. In this section we implement the proposed fractional order adaptive sliding mode controllers (FOASMC) derived in (23) along with the fractional parameter update laws (24) and sliding surfaces (13). For implementation of the entire control scheme we use Virtex 7 (Device: xc7vx980t-1ffg1926). The fractional order of the FOPF master system, slave system, and the FOASMC is kept as  $q = 0.998$ . For analyzing the power consumed by the controllers, we use the approximation methodology discussed in [43]. It confirms that larger power will be consumed by the controller when the master and the slave system show largest Lyapunov exponents. Figure 15 shows the RTL schematics of the fractional order ASMC

TABLE 1: Resources utilized by the FOPF system.

Kintex 7 kl60t	Utilization	Available	Utilization%	Clock frequency	
				$f_{\max}$	Used
LUT	974	101400	0.96	500 Mhz	214 Mhz
FF	850	202800	0.42	300 Mhz	132 Mhz
DSP	36	600	6.00	500 Mhz	244 Mhz
IO	129	285	45.26	250 Mhz	129 Mhz
BUFG	1	32	3.13	300 Mhz	112 Mhz

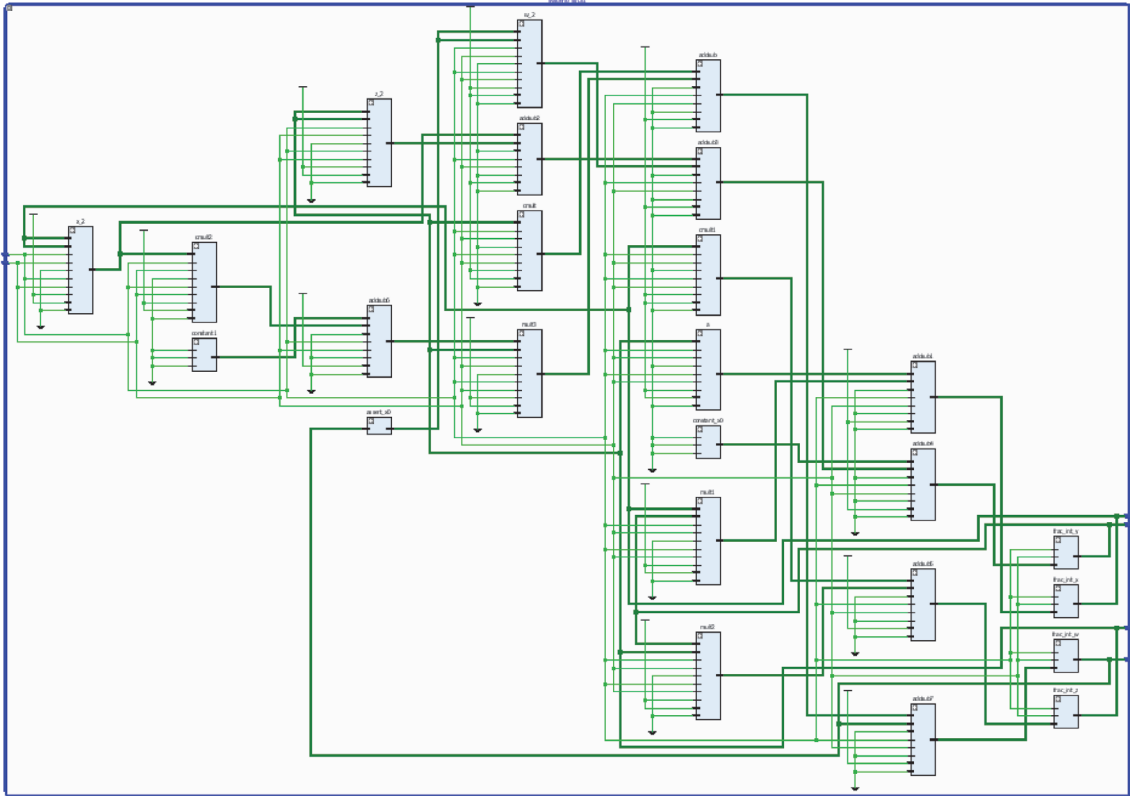
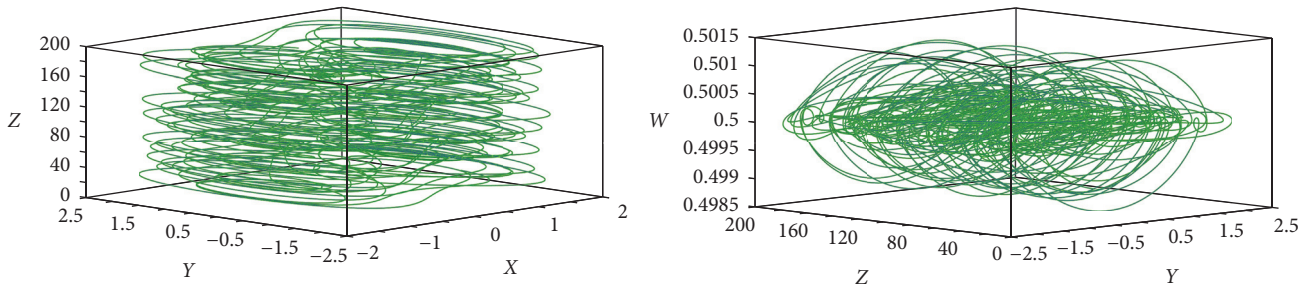
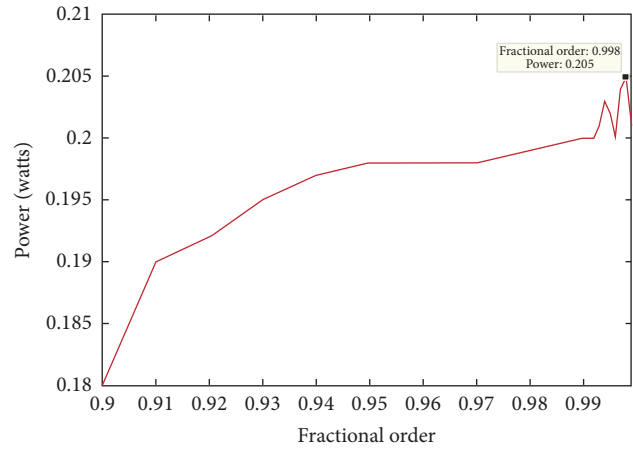
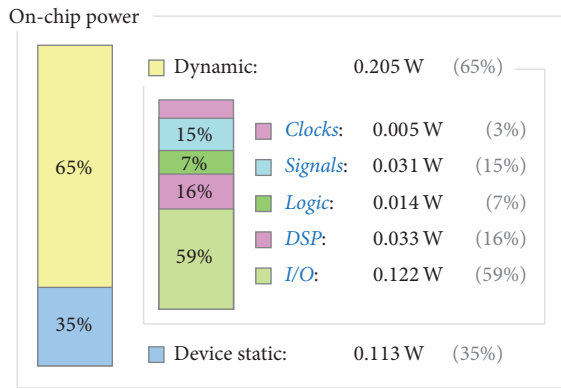


FIGURE 12: Xilinx RTL schematics of the FOPF system implemented in Kintex 7.

FIGURE 13: 3D phase portraits of the FOPF system implemented in FPGA with order  $q = 0.998$ .

controllers implemented in Virtex 7 (Device: xc7vx980t-1ffg1926). Figures 16(a) and 16(b) show the power utilization of the controller and power utilization with change in fractional orders, respectively. Figures 17 and 18 show

the controlled states and estimated parameters of the FOPF system, respectively. To utilize the power of FPGA, the computation needs to be divided into several independent blocks of threads that can be executed simultaneously. The



(a) Power utilized and (b) power utilization versus fractional order of FOPE.

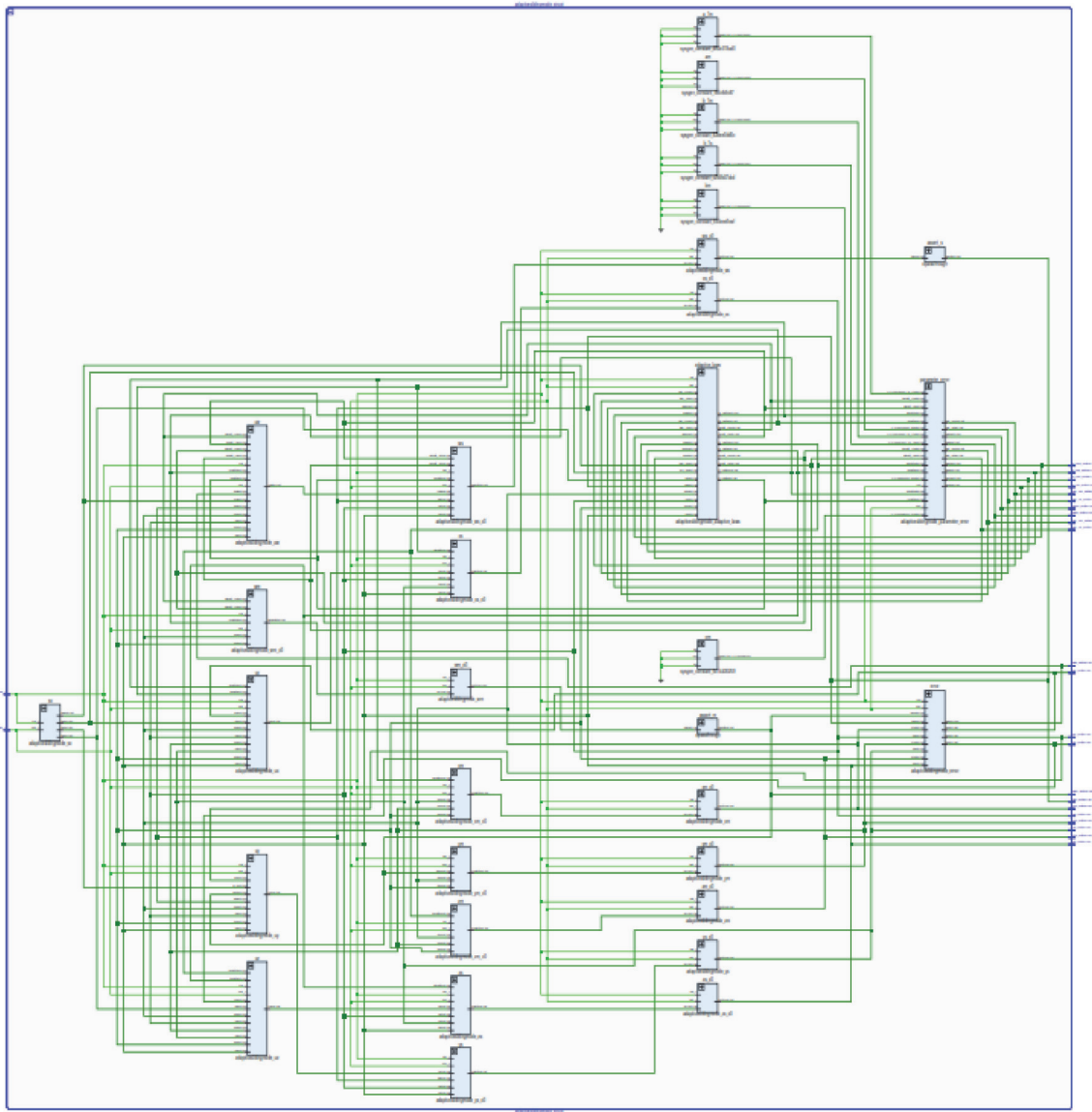
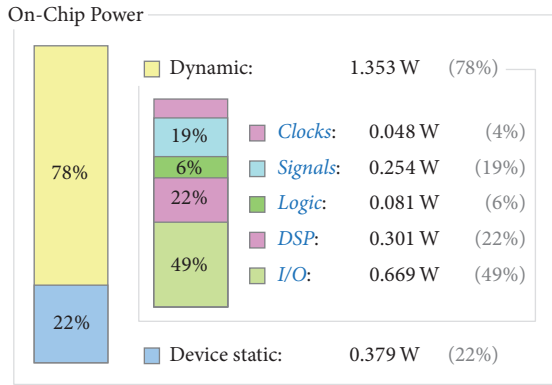
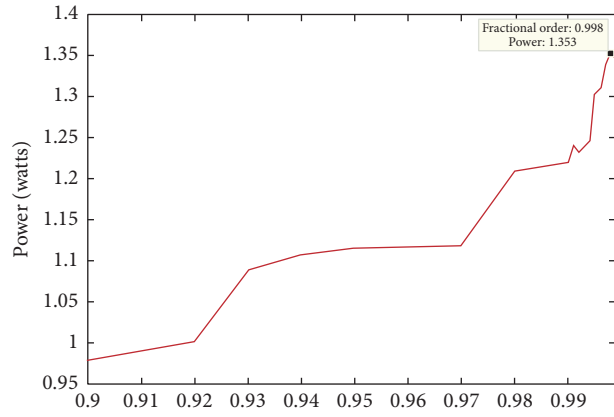


FIGURE 15: Xilinx RTL schematics of the FOASMC controllers implemented in Virtex 7.



(a)



(b)

FIGURE 16: (a) Power utilized and (b) power utilization versus fractional order of FOASMC.

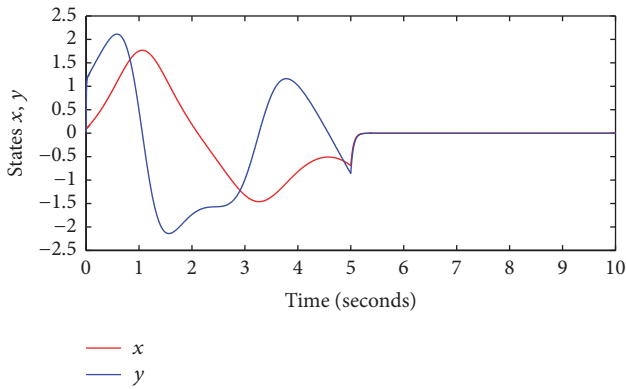


FIGURE 17: Controlled states of FOPF system (controller in action at  $t = 5$  s).

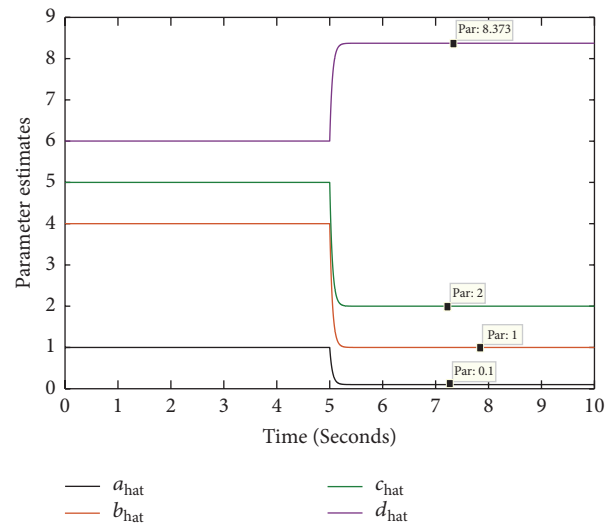


FIGURE 18: Estimated parameters of FOPF system (controller in action at  $t = 5$  s).

performance on FPGA is directly related to the number of threads and its performances decrease when number of branching instructions increases. The fractional order operators are implemented as building blocks and the so-called “frame delay” is not noticeable in the FPGA hardware implementation due to its parallel data structure, unlike a microprocessor-based implementation. While FPGA implementation has a reputation for being difficult to design, with the help of systematic methodology, a system can be put together with less work than is required for more traditional software-based realizations.

### 7. Conclusion

Most of the literatures have investigated chaotic oscillations in an integer order portal frame with nonideal loading. In this paper we investigated the chaotic oscillations of a fractional order portal frame. Existence of chaotic oscillations in a fractional order portal frame is investigated with a positive Lyapunov exponent. Bifurcation plots in the parameter space are investigated for the regions of chaotic oscillations.

Investigation of bicoherence contours shows the quadratic nonlinearities and its existence because of autocorrelation and cross correlation. To control the chaotic oscillations an adaptive sliding mode control scheme is derived and numerically verified. As can be seen from Figures 9 and 10, the proposed control scheme is effective even in the presence of uncertainties in the parameters. For real-time implementation, the fractional order portal frame system with the adaptive sliding mode control algorithm is implemented in FPGA and as can be seen from Figures 16 and 17, the FPGA implemented controllers are effective in chaos suppression. For real-time chaos suppression, the output voltages from the FPGA pins can be connected to MR dampers.

### Conflicts of Interest

The authors declare that there are no conflicts of interest regarding the publication of this paper.

## References

- [1] K. A. Castaño, L. C. S. Goes, and J. M. Balthazar, "A note on the attenuation of the sommerfeld effect of a non-ideal system taking into account a MR damper and the complete model of a DC motor," *Journal of Vibration and Control*, vol. 17, no. 7, pp. 1112–1118, 2010.
- [2] A. A. Nanha Djanan, B. R. Nana Nbandjo, and P. Woafu, "Electromechanical control of vibration on a plate submitted to a non-ideal excitation," *Mechanics Research Communications*, vol. 54, pp. 72–82, 2013.
- [3] A. M. Tusset, V. Piccirillo, J. M. Balthazar, and R. M. L. Rebello Da Fonseca Brasil, "On suppression of chaotic motions of a portal frame structure under non-ideal loading using a magneto-rheological damper," *Journal of Theoretical and Applied Mechanics*, vol. 53, no. 3, pp. 653–664, 2015.
- [4] A. D. S. Barr and D. C. McWhannell, "Parametric instability in structures under support motion," *Journal of Sound and Vibration*, vol. 14, no. 4, pp. 491–509, 1971.
- [5] M. L. R. M. Brasil and C. E. N. Mazzilli, "A general FEM formulation of nonlinear dynamics applied to accessing the static loading effect upon the dynamic response of planar frames," *Applied Mechanics Reviews*, vol. 46, no. 11, pp. 110–117, 1993.
- [6] R. M. L. R. F. Brasil and J. M. Balthazar, "Chaotic Motions of a Simple Portal Frame, 2000," <http://www.abcm.org.br/anais/conem/2000/NC9196.pdf>.
- [7] M. Rafikov, J. M. Balthazar, and A. M. Tusset, "An optimal linear control design for nonlinear systems," *Journal of the Brazilian Society of Mechanical Sciences and Engineering*, vol. 30, no. 4, pp. 279–284, 2008.
- [8] R. M. L. R. F. Brasil and J. M. Balthazar, "Nonlinear oscillations of a portal frame structure excited by a nonideal motor," in *Proceedings of the 2000 2nd International Conference Control of Oscillations and Chaos Proceedings*, vol. 2, pp. 275–278, St. Petersburg, Russia, July 2000.
- [9] J. M. Balthazar, R. M. L. F. Brasil, J. L. P. Felix et al., "Dynamics behaviour of an elastic non-ideal (NIS) portal frame, including fractional nonlinearities," *Journal of Physics: Conference Series*, vol. 721, no. 1, Article ID 12004, 2016.
- [10] J. L. Palacios Felix, J. M. Balthazar, and R. M. L. R. F. Brasil, "On saturation control of a non-ideal vibrating portal frame foundation type shear-building," *Journal of Vibration and Control*, vol. 11, no. 1, pp. 121–136, 2005.
- [11] I. Iliuk, J. Balthazar, A. Tusset et al., "A non-ideal portal frame energy harvester controlled using a pendulum," *The European Physical Journal Special Topics*, vol. 222, no. 7, pp. 1575–1586, 2013.
- [12] D. Baleanu, K. Diethelm, E. Scalas, and J. J. Trujillo, *Fractional Calculus: Models and Numerical Methods*, World Scientific, Singapore, 2014.
- [13] Y. Zhou, *Basic Theory of Fractional Differential Equations*, World Scientific, Singapore, 2014.
- [14] K. Diethelm, *The Analysis of Fractional Differential Equations*, vol. 2004 of *Lecture Notes in Mathematics*, Springer, Berlin, Germany, 2010.
- [15] M. Pourmahmood Aghababa, "Robust finite-time stabilization of fractional-order chaotic systems based on fractional lyapunov stability theory," *Journal of Computational and Nonlinear Dynamics*, vol. 7, no. 2, Article ID 021010, pp. 21–31, 2012.
- [16] E. A. Boroujeni and H. R. Momeni, "Non-fragile nonlinear fractional order observer design for a class of nonlinear fractional order systems," *Signal Processing*, vol. 92, no. 10, pp. 2365–2370, 2012.
- [17] Z. Ruoxun and J. Gong, "Synchronization of the fractional-order chaotic system via adaptive observer," *Systems Science & Control Engineering*, vol. 2, no. 1, pp. 751–754, 2014.
- [18] I. Petras, "Methods for simulation of the fractional order chaotic systems," *Acta montanastica Slovaca*, vol. 11, no. 4, pp. 273–277, 2006.
- [19] W. Trzaska Zdzislaw, "Matlab Solutions of Chaotic Fractional Order Circuits," *Intech Open*, 2013, <https://cdn.intechopen.com/pdfs-wm/21404.pdf>.
- [20] L.-L. Li, G.-Y. Gu, and L.-M. Zhu, "A fractional-order active damping control approach for piezo-actuated nanopositioning stages," in *Proceedings of the 1st International Conference on Manipulation, Automation and Robotics at Small Scales (MARSS '16)*, pp. 1–6, Paris, France, July 2016.
- [21] A. Chevalier, C. Copot, D. Copot, C. M. Ionescu, and R. De Keyser, "Fractional-order feedback control of a poorly damped system," in *Proceedings of the 19th IEEE International Conference on Automation, Quality and Testing, Robotics (AQTR '14)*, pp. 1–4, Cluj-Napoca, Romania, May 2014.
- [22] C. I. Muresan, E. H. Dulf, and O. Prodan, "A fractional order controller for seismic mitigation of structures equipped with viscoelastic mass dampers," *Journal of Vibration and Control*, vol. 22, no. 8, pp. 1980–1992, 2016.
- [23] H. Sheng, Y. Q. Chen, and T. S. Qiu, "Optimal Fractional-Order Damping Strategies," in *Fractional Processes and Fractional-Order Signal Processing: Techniques and Applications*, Springer London, London, UK, 2011.
- [24] Y. Li, Y. Chen, and I. Podlubny, "Stability of fractional-order nonlinear dynamic systems: Lyapunov direct method and generalized Mittag-Leffler stability," *Computers & Mathematics with Applications*, vol. 59, no. 5, pp. 1810–1821, 2010.
- [25] J. A. Gallegos and M. A. Duarte-Mermoud, "On the Lyapunov theory for fractional order systems," *Applied Mathematics and Computation*, vol. 287/288, pp. 161–170, 2016.
- [26] M. S. Tavazoei and M. Haeri, "Chaos control via a simple fractional-order controller," *Physics Letters A*, vol. 372, no. 6, pp. 798–807, 2008.
- [27] Y. Gao and K. T. Chau, "Hopf bifurcation and chaos in synchronous reluctance motor drives," *IEEE Transactions on Energy Conversion*, vol. 19, no. 2, pp. 296–302, 2004.
- [28] G. Revel, A. E. Leon, D. M. Alonso, and J. L. Moiola, "Multi-parameter bifurcation analysis of subsynchronous interactions in DFIG-based wind farms," *Electric Power Systems Research*, vol. 140, pp. 643–652, 2016.
- [29] A. Zarei and S. Tavakoli, "Hopf bifurcation analysis and ultimate bound estimation of a new 4-D quadratic autonomous hyperchaotic system," *Applied Mathematics and Computation*, vol. 291, pp. 323–339, 2016.
- [30] Y. A. Kuznetsov, *Elements of Applied Bifurcation Theory*, vol. 112 of *Applied Mathematical Sciences*, Springer, Berlin, Germany, 1995.
- [31] N. Jabli, H. Khammari, M. F. Mimouni, and R. Dhifaoui, "Bifurcation and chaos phenomena appearing in induction motor under variation of PI controller parameters," *WSEAS Transactions on Systems*, vol. 9, no. 7, pp. 784–793, 2010.
- [32] E. Tlelo-Cuautle, A. D. Pano-Azucena, J. J. Rangel-Magdaleno, V. H. Carbajal-Gomez, and G. Rodriguez-Gomez, "Generating a 50-scroll chaotic attractor at 66 MHz by using FPGAs," *Nonlinear Dynamics*, vol. 85, no. 4, pp. 2143–2157, 2016.

- [33] Q. Wang, S. Yu, C. Li et al., "Theoretical design and FPGA-based implementation of higher-dimensional digital chaotic systems," *IEEE Transactions on Circuits and Systems I: Regular Papers*, vol. 63, no. 3, pp. 401–412, 2016.
- [34] E. Dong, Z. Liang, S. Du, and Z. Chen, "Topological horseshoe analysis on a four-wing chaotic attractor and its FPGA implementation," *Nonlinear Dynamics*, vol. 83, no. 1-2, pp. 623–630, 2016.
- [35] E. Tlelo-Cuautle, V. H. Carbajal-Gomez, P. J. Obeso-Rodelo, J. J. Rangel-Magdaleno, and J. C. Núñez-Pérez, "FPGA realization of a chaotic communication system applied to image processing," *Nonlinear Dynamics*, vol. 82, no. 4, pp. 1879–1892, 2015.
- [36] V. Rashtchi and M. Nourazar, "FPGA implementation of a real-time weak signal detector using a duffing oscillator," *Circuits, Systems, and Signal Processing*, vol. 34, no. 10, pp. 3101–3119, 2015.
- [37] E. Tlelo-Cuautle, J. J. Rangel-Magdaleno, A. D. Pano-Azucena, P. J. Obeso-Rodelo, and J. C. Nunez-Perez, "FPGA realization of multi-scroll chaotic oscillators," *Communications in Nonlinear Science and Numerical Simulation*, vol. 27, no. 1-3, pp. 66–80, 2015.
- [38] Y.-M. Xu, L.-D. Wang, and S.-K. Duan, "A memristor-based chaotic system and its field programmable gate array implementation," *Acta Physica Sinica*, vol. 65, no. 12, Article ID 120503, 2016.
- [39] K. Rajagopal, A. Karthikeyan, and A. K. Srinivasan, "FPGA implementation of novel fractional-order chaotic systems with two equilibriums and no equilibrium and its adaptive sliding mode synchronization," *Nonlinear Dynamics*, vol. 87, no. 4, pp. 2281–2304, 2017.
- [40] K. Rajagopal, L. Guessas, S. Vaidyanathan, A. Karthikeyan, and A. Srinivasan, "Dynamical analysis and FPGA implementation of a novel hyperchaotic system and its synchronization using adaptive sliding mode control and genetically optimized PID Control," *Mathematical Problems in Engineering*, vol. 2017, Article ID 7307452, 14 pages, 2017.
- [41] D. M. W. Leenaerts, "Higher-order spectral analysis to detect power-frequency mechanisms in a driven Chua's circuit," *International Journal of Bifurcation and Chaos*, vol. 7, no. 6, pp. 1431–1440, 1997.
- [42] C. Pezeshki, "Bispectral analysis of possessing chaotic motion," *Journal of Sound and Vibration*, vol. 137, no. 3, pp. 357–368, 1990.
- [43] C. Wang, R. Chu, and J. Ma, "Controlling a chaotic resonator by means of dynamic track control," *Complexity*, vol. 21, no. 1, pp. 370–378, 2015.
- [44] K. Rajagopal, S. Vaidhyathan, and A. Karthikeyan, "Dynamic analysis and chaos suppression in a fractional order brushless DC motor," *Electrical Engineering*, vol. 99, no. 2, pp. 721–733, 2017.
- [45] H. K. Khalil, *Nonlinear Systems*, Pearson Education, New York, NY, USA, 3rd edition, 2002.

## Research Article

# Drivability Improvement Control for Vehicle Start-Up Applied to an Automated Manual Transmission

**Danna Jiang, Ying Huang, Zhe Zuo, and Huan Li**

*Research Center of Power Machinery, Beijing Institute of Technology, Beijing 100081, China*

Correspondence should be addressed to Zhe Zuo; [zuzeus@bit.edu.cn](mailto:zuzeus@bit.edu.cn)

Received 22 November 2016; Accepted 21 February 2017; Published 11 May 2017

Academic Editor: Angelo Marcelo Tusset

Copyright © 2017 Danna Jiang et al. This is an open access article distributed under the Creative Commons Attribution License, which permits unrestricted use, distribution, and reproduction in any medium, provided the original work is properly cited.

Drivability is the key factor for the automated manual transmission. It includes fast response to the driver's demand and the driving comfort. This paper deals with a control methodology applied to an automated manual transmission vehicle for drivability enhancement during vehicle start-up phase. Based on a piecewise model of powertrain, a multiple-model predictive controller (mMPC) is designed with the engine speed, clutch disc speed, and wheel speed as the measurable input variables and the engine torque reference and clutch friction torque reference as the controller's output variables. The model not only includes the clutch dynamic, the flexible shaft dynamic, but also includes the actuators' delay character. Considering the driver's intention, a slipping speed trajectory is generated based on the acceleration pedal dynamically. The designed control strategy is verified on a complete powertrain and longitudinal vehicle dynamic model with different driver's torque demands.

## 1. Introduction

Automated manual transmission (AMT) is widely used in modern vehicles especially in trucks due to the advantage of its low weight, low cost, and high efficiency just like a manual transmission (MT) and driving comfort without directly operating the clutch and gearshift just like an automated transmission (AT) [1]. Another transmission using a dual clutch system also has the advantage of low weight, high efficiency, and driving comfort, but it is not as simple or as cost-effective as the AMT. Therefore, AMT is considered as an inexpensive add-on solution for classical MT [2].

In AMT, the start-up or gearshift phase is managed by an actuator driven clutch which is controlled by the transmission control unit (TCU) with communication to engine management system (EMS) for coordination control. It can be acceptable to the customers provided that the control strategies are able to limit the variation of the vehicle acceleration during vehicle start-up or gearshifts. That is one of the most important aspects of vehicle drivability [3]. Therefore, the drivability control in the clutch control is the key factor to guarantee the AMT performance.

Many solutions for dry clutch control in AMT have been presented in recent years. There are many different approaches proposed for dry clutch control in the literatures, for example, the classical control [4], fuzzy control [5], linear-quadratic based optimal control [6–8], decoupling control [9], robust control [10], predictive control [2, 11], and the hybrid control [6, 12].

However, the clutch control is expected to satisfy the different and sometimes conflicting objectives, such as fast and smooth start-up. Hence, optimization based algorithm becomes a potential solution for this problem. Because the clutch dynamics in slipping and engagement phases are typical nonlinear processes, nonlinear based control methods are also needed for this problem. In this paper, we choose multiple-model predictive control strategy to design the clutch controller algorithm considering that it can handle multivariable control problem naturally and deal with nonlinear system with switching the subcontrollers. And the calculation speed is higher than hybrid predictive control strategy when the system has high order.

Unlike other researches of clutch control, this paper aims at drivability enhancement in the start-up phase of a heavy-duty truck with an automated manual transmission. Not

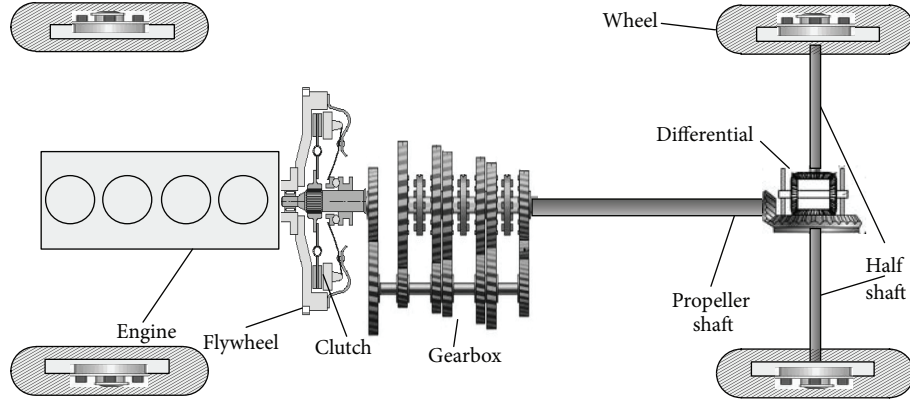


FIGURE 1: Overall structure of the AMT truck.

only the slipping time and jerk considered in the controller design but also the torsion vibration and actuator delays which have bad effects on the drivability of the vehicle and driver's intentions which directly affect the driver's feeling are considered as well.

The approach proposed in this paper deals with the clutch control of multiphases defined by the clutch position. In different phases, different control objectives are used. Torsion vibration which is associated with drivability and comfort is selected as one of the control objectives in every phase. In clutch going to engagement slipping phase, the other control objective is the driver's intention to decide slipping speed trajectory tracking. A hierarchical approach is used. The high level is torque reference control for engine and clutch actuator, considering the modern engine controller widely adopting torque-based method. Three angular speeds are measured as the controller inputs. They are the engine speed, clutch disk speed, and the wheel speed. The controller outputs are the optimized engine torque requirement and the clutch friction torque requirement. In this paper, we just focus on the high level of the clutch control. And the low level controller is assumed as an ideal one.

This paper is organized as follows. In Section 2, the structure of an automotive driveline is discussed, and a simplified driveline is introduced, with the dry clutch, flexible drive shaft and actuators, engine, and the clutch pneumatic actuator dynamic considered in the model. In Section 3, the different control objectives for different phase of the AMT are stated. And driver's intention is also considered in the control objectives. In this section, the control scheme based on constrained MPC strategy is presented. The switching logic is designed for different MPC controllers. In the scheme, a Kalman estimator is designed to estimate the vehicle load torque. With the estimated load torque, the prediction can be much more accurate. In Section 4, the proposed strategy is tested and discussed. Finally, the concluding remarks are given in Section 5.

## 2. System Modeling

Figure 1 shows a rear-driven heavy-duty truck. The driveline mainly consists of the dry clutch, gearbox, propeller shaft,

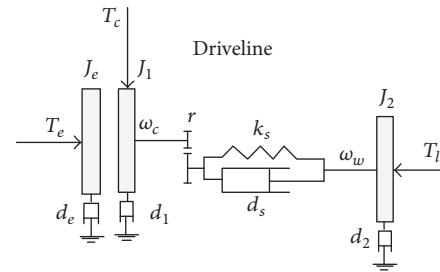


FIGURE 2: Simplified model of the driveline.

differential, half driven shafts, and wheels. The clutch electro-pneumatic circuit is the actuator to drive the clutch close or open. The engine is the power source which is also an actuator working together with clutch actuators.

Figure 2 shows a simplified driveline model, whereas a three-inertia model is used in this study. One inertia indicates the engine flywheel  $J_e$  with viscous friction  $d_e$ . Another inertia indicates the equivalent mass moment from the clutch disc to the differential gear, which is summarized to  $J_1$  with viscous friction  $d_1$  between the clutch disc and gearbox, and the last inertia  $J_2$  indicates the equivalent mass moment of remaining driveline and the vehicle with viscous friction  $d_2$ .

The clutch friction torque is represented by  $T_c$  and the engine torque is represented by  $T_e$ . The gearbox ratio together with the final gear is described by the ratio  $r$ . It is assumed that the flexibility of drivetrain is equivalent to a spring and damper represented by  $k_s$  and  $d_s$ . Wheel slip is neglected for simplicity. The driving resistance torque is described by  $T_l$ , which consists of the rolling resistance torque, grade resistance torque, and the aerodynamics drag torque. Usually, the resistance torques is unknown.

The equivalent inertia of  $J_1$  can be calculated using (1) as follows:

$$J_1 = J_c + J_{g1} + \frac{J_{g2}}{r_g^2} + \frac{J_d}{r_g r_d^2}, \quad (1)$$

where  $J_c$  is the inertia of clutch;  $J_{g1}$  is the inertia of the input gear of the transmission;  $J_{g2}$  is the inertia of the output gear

of the transmission;  $J_d$  is inertia of differential input gear;  $r_g$  is the gear transmission ratio; and  $r_d$  is the differential ratio.

The equivalent inertia of  $J_2$  can be calculated using (2) as follows:

$$J_2 = J_w + mR_w^2, \quad (2)$$

where  $J_w$  is the wheel inertia,  $m$  is the mass of vehicle body, and  $R_w$  is the tire radius.

The equivalent stiffness of  $k_s$  can be calculated using (3) as follows. (The damping coefficient of  $d_s$  is calculated by the same equation with replacing the stiffness coefficient by the damping coefficient.) The model acts as if there are several damped springs in series and parallel:

$$\frac{1}{k_s} = \frac{1}{k_c r^2} + \frac{1}{k_p r_d^2} + \frac{1}{k_{h1} + k_{h2}}, \quad (3)$$

where  $k_c$  is the stiffness coefficient of clutch torsion damper,  $k_p$  is the stiffness coefficient of propeller shaft,  $k_{h1}$  is the stiffness coefficient of left half shaft, and  $k_{h2}$  is the stiffness coefficient of right half shaft

The dynamic of the drive train is decided by the clutch status. When the clutch is slipping, it is shown in

$$\begin{aligned} J_e \dot{\omega}_e &= T_e - T_c - d_e \dot{\omega}_e \\ J_1 \dot{\omega}_c &= T_c - d_1 \dot{\omega}_c - \frac{k_s \theta_s + d_s \dot{\theta}_s}{r} \\ J_2 \dot{\omega}_w &= -T_l - d_2 \dot{\omega}_w + k_s \theta_s + d_s \dot{\theta}_s \\ \dot{\theta}_s &= \frac{\dot{\theta}_c}{r} - \dot{\theta}_w = \frac{\omega_c}{r} - \omega_w, \end{aligned} \quad (4)$$

where  $\theta_s$  is the drive shaft torsion angle;  $\omega_e$  is the engine speed;  $\omega_c$  is the clutch speed;  $\omega_w$  is the wheel speed.

At this time, the clutch friction torque is generated by Coulomb friction and decided mainly by the actuator force  $F_n$ , as shown in

$$T_c = F_n \mu R_a \text{sign}(\omega_e - \omega_c), \quad (5)$$

where  $F_n$  is the press force actuating on the clutch plate,  $\mu$  is the dynamic friction coefficient of the clutch surface material, and  $R_a$  is the effective radius of the clutch plate.

When the clutch is engaged, the engine is rigidly coupled to the driveline. At this time, the clutch slipping speed

$\omega_{sl} = \omega_e - \omega_c = 0$ . Consequently, the two equations of motion of the engine and the clutch are merged into a single equation:

$$(J_e + J_1) \dot{\omega}_{e/c} = T_e - (d_e + d_1) \dot{\omega}_{e/c} - \frac{k_s \theta_s + d_s \dot{\theta}_s}{r}. \quad (6)$$

Moreover, during engaged phase, the torque through the clutch cannot be altered by the actuator force anymore. Instead of a controlled input, it becomes a constrained variable.

$$|T_c| \leq T_{c,\max} = F_n \mu_0 R_a, \quad (7)$$

where  $T_{c,\max}$  is the maximum friction torque of the clutch disc and  $\mu_0$  is the static friction coefficient.

So the switch logic model is shown in Figure 3. We define two statuses of the clutch as Slipping and Engaged.

Considering the effect of the engine and clutch actuator dynamics, the engine torque and the clutch friction torque are modeled as first-order dynamics with time delays  $\tau_e$  and  $\tau_c$ , respectively. The equations are as follows:

$$\begin{aligned} \tau_e \dot{T}_e + T_e &= T_{e,\text{sp}} + T_{e,\text{req}} \\ \tau_c \dot{T}_c + T_c &= T_{c,\text{sp}}, \end{aligned} \quad (8)$$

where  $T_{e,\text{sp}}$  and  $T_{c,\text{sp}}$  are the set points of the clutch controller for the engine controller and clutch actuator controller. And  $T_{e,\text{req}}$  is the driver demand torque. The torque-based controls are now commonly used in modern engine controllers. The torque requirement from the clutch controller will be added to the driver demand torque in the engine controller. Therefore, the real engine torque is the sum of these requirements.

The engine torque delay is related to the engine speed and engine cylinder number, which is often presented by (9), where the cylinder number of the engine is  $n_{\text{cylinder}}$  and the engine speed is  $n_e$  in revolutions per second.

$$\tau_e = \frac{2}{n_{\text{cylinder}} n_e}. \quad (9)$$

And for the clutch actuator time delay parameter, we can use simulation result of the detailed clutch actuator model to identify it. Literature [9] has shown that the first-order linear function with the identified parameters has a similar simulation result to the detailed model.

In the continuous state-space representation, the driveline model can be written as follows (10). In the equation, the controller outputs and disturbance torque are distinguished.

$$\begin{aligned} \dot{x} &= A_c x + B_{cu} u + B_{cr} T_{e,\text{req}} + B_{cl} T_l = \begin{cases} A_{c1} x + B_{cu1} u + B_{cr} T_{e,\text{req}} + B_{cl} T_l & (\text{clutch status} = \text{Slipping}) \\ A_{c2} x + B_{cu2} u + B_{cr} T_{e,\text{req}} + B_{cl} T_l & (\text{clutch status} = \text{Engaged}) \end{cases} \\ y &= C_c x, \end{aligned} \quad (10)$$

where the state variables, input variables, and output variables are defined in as follows:

$$\begin{aligned} x &= [\omega_e \ \theta_s \ \omega_c \ \omega_w \ T_e \ T_c]^T \\ u &= [T_{e,sp} \ T_{c,sp}] \\ y &= [\omega_e \ \omega_{sl} \ \omega_s \ T_e \ T_c]. \end{aligned} \quad (11)$$

State-space equation parameters are defined as follows:

$$A_{c1} = \begin{bmatrix} -\frac{d_e}{J_e} & 0 & 0 & 0 & \frac{1}{J_e} & -\frac{1}{J_e} \\ 0 & 0 & \frac{1}{r} & -1 & 0 & 0 \\ 0 & -\frac{k_s/r}{J_1} & -\frac{d_1+d_s/r^2}{J_1} & \frac{d_s/r}{J_1} & 0 & \frac{1}{J_1} \\ 0 & \frac{k_s}{J_2} & \frac{d_s/r}{J_2} & -\frac{d_1+d_s}{J_2} & 0 & 0 \\ 0 & 0 & 0 & 0 & \frac{1}{\tau_e} & 0 \\ 0 & 0 & 0 & 0 & 0 & \frac{1}{\tau_c} \end{bmatrix} \quad (12a)$$

$$\begin{aligned} A_{c2} &= \begin{bmatrix} 0 & -\frac{k_s/r}{J_e+J_1} & -\frac{d_e+d_1+d_s/r^2}{J_e+J_1} & \frac{d_s/r}{J_e+J_1} & \frac{1}{J_e+J_1} & 0 \\ 0 & 0 & \frac{1}{r} & -1 & 0 & 0 \\ 0 & -\frac{k_s/r}{J_e+J_1} & -\frac{d_e+d_1+d_s/r^2}{J_e+J_1} & \frac{d_s/r}{J_e+J_1} & \frac{1}{J_e+J_1} & 0 \\ 0 & \frac{k_s}{J_2} & \frac{d_s/r}{J_2} & -\frac{d_1+d_s}{J_2} & 0 & 0 \\ 0 & 0 & 0 & 0 & \frac{1}{\tau_e} & 0 \\ 0 & 0 & 0 & 0 & 0 & 0 \end{bmatrix} \\ B_{cu1} &= \begin{bmatrix} 0 & 0 & 0 & 0 & \frac{1}{\tau_e} & 0 \\ 0 & 0 & 0 & 0 & 0 & \frac{1}{\tau_c} \end{bmatrix}^T \\ B_{cu2} &= \begin{bmatrix} 0 & 0 & 0 & 0 & \frac{1}{\tau_e} & 0 \\ 0 & 0 & 0 & 0 & 0 & 0 \end{bmatrix}^T \\ B_{cr} &= \begin{bmatrix} 0 & 0 & 0 & 0 & \frac{1}{\tau_e} & 0 \end{bmatrix}^T \\ B_{cl} &= \begin{bmatrix} 0 & 0 & 0 & -\frac{1}{J_2} & 0 & 0 \end{bmatrix}^T \end{aligned} \quad (12b)$$

### 3. Controller Design

**3.1. Control Objectives.** For the AMT clutch controller design, different phases need different control objectives. Usually, when vehicle is starting up, the clutch status is Slipping and Engaged in turn. Because the slipping time and the driving

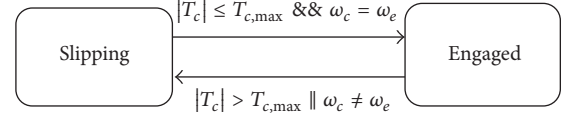


FIGURE 3: Switching logic of the clutch statuses.

comfort are conflicted, a driver intention will be used to change the slipping time dynamically. When the driver wants a faster dynamic process, the slipping time will be decreased. But when the driver does not need so fast dynamic process, then the slipping time could be increased, so as to increase the driving comfort.

Because the torsion vibration influences the driving comfort badly, the objective of torsion speed  $\dot{\theta}_s$  should be controlled in every phase. Good drivability also means that vehicle responds to the driver's demand exactly with no delay. In this sense, the controller output should not have a big effect on the driver's intended torque. Therefore, the controller is expected to minimize the engine torque requirement from the clutch controller in clutch Engaged phase.

Moreover, the controller should satisfy the constraints such as that the engine torque and clutch torque set points should be limited in the permitted minimum and maximum values. And in order to keep the engine in the so-called no-kill condition [9], the engine speed should be bigger higher than the idle speed.

For every phase, the control objective is defined as follows.

**3.1.1. Slipping Phase.** In Slipping phase, the conversion condition is  $\omega_{sl} = 0$ . We design a reference trajectory for clutch slipping speed as follows (13). Typical trajectory is showed in Figure 4.

$$\begin{aligned} \omega_{sl}^{\text{ref}} &= 2\omega_{sl,0} \left( \frac{t-t_{0,\text{slipping}}}{t_{f,\text{slipping}}} \right)^3 \\ &\quad - 3\omega_{sl,0} \left( \frac{t-t_{0,\text{slipping}}}{t_{f,\text{slipping}}} \right)^2 + \omega_{sl,0}. \end{aligned} \quad (13)$$

It obeys the constraint as follows:

$$\begin{aligned} \omega_{sl}^{\text{ref}}(t_{0,\text{slipping}}) &= \omega_{sl,0}, \\ \omega_{sl}^{\text{ref}}(t_{f,\text{slipping}}) &= 0, \\ \dot{\omega}_{sl}^{\text{ref}}(t_{0,\text{slipping}}) &= \dot{\omega}_{sl}^{\text{ref}}(t_{f,\text{slipping}}) = 0, \end{aligned} \quad (14)$$

where  $\omega_{sl}^{\text{ref}}$  is the reference slipping speed,  $\omega_{sl,0}$  is the initial slipping speed,  $t_{0,\text{slipping}}$  is the time of slipping start, and  $t_{f,\text{slipping}}$  is the duration of slipping; it is a variable which is a function of driver acceleration pedal  $\alpha$ , shown in (15), where  $t_{f,\text{slipping}}^{\text{max}}$  and  $t_{f,\text{slipping}}^{\text{min}}$  are the maximum and minimum permitted opening time, respectively:

$$t_{f,\text{slipping}} = t_{f,\text{slipping}}^{\text{max}} - (t_{f,\text{slipping}}^{\text{max}} - t_{f,\text{slipping}}^{\text{min}}) \alpha. \quad (15)$$

Meanwhile the torsion vibration should be kept small. And the engine torque should be kept close to the driver

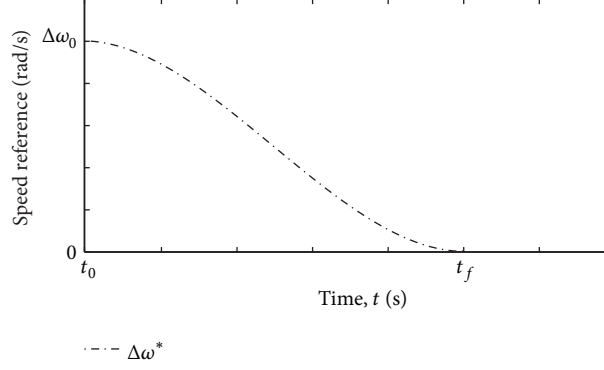


FIGURE 4: Reference trajectory of clutch slipping speed.

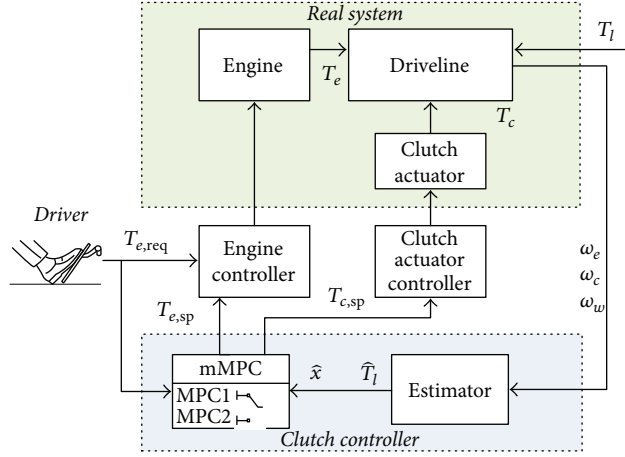


FIGURE 5: mMPC based clutch controller scheme.

torque intended. Therefore, the control objective can be written as (16).  $J_{\text{slipping}}$  is the cost function of this phase.

$$\min (J_{\text{slipping}}) = \min \left( \left\| \lambda_{1,\text{slipping}} (\gamma_2 - \omega_{\text{sl}}^{\text{ref}}) \right\|^2 + \left\| \lambda_{2,\text{slipping}} \gamma_3 \right\|^2 + \left\| \lambda_{3,\text{slipping}} u_1 \right\|^2 \right), \quad (16)$$

where  $\lambda_{1,\text{slipping}}$ ,  $\lambda_{2,\text{slipping}}$ , and  $\lambda_{3,\text{slipping}}$  are weighting factors of slipping time, torsion vibration, and driver torque intended.

**3.1.2. Engaged Phase.** In Engaged phase, the engine is synchronized with the transmission. The clutch torque does not influence the dynamics of the driveline. But the clutch maximum static friction torque should be kept not smaller than the engine torque, so that slipping is avoided. Meanwhile, the torsion vibration should be reduced, and the engine torque should be close to the driver torque intended. So the control objective can be written as (17).  $J_{\text{engaged}}$  is the cost function of this phase.

$$\min (J_{\text{engaged}}) = \min \left( \left\| \lambda_{2,\text{engaged}} \gamma_3 \right\|^2 + \left\| \lambda_{3,\text{engaged}} u_1 \right\|^2 \right) \quad (17)$$

$$T_{c,\text{sp}} > T_{e,\text{sp}}, \quad (18)$$

where  $\lambda_{2,\text{engaged}}$  and  $\lambda_{3,\text{engaged}}$  are weighting factors of torsion vibration and driver torque intended.

**3.2. Control Scheme.** Multiple-MPC (mMPC) strategy is used for clutch control, due to the ability to handle multivariable system, to take time-domain constraints into account explicitly and deal with multiple objectives in a somehow optimal sense. What is more, there are multiphases with different control targets, so we design different controllers for different phases and switch the controllers by the clutch status.

The principle of MPC is to calculate a sequence of control actions over a finite receding horizon by optimizing the certain optimization function, while only implementing the first element on the control plant each time. In this application, the clutch control scheme is shown in Figure 5.

An estimator uses the measured engine speed, clutch speed, and wheel speed to estimate the unmeasured disturbance  $T_l$  and other state variables of the state-space equation in (10). Therefore, all of the state variables and disturbance input variables are measured. We can predict the future output variables of the equation. And an optimization function which is defined in Section 3.1 could be solved to calculate the target engine torque and clutch friction torque.

**3.3. Load and State Variables Estimation.** The vehicle is subjected to various load disturbances. Since the load mainly depends on unmeasured entities, such as slope, it is difficult to include it in the model. The literature [13] presented a method to estimate the load torque  $T_l$ . The method is based on the assumption that the load disturbance is constant or slowly varying, so it can be described or modeled as follows:

$$\dot{T}_l = 0. \quad (19)$$

Treating  $T_l$  as a state variable, the system can be described as follows:

$$\begin{aligned} \begin{bmatrix} \dot{x} \\ \dot{T}_l \end{bmatrix} &= \begin{bmatrix} A_c & B_{cl} \\ 0 & 0 \end{bmatrix} \begin{bmatrix} x \\ T_l \end{bmatrix} + \begin{bmatrix} B_{cu} & B_{cr} \\ 0 & 0 \end{bmatrix} [u \quad T_{e,req}] \\ &= A_l x_l + B_l u_l \end{aligned} \quad (20)$$

$$y = [C_c \quad 0] \begin{bmatrix} x \\ T_l \end{bmatrix} = C_l x_l.$$

The state estimation is given by

$$\hat{x}_l = A_l \hat{x}_l + B_l u_l + K_l (y - C_l \hat{x}_l). \quad (21)$$

Then  $K_l$  is a Kalman estimator coefficient and can be calculated using the algebraic Riccati equation to minimize the estimation error.

By now, the disturbance torques  $T_{e,req}$  and  $T_l$  can be treated the same. So we define two new symbols as follows:

$$\begin{aligned} T_d &= [T_{e,req} \quad T_l] \\ B_{cd} &= [B_{cr} \quad B_{cl}]^T. \end{aligned} \quad (22)$$

So the state-space equation (10) can be rewritten as follows:

$$\dot{x} = A_c x + B_{cu} u + B_{cd} T_d. \quad (23)$$

**3.4. Multiple-Model Predictive Controller.** Because the system state-space equation considers the engine time delay which is not a constant, the coefficients of the state equation are changed step by step. If we use method of nonlinear MPC, it will be very complex and not suitable for real-time application. Here, we introduce a new method for solving this problem. Because the delay time of the engine torque generation does not change much in a prediction horizon, we assume that the delay time is a constant in a prediction horizon. Then we can deal with the equation as a linear system

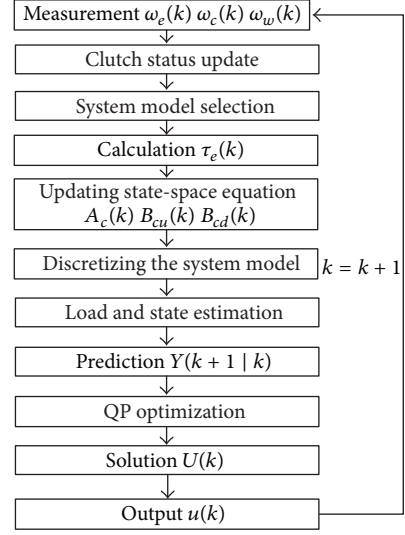


FIGURE 6: mMPC clutch controller process.

in every prediction process and keep the delay time updating step by step. So in every step, we need to firstly calculate the delay time  $\tau_e(k)$  using the measured state  $\omega_e(k)$  and select the right model based on the clutch status in (10). Then we update the coefficients of the state-space equation  $A_c(k)$ ,  $B_{cu}(k)$ , and  $B_{cr}(k)$ , which have relationship with  $\tau_e(k)$ . We convert the updated continuous state-space equation to discrete state-space equation using forward Euler method. Using the discrete state-space equation, we estimate the load torque  $\hat{T}_l(k)$  and state variables which are not measured directly based on Kalman filter strategy. After that, we can predict the output vector of the system  $Y(k + 1 | k)$  in predictive horizon. By solving the right optimization function based on the clutch status defined in Section 3.1 with constraints, the control vector in control horizon  $U(k)$  can be calculated. The first element of  $U(k)$  is selected to be the controller output. The whole process of the mMPC is described in Figure 6.

According to the main principle of predictive control [14], with the measured state vector  $\hat{x}(k)$  as the initial condition at time  $k$ , the future torsion speed is predicted on the discrete system model. In this paper, the prediction horizon is illustrated with  $p$ . The control horizon is illustrated with  $m$ , satisfying  $m \leq p$ . In order to reduce the system prediction equations, the assumptions are set as follows.

Out of control horizon, the control variable keeps unchanged.

Disturbance torque keeps unchanged in prediction horizon.

We define that the predicted output vector in horizon  $p$  is  $Y(k + 1 | k)$  and the predicted input vector in horizon  $m$  is  $U(k)$  as shown in

$$Y(k + 1 | k) = \begin{bmatrix} Y(k + 1 | k) \\ Y(k + 2 | k) \\ \vdots \\ y(k + p | k) \end{bmatrix}_{p \times 1},$$

$$U(k) = \begin{bmatrix} u(k) \\ u(k+1) \\ \vdots \\ u(k+m-1) \end{bmatrix}_{m \times 1}, \quad (24)$$

where  $k+1 | k$  represents the prediction of time  $k+1$  at time  $k$ .

According to the basis of MPC and exploiting above contents, we can infer the sequences of outputs to be predicted and present them in the form of

$$Y(k+1 | k) = S_x \hat{x}(k) + S_u U(k) + S_d \hat{T}_d(k), \quad (25)$$

where  $S_x$ ,  $S_d$ , and  $S_u$  are calculated by (26) and  $\hat{T}_d(k)$  is calculated using the estimation variable  $\hat{T}_l(k)$ , which is obtained from (27).

$$S_x = \begin{bmatrix} CA \\ CA^2 \\ \vdots \\ CA^p \end{bmatrix}_{p \times 1}$$

$$S_d = \begin{bmatrix} CB_d \\ \sum_{i=1}^2 CA_d^{i-1} B_d \\ \vdots \\ \sum_{i=1}^p CA_d^{i-1} B_d \end{bmatrix}_{p \times 1} \quad (26)$$

$$S_u = \begin{bmatrix} CB_u & 0 & \cdots & 0 \\ CAB_u & CB_u & \cdots & 0 \\ \vdots & \vdots & \vdots & \vdots \\ CA^{p-1}B_u & CA^{p-2}B_u & \cdots & CA^{p-m}B_u \end{bmatrix}_{p \times m}$$

$$\hat{T}_d(k) = [T_r(k) \quad \hat{T}_l(k)]^T. \quad (27)$$

Because the main control requirement is to minimize the cost function, the optimization function can be defined as

$$\begin{aligned} \min_{U(k)} J(U(k), Y(k+1 | k)) \\ = \|W_y (Y(k+1 | k) - \text{Re}(k+1 | k))\|^2 \\ + \|W_u U(k)\|^2, \end{aligned} \quad (28)$$

where  $W_y$  and  $W_u$  are the weighting factor matrixes of the two objectives, respectively.  $\text{Re}(k+1 | k)$  is the reference trajectory matrix. In different phases, these two weighting factors are composed with  $\lambda$  defined in Section 3.1. For the

reference trajectory, because it includes time information, in every prediction step, the value can be calculated based on the time step.

The optimization problem (28) can be formulated as a quadratic programming (QP) problem in

$$\min_{U(k)} U(k)^T H U(k) - G(k+1 | k)^T U(k), \quad (29)$$

where

$$H = S_u^T W_y^T W_y S_u + W_u^T W_u \quad (30a)$$

$$G(k+1 | k) = 2S_u^T W_y^T W_y E_p(k+1 | k) \quad (30b)$$

$$E_p(k+1 | k) = \text{Re}(k+1) - S_x \hat{x}(k) - S_d \hat{T}_d(k). \quad (30c)$$

We assume that the constraints are also kept unchanged in prediction horizon. Solving the optimization function with the constraints can get the control sequence  $U(k)$ . Applying the first element  $u(k)$  to the plant and this process is repeated at every time step.

## 4. Evaluation the Controllers by Simulation

**4.1. Simulation Model.** In this section, some simulation results are given and analyzed to evaluate the controllers. In order to simulate, a simulation model shown in Figure 7 is built in Matlab/Simulink/Simscape. It includes the longitudinal vehicle dynamics, lumped mass driveline, mean value engine model, pneumatic clutch actuator, and the engine controller and clutch actuator controller model. The constructed simulation model can capture the important transient dynamics of the driveline, such as the delay of the engine torque generation, the delay of the clutch actuator, clutch damper vibration, flexible drive shaft, and half drive shaft oscillation. As well as tire slip, even road slope and road surface which may have an effect on the clutch controller are all included in the model. Some main vehicle parameters are listed in Table 1.

For the engine model, the input is fuel mass and, for the clutch actuator, the input is solenoid On/Off valves; an engine controller and clutch actuator controller are also modeled with simplified control strategy. And we assume that these two controllers have high control accuracy. In order to simulate the gearshift, a simple gear controller is modeled. It just includes gearshift timing. And the clutch control strategy described in this paper is also built as a model in Simulink. In this simulation, the sampling period for MPC control updating is set to 10 ms, and the simulation updating period is 1 ms.

**4.2. Simulation Results.** In order to fully evaluate the controllers, there are several maneuvers defined as follows:

- (1) Open loop control for the start-up with low torque demand (M1)
- (2) Open loop control for the start-up with high torque demand (M2)
- (3) Close loop control for the start-up with low torque demand (M3)

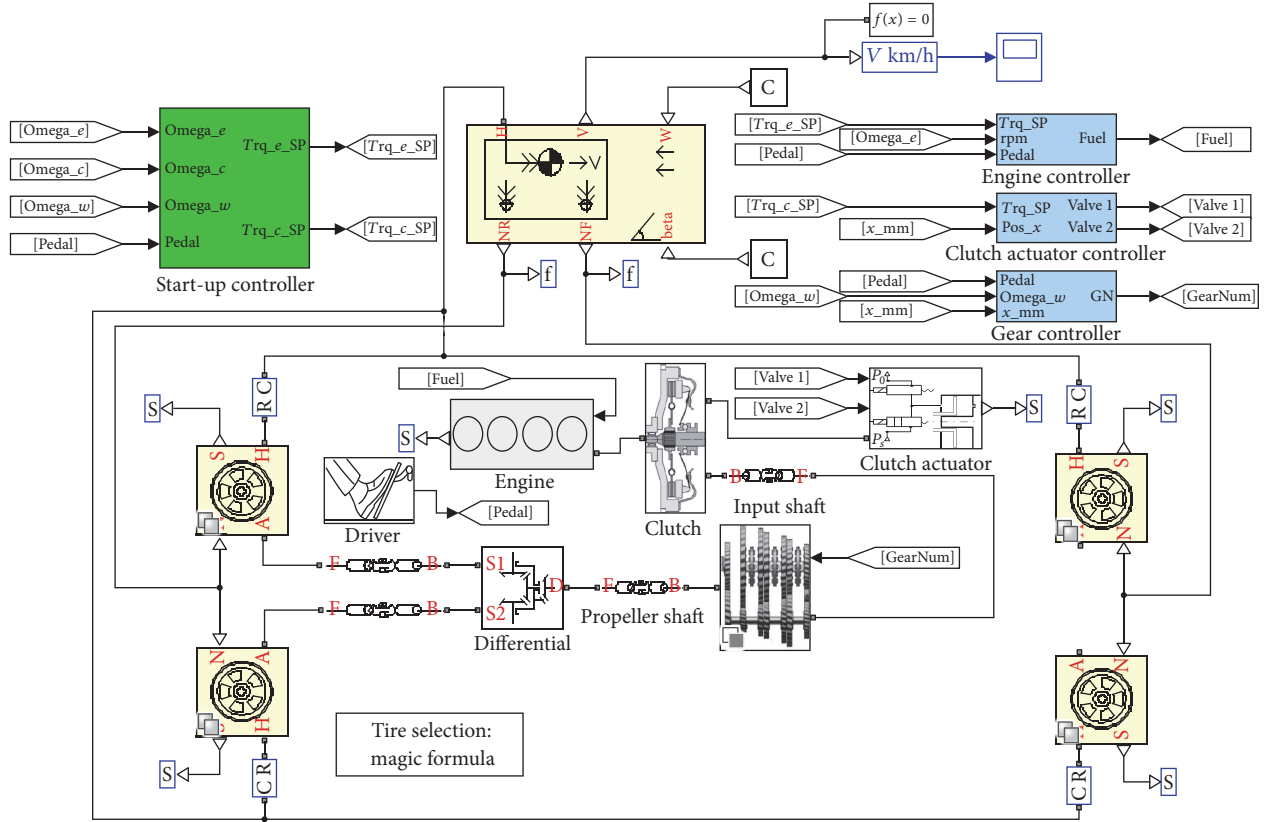


FIGURE 7: Simulation model of a heavy-duty truck.

TABLE 1: Normal values of parameters of simulation model.

Symbol	Parameters	Value & unit
$J_e$	Engine flywheel inertia	2.1 kg/m <sup>2</sup>
$J_c$	Clutch disk inertia	0.1 kg/m <sup>2</sup>
$J_{g1}$	Equivalent inertia of gearbox primary shaft	0.1 kg/m <sup>2</sup>
$J_{g2}$	Equivalent inertia of gearbox secondary shaft	0.1 kg/m <sup>2</sup>
$J_d$	Equivalent inertia of propeller shaft and differential gear inertia	0.1 kg/m <sup>2</sup>
$J_2$	Equivalent inertia of half drive shaft and wheels and vehicle	4020 kg/m <sup>2</sup>
$d_e$	Damping of engine shaft to bearings	0.1 Nm/rad/s
$d_c$	Damping of clutch shaft to bearings	0.1 Nm/rad/s
$d_2$	Damping of wheels to bearings	2 Nm/rad/s
$d_s$	Damping of the drive shaft	3 kNm/rad/s
$k_s$	Stiffness of the drive shaft	175 kNm/rad
$r$	Transmission ratio of drive train	35.04
$n$	Engine cylinder number	6
$\tau_c$	Clutch actuator delay time	0.3 s
$m$	Vehicle mass	16 ton
$R_w$	Radius of tire	0.5 m

## (4) Close loop control for the start-up with high torque demand (M4)

Figures 8 and 9 are the simulation results of maneuvers M1 and M2. M1 and M2 are maneuvers without clutch optimization controller. M1 starts with a low driver demand engine torque which is 100 Nm. And clutch friction torque is also set to 100 Nm. M2 starts with a high driver demand engine torque which is 800 Nm. And clutch friction torque is also set to 800 Nm. From the simulation results, we can see that, for both M1 and M2, there are torsion vibrations in both Slipping and Engaged phase. And the vibration frequency in Slipping phase is higher than that in Engaged phase. Higher torque can evoke serious oscillation but can shorten the slipping time. From Figures 8(c) and 9(c), we can see that the acceleration curves also show many shakes and jerks in the whole process. The shake and jerk evoke a bad drivability.

Figure 10 is the simulation results of maneuver M3. M3 is the start-up maneuver with optimization controller with low driver torque demand which is 100 Nm. It is a low driver pedal position input. Therefore, the controller generates a reference slipping speed trajectory as shown in Figure 10(d) lasted about 5 s. From the simulation results in Figures 10(a)–10(d), we can see that the torsion vibration is reduced and the engine speed tends to increase at a nearly fixed rate. The acceleration of the whole process does not have many shakes

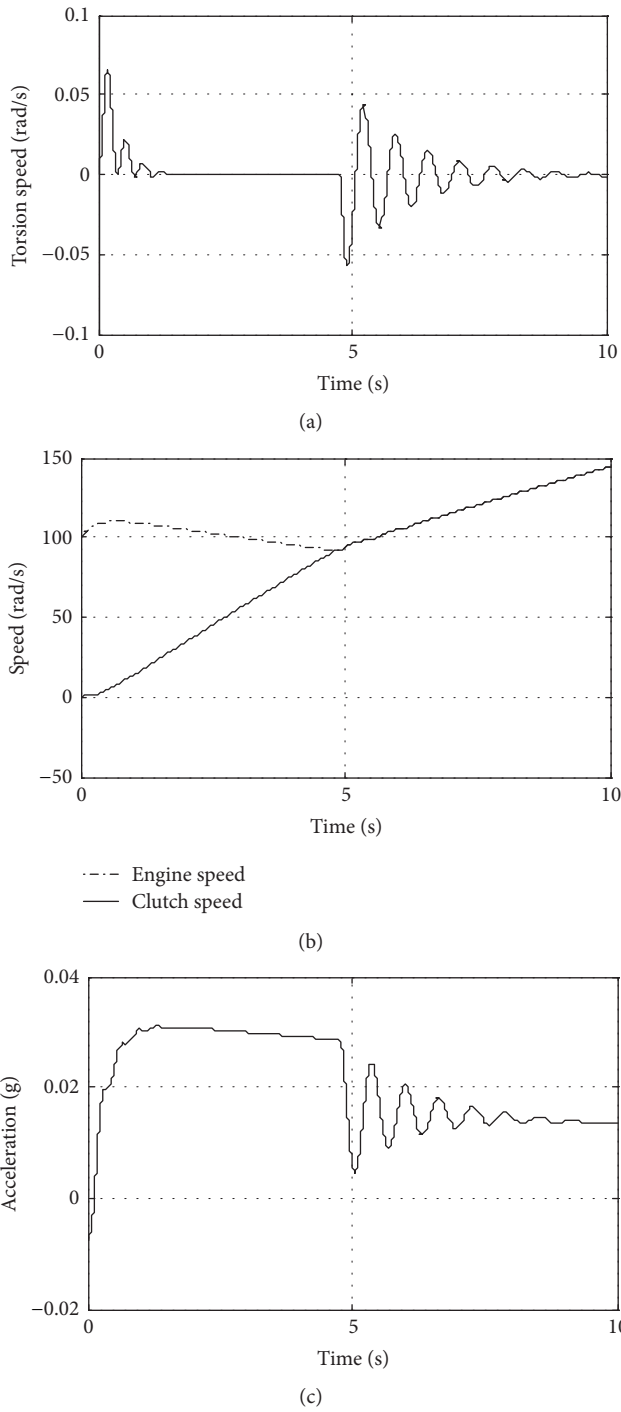


FIGURE 8: M1 maneuver simulation results.

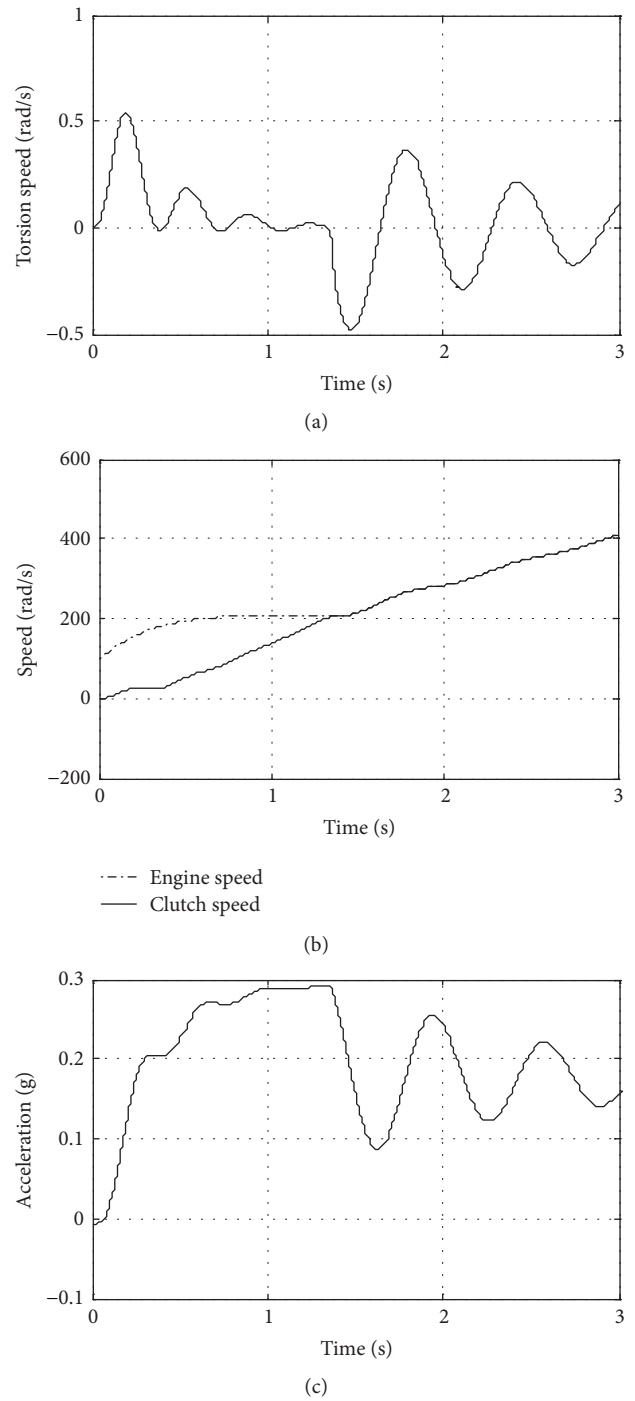


FIGURE 9: M2 maneuver simulation results.

and jerks, and the slipping speed has a good tracking to the reference trajectory. From Figures 10(e)-10(f), we can see that the controller outputs are in the area of constraints. We set the constraint of engine torque requirement from clutch control as  $[-100 \text{ Nm}, 200 \text{ Nm}]$ . The minimum value is based on that the engine real torque cannot be lower than zero. The maximum value is based on the low driver pedal maximum engine torque limit. We set the constraint of the

clutch friction torque as  $[0, 300 \text{ Nm}]$ , with considering that the clutch torque should not be larger or lower than engine torque.

Figure 11 shows the simulation results of maneuver M4. M4 is the start-up maneuver with optimization controller with high driver torque demand which is 800 Nm. It is a high driver pedal position input. So the controller generates a reference slipping speed trajectory as shown in Figure 11(d)

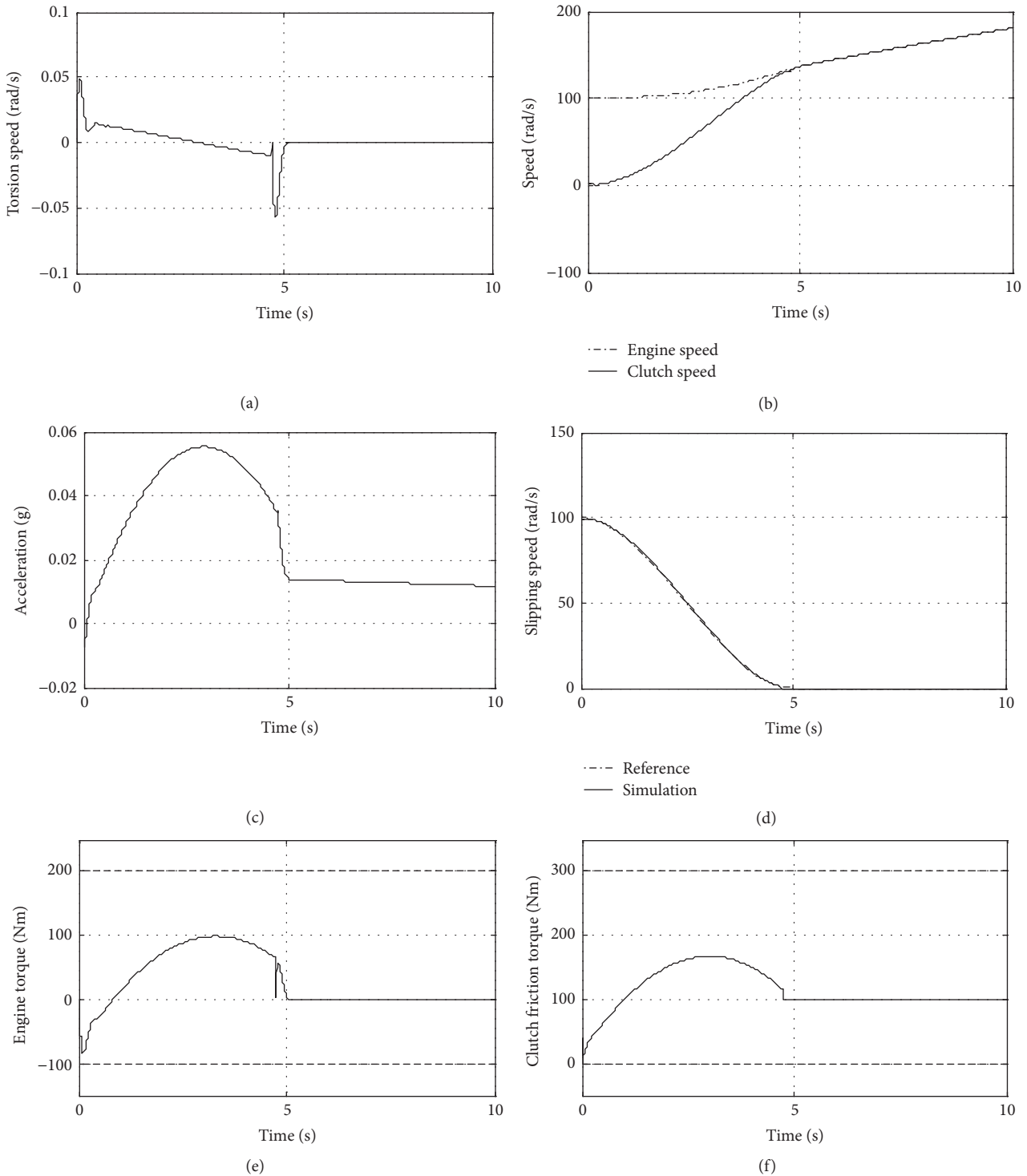


FIGURE 10: M3 maneuver simulation results.

lasted about 1.5 s. From the simulation results in Figures 11(a)–11(d), we can see that the torsion vibration is reduced and the engine speed tends to increase at nearly fixed rate. The acceleration of the whole process does not have many shakes and jerks, and the slipping speed has a good tracking to the reference trajectory. From Figures 11(e)–11(f), we can

see the controller outputs are in the area of constraints. We set the constraint of engine torque requirement from clutch control to  $[-800 \text{ Nm}, 300 \text{ Nm}]$ . The minimum value is based on that the engine real torque cannot be lower than zero. The maximum value is based on the high driver pedal maximum engine torque limit. We set the constraint of the

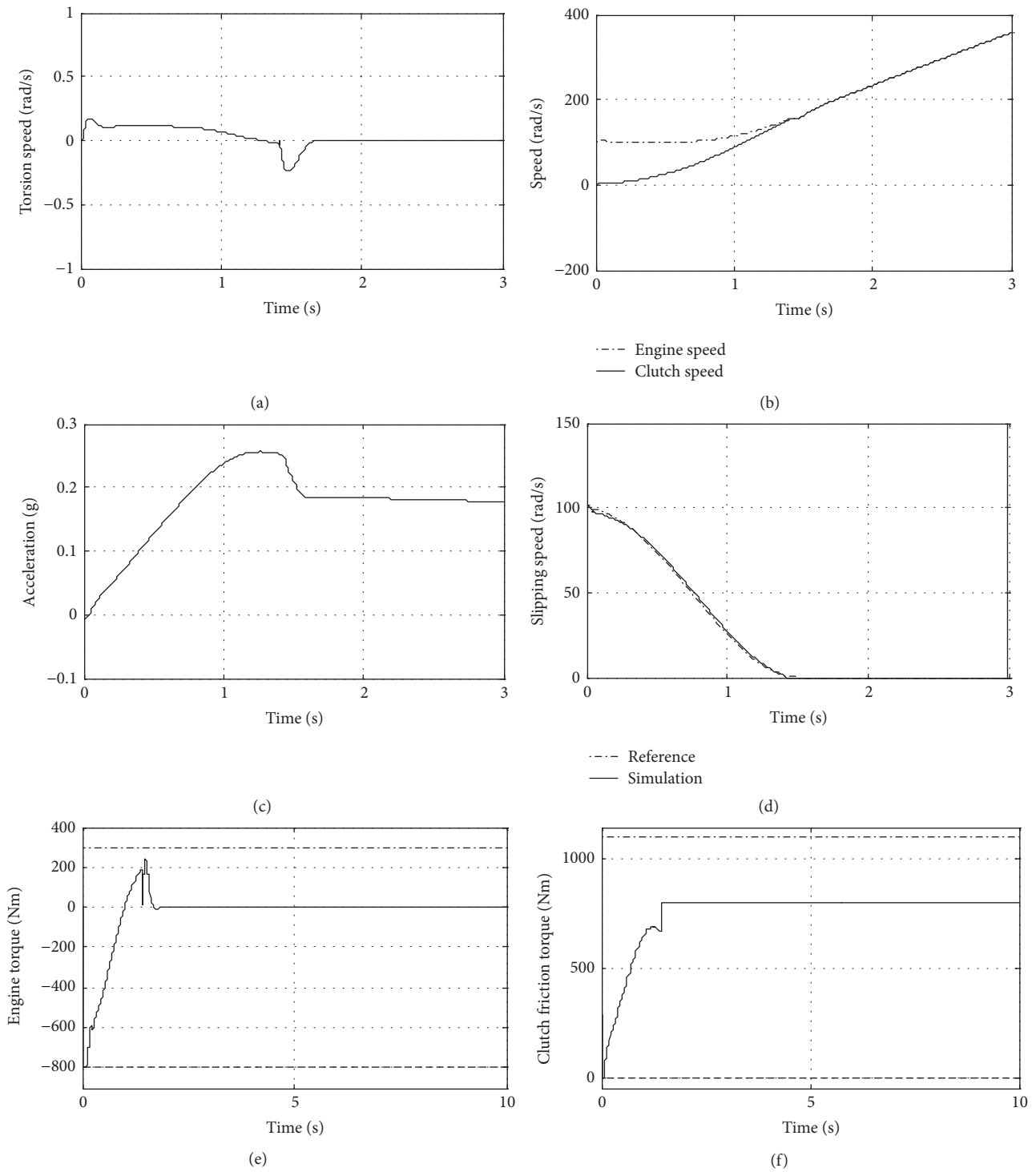


FIGURE 11: M4 maneuver simulation results.

clutch friction torque to  $[0, 1100 \text{ Nm}]$ , with considering that the clutch torque should not be larger or lower than the engine torque.

### 5. Conclusions

A multiple-MPC for dry clutch control for AMT truck has been proposed. Two driveline models are built based on the

clutch position. Two different control objectives are designed for different phases including Slipping and Engaged phases. Therefore, two MPC controllers with two prediction models are designed for the AMT clutch control for the start-up process. In these controllers, the clutch slipping time is decided by the driver's intention. The torsion vibration is controlled not only in the Engaged phase but also in the Slipping phase. Simulation results have shown the mMPC

controllers have good performance in each phase during start-up process in AMT truck. The drivability of the vehicle is enhanced with the optimization controller.

The proposed scheme is only for the start-up process control so far, it will be enhanced in the future for the gearshift process control to form a complete high level controller for the AMT clutch control.

### Conflicts of Interest

The authors declare that there are no conflicts of interest regarding the publication of this paper.

### Acknowledgments

The authors would like to acknowledge the National Natural Science Foundation of China for financially supporting this research under Project no. 51475043.

### References

- [1] G. Lucente, M. Montanari, and C. Rossi, "Modelling of an automated manual transmission system," *Mechatronics*, vol. 17, no. 2-3, pp. 73–91, 2007.
- [2] R. Amari, M. Alamir, and P. Tona, "Unified MPC strategy for idle speed control, vehicle start-up and gearing applied to an automated manual transmission," in *Proceeding of the 17th IFAC World Congress*, Seoul, South Korea, 2008.
- [3] R. E. Dorey and C. B. Holmes, "Vehicle driveability—Its characterisation and measurement," SAE Technical Papers, 1999.
- [4] R. Zanasi, A. Visconti, G. Sandoni, and R. Morselli, "Dynamic modeling and control of a car transmission system," in *Proceeding of the IEEE/ASME International Conference on Advanced Intelligent Mechatronics*, Como, Italy, 2001.
- [5] V. T. Minh and A. A. Rashid, "Automatic control of clutches and simulations for parallel hybrid vehicles," *International Journal of Automotive Technology*, vol. 13, no. 4, pp. 645–651, 2012.
- [6] A. C. Van der Heijden, A. F. Serrarens, M. K. Camlibel, and H. Nijmeijer, "Hybrid optimal control of dry clutch engagement," *International Journal of Control*, vol. 80, no. 11, pp. 1717–1728, 2007.
- [7] P. Dolcini, H. Béchart, and C. C. De Wit, "Observer-based optimal control of dry clutch engagement," in *Proceedings of the 44th IEEE Conference on Decision and Control, and the European Control Conference, (CDC-ECC '05)*, pp. 440–445, Prague, Czech, December 2005.
- [8] P. Dolcini, C. Canudas de Wit, and H. Béchart, "Lurch avoidance strategy and its implementation in AMT vehicles," *Mechatronics*, vol. 18, no. 5-6, pp. 289–300, 2008.
- [9] L. Glielmo, L. Iannelli, V. Vacca, and F. Vasca, "Gearshift control for automated manual transmissions," *IEEE/ASME Transactions on Mechatronics*, vol. 11, no. 1, pp. 17–26, 2006.
- [10] G. J. L. Naus, M. A. Beenackers, R. G. M. Huisman, M. J. G. Van De Molengraft, and M. Steinbuch, "Robust control of a clutch system to prevent judder-induced driveline oscillations," vol. 48, pp. 1379–1394, Proceedings of the 8th International Symposium on Advanced Vehicle Control, Kobe, Japan.
- [11] M. Pisaturo, M. Cirrincione, and A. Senatore, "Multiple constrained MPC design for automotive dry clutch engagement," *IEEE/ASME Transactions on Mechatronics*, vol. 20, no. 1, pp. 469–480, 2015.
- [12] A. Bemporad, F. Borrelli, L. Glielmo, and F. Vasca, "Hybrid control of dry clutch engagement," in *Proceeding of the 6th European Control Conference, (ECC '01)*, Porto, Portugal, 2001.
- [13] J. Fredriksson, H. Weiefors, and B. Egardt, "Powertrain control for active damping of driveline oscillations," *Vehicle System Dynamics*, vol. 37, no. 5, pp. 359–376, 2010.
- [14] D. Q. Mayne, J. B. Rawlings, C. V. Rao, and P. O. Scokaert, "Constrained model predictive control: stability and optimality," *Automatica*, vol. 36, no. 6, pp. 789–814, 2000.

## Research Article

# Predicting the Pullout Capacity of Small Ground Anchors Using Nonlinear Integrated Computing Techniques

Mosbeh R. Kaloop,<sup>1,2,3</sup> Jong Wan Hu,<sup>1,2</sup> and Emad Elbeltagi<sup>4,5</sup>

<sup>1</sup>Department of Civil and Environmental Engineering, Incheon National University, Incheon, Republic of Korea

<sup>2</sup>Incheon Disaster Prevention Research Center, Incheon National University, Incheon, Republic of Korea

<sup>3</sup>Department of Public Works and Civil Engineering, Mansoura University, Mansoura, Egypt

<sup>4</sup>Department of Structural Engineering, Mansoura University, Mansoura, Egypt

<sup>5</sup>Department of Civil Engineering, Mansoura Higher Institute for Engineering and Technology, Talkha, Egypt

Correspondence should be addressed to Jong Wan Hu; [jongp24@incheon.ac.kr](mailto:jongp24@incheon.ac.kr)

Received 6 January 2017; Accepted 29 March 2017; Published 19 April 2017

Academic Editor: Paulo B. Gonçalves

Copyright © 2017 Mosbeh R. Kaloop et al. This is an open access article distributed under the Creative Commons Attribution License, which permits unrestricted use, distribution, and reproduction in any medium, provided the original work is properly cited.

This study investigates predicting the pullout capacity of small ground anchors using nonlinear computing techniques. The input-output prediction model for the nonlinear Hammerstein-Wiener (NHW) and delay inputs for the adaptive neurofuzzy inference system (DANFIS) are developed and utilized to predict the pullout capacity. The results of the developed models are compared with previous studies that used artificial neural networks and least square support vector machine techniques for the same case study. The in situ data collection and statistical performances are used to evaluate the models performance. Results show that the developed models enhance the precision of predicting the pullout capacity when compared with previous studies. Also, the DANFIS model performance is proven to be better than other models used to detect the pullout capacity of ground anchors.

## 1. Introduction

Light structures, which are built in open areas, are supported with the ground using small anchors. Such anchors are designed to resist tensile and uplift forces [1–4] and are usually supported at a shallow depth (about 1 m) with small pullout capacity [2, 5, 6]. Therefore, designers rarely put efforts into designing such small ground anchors [5]. In contrast, Shahin and Jaksa [7] introduced new design criteria for small anchors based on advanced prediction models.

The numerical prediction models are used to detect the pullout capacity of small ground anchors based on input-output mapping for the in situ data. Shahin and Jaksa [7] utilized 119 anchors' test data to introduce prediction models. They used the neural networks technique to extract the pullout capacity [7]. In addition, Shahin and Jaksa [2, 6] used artificial neural network (ANN) model for the design of small anchors and they were able to predict the pullout capacity. Samui et al. [5] developed a prediction model based on the least square support vector machine (LSSVM) to detect the

pullout capacity of small anchors; and they concluded that the LSSVM performs better than the ANN [5].

Nowadays, integrated system identifications are used to design nonlinear input-output prediction models [8, 9]. In general, these models can be divided into multi-input multi-output (MIMO), single-input single-output (SISO), or multi-input single-output (MISO). The selection of the appropriate model depends on the collected data and sensitivity of the input and output variables. Most common integrated identification models are presented in [8] and it is reported that the Hammerstein-Wiener model outperformed other models [8]. Also, it is found that the nonlinear Hammerstein-Wiener model performance is better than the linear one [10]. On the other hand, the adaptive neurofuzzy inference system (ANFIS) is used widely for the designing of prediction's models; more details on the ANFIS model design and previous studies can be found in [11–14]. The performance of the ANFIS model is better with MISO variables [13, 14]. Arsava et al. [14] introduced a time delayed-ANFIS (DANFIS) prediction model for the control structures, and

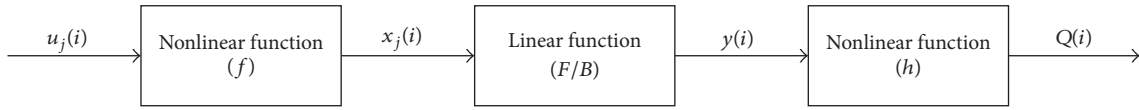


FIGURE 1: MISO-NHW model diagram structure.

they found that DANFIS model performance is much better than conventional ANFIS models. Based on the above review, the nonlinear Hammerstein-Wiener (NHW) and DANFIS models can be used to detect the pullout capacity. Therefore, a new model will be developed to detect the pullout capacity, and the results will be compared with ANN [2] and LSSVM [5] models based on Shahin and Jaksa [2] data collection.

The objectives of this study are the following: (1) to examine the capability of the NHW and DANFIS models for predicting small ground anchors pullout capacity; (2) to compare the performance of developed models with previous studies; and (3) to study the significance of input variables on pullout capacity of small ground anchor.

## 2. Material and Methods

**2.1. Prediction Models.** The MISO prediction models, NHM and DANFIS, are utilized in this study to extract the pullout capacity of small ground anchors. These models are described in the following subsections.

**2.1.1. Nonlinear Hammerstein-Wiener Model.** The NHW model is an integrated prediction model using nonlinear and linear transforming functions [8]. The model includes input and output nonlinear functions and linear model connected the input and output functions [10]. The nonlinear one-layer sigmoid and wavelet networks, saturation, one-dimension polynomial, and piecewise functions are used for the input ( $f$ ) and output ( $h$ ) transforming [15]. In addition, the similar polynomial functions ( $B$  and  $F$ ) are defined in the time-shift operator. Figure 1 represents the NHW model diagram. To predict the pullout capacity ( $Q(i)$ ), the input variables ( $u_j(i)$ ), and transforming results  $x_j(i)$  and  $y(i)$  are utilized and calculated. More details for the NHW model can be found in [16, 17].

In this study, four input variables are used to predict the pullout capacity of a MISO model. The trail and errors method is used to select the input and output nonlinearity functions. Therefore, the nonlinearity input function is applied to each input variable ( $j$ ), and the output  $x_j(i)$  of each variable can be calculated as follows:

$$x_j(i) = f(u_j(i)). \quad (1)$$

The linear output block  $y(i)$  is a summation of the inputs as follows:

$$y(i) = \sum_{j=1}^n \frac{B_j(k)}{F_j(k)} x_j(i), \quad (2)$$

where  $n$  is the number of inputs for a MISO model and  $B_j(k)$  and  $F_j(k)$  are polynomials defined in the time-shift operator

$k$ . The model order is chosen based on zero order ( $B_j$ ) and pole order ( $F_j$ ), with delays set to zero and  $n$  selected as 4. The zero-pole orders are obtained using the prediction error method. As such, the pullout capacity can be calculated as follows:

$$Q(i) = h(y(i)). \quad (3)$$

In this paper, the prediction trials were performed with the Matlab command *nllhw* of the system identification toolbox. Moreover, the models were obtained using model error in which the minimized criterion is the square of the errors, normalized by the length of the data set. In addition, the models performances are evaluated.

**2.1.2. Delay Inputs for the Adaptive Neurofuzzy Inference System (DANFIS).** The time delayed adaptive neurofuzzy inference system (DANFIS) is proposed in [14] to predict the complex nonlinear behavior of smart structures. In this paper, the DANFIS model is developed to predict the pullout capacity of small ground anchors based on MISO parameters. Figure 2 illustrates the developed model using four input data sets and one delay for the output variable. The ANFIS model consists of a set of fuzzy rules with appropriate membership functions to generate the stipulated input-output pairs in the solution of uncertain and ill-defined systems [12, 14, 18, 19]. As presented in Figure 2, the ANFIS model contains five layers that are the input, input membership function (MF), rules list, output MF, and the output layers. Therefore, it is important to define the types and the values of MF for each input variable. Figure 2 shows two MFs for each variable, as shown in the input MF layer.

The process of the ANFIS model can be found in [14, 18]. As presented in Figure 2, the ANFIS model can be used for mapping the nonlinear MISO variables [20]. In this case, the nonlinear MISO mapping model can be expressed as follows [14, 20]:

$$Q(l) = g(u_1^{l-d}, u_2^{l-d}, \dots, u_n^{l-d}, Q^{l-d}, e^{l-d}) + e(l), \quad (4)$$

where  $[u_1, u_2, \dots, u_n]$  are the input variables,  $Q$  is the model output (pullout capacity),  $e$  is the model error,  $g$  is a scalar nonlinear mapping function, and the time delay is represented by the term  $d$ . In this study, four input variables are used and the time delay is assigned a value of one. In general, the if-then rules for the ANFIS model depend on the number of MFs. For each rule, the ANFIS fuzzy model of Takagi and Sugeno (TS) [21] can be applied as follows [18].

Assuming first that  $l = 2$ , while  $l = 2, 3, \dots, n$ ;  $n$  is the number of measurements; and  $d = 1$ , as presented in Figure 2, the model rule  $i$  for the four inputs can be processed as follows.

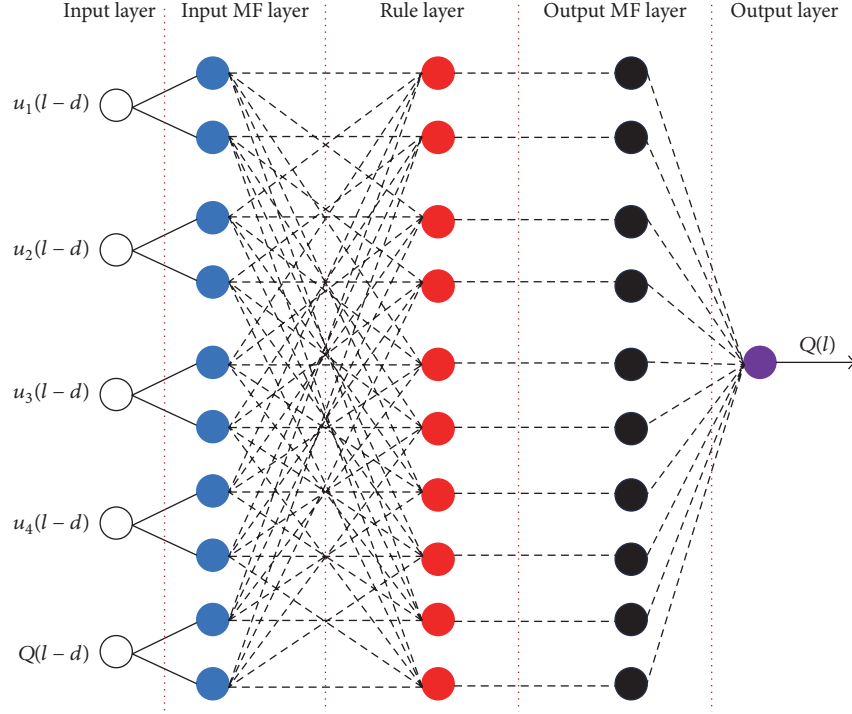


FIGURE 2: MISO-DANFIS model diagram structure.

Rule  $i$  is as follows: if  $u_1$  is  $A$ ,  $u_2$  is  $B$ ,  $u_3$  is  $C$ ,  $u_4$  is  $D$ , and  $Q$  is  $F$ , then

$$f_i = p_i u_1 + q_i u_2 + k_i u_3 + m_i u_4 + g_i Q + r_i, \quad (5)$$

where  $[u_1, u_2, u_3, u_4]$  are the input variables,  $Q$  is the delayed output variable (pullout capacity),  $f$  is the output of the TS fuzzy system, and  $p_i, q_i, k_i, m_i, g_i, r_i$  are the consequent parameters [18]. Therefore, as shown in Figure 2, the output of the five layers can be presented as follows:

*The Output of the Input MF Layer ( $O_i^1$ )*

$$O_i^1 = \mu_{A_i}(u_1), \mu_{B_i}(u_2), \mu_{C_i}(u_3), \mu_{D_i}(u_4), \mu_{F_i}(Q), \quad (6)$$

where  $\mu_{A_i}, \mu_{B_i}, \mu_{C_i}, \mu_{D_i}$ , and  $\mu_{F_i}$  are the MFs for the input variables of the model. The MF shape is divided into continuous and piecewise differentiable functions with normalized output (0–1) [12, 18]. Triangular MFs are used which can be presented for the first input ( $u_1$ ) as follows (the same relation can be found for each input variable):

$$\mu_{A_i}(u_1) = \max\left(\min\left(\frac{u_1 - a}{b - a}, \frac{c - u_1}{c - b}\right), 0\right), \quad (7)$$

where the parameters  $a, b$ , and  $c$  are the triangular MF values. These parameters can be called the premise parameters as they are the adjustable parameters in the premise part.

*The Output of the Rule Layer.* This layer has two processes; the first is calculating the firing strength of each fuzzy rule, as follow:

$$\begin{aligned} O_i^2 &= w_i \\ &= \mu_{A_i}(u_1) \times \mu_{B_i}(u_2) \times \mu_{C_i}(u_3) \times \mu_{D_i}(u_4) \\ &\quad \times \mu_{F_i}(Q). \end{aligned} \quad (8)$$

The second is normalizing the firing strength, as follows:

$$O_i^3 = \bar{w}_i = \frac{w_i}{\sum_{j=1}^N w_j}, \quad (9)$$

where,  $N$  is the number of input variables.

*The Output of the Output MF Layer.* In this layer, the node functions ( $f_i$ ) are applied with the previous layer output; the first-order TS model is used and the output of this layer can be expressed as follows:

$$O_i^4 = \bar{w}_i \times f_i. \quad (10)$$

*The Output of the Output Layer.* As the last step, the output of this layer is calculated as follows:

$$O_i^5 = Q(l) = \sum_{i=1}^N \bar{w}_i \times f_i. \quad (11)$$

Based on (4) and (11), to estimate the  $j$  element ( $j = i - 1$ ), the DANFIS output is calculated as follows [14, 22]:

$$O_j^5 = Q(l) = \sum_{j=1}^N \bar{w}_j \times f_j. \quad (12)$$

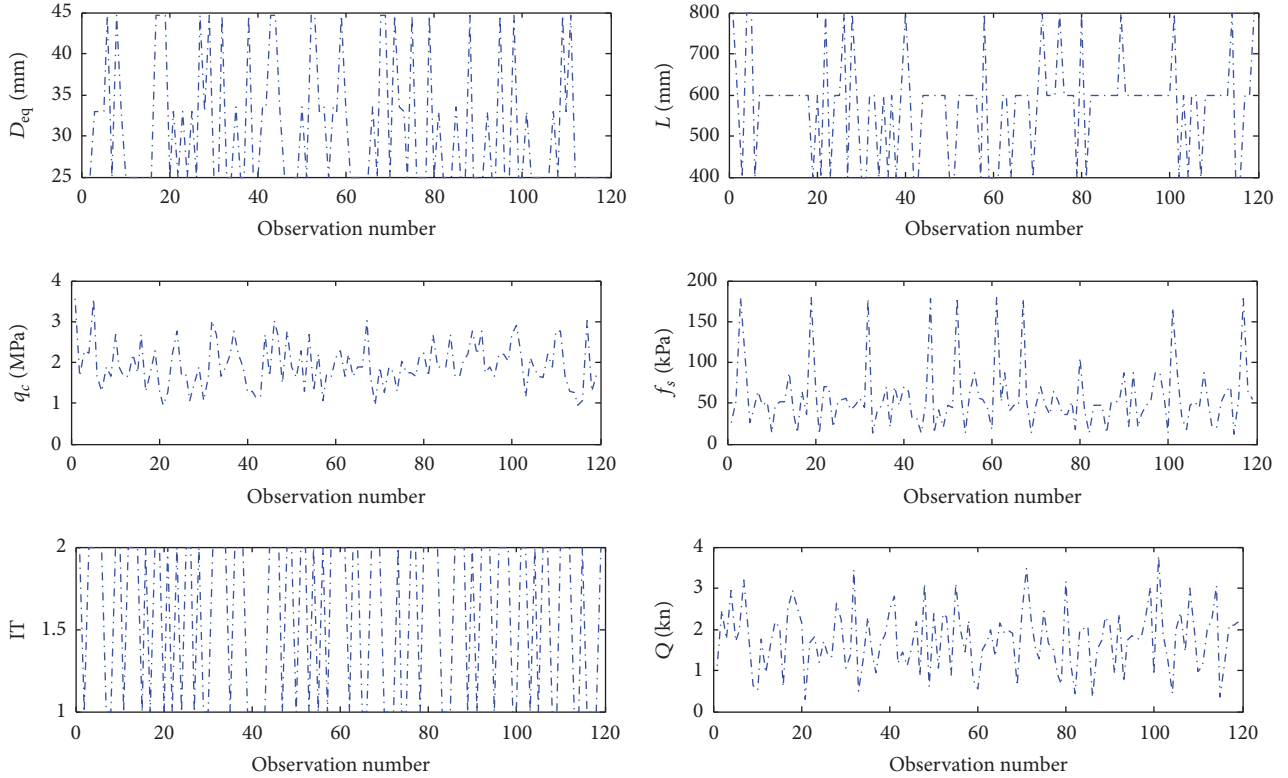


FIGURE 3: Database for field pullout tests (from Samui et al. [5]).

**2.2. Case Study.** To evaluate the developed models, the field data of 119 anchors are derived using an in situ test database from Shahin and Jaksa [2]. Figure 3 represents the data points and parameters that are considered in this study. As presented in Figure 3, the input variables are the equivalent anchor diameter ( $D_{eq}$ ), embedment depth ( $L$ ), average cone resistance ( $q_c$ ) along the embedment depth, average sleeve friction ( $f_s$ ) along the embedment depth, and installation technique (IT) and the anchor pullout capacity, ( $Q$ ), is the output. The installation techniques used in this case are static and dynamic cases which are represented by 1 and 2, respectively, as shown in Figure 3. The anchor's types and properties and the anchor's tests process are discussed and presented in [2]. Moreover, the input variables measurements and evaluation, soil properties, and number of tests, as well the monitoring of the anchor pullout capacity, are presented in [7].

The data are divided into training and testing subsets as presented in [5]. The first 83 data points (70%) are selected as the training dataset and the remaining 36 data points (30%) are considered as the testing datasets. The statistical analyses (maximum (Max.), minimum (Min.), mean ( $M$ ), and standard deviation (SD) values) for the training and testing datasets are presented in Table 1.

From Table 1, the statistical measurements for the training and testing datasets show good agreement, meaning that both of them represent almost similar distributions. Before the models simulation, the input and output parameters are normalized by scaling them between 0.2 and 0.8 using (13) to eliminate their dimension effects and to ensure that all

variables receive equal attention during training; moreover, it gives the models more flexibility to estimate beyond the training range [23].

$$x_{eq} = a_1 (x - x_{min}) \setminus (x_{max} - x_{min}) + a_2, \quad (13)$$

where  $x_{min}$  and  $x_{max}$  are minimum and maximum values, respectively; the constant range values  $a_1$  and  $a_2$  equal 0.6 and 0.2, respectively; the equivalent parameter  $x_{eq}$  is scaled between 0.2 and 0.8.

**2.3. Sensitivity of the Input Variables and Model Performance Criteria.** The data sensitivity is studied based on the previous models designed with the same database [2, 5, 7]. Shahin and Jaksa [7] evaluated the sensitivity of the ANN model with different input variables. Their results show that, during training, the best performance was obtained using the  $D_{eq}$ ,  $L$ ,  $f_s$ , and IT input variables, while during validation, the model performed better when using the  $D_{eq}$ ,  $L$ ,  $q_c$ , and  $f_s$  input variables. Moreover, Shahin and Jaksa [2] concluded that the ANN model with four input variables,  $D_{eq}$ ,  $L$ ,  $f_s$ , and IT, performed the best, while Samui et al. [5] found that the sensitivity of the  $q_c$  and  $f_s$  is higher than that of  $D_{eq}$ ,  $L$  and the sensitivity of the IT is low. Therefore, because of the inconsistency of the previous studies, the sensitivity of the input variables should be studied first. However, the correlation coefficient between the inputs and output variables is studied first to evaluate the sensitivity of variables, while it can be used to measure the interdependency between successive input and output variables [24]. Second, simple

TABLE 1: Statistical measurements for the training and testing datasets.

Statistical parameters	$D_{eq}$ (mm)	$L$ (mm)	$q_c$ (MPa)	$f_s$ (kPa)	IT	Q (kN)
Training dataset						
Max.	44.60	800.00	3.55	179.71	2.00	3.47
Min.	25.00	400.00	0.95	12.22	1.00	0.29
$M$	31.66	571.08	1.91	58.01	1.60	1.73
SD	7.88	125.46	0.58	42.18	0.49	0.77
Testing dataset						
Max.	44.60	800.00	3.03	178.26	2.00	3.80
Min.	25.00	400.00	0.95	12.22	1.00	0.35
$M$	28.85	594.44	1.98	56.62	1.56	1.80
SD	7.00	101.26	0.55	36.70	0.50	0.78

TABLE 2: Correlation coefficient between input and output variables.

Variables	$D_{eq}$	$L$	$q_c$	$f_s$	IT
Q	0.15	0.44	-0.11	0.54	-0.26

regression model is used to identify the sensitivity of the input variables, as follows:

$$Q = a + b_1 D_{eq} + b_2 L + b_3 q_c + b_4 f_s + b_5 IT, \quad (14)$$

where,  $a$ ,  $b_1$ ,  $b_2$ ,  $b_3$ ,  $b_4$ ,  $b_5$  are the unknown parameters for the regression model. These parameters can be estimated and evaluated using the least square method, as presented in [25, 26]. To examine the significance of each variable, the  $t$ -test, statistical evaluation, is studied. The  $t$  values are compared with predetermined 95% confidence and  $t_{f,95\%}$  confidence limit of  $t$  distribution;  $f$  is the freedom order. The variables within 95% are considered highly significant to predict the pullout capacity.

In this study, three criteria are used to evaluate the performance of the models design. The first criterion is the correlation coefficient ( $R$ ), which provide linear dependency information between observation and prediction values. The second statistical criterion is the mean absolute error (MAE), which measures the close prediction values to the eventual outcomes. Finally, the root mean square error (RMSE) is utilized to describe the average magnitude of the errors by giving more weight to large errors.

### 3. Results and Discussions

**3.1. Sensitivity Analysis.** The scaled data are used in this section to evaluate the variables sensitivity. The correlations between the input and output variables are presented in Table 2.

From Table 2, it can be seen that the degrees of linear dependence between pullout capacity and average sleeve friction and embedment depth are higher than equivalent anchor diameter variables. In addition, the dependencies of the variables on the average cone resistance and installation technique to predict the pullout capacity are low. This indicates that the average sleeve friction, embedment depth, and equivalent anchor diameter variables have more influence on

the pullout capacity and this is also reported by Shahin and Jaksa [2].

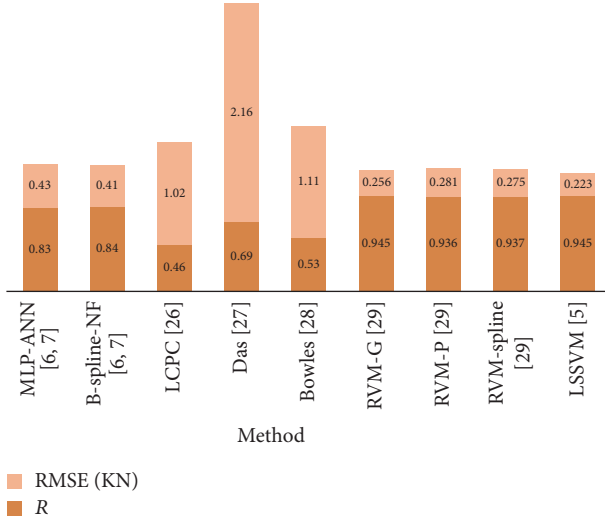
The simple regression model, as presented in (14), is evaluated and analyzed in Table 3. Four regression models based on the previous studies, [2, 5–7], are presented to evaluate the sensitivity of the input variables. The models are applied to study the effect of each variable on predicting the pullout capacity, and the correlation coefficients ( $R$ ) for the prediction models are calculated. The standard deviations of these coefficients are estimated by the least square method. The significance of the estimated coefficients is tested from the zero-expected value in accordance with the  $t_{f,95\%}$  confidence limit of the  $t$  distribution dependent on the  $f$  degree of freedom at the 95% confidence level.

As a result of the models correlation and  $t$ -test evaluations, the prediction pullout capacity of models 1 and 3 was found to be equally correlated with original pullout capacity. Moreover, it can be seen that the coefficients variables of  $D_{eq}$ ,  $L$ , and  $f_s$  are significant for the four models, while the coefficients variables of  $q_c$  and IT are not significant. Hence, the linear trend of  $D_{eq}$ ,  $L$ , and  $f_s$  variables are high and the prediction effectiveness of the  $q_c$  variable is higher than the IT variable. Therefore, the sensitivity effects of variables  $D_{eq}$ ,  $L$ ,  $q_c$ , and  $f_s$  in the prediction model are high, and these variables are considered in this study. Herein, it should be mentioned that the sensitivity results in this study are in agreement with Samui et al. [5] and the validation evaluation of the ANN of Shahin and Jaksa [7] for the same case study.

**3.2. Models Analysis.** Shahin and Jaksa [6] predicted the pullout capacity based on two models and three methods; B-spline neurofuzzy (B-spline-NF) and back-propagation multilayer perceptrons ANN (MLP-ANN) models are used, and the Laboratories Central des Ponts et Chaussées (LCPC) [27], Das [28], and Bowles [29] methods are utilized. In addition, Samui and Sitharam [30] applied the Relevance Vector Machine (RVM) prediction model with different kernels (Gaussian (RVM-G), polynomial (RVM-P), and spline (RVM-spline)). Also, Samui et al. [5] predicted the pullout capacity using least square support vector machine (LSSVM) model. Figure 4 illustrates the  $R$  and RMSE values for the previous studies.

TABLE 3: Linear trend component and coefficient test for the regression models.

	Model	$t_a$	$t_{b_1}$	$t_{b_2}$	$t_{b_3}$	$t_{b_4}$	$t_{b_5}$	$R$
1	$Q = a + b_1 D_{eq} + b_2 L + b_3 q_c + b_4 f_s + b_5 IT$	5.5	2.5	7.6	-3.8	9.8	-2.8	0.77
2	$Q = a + b_1 D_{eq} + b_2 L + b_4 f_s$	2.4	2.6	6.2	—	7.5	—	0.70
3	$Q = a + b_1 D_{eq} + b_2 L + b_3 q_c + b_4 f_s$	4.9	2.6	8.3	-5.2	9.2	—	0.77
4	$Q = a + b_1 D_{eq} + b_2 L + b_4 f_s + b_5 IT$	4.1	2.6	6.1	—	9.1	-4.4	0.74

FIGURE 4: Correlation coefficient ( $R$ ) and RMSE for the predicted pullout capacity of previous studies.

From Figure 4, the vector machine method is the best to detect the pullout capacity of small ground anchors, while the worst case is the Das method. The better method is the LSSVM with high  $R = 0.945$  and low RMSE = 0.223. Samui et al. [5] used all variables to design the model and they found that the sensitivity of  $q_c$  is higher than  $D_{eq}$ ,  $L$ , and  $f_s$  variables. Based on Samui et al. [5] and the sensitivity analysis performed in Section 3.1, the current models are designed. In this study, two models are developed, NHW and DANFIS, using  $D_{eq}$ ,  $L$ ,  $q_c$ , and  $f_s$  as input variables and pullout capacity ( $Q$ ) as the output variable.

To assess the developed models, the models are programmed on Matlab. In the training phase, 83 datasets are selected and the coefficients of the models have been chosen by trial and error. In the NHW model, the same nonlinear functions for the inputs and output are used. The input-output nonlinear sigmoid functions and wavelet networks, saturation, one-dimension polynomial, and piecewise functions are applied with 50 iterations. In addition, the order chosen of linear function ( $B_j$  and  $F_j$ ) was  $[1 \ 1 \ 1 \ 1]$  and  $[2 \ 2 \ 8 \ 8]$  with delays set to zero for  $D_{eq}$ ,  $L$ ,  $q_c$ , and  $f_s$ , respectively. This order is selected to compare the functions based on trial-and-error approach. The  $R$ -values for the sigmoid, wavelet, and piecewise functions are found to be 0.99, 0.35, and 0.60, respectively. Therefore, the sigmoid function is selected as a nonlinear function for the input and output mapping. The better trials for the linear function orders are presented in Table 4.

TABLE 4: Linear function order trails evaluation.

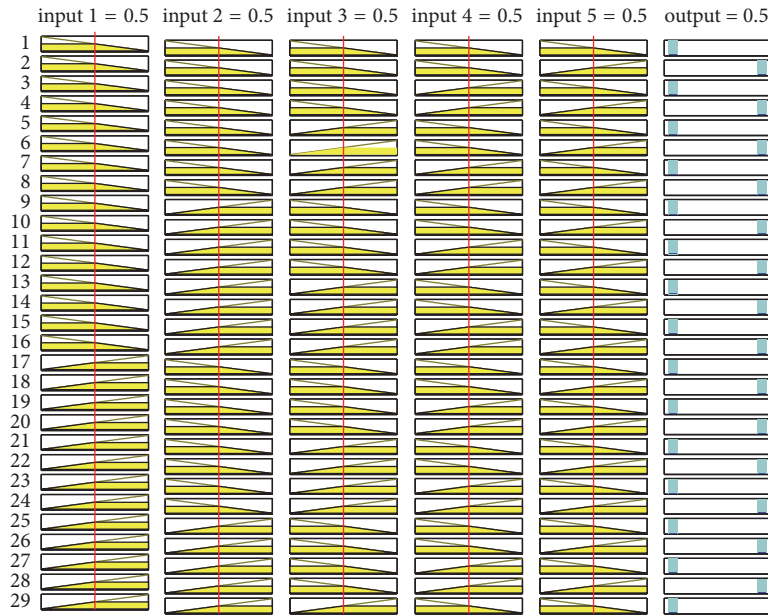
$[B_{D_{eq}} \ B_L \ B_{q_c} \ B_{f_s}]$	$[F_{D_{eq}} \ F_L \ F_{q_c} \ F_{f_s}]$	$R$
$[2 \ 2 \ 2 \ 2]$	$[2 \ 2 \ 2 \ 2]$	0.70
$[1 \ 1 \ 1 \ 1]$	$[2 \ 2 \ 5 \ 5]$	0.95
$[1 \ 1 \ 1 \ 1]$	$[2 \ 2 \ 8 \ 8]$	0.99
$[1 \ 1 \ 1 \ 1]$	$[8 \ 8 \ 2 \ 2]$	0.90

The presented values in Table 4 show that the model order of pole is more effective than zeros order; in addition, it is seen that with increased values of the orders for the  $q_c$  and  $f_s$  variables, the performance of the model becomes better. That means the sensitivity of  $q_c$  and  $f_s$  is higher than that of  $D_{eq}$ ,  $L$ . However, the NHW model contains a sigmoid function for the input and output variables, and  $[1 \ 1 \ 1 \ 1]$  and  $[2 \ 2 \ 8 \ 8]$  orders for the linear function are utilized to predict the pullout capacity.

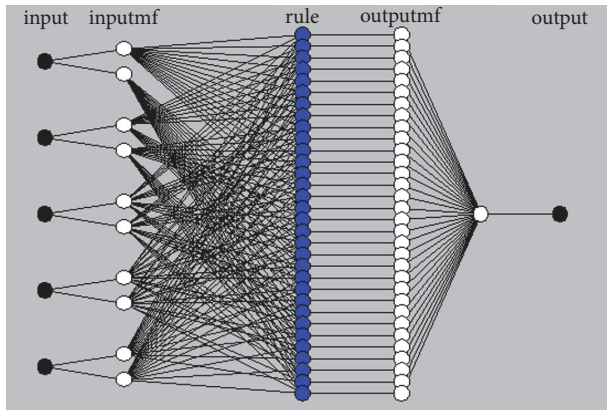
On the other hand, the DANFIS model is designed using the four input variables and one-time-delayed output; and the pullout capacity is the output value. Two MF functions for each variable are used in this case with 92 nodes and 62 model coefficients. Different MF types are evaluated with 50 iterations, and the best predicted pullout capacity ( $R = 0.99$ ) is obtained using triangular MFs, and this result is reported, also, in Shahin and Jaksa [6, 7]. Figure 5 represents the DANFIS model design.

In this model, 32 fuzzy rules are used, and the numbers of linear and nonlinear coefficients are 32 and 30, respectively. The application of the model is presented in Figure 5(a) which includes the five basic steps of the calculation. The model begins with the fuzzification of the inputs; then the rules are applied using the fuzzy operation (AND) and the implication and transfer data from premise to consequent. After that, the aggregation of the consequents across rules and output defuzzification are defined to estimate the pullout capacity. The typical model is presented in Figure 5(b), and the adjusted MFs for the five input variables are shown in Figure 5(c).

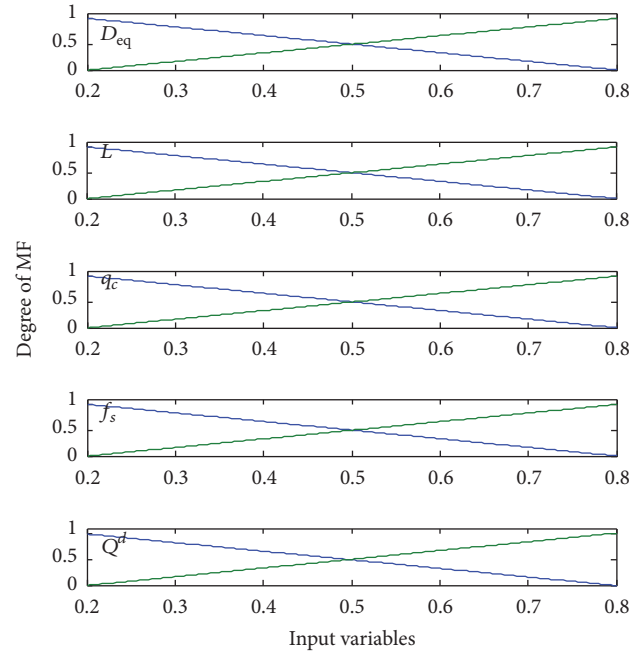
The performances of the designed NHW and DANFIS models are presented in Figure 6 and Table 5. Figure 6 illustrates the scatter plot of the training dataset, and Table 5 presents the statistical performance and comparison of the developed models and the LSSVM model. From Figure 6, it can be seen that the performance of the DANFIS model is better than the NHW model. The coefficients of the linear fitting for the relation between the observed and predicted



(a)



(b)



Input variables

(c)

FIGURE 5: DANFIS model design: (a) model application, (b) typical model architecture with five inputs, and (c) adjusted MF for the five inputs variables.

pullout capacity of small ground anchors are better with the DANFIS model. In addition, the NHW and the DANFIS models performed better than the LSSVM [5] model. As such, the developed models performances are acceptable to predict the pullout capacity without information losses of the measured values.

The observed and the predicted values of the pullout capacity by the NHW and the DANFIS models are shown in Figure 7 for the testing dataset with high agreement between them. Table 6 shows the statistical performance of the developed models and the LSSVM model for the testing

TABLE 5: Comparison between the developed models and the LSSVM [5] model for the training data.

Model	RMSE (KN)	MAE (KN)	R
LSSVM [5]	0.22	0.19	0.94
NHW	$6.65E - 3$	$8.25E - 3$	0.99
DANFIS	$3.91E - 6$	$2.40E - 6$	0.99

dataset. The LSSVM model outperforms the ANN model results for the testing dataset; the MAE is 0.31 and 0.21 KN,

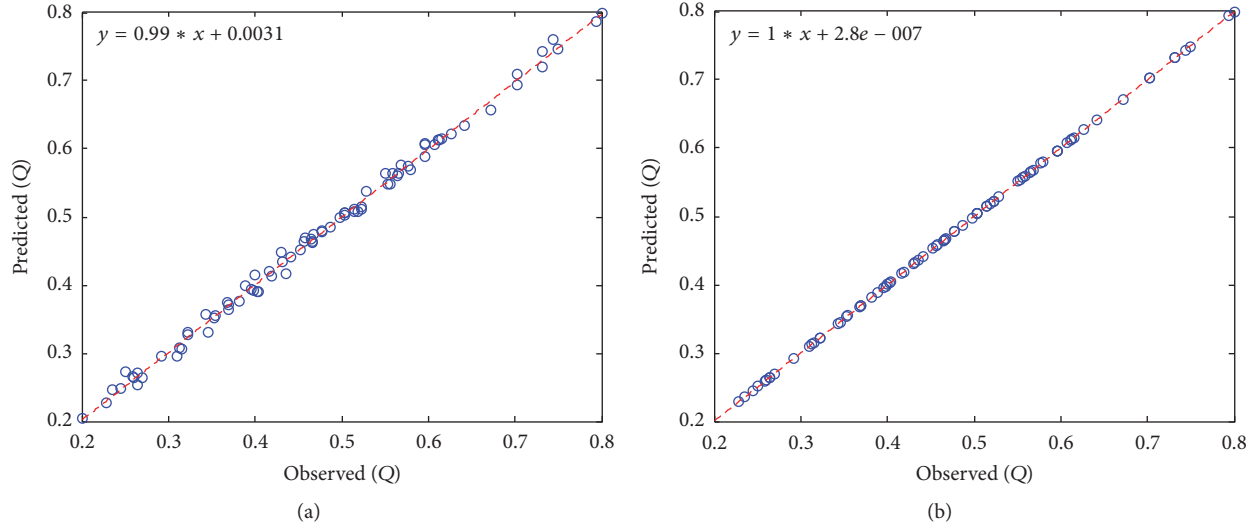


FIGURE 6: Training performance of the designed models (a) NHW and (b) DANFIS.

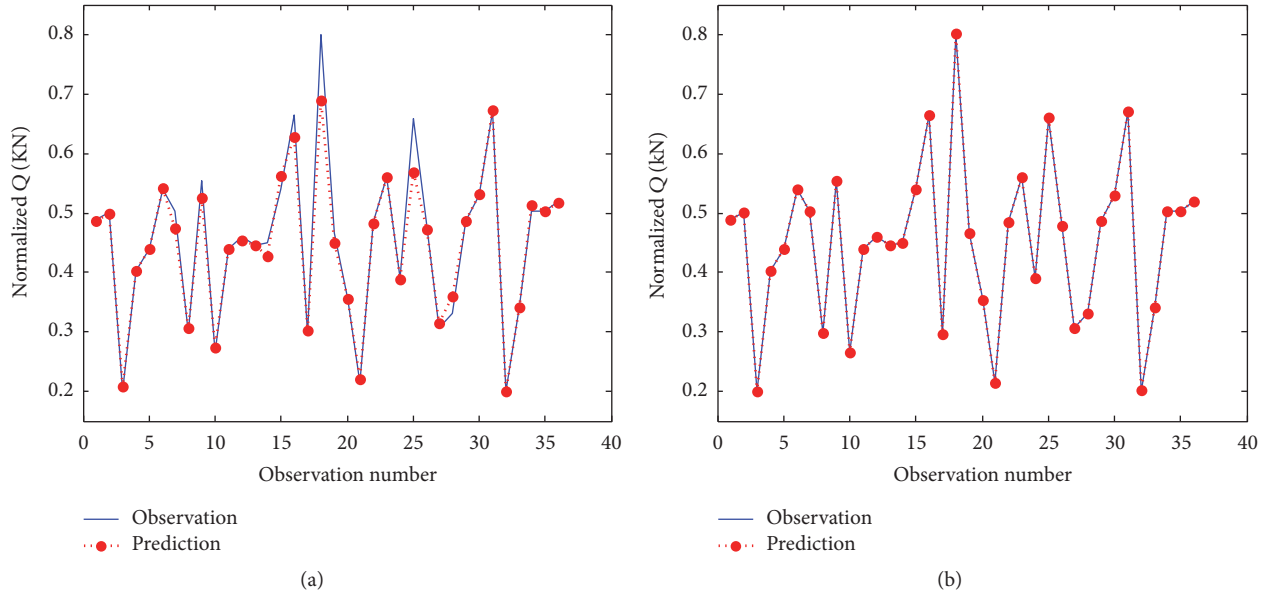


FIGURE 7: Testing performance of the designed models (a) NHW and (b) DANFIS.

TABLE 6: Comparison between designed models and LSSVM [5] model for the testing data.

Model	RMSE (KN)	MAE (KN)	R
LSSVM [5]	0.26	0.20	0.94
NHW	$2.71E-2$	$1.32E-2$	0.98
DANFIS	$6.47E-4$	$4.03E-4$	0.99

for the ANN and LSSVM models, respectively [5]. As shown in Table 6 and Figure 7, the developed models predict the pullout capacity for the testing data with less RMSE ( $2.71E-2$  and  $6.47E-4$ , for the NHW and DANFIS, resp.) and higher accuracy of  $R$  (0.98 and 0.99, for the NHW and DANFIS, resp.). Accordingly, the performance of the DANFIS model

is better than the other models in predicting the pullout capacity of ground anchors.

Finally, the models proposed, DANFIS and NHW, can be used to detect the pullout capacity with high accuracy with the DANFIS performing better than the NHW.

#### 4. Conclusions

In this study, two models are developed using nonlinear integrated system, which are nonlinear Hammerstein-Wiener (NHW) and delay inputs for the adaptive neurofuzzy inference system (DANFIS) to predict the pullout capacity of small ground anchors. The input variables sensitivity is studied to evaluate the variables effectiveness in prediction using polynomial regression model. The sensitivity analysis shows

high effect of the equivalent anchor diameter, embedment depth, average cone resistance along the embedment depth, and average sleeve friction along the embedment depth variables in predicting the pullout capacity. The results of the developed models are evaluated using case study data and compared with previous studies. It is concluded that the two proposed models can be used to predict the pullout capacity with high accuracy. Moreover, the performance of the DANFIS outperforms the NHW model in training and testing dataset.

## Conflicts of Interest

The authors declare that there are no conflicts of interest regarding the publication of this paper

## Acknowledgments

This research was supported by Post-Doctor Research Program in 2017 through the Incheon National University (INU), Incheon, South Korea.

## References

- [1] R. S. Merifield and S. W. Sloan, "The ultimate pullout capacity of anchors in frictional soils," *Canadian Geotechnical Journal*, vol. 43, no. 8, pp. 852–868, 2006.
- [2] M. A. Shahin and M. B. Jaksa, "Pullout capacity of small ground anchors by direct cone penetration test methods and neural networks," *Canadian Geotechnical Journal*, vol. 43, no. 6, pp. 626–637, 2006.
- [3] A. M. Fahmy, J. R. de Bruyn, and T. A. Newson, "Numerical investigation of the inclined pullout behavior of anchors embedded in clay," *Geotechnical and Geological Engineering*, vol. 31, no. 5, pp. 1525–1542, 2013.
- [4] Z. A. Ardebili, M. A. Gabr, and M. S. Rahman, "Uplift capacity of plate anchors in saturated clays: analyses with different constitutive models," *International Journal of Geomechanics*, vol. 16, no. 2, Article ID 4015053, 11 pages, 2016.
- [5] P. Samui, D. Kim, and B. G. Aiyer, "Pullout capacity of small ground anchor: a least square support vector machine approach," *Journal of Zhejiang University: Science A*, vol. 16, no. 4, pp. 295–301, 2015.
- [6] M. A. Shahin and M. B. Jaksa, "Neural network prediction of pullout capacity of marquee ground anchors," *Computers and Geotechnics*, vol. 32, no. 3, pp. 153–163, 2005.
- [7] M. Shahin and M. Jaksa, "Modelling the pullout capacity of marquee ground anchor," Research Report R174, School of civil and environmental Engineering, University of Adelaide, Adelaide, Australia, 2003.
- [8] L. Ljung, Q. Zhang, P. Lindskog, and R. Singh, "An integrated system identification tool-box for linear and non-linear models," in *Proceedings of the 14th IFAC Symposium on Identification and System Parameter Estimation*, pp. 931–936, Newcastle, Australia, 2006.
- [9] L. Ljung, "System identification toolbox," *Matlab User's Guid*, vol. 1, article 237, 2011.
- [10] D. Zambrano, S. Tayamon, and B. Carlsson, "Identification of a discrete-time nonlinear Hammerstein-Wiener model for a selective catalytic reduction system," in *Proceedings of the American Control Conference (ACC '11)*, pp. 8–13, June 2011.
- [11] M. R. Kaloop, J. W. Hu, and M. A. Sayed, "Bridge performance assessment based on an adaptive neuro-fuzzy inference system with wavelet filter for the GPS measurements," *ISPRS International Journal of Geo-Information*, vol. 4, no. 4, pp. 2339–2361, 2015.
- [12] M. Eldessouki and M. Hassan, "Adaptive neuro-fuzzy system for quantitative evaluation of woven fabrics' pilling resistance," *Expert Systems with Applications*, vol. 42, no. 4, pp. 2098–2113, 2015.
- [13] O. Kisi and J. Shiri, "Prediction of long-term monthly air temperature using geographical inputs," *International Journal of Climatology*, vol. 34, no. 1, pp. 179–186, 2014.
- [14] K. S. Arsava, Y. Kim, T. El-Korchi, and H. S. Park, "Nonlinear system identification of smart structures under high impact loads," *Smart Materials and Structures*, vol. 22, no. 5, Article ID 055008, 2013.
- [15] F. Guo, *A new identification method for Wiener and Hammerstein systems [Ph.D. thesis]*, Institute for Applied Computer Science, Karlsruhe, Germany, 2004.
- [16] T. Patikirikorala, L. Wang, A. Colman, and J. Han, "Hammerstein-Wiener nonlinear model based predictive control for relative QoS performance and resource management of software systems," *Control Engineering Practice*, vol. 20, no. 1, pp. 49–61, 2012.
- [17] A. Wills, T. B. Schön, L. Ljung, and B. Ninness, "Identification of Hammerstein-Wiener models," *Automatica*, vol. 49, no. 1, pp. 70–81, 2013.
- [18] J.-S. R. Jang, "ANFIS: adaptive-network-based fuzzy inference system," *IEEE Transactions on Systems, Man and Cybernetics*, vol. 23, no. 3, pp. 665–685, 1993.
- [19] K. S. Arsava, Y. Kim, K. H. Kim, and B.-S. Shin, "Smart fuzzy control of reinforced concrete structures excited by collision-type forces," *Expert Systems with Applications*, vol. 42, no. 21, pp. 7929–7941, 2015.
- [20] H. Adeli and X. Jiang, "Dynamic fuzzy wavelet neural network model for structural system identification," *Journal of Structural Engineering*, vol. 132, no. 1, pp. 102–111, 2006.
- [21] T. Takagi and M. Sugeno, "Fuzzy identification of systems and its applications to modeling and control," *IEEE Transactions on Systems, Man and Cybernetics*, vol. 15, no. 1, pp. 116–132, 1985.
- [22] M. R. Kaloop, J. W. Hu, and Y. Bigdeli, "Identification of the response of a controlled building structure subjected to seismic load by using nonlinear system models," *Applied Sciences*, vol. 6, no. 10, p. 301, 2016.
- [23] I. Mansouri, A. Gholampour, O. Kisi, and T. Ozbakkaloglu, "Evaluation of peak and residual conditions of actively confined concrete using neuro-fuzzy and neural computing techniques," *Neural Computing and Applications*, pp. 1–16, 2016.
- [24] H. Erdogan and E. Gulal, "The application of time series analysis to describe the dynamic movements of suspension bridges," *Nonlinear Analysis. Real World Applications*, vol. 10, no. 2, pp. 910–927, 2009.
- [25] M. R. Kaloop, J. W. Hu, and E. Elbeltagi, "Time-series and frequency-spectrum correlation analysis of bridge performance based on a real-time strain monitoring system," *ISPRS International Journal of Geo-Information*, vol. 5, no. 5, article 61, 2016.
- [26] H. Erdogan and E. Gulal, "Identification of dynamic systems using multiple input-single output (MISO) models," *Nonlinear Analysis. Real World Applications*, vol. 10, no. 2, pp. 1183–1196, 2009.

- [27] M. Bustamente and L. Gianceselli, "Pile bearing capacity prediction by means of static penetrometer CPT," in *Proceedings of the 2nd European Symposium on Penetration Testing*, pp. 493–500, 1982.
- [28] B. M. Das, *Principles of Foundation Engineering*, Cengage Learning, Boston, Mass, USA, 7th edition, 2010.
- [29] J. E. Bowles, *Foundation Analysis*, McGraw-Hill, New York, NY, USA, 3rd edition, 2001.
- [30] P. Samui and T. G. Sitharam, "Pullout capacity of small ground anchors: a relevance vector machine approach," *Geomechanics and Engineering*, vol. 1, no. 3, pp. 259–262, 2009.

## Research Article

# Nonlinear Resonance Analysis of Slender Portal Frames under Base Excitation

Luis Fernando Paulo Muñoz,<sup>1</sup> Paulo B. Gonçalves,<sup>1</sup>  
Ricardo A. M. Silveira,<sup>2</sup> and Andréa Silva<sup>2</sup>

<sup>1</sup>Civil Engineering Department, Pontifical Catholic University of Rio de Janeiro, Rio de Janeiro, RJ, Brazil

<sup>2</sup>Civil Engineering Department, Federal University of Ouro Preto, Ouro Preto, MG, Brazil

Correspondence should be addressed to Luis Fernando Paulo Muñoz; lfernand@tecgraf.puc-rio.br

Received 22 November 2016; Accepted 16 February 2017; Published 30 March 2017

Academic Editor: Marcello Vanali

Copyright © 2017 Luis Fernando Paulo Muñoz et al. This is an open access article distributed under the Creative Commons Attribution License, which permits unrestricted use, distribution, and reproduction in any medium, provided the original work is properly cited.

The dynamic nonlinear response and stability of slender structures in the main resonance regions are a topic of importance in structural analysis. In complex problems, the determination of the response in the frequency domain indirectly obtained through analyses in time domain can lead to huge computational effort in large systems. In nonlinear cases, the response in the frequency domain becomes even more cumbersome because of the possibility of multiple solutions for certain forcing frequencies. Those solutions can be stable and unstable, in particular saddle-node bifurcation at the turning points along the resonance curves. In this work, an incremental technique for direct calculation of the nonlinear response in frequency domain of plane frames subjected to base excitation is proposed. The transformation of equations of motion to the frequency domain is made through the harmonic balance method in conjunction with the Galerkin method. The resulting system of nonlinear equations in terms of the modal amplitudes and forcing frequency is solved by the Newton-Raphson method together with an arc-length procedure to obtain the nonlinear resonance curves. Suitable examples are presented, and the influence of the frame geometric parameters and base motion on the nonlinear resonance curves is investigated.

## 1. Introduction

Lightweight framed structures are extensively used in engineering applications such as buildings, industrial constructions, off-shore platforms, and aerospace structures. In civil engineering, framed metal structures such as gabled frames are efficient structural forms to withstand various loads such as live, snow, wind, earthquake, and crane loads. Linear models are usually used for the design of these structures. However, as its slenderness increases, the degree of geometric nonlinearity increases as well as the occurrence of instability phenomena. Under dynamic loads, slender frames may be subjected to unwanted (or unsafe) large vibration amplitudes and accelerations and dynamic jumps in the main resonance regions due to hardening or softening frequency-amplitude relation and modal couplings. Therefore, an accurate nonlinear dynamic analysis is required. Recent earthquakes have increased the interest in the development of reliable

analytical methods of assessing the dynamic response of existing structures and, if necessary, developing effective retrofit strategies. So, understanding the nonlinear dynamics of framed structures under base excitation constitutes an essential step for their safe design.

The seminal works by Koiter [1] and Roorda [2] have shown the complex postbuckling paths exhibited by slender frames; subsequently, several authors have studied the nonlinear behavior of reticulated structures liable to buckling under prescribed loading conditions. A compilation of these first results can be found in Bazant and Cedolin [3] who summarize many topics about the stability of slender frames. Design prescriptions are found, for example, in Galambos [4]. More recently, Silvestre and Camotim [5] presented a semianalytical method to analyze the geometrically nonlinear behavior of plane frames, including the influence of eventual buckling mode interaction phenomena. Later, they presented the results concerning the elastic in-plane stability and

second-order behavior of unbraced single-bay pitched-roof steel frames and proposed a methodology to design this type of commonly used structure. In particular, they showed that, due to the rafter slope, the geometrically nonlinear behaviors of orthogonal beam-and-column and pitched-roof frames are qualitatively different [6]. The dynamics of such frames will be investigated in this work. More recently, Galvão et al. [7] assessed the effect of geometric imperfections and boundary conditions on the postbuckling response and imperfection-sensitivity of L-frames.

The dynamic response of slender frames in the main resonance regions is an important topic in the analysis of these structures under time varying loads. Several nonlinear phenomena have been studied in the last decades. Simitses [8] studied the effect of static preloading and suddenly applied loads on the nonlinear vibrations and instabilities of slender structures. Chan and Ho [9] conducted the nonlinear vibration analysis of steel frames with flexible connections. Mazzilli and Brasil [10] presented an analytical study of the nonlinear vibrations in a three-time redundant portal frame, considering the effect of axial forces upon the natural frequencies. The axial forces play an important role in tuning the sway mode and the first symmetrical mode into a 1:2 internal resonance. Harmonic support excitations resonant with the first symmetrical mode are then introduced and the amplitudes of nonlinear steady states are computed based upon a multiple scales solution. Later, Soares and Mazzilli [11] described the implementation of a computer program to calculate nonlinear normal modes of structural systems and generate individual modes of planar framed structures exhibiting geometrically nonlinear behavior. The procedure follows the invariant manifold approach, adapted to handle equations of motion of systems discretized by finite element techniques. Chan and Chui [12] examined, based on their previous works, the nonlinear static and cyclic behavior of steel frames with semirigid connections. McEwan et al. [13] proposed a method for modeling the large deflection beam response involving multiple vibration modes, while Ribeiro [14] analyzed the geometrically nonlinear vibrations of beams and plane frames by the hierarchical finite element method and examined the suitability of the proposed formulation for time domain nonlinear analyses. Da Silva et al. [15] studied the nonlinear dynamics of a low-rise portal frame using the ANSYS finite element software. The results show the influence of semirigid joints and geometrical nonlinearity on the steel frames dynamics. More recently, Galvão et al. [16] investigated the effect of semirigid connections on the nonlinear vibrations of slender frames and obtained the nonlinear relation between the natural frequencies and static preloading. Su and Cesnik [17] introduced a strain-based geometrically nonlinear beam formulation for structural and aeroelastic modeling and analysis of slender wings of very flexible aircraft. Solutions of different beam configurations under static loads and forced dynamic excitations are compared against ones from other geometrically nonlinear beam formulations. Gonçalves et al. [18] published an experimental analysis of the nonlinear vibrations of a slender metal column under self-weight. Masoodi and Moghaddam [19] studied the nonlinear dynamics and natural frequencies of gabled

frames having flexible restraints and connections. To control unwanted nonlinear phenomena and vibrations of frames, several control techniques are proposed in literature. For example, Palacios Felix et al. [20] examined the nonlinear control method based on the saturation phenomenon. The interaction of a nonideal source with a portal frame leads to the occurrence of interesting nonlinear phenomena during the passage through resonance when the nonideal excitation frequency is near the portal frame natural frequency and when the nonideal system frequency is approximately twice the controller frequency (two-to-one internal resonance). They also suggest the use of the portal frame for energy harvesting.

The determination of a structure's response in the frequency domain, characterized by the resonance curves and bifurcation diagrams, is, in some cases, indirectly obtained through a series of analyses in time domain, varying step by step a selected control parameter (see Parker and Chua [21]). In this brute force approach, for each control parameter value, the equations of motion must be integrated long enough to reach the steady-state regime. This leads to a huge computational effort when analyzing structures with a large number of degrees of freedom [16]. In nonlinear cases, the response in the frequency domain becomes even more cumbersome because of the possibility of multiple solutions for certain forcing frequencies. Those solutions can be stable and unstable, and bifurcations can appear, in particular saddle-node bifurcation at the turning points along the resonance curves. To predict the nonlinear response in frequency domain, some methods are used, such as the harmonic balance method (HBM) and other integral transformations. Based on the HBM, Nakhla and Valch [22] proposed a method for the solution of nonlinear periodic networks, avoiding the time domain solution of the dynamic equations. Lau et al. [23] formulated an incremental variational process based on the HBM to study the nonlinear vibrations of elastic systems. Further, Cheung and Chen [24] used the formulation of the incremental harmonic balance method (IHB) to solve a system of differential equations with cubic nonlinearity, which governs a wide range of engineering problems such as large-amplitude vibration of beams or plates. An incremental arc-length method combined with a cubic extrapolation technique is adopted to trace the response curves. Chen et al. [25] generalized this technique to use the incremental HBM in a finite element context, being able to use the HBM in the study of systems with several degrees of freedom. Due to its simple formulation and relatively easy implementation, the HBM is one of the most popular methods to study the nonlinear vibrations of structures [26]. The algebraic system of nonlinear equations, which results from the HBM, requires a numerical procedure to obtain the solutions. Frequently, Newton's method is adopted to solve the nonlinear system. However, in many cases, the resonance curves exhibit limit points and, in such cases, the use of continuation methods is necessary. For example, Ribeiro and Petyt [27] studied the free and steady-state forced vibrations of thin plates. Symbolic computation is employed in the derivation of the model and the equations of motion are solved by the Newton and continuation methods. Von Groll and Ewins [28] described a

numerical algorithm based on the harmonic balance method to study rotor/stator interaction dynamics under periodic excitation. The algorithm also calculates turning points and follows solution branches via arc-length continuation. More recently, Ferreira and Serpa [29] described the application of the arc-length method to solve a system of nonlinear equations obtaining as a result the nonlinear frequency response. In a recent work, Londoño et al. [30] used continuation methods in frequency domain to obtain the backbone curves of several nonlinear systems, while Renson et al. [31] presented numerical methodologies for the computation of nonlinear normal modes in mechanical system.

Stoykov and Ribeiro [32, 33] investigated the geometrically nonlinear free vibrations of beams using a  $p$ -version finite element method. The variation of the amplitude of vibration with the frequency of vibration is determined and presented in the form of backbone curves. Coupling between modes is investigated, internal resonances are found, and the ensuing multimodal oscillations are described. Formica et al. [34] present a computational framework to perform parameter continuation of periodic solutions of nonlinear, distributed-parameter systems represented by partial differential equations with time-dependent coefficients and excitations. As a case study, they consider a nonlinear beam subject to a harmonic excitation.

An important design concern is the dynamics of slender frames subjected to seismic loads. In such cases, the response of the structure in frequency domain is important, since the vulnerability of structure during an earthquake is related to the relation between the natural vibration frequencies of the structure and the frequency content of the seismic load, as studied in Paullo Muñoz et al. [35] who assess the frequency domain response of slender frames under seismic excitation. In seismic events, the ground acceleration magnitude is a crucial parameter, since the effect of the excitation on the structure is directly related to acceleration magnitude. Most recorded events have a magnitude lower than  $1g$ . However, peak acceleration greater than  $1g$  has been registered. For example, an acceleration magnitude of  $1.7g$  was registered for the Los Angeles earthquake, and a peak acceleration of  $2.99g$  was registered for the 2011 Tohoku earthquake [36]. Douglas [37] presented a review of equations for the estimation of peak ground acceleration using strong-motion records, while Katsanos et al. [38] reviewed alternative selection procedures for incorporating strong ground motion records within the framework of seismic design of structures. There are many other research areas where the influence of base acceleration on structural components is important, including subsurface explosions, rotating machinery, and launching vehicles.

In this work, an incremental technique for the direct calculation of the nonlinear dynamic response in frequency domain of nonlinear plane frames discretized by the finite element method and subjected to a base excitation is proposed. The transformation of discretized equations of motion, in the finite element context, to the frequency domain is accomplished here through the classical harmonic balance method (HBM). For the nonlinear analysis, a particular adaptation of the HBM-Galerkin methodology presented by Cheung and Chen [24] and generalized for the use in FEM context

by Chen et al. [25] is proposed here. The resulting system of nonlinear equations in terms of the modal amplitudes and forcing frequency is solved by the Newton-Raphson method together with an arc-length procedure to obtain the nonlinear resonance curves. Examples of commonly used frame geometries are presented and the influence of vertical and horizontal base motions on the frame nonlinear response as a function of the frame geometric parameters is analyzed.

## 2. Formulation

*2.1. Equations of Motion.* For a structural system under the action of harmonic forcing with a prescribed forcing frequency  $\Omega$ , the nonlinear equations of motion can be written as

$$\mathbf{M}\ddot{\mathbf{u}}(t) + \mathbf{C}\dot{\mathbf{u}}(t) + \mathbf{F}\mathbf{i}(\mathbf{u}(t)) = F \cos(\Omega t) \mathbf{f}, \quad (1)$$

where  $\mathbf{M}$ ,  $\mathbf{C}$ , and  $\mathbf{F}\mathbf{i}$  are the mass matrix, damping matrix, and the vector of nonlinear elastic forces, respectively, with  $\mathbf{F}\mathbf{i}$  being dependent on the nodal displacement vector  $\mathbf{u}(t)$  and on the geometric nonlinear formulation;  $\mathbf{f}$  is the vector of external applied loads at the nodal points, which gives the amount of forces at each DOF, and  $F$  and  $\Omega$  are, respectively, the magnitude and frequency of the harmonic excitation.

*2.2. Harmonic Balance Method (HBM) for Linear Analysis.* The HBM is one of the most popular methods for the nonlinear analysis of dynamical systems. In this method, the displacement field is approximated by a finite Fourier series of the form

$$\mathbf{u}(t) = \sum_{n=0}^N [\mathbf{A}_n \cos(n\Omega t) + \mathbf{B}_n \sin(n\Omega t)], \quad (2)$$

where  $\mathbf{A}_n$  and  $\mathbf{B}_n$  are the modal amplitude vectors corresponding to the  $n$ th harmonic and  $N$  is the number of terms considered in the approximation. For the linear damped case, it is only necessary to retain the second term in (2). Thus, the nodal displacement vector takes the form

$$\mathbf{u}(t) = \mathbf{A}_1 \cos(\Omega t) + \mathbf{B}_1 \sin(\Omega t). \quad (3)$$

Introducing (3) into (1) results in

$$\begin{aligned} & (\Omega \mathbf{C} \mathbf{A}_1 - \Omega^2 \mathbf{M} \mathbf{B}_1) \cos(\Omega t) \\ & - (\Omega^2 \mathbf{M} \mathbf{A}_1 + \Omega \mathbf{C} \mathbf{B}_1) \sin(\Omega t) = F \mathbf{f} \cos(\Omega t). \end{aligned} \quad (4)$$

Taking  $F \mathbf{f} = \mathbf{F}_0$  and  $\mathbf{F}\mathbf{i} = \mathbf{K}\mathbf{u}(t)$ , where  $\mathbf{K}$  is the linear stiffness matrix, and applying the HBM to equation (4), the following system is obtained:

$$\begin{bmatrix} \mathbf{C} & -\Omega \mathbf{M} + \mathbf{K} \\ -\Omega^2 \mathbf{M} + \mathbf{K} & -\Omega \mathbf{C} \end{bmatrix} \begin{Bmatrix} \mathbf{A}_1 \\ \mathbf{B}_1 \end{Bmatrix} = \begin{Bmatrix} \mathbf{F}_0 \\ \mathbf{0} \end{Bmatrix}. \quad (5)$$

Equation (5) can be expressed in a more compact form as

$$\overline{\mathbf{K}}(\Omega) \overline{\mathbf{D}} - \overline{\mathbf{F}} = \mathbf{0}, \quad (6)$$

where

$$\begin{aligned}\bar{\mathbf{K}}(\Omega) &= \begin{bmatrix} \Omega \mathbf{C} & -\Omega^2 \mathbf{M} + \mathbf{K} \\ -\Omega^2 \mathbf{M} + \mathbf{K} & -\Omega \mathbf{C} \end{bmatrix}, \\ \bar{\mathbf{D}} &= \begin{Bmatrix} \mathbf{A}_1 \\ \mathbf{B}_1 \end{Bmatrix}, \\ \bar{\mathbf{F}} &= \begin{Bmatrix} \mathbf{F}_0 \\ \mathbf{0} \end{Bmatrix}.\end{aligned}\quad (7)$$

As a result of the transformation of the system of equations to the frequency domain and the use of continuation techniques together with an arc-length constraint, the forcing frequency  $\Omega$  and the modal amplitude vector  $\bar{\mathbf{D}}$  are the unknowns in (7) [29, 39, 40]. Even in the linear case, the transformation of (1) to the frequency domain leads to a nonlinear system of algebraic equations, with the use of nonlinear techniques such as the Newton-Raphson method being necessary.

**2.3. HBM-Galerkin Methodology for Nonlinear Analysis.** For the nonlinear analysis, considering that the steady-state response is periodic, it is convenient to use a periodic nondimensional time variable defined as

$$\tau = \Omega t. \quad (8)$$

Substituting (8) into (1), the equation of motion can be rewritten as

$$\Omega^2 \mathbf{M} \ddot{\mathbf{u}}(\tau) + \Omega \mathbf{C} \dot{\mathbf{u}}(\tau) + \mathbf{F} \mathbf{i}(\mathbf{u}(\tau)) = F \cos(\tau) \mathbf{f} \quad (9)$$

and each component of the displacement vector can be approximated by

$$u_i(\tau) = \sum_{n=0}^N [a_{i,n} \cos(\tau) + b_{i,n} \sin(\tau)]. \quad (10)$$

For a damped system with quadratic nonlinearity, at least the first two terms of the Fourier series must be considered [39]:

$$u_i(\tau) = a_{i,0} + b_{i,1} \cos(\tau) + c_{i,1} \sin(\tau). \quad (11)$$

For a damped system with only cubic nonlinearity, it is necessary to consider at least the following terms [39]:

$$u_i(\tau) = a_{i,1} \cos(\tau) + b_{i,1} \sin(\tau). \quad (12)$$

Plane frames exhibit quadratic and cubic nonlinearities. Define

$$u_i = \mathbf{C}(\tau) \bar{\mathbf{d}}_i \quad (13)$$

with

$$\begin{aligned}\mathbf{C}(\tau) &= \langle 1, \sin(\tau), \cos(\tau) \rangle, \\ \bar{\mathbf{d}}_i &= \langle a_{i,0}, b_{i,1}, c_{i,1} \rangle^T.\end{aligned}\quad (14)$$

Consider the following relation:

$$\mathbf{u}(\tau) = \mathbf{S}(\tau) \bar{\mathbf{D}}, \quad (15)$$

where

$$\mathbf{S}(\tau) = \begin{bmatrix} \mathbf{C}(\tau) & \mathbf{0} & \mathbf{0} & \mathbf{0} & \cdots & \mathbf{0} \\ \mathbf{0} & \mathbf{C}(\tau) & \mathbf{0} & \mathbf{0} & \cdots & \mathbf{0} \\ \mathbf{0} & \mathbf{0} & \mathbf{C}(\tau) & \mathbf{0} & \cdots & \mathbf{0} \\ \mathbf{0} & \mathbf{0} & \mathbf{0} & \mathbf{C}(\tau) & \cdots & \vdots \\ \vdots & \vdots & \vdots & \vdots & \ddots & \mathbf{0} \\ \mathbf{0} & \mathbf{0} & \mathbf{0} & \cdots & \mathbf{0} & \mathbf{C}(\tau) \end{bmatrix}_{N \times 3N}, \quad (16)$$

$$\bar{\mathbf{D}} = \langle \bar{\mathbf{d}}_1, \bar{\mathbf{d}}_2, \dots, \bar{\mathbf{d}}_N \rangle_{1 \times 3N}^T.$$

$N$  is total number of degrees of freedom. Introducing (15) into (9), the following matrix equation is obtained:

$$\Omega^2 \mathbf{M} \ddot{\mathbf{S}}(\tau) \bar{\mathbf{D}} + \Omega \mathbf{C} \dot{\mathbf{S}}(\tau) \bar{\mathbf{D}} + \mathbf{F} \mathbf{i}(\mathbf{S}(\tau) \bar{\mathbf{D}}) = \mathbf{F}_0 \cos(\tau). \quad (17)$$

Considering that the solution is periodic, multiplying both sides of (17) by  $\mathbf{S}(\tau)^T$  and integrating the resulting expression over a period, one obtains [40]

$$\begin{aligned}\int_0^{2\pi} \mathbf{S}(\tau)^T [\Omega^2 \mathbf{M} \ddot{\mathbf{S}}(\tau) \bar{\mathbf{D}} + \Omega \mathbf{C} \dot{\mathbf{S}}(\tau) \bar{\mathbf{D}} \\ + \mathbf{F} \mathbf{i}(\mathbf{S}(\tau) \bar{\mathbf{D}})] d\tau = \int_0^{2\pi} \mathbf{S}(\tau)^T \mathbf{F}_0 \cos(\tau) d\tau.\end{aligned}\quad (18)$$

In a compact form, (18) can be expressed as

$$\Omega^2 \bar{\mathbf{M}} \bar{\mathbf{D}} + \Omega \bar{\mathbf{C}} \bar{\mathbf{D}} + \bar{\mathbf{F}} \mathbf{i}(\bar{\mathbf{D}}) = \bar{\mathbf{F}}, \quad (19)$$

where

$$\begin{aligned}\bar{\mathbf{M}} &= \int_0^{2\pi} \mathbf{S}(\tau)^T \mathbf{M} \ddot{\mathbf{S}}(\tau) \cdot d\tau, \\ \bar{\mathbf{C}} &= \int_0^{2\pi} \mathbf{S}(\tau)^T \mathbf{C} \dot{\mathbf{S}}(\tau) \cdot d\tau \\ \bar{\mathbf{F}} &= \int_0^{2\pi} \mathbf{S}(\tau)^T \mathbf{F}_0 \cos(\tau) d\tau, \\ \bar{\mathbf{F}} \mathbf{i}(\bar{\mathbf{D}}) &= \int_0^{2\pi} \mathbf{S}(\tau)^T \mathbf{F} \mathbf{i}(\mathbf{S}(\tau) \cdot \bar{\mathbf{D}}) d\tau.\end{aligned}\quad (20)$$

Equation (19) is a nonlinear system of algebraic equations, in which the unknowns are the forcing frequency  $\Omega$  and the modal amplitude vector  $\bar{\mathbf{D}}$ . The internal force vector in frequency domain  $\bar{\mathbf{F}} \mathbf{i}(\bar{\mathbf{D}})$  is obtained from the transformation of  $\mathbf{F} \mathbf{i}(\mathbf{u}(\tau))$ . In this context, an explicit expression for  $\mathbf{F} \mathbf{i}(\mathbf{u}(\tau))$  is necessary. The next step is the solution of the nonlinear system of algebraic equations.

*2.4. Solution of the Nonlinear System of Equations.* The transformation of the equations of motion from time to frequency domain results in a nonlinear system of algebraic equations both for the linear and nonlinear cases, as shown by (6) and (19), with the unknown variables being the forcing frequency and the modal amplitudes. In this section, the technique to solve the nonlinear system of equations must consider the possibility of frequency and amplitude limit points. In this context, (6) can be defined in a general form as

$$\mathbf{R}(\Omega, \bar{\mathbf{D}}) = \mathbf{0}. \quad (21)$$

Through an incremental analysis, the dynamic equilibrium in the  $i$ th step is given by

$$\mathbf{R}(\Omega_i, \bar{\mathbf{D}}_i) = \mathbf{0}. \quad (22)$$

The unknown variables in the  $i$ th step are obtained by the incremental analysis as

$$\begin{aligned} \Omega_i &= \Omega_{i-1} + \Delta\Omega_i, \\ \bar{\mathbf{D}}_i &= \bar{\mathbf{D}}_{i-1} + \Delta\bar{\mathbf{D}}_i. \end{aligned} \quad (23)$$

Introducing (22) into (21) results in

$$\mathbf{R}(\Omega_{i-1} + \Delta\Omega_i, \bar{\mathbf{D}}_{i-1} + \Delta\bar{\mathbf{D}}_i) = \mathbf{0}. \quad (24)$$

The frequency and amplitude increments  $\Delta\Omega_i$  and  $\Delta\bar{\mathbf{A}}_i$  can be calculated iteratively as

$$\begin{aligned} \Delta\Omega_i^k &= \Delta\Omega_i^{k-1} + \delta\Omega_i^k, \\ \Delta\bar{\mathbf{D}}_i^k &= \Delta\bar{\mathbf{D}}_i^{k-1} + \delta\bar{\mathbf{D}}_i^k, \end{aligned} \quad (25)$$

where  $\delta\Omega_i^k$  and  $\delta\bar{\mathbf{D}}_i^k$  are the correctors which can be obtained through the first variation of (24) as

$$\delta\mathbf{R}^k = \frac{\partial\mathbf{R}^{k-1}}{\partial\bar{\mathbf{D}}_i} \delta\bar{\mathbf{D}}_i^k + \frac{\partial\mathbf{R}^{k-1}}{\partial\Omega_i} \delta\Omega_i^k \quad (26)$$

or, in a more compact form, as

$$\overline{\mathbf{K}\mathbf{m}}^{k-1} \delta\bar{\mathbf{D}}_i^k + \delta\Omega_i^k \bar{\mathbf{f}}^{k-1} = \delta\mathbf{R}^k. \quad (27)$$

To solve (27), an additional constraint equation is necessary. In this work, a spherical arc-length constraint is used [41, 42]:

$$\Delta\bar{\mathbf{D}}_i^T \Delta\bar{\mathbf{D}}_i + (\Delta\Omega_i^k)^2 \bar{\mathbf{f}}^{k-1T} \bar{\mathbf{f}}^{k-1} - \Delta l_i^2 = 0. \quad (28)$$

From (24), (25), (27), and (28), it is possible to obtain the iterative frequency corrector as

$$\delta\Omega_i^k = \begin{cases} \pm \frac{\Delta l_i^2}{\sqrt{\mathbf{v}^T \mathbf{v} + \bar{\mathbf{f}}^{k-1T} \bar{\mathbf{f}}^{k-1}}} & \text{for } k = 1 \\ -\frac{\mathbf{r}^k{}^T \mathbf{v}^k}{\mathbf{v}^k{}^T \mathbf{v}^k} & \text{for } k > 1, \end{cases} \quad (29)$$

where

$$\begin{aligned} \mathbf{v}^k &= \left( \overline{\mathbf{K}\mathbf{m}}^{k-1} \right)^{-1} \bar{\mathbf{f}}^{k-1}, \\ \mathbf{r}^k &= \left( \overline{\mathbf{K}\mathbf{m}}^{k-1} \right)^{-1} \mathbf{R}^{k-1}. \end{aligned} \quad (30)$$

The signal of the first frequency corrector, also called frequency predictor, can be obtained using the positive work criterion as

$$\text{sign}(\delta\Omega_i^1) = \text{sign}\left( (\mathbf{v}^1)^T \cdot \bar{\mathbf{f}}^{k-1} \right). \quad (31)$$

For linear systems,  $\overline{\mathbf{K}\mathbf{m}}$  and  $\bar{\mathbf{f}}$  can be defined by the following expressions:

$$\begin{aligned} \overline{\mathbf{K}\mathbf{m}} &= \begin{bmatrix} \Omega\mathbf{C} & -\Omega^2\mathbf{M} + \mathbf{K} \\ -\Omega^2\mathbf{M} + \mathbf{K} & -\Omega\mathbf{C} \end{bmatrix}, \\ \bar{\mathbf{f}} &= \begin{bmatrix} \mathbf{C} & -2\omega\mathbf{M} \\ -2\omega\mathbf{M} & -\mathbf{C} \end{bmatrix} \bar{\mathbf{D}}. \end{aligned} \quad (32)$$

Analogously, for the nonlinear case,  $\overline{\mathbf{K}\mathbf{m}}$  and  $\bar{\mathbf{f}}$  can be obtained from the following relations:

$$\begin{aligned} \overline{\mathbf{K}\mathbf{m}} &= \Omega^2 \overline{\mathbf{M}} + \Omega \overline{\mathbf{C}} + \frac{\partial \bar{\mathbf{F}}_i(\bar{\mathbf{D}})}{\partial \bar{\mathbf{D}}}, \\ \bar{\mathbf{f}} &= (2\Omega \overline{\mathbf{M}} + \overline{\mathbf{C}}) \cdot \bar{\mathbf{D}}. \end{aligned} \quad (33)$$

*2.5. Geometric Nonlinear Consideration.* An explicit expression for  $\mathbf{F}_i(\mathbf{u}(\tau))$  is necessary. Considering an incremental analysis, the nodal displacement vector can be expressed as

$$\mathbf{u}(t_i) = \mathbf{u}(t_{i-1}) + \Delta\mathbf{u}(t). \quad (34)$$

Analogously, the internal forces vector can be calculated as

$$\mathbf{F}_i(t_i) = \mathbf{F}_i(t_{i-1}) + \Delta\mathbf{F}_i(t). \quad (35)$$

$\mathbf{F}_i$  can be derived once the kinematic relations and constitutive law are defined. These relations depend on the adopted nonlinear strain measure formulation [7, 16]. In this paper, only the geometric nonlinearity is considered. In this context, the internal force increment vector can be approximated as

$$\Delta\mathbf{F}_{\text{int}} = (\mathbf{K}_L + \mathbf{K}_{\text{NL}}) \Delta\mathbf{u}, \quad (36)$$

where  $\mathbf{K}_L$  is the linear elastic stiffness matrix and  $\mathbf{K}_{\text{NL}}$  is the nonlinear stiffness matrix. Considering a linearized formulation, the nonlinear stiffness matrix for an Euler-Bernoulli beam-column plane element in a local system of reference can be defined as [7, 16]

$$\mathbf{K}_{\text{NL}} = \begin{bmatrix} \frac{P}{L} & \frac{M1+M2}{L^2} & 0 & -\frac{P}{L} & -\frac{M1+M2}{L^2} & 0 \\ \frac{M1+M2}{L^2} & \frac{6P}{5L} & \frac{P}{10} & -\frac{M1+M2}{L^2} & -\frac{6P}{5L} & \frac{P}{10} \\ 0 & \frac{P}{10} & \frac{PL}{15} & 0 & -\frac{P}{10} & -\frac{PL}{30} \\ -\frac{P}{L} & -\frac{M1+M2}{L^2} & 0 & \frac{P}{L} & \frac{M1+M2}{L^2} & 0 \\ -\frac{M1+M2}{L^2} & -\frac{6P}{5L} & -\frac{P}{10} & \frac{M1+M2}{L^2} & \frac{6P}{5L} & -\frac{P}{10} \\ 0 & \frac{P}{10} & -\frac{PL}{30} & 0 & -\frac{P}{10} & \frac{PL}{15} \end{bmatrix}, \quad (37)$$

where  $P$  is the average internal axial force and  $M1$  and  $M2$  are the internal bending moments in the initial and the end nodes, respectively. For a prismatic beam-column element, the internal forces can be expressed as a function of the axial and transversal displacements, respectively,  $u(x)$  and  $v(x)$ , as

$$P = EA \left( \frac{\partial u(x)}{\partial x} + \frac{1}{L} \int_0^L \left( \frac{\partial v(x)}{\partial x} \right)^2 \cdot dx \right) \quad (38)$$

$$M = EI \left( \frac{\partial^2 v(x)}{\partial x^2} \right),$$

where  $E$  is Young's modulus,  $A$  is the cross-sectional area, and  $I$  is the moment of inertia. The displacement fields can be expressed by interpolation of nodal displacement components as

$$u(x) = \sum_{i=1}^2 H_i(x) u_i, \quad (39)$$

$$v(x) = \sum_{i=3}^6 H_i(x) u_i,$$

where  $H_i(x)$  is the shape function used for the finite element discretization. Analogous to (15), the increment of the nodal displacement vector can be calculated as

$$\Delta \mathbf{u}(t) = \mathbf{S}(\tau) \Delta \bar{\mathbf{D}}. \quad (40)$$

Solving (15), (35), (36), and (40), the nodal internal force vector  $\mathbf{F}_i$  at the  $i$ th increment can be obtained as

$$\mathbf{F}_i = \mathbf{K}_L \mathbf{S}(\tau) \bar{\mathbf{D}} + \mathbf{F}_{i-1} + \mathbf{K}_{\text{NL}} \mathbf{S}(\tau) \Delta \bar{\mathbf{D}}. \quad (41)$$

Finally, the nodal internal force vector in frequency domain defined in (20) can be calculated as

$$\bar{\mathbf{F}}_i(\bar{\mathbf{D}}) = \bar{\mathbf{K}}_L \bar{\mathbf{D}}_i + \bar{\mathbf{K}}_{\text{NL}} \Delta \bar{\mathbf{D}} + \bar{\mathbf{F}}_{i-1}(\bar{\mathbf{D}}), \quad (42)$$

where

$$\bar{\mathbf{K}}_L = \int_0^{2\pi} \mathbf{S}(\tau)^T \mathbf{K}_L \mathbf{S}(\tau) d\tau$$

$$\bar{\mathbf{K}}_{\text{NL}} = \int_0^{2\pi} \mathbf{S}(\tau)^T \mathbf{K}_{\text{NL}} \mathbf{S}(\tau) d\tau \quad (43)$$

$$\bar{\mathbf{F}}_{i-1}(\bar{\mathbf{D}}) = \int_0^{2\pi} \mathbf{S}(\tau)^T \mathbf{F}_{\text{NL}i-1} d\tau.$$

In linear case,  $\bar{\mathbf{F}}_i(\bar{\mathbf{D}}) = \bar{\mathbf{K}}_L \bar{\mathbf{D}}$ , and the resultant nonlinear system of equations defined by (19) is the same as the system obtained through the classical HBM (see (5)).

**2.6. Equivalent Rotation Matrix.** In order to assemble the global system of equations, the matrices  $\mathbf{M}$ ,  $\mathbf{C}$ ,  $\mathbf{K}_L$ , and  $\mathbf{K}_{\text{NL}}$  must be defined in global coordinates. The matrices  $\mathbf{M}$ ,  $\mathbf{C}$ , and  $\mathbf{K}_L$  are the same for any reference system, since they are constant. On the other hand,  $\mathbf{K}_{\text{NL}}$ , defined by (37), is formulated in a local reference frame. Thus, its rotation to the global reference system is necessary. It is defined in global reference frame by

$$\bar{\mathbf{K}}_{\text{NL}} = \int_0^{2\pi} \mathbf{S}(\tau)^T \mathbf{T}^T \mathbf{K}_{\text{NL}} \mathbf{T} \mathbf{S}(\tau) d\tau, \quad (44)$$

where  $\mathbf{T}$  is a rotation matrix. The rotation matrix for a plane beam-column element can be found in [15]. In terms of the computational implementation, it is not convenient to rotate the stiffness matrix  $\mathbf{K}_{\text{NL}}$  before frequency domain transformation, since the elements of  $\mathbf{K}_{\text{NL}}$  have large expression which depend on nodal displacement, even in the local reference frame. So, it is convenient to rotate  $\mathbf{K}_{\text{NL}}$  after the transformation of the equations to the frequency domain, using an equivalent rotation matrix. In this case, it takes the form

$$\bar{\mathbf{K}}_{\text{NL}} = \mathbf{T}'^T \int_0^{2\pi} \mathbf{S}(\tau)^T \mathbf{K}_{\text{NL}} \mathbf{S}(\tau) d\tau \mathbf{T}', \quad (45)$$

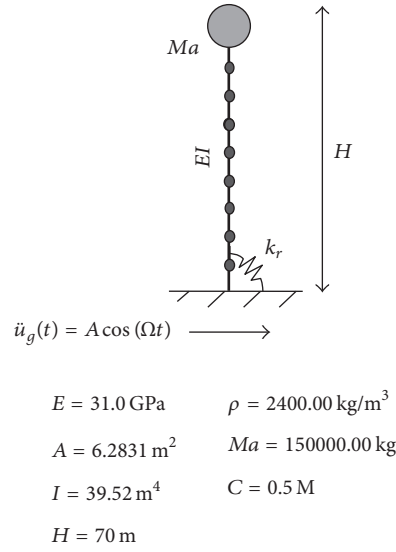


FIGURE 1: Tower model with concentrated mass at top and elastoplastic support.

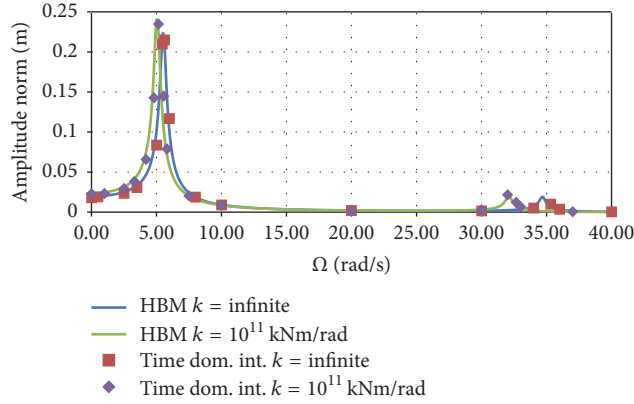


FIGURE 2: Variation of the maximum displacement at the top of the tower as a function of the forcing frequency  $\Omega$  obtained with the harmonic balance method (HBM) and with time domain integration.  $A_x = 0.8g$ .

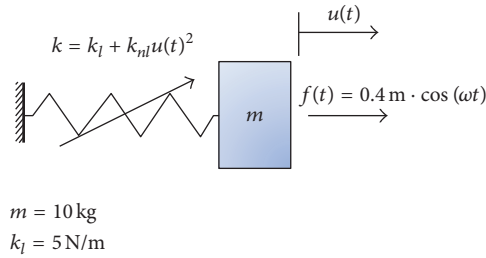


FIGURE 3: 1-DOF model with cubic nonlinear stiffness under harmonic excitation.

where  $\mathbf{T}'$  is the equivalent rotation matrix, which satisfies the following condition:

$$\mathbf{T}'^T \mathbf{S}(\tau)^T = \mathbf{S}(\tau)^T \mathbf{T}^T. \quad (46)$$

Taking into account the block-diagonal characteristic of  $\mathbf{S}(\tau)$  and since  $\mathbf{T}$  is an orthogonal matrix, it is possible to find

an explicit expression for  $\mathbf{T}'$  as a function of  $\mathbf{T}$  through the following expression:

$$\mathbf{T}' = \begin{bmatrix} \mathbf{t}'_{1,1} & \cdots & \mathbf{t}'_{1,NGL} \\ \vdots & \ddots & \vdots \\ \mathbf{t}'_{NGL,1} & \cdots & \mathbf{t}'_{NGL,NGL} \end{bmatrix}, \quad (47)$$

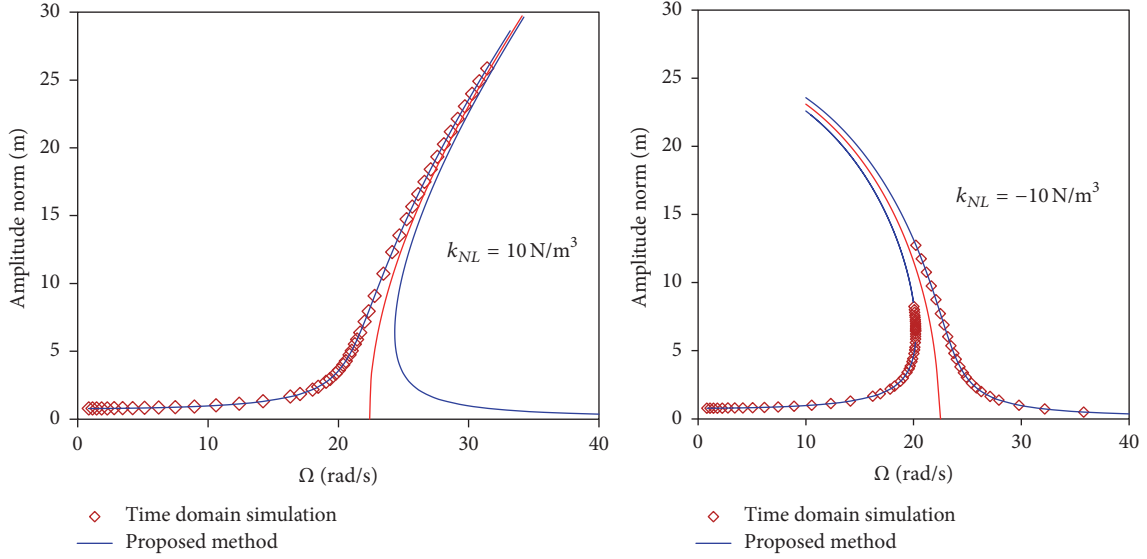


FIGURE 4: Nonlinear resonance curves. Maximum amplitude as a function of the forcing frequency.

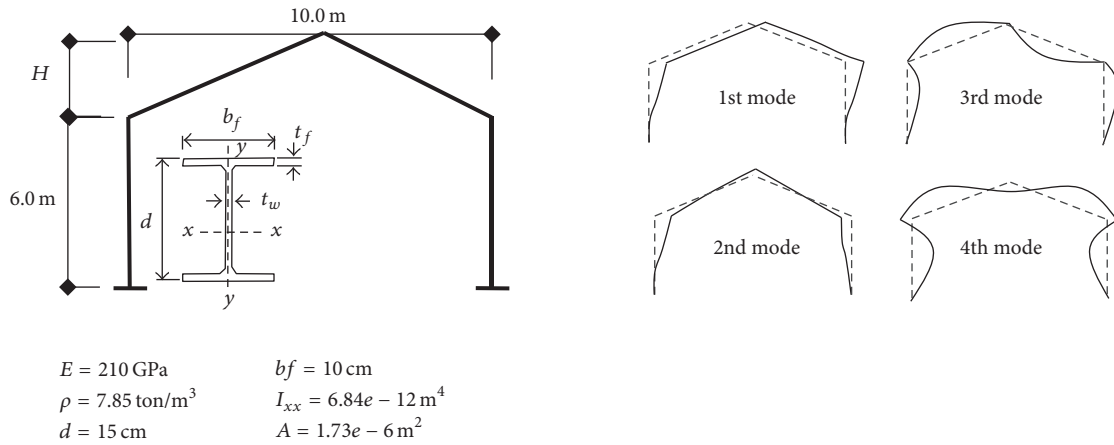


FIGURE 5: Pitched-roof frame model and four first natural vibration modes.

where NGL is the number of degrees of freedom and  $\mathbf{t}'_{i,j}$  is a submatrix given by

$$\mathbf{t}'_{i,j} = \mathbf{T}_{i,j} \mathbf{I}_3, \quad (48)$$

where  $\mathbf{I}_3$  is an identity matrix of order three.

### 3. Numerical Examples

**3.1. Linear Analysis Validation.** As a first example, a simple tower model with a concentrated mass at the top and an elastic rotational support at the base is studied to validate the linear formulation. The finite element model is composed of 10 beam-column Euler-Bernoulli elements. The geometrical and material properties are shown in Figure 1. The tower is under the action of a horizontal harmonic base displacement.

Figure 2 shows the variation of the maximum displacement at the top of the tower as a function of the forcing

frequency  $\Omega$  (resonance curve) for a forcing magnitude  $A_x = 0.8g$ , where  $g$  is the acceleration of gravity, considering two values of the elastic support stiffness  $k_r$ . The results obtained with the present formulation and continuation scheme agree with the results obtained from a time domain analysis. This shows the coherence of the result obtained with the proposed method.

**3.2. Nonlinear Analysis Validation.** As a second example, a simple mass-spring system with cubic nonlinearity under harmonic excitation is studied to validate the nonlinear formulation. The schematic representation of the system and relevant properties are shown in Figure 3. In this example, damping is not considered.

Figure 4 shows the nonlinear resonance curves obtained through the present HBM-Galerkin methodology and time domain simulations for positive (hardening) and negative (softening) cubic nonlinearity ( $k_{nl} = \pm 10 \text{ N/m}^3$ ). The results

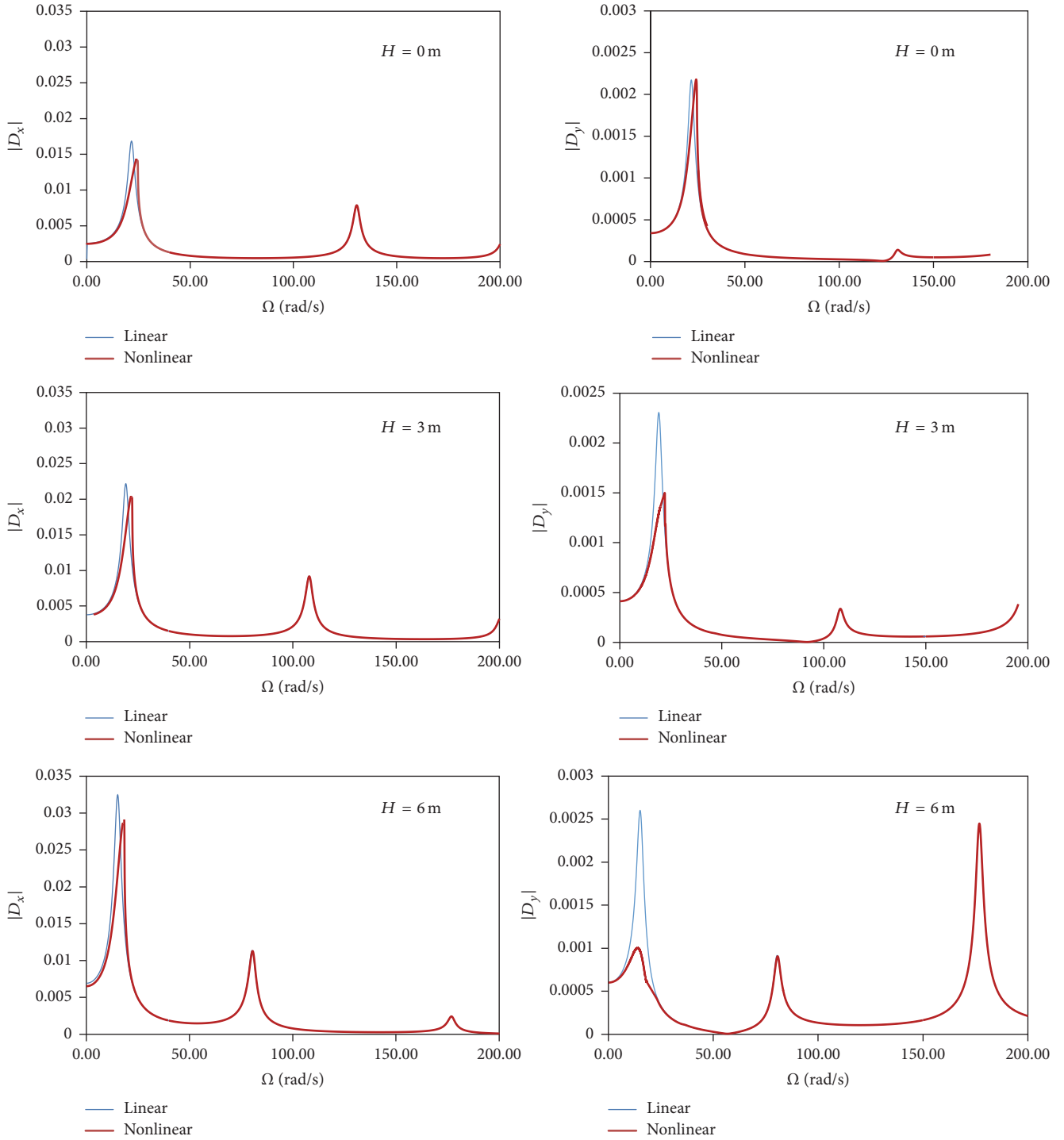


FIGURE 6: Variation of the norm of the horizontal and vertical vibration amplitudes at the roof top as a function of the excitation frequency for a horizontal base excitation and three values of the roof height  $H$ .  $A_x = 0.96g$ .

obtained with the present HBM-Galerkin scheme and with time domain simulations are very close, validating the non-linear formulation. It can be also observed that the algorithm is able to bypass the limit point associated with the saddle-node bifurcation. As expected, the time domain analysis is not able to trace the unstable branches of resonance curves.

### 3.3. Frequency Domain Analysis of Slender Frames

3.3.1. *Pitched-Roof Frame.* A pitched-roof frame fixed at the base and with a constant cross section is studied to assess the behavior of this type of commonly used structure under horizontal and vertical base excitation. The geometry and material properties of the frame are shown in Figure 5, as well

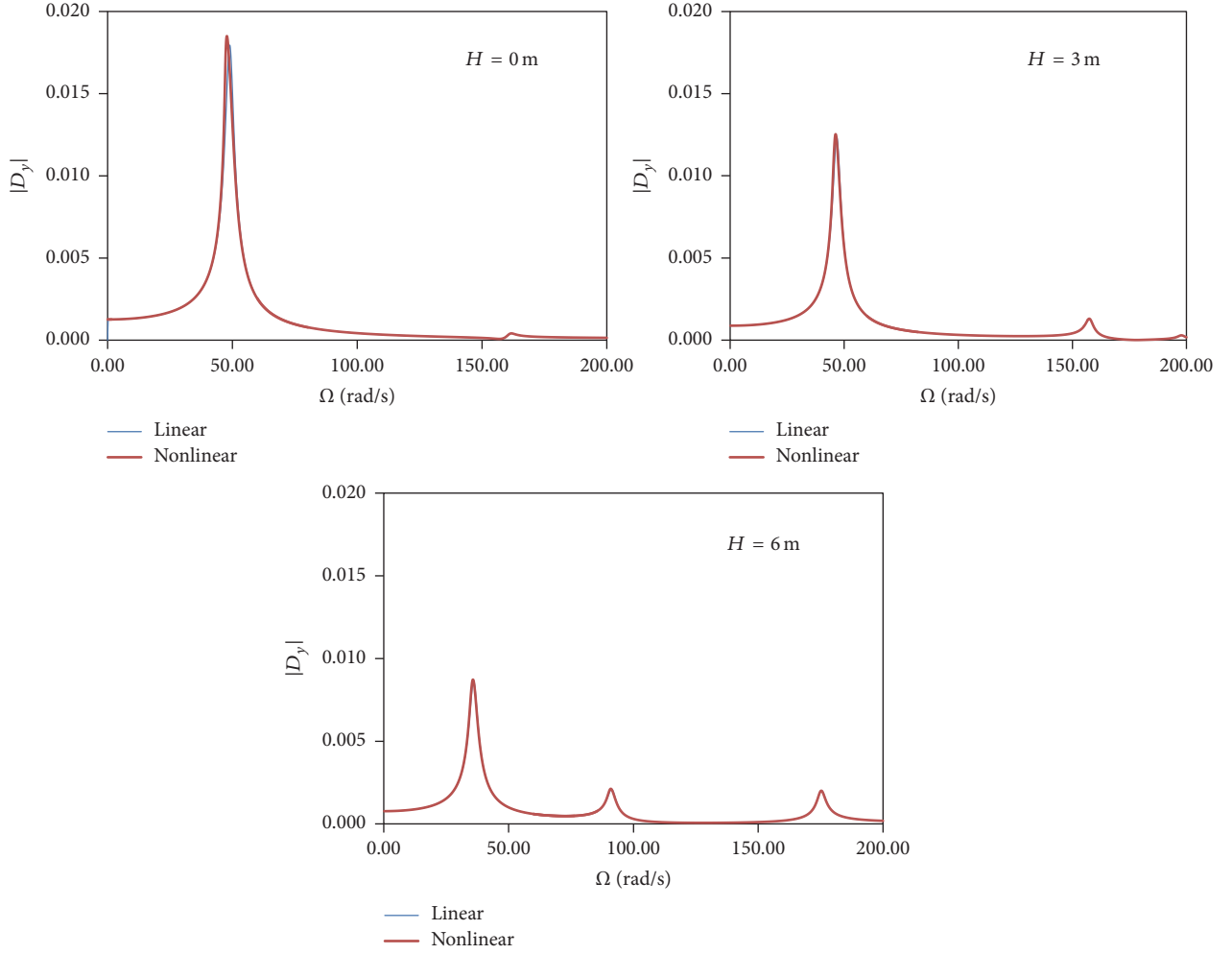


FIGURE 7: Variation of the norm of the vertical vibration amplitude at the roof top as a function of the excitation frequency for a vertical base excitation and three values of the roof height  $H$ .  $A_y = 0.96g$ .

TABLE 1: Four first natural frequencies of the pitched-roof frame.

$H$ (m)	Natural vibration frequency (rad/s)			
	1st mode	2nd mode	3rd mode	4th mode
0.0	21.82	48.97	130.54	161
3.0	19.61	47.14	108.23	159.80
6.0	15.40	36.42	83.21	92.08

as the configuration of the first four natural vibration modes, with the first and third modes being antisymmetric and the second and fourth modes being symmetric. The influence of the roof height on the response is also investigated. Table 1 shows the first four natural frequencies for the three values of  $H$  considered in the numerical analysis. The vibration frequencies decrease with  $H$ , as the frame slenderness increases. The structure is modeled with twenty beam-column elements: 8 elements of the same size for the columns and 12 elements for the roof.

Figure 6 shows the variation of the norm of the horizontal and vertical components of the displacement at top of the

frame,  $D_x$  and  $D_y$ , respectively, as a function of the forcing frequency,  $\Omega$ , considering both linear (blue) and nonlinear (red) FE formulations for three values of the height of the roof pitches ( $H = 0$  m, 3 m, and 6 m) and considering a horizontal excitation magnitude:  $A_x = 0.96g$ . The horizontal base motion excites the first and the third modes only, which correspond to predominantly lateral deformation modes. The nonlinear effect is present in the first resonance region, where a hardening behavior is observed. The first peak and, consequently, the nonlinearity increase with increasing roof height, with the nonlinear maximum vibration amplitude being slightly lower than the linear one. After the first peak, the nonlinear and linear responses are practically coincident. The vertical displacement  $D_y$  is smaller than the vertical component and is overestimated in a linear analysis. Figure 7 displays the response for a vertical excitation magnitude:  $A_y = 0.96g$ . The vertical base motion excites the second and fourth modes; these modes correspond to symmetric vibration modes with predominantly vertical motion. For vertical base excitation, the resonance peak of the vertical motion decreases when the roof height increases and the

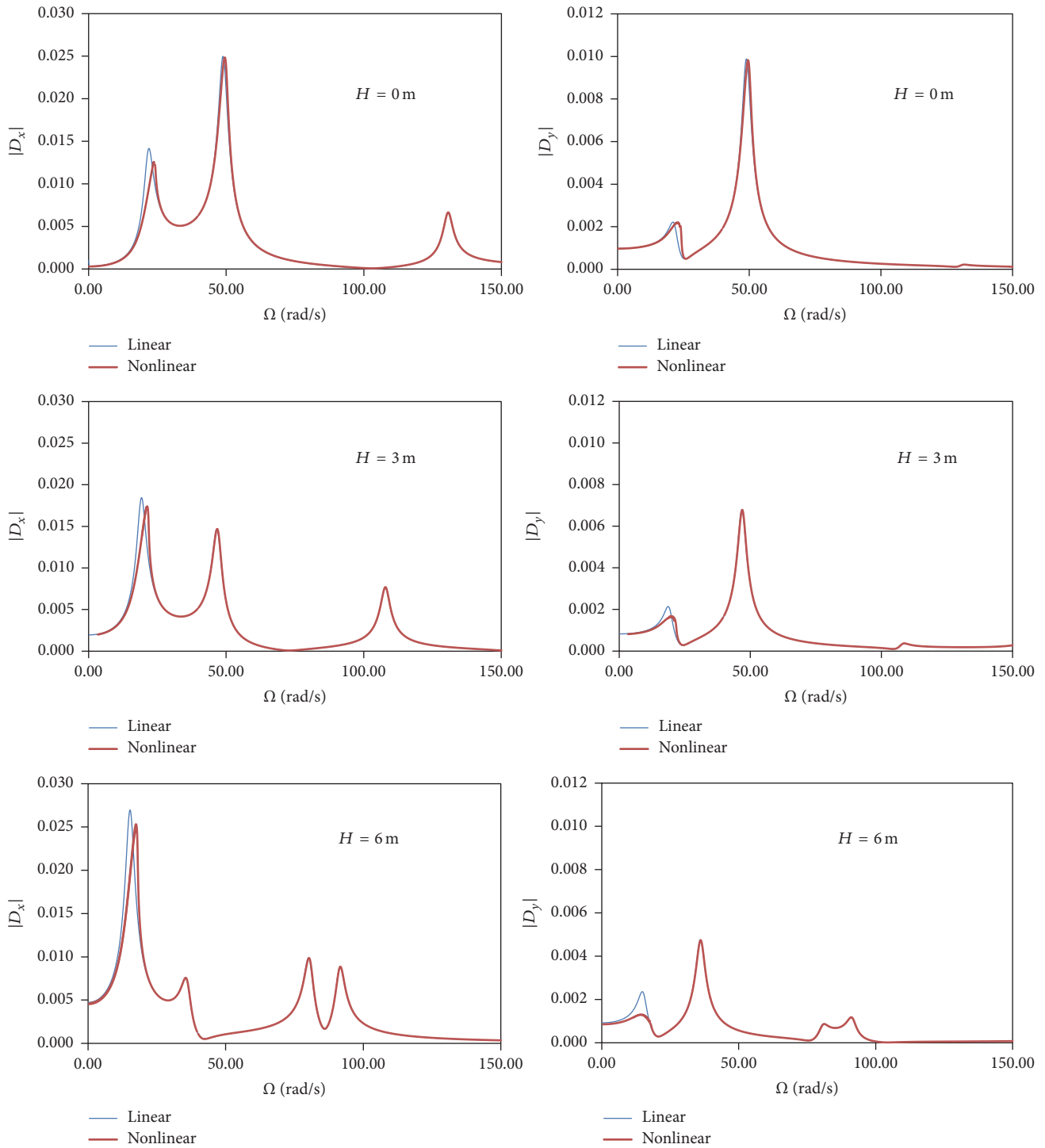


FIGURE 8: Variation of the norm of the vertical and horizontal vibration amplitudes at the roof top as a function of the excitation frequency for simultaneous vertical and horizontal excitation and three values of the roof height  $H$ .  $A_x = 0.8g$  and  $A_y = 0.667A_x$ .

effect of nonlinearity is negligible. In this case, due to the symmetry of the displacement field, the lateral motion of the top node is zero.

Figure 8 shows the norm of the horizontal and vertical displacement as a function of the forcing frequency for the frame excited in both the horizontal and vertical directions.

This is a typical excitation in seismic analysis where both components are usually present. Following the suggestion of some seismic code [43], the intensity of the vertical base motion is adopted as 0.67 times the intensity of the horizontal base motion ( $A_y = 0.66A_x$ ). In this case, all vibration modes are excited. The influence of geometric nonlinearity is

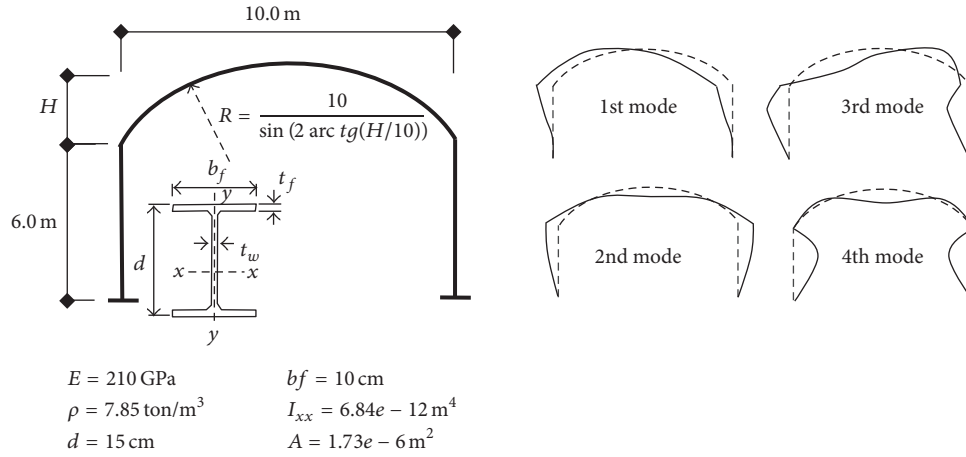


FIGURE 9: Arched-roof frame model and four first natural vibration modes.

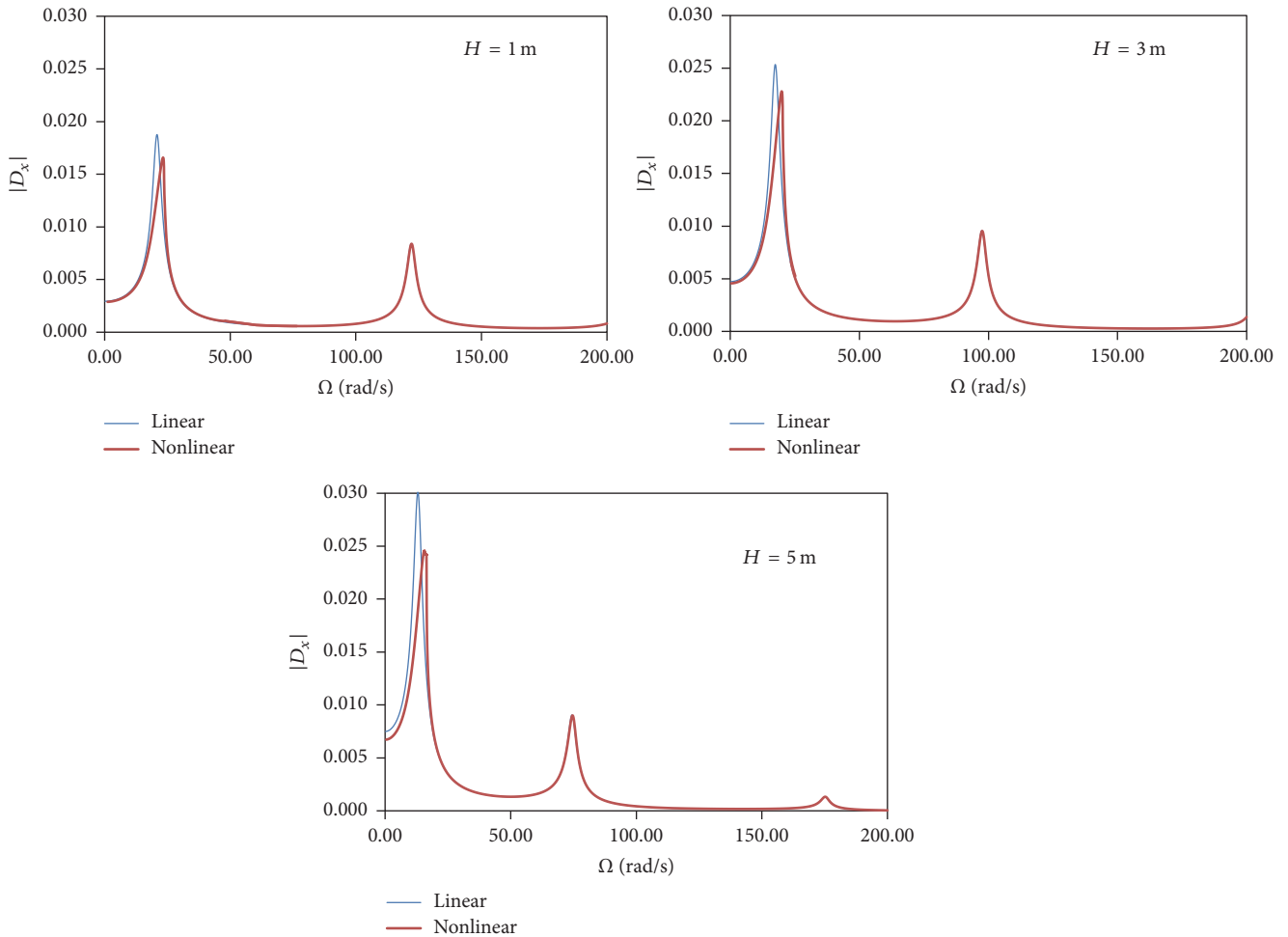


FIGURE 10: Influence of the roof height on the nonlinear response of the arched-roof frame under horizontal excitation.  $A_x = 0.96g$ .

evident in the two first resonance regions, where a hardening behavior, leading to possible dynamic jumps, is observed. As the roof height increases, the magnitude of  $D_x$  corresponding to the first resonant peak increases, while the magnitude of second peak decreases. On the other hand, the magnitude

of vertical displacement  $D_y$  is reduced in the two first resonance regions with the increase of the roof height. These nonlinear resonance curves exhibit amplitude and frequency limit points. This indicates the existence of fold (saddle-node) bifurcations, which can only be mapped by the use of

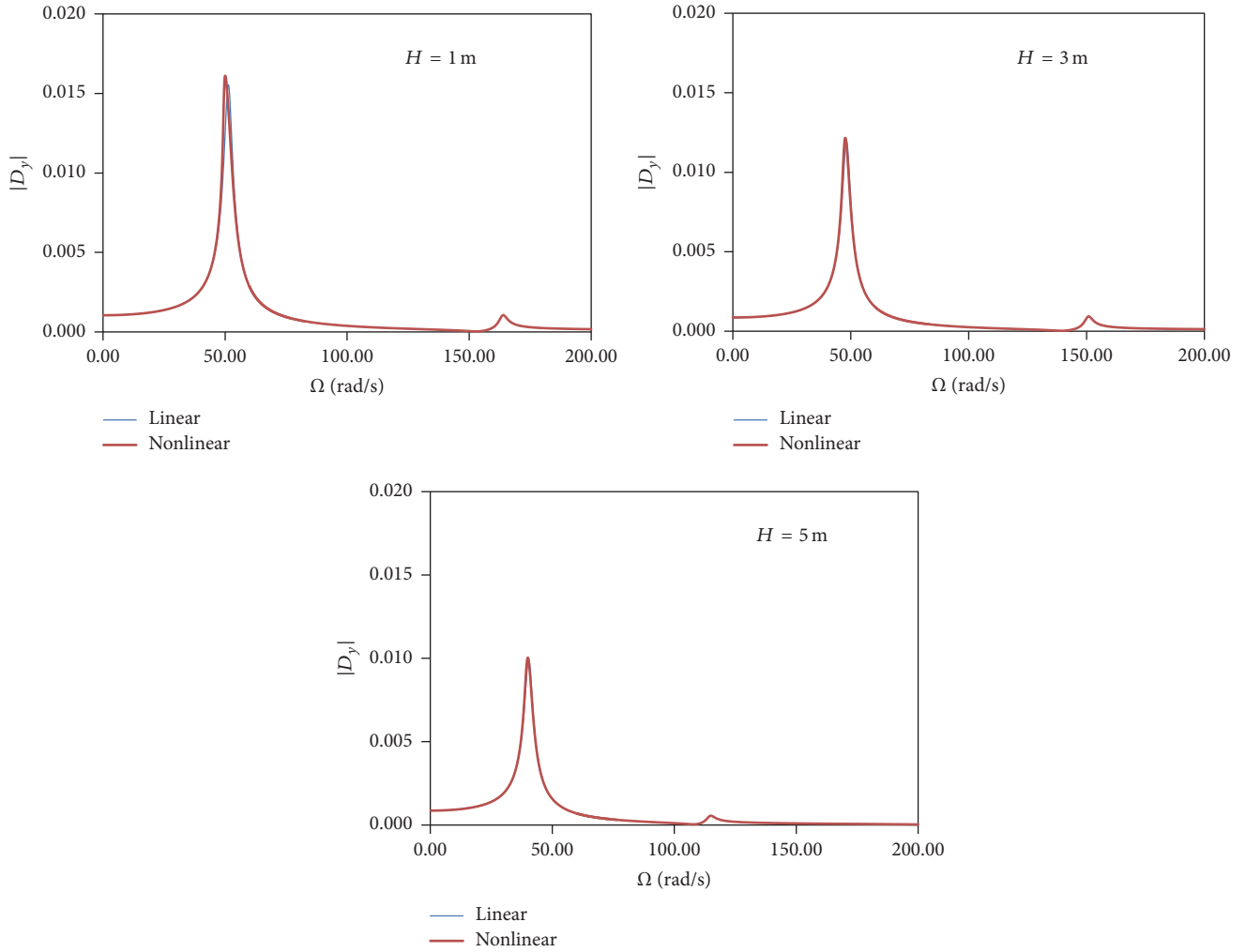


FIGURE 11: Influence of the roof height on the nonlinear response of the arched-roof frame under vertical excitation.  $A_y = 0.96g$ .

continuation techniques. The solutions between the two limit points are unstable.

**3.3.2. Arched-Roof Frame.** Now, an arched-roof frame fixed at the base and with a constant cross section is studied to assess the behavior of this typical structural form under horizontal and vertical base excitation. The structure has the same span, column height, and cross section as the pitched roof, as well as the same material properties, as shown in Figure 9, to enable comparisons of the results. An incomplete circular arch with height  $H$  is considered. Figure 9 also shows the configuration of the first four vibration modes. Table 2 shows the first four natural frequencies for three values of the arch height,  $H$ . As in the previous example, the first and third modes are antisymmetric, while the second and fourth modes are symmetric.

Figures 10 and 11 show the variation of the norm of the vertical and horizontal displacements at top of the arch as a function of the forcing frequency for horizontal and vertical harmonic excitation, respectively, and considering both linear (blue) and nonlinear (red) formulations. For the

TABLE 2: Natural vibration frequencies of the arched-roof frame.

$H$ (m)	Natural vibration frequency (rad/s)			
	1st mode	2nd mode	3rd mode	4th mode
1.0	21.02	51.73	122.60	167.05
3.0	17.81	48.51	97.77	151.60
5.0	13.20	40.79	74.02	113.41

horizontal base excitation, the first and the third modes are excited and the nonlinear effect is only noticed in the first peak leading to a hardening behavior and decrease of the maximum lateral displacement. As in the previous example, the first peak increases with the increase of the roof height. For vertical base excitation, only the second and fourth modes are excited and the nonlinear effect is slightly noted in the first peak only, where a softening behavior is observed. In this case, the first peak amplitude decreases when the roof height increases. Comparing the results of the pitched roof and arched roof for  $H = 3$  m, one can observe that the arched roof is more flexible, leading to higher vibration amplitudes.

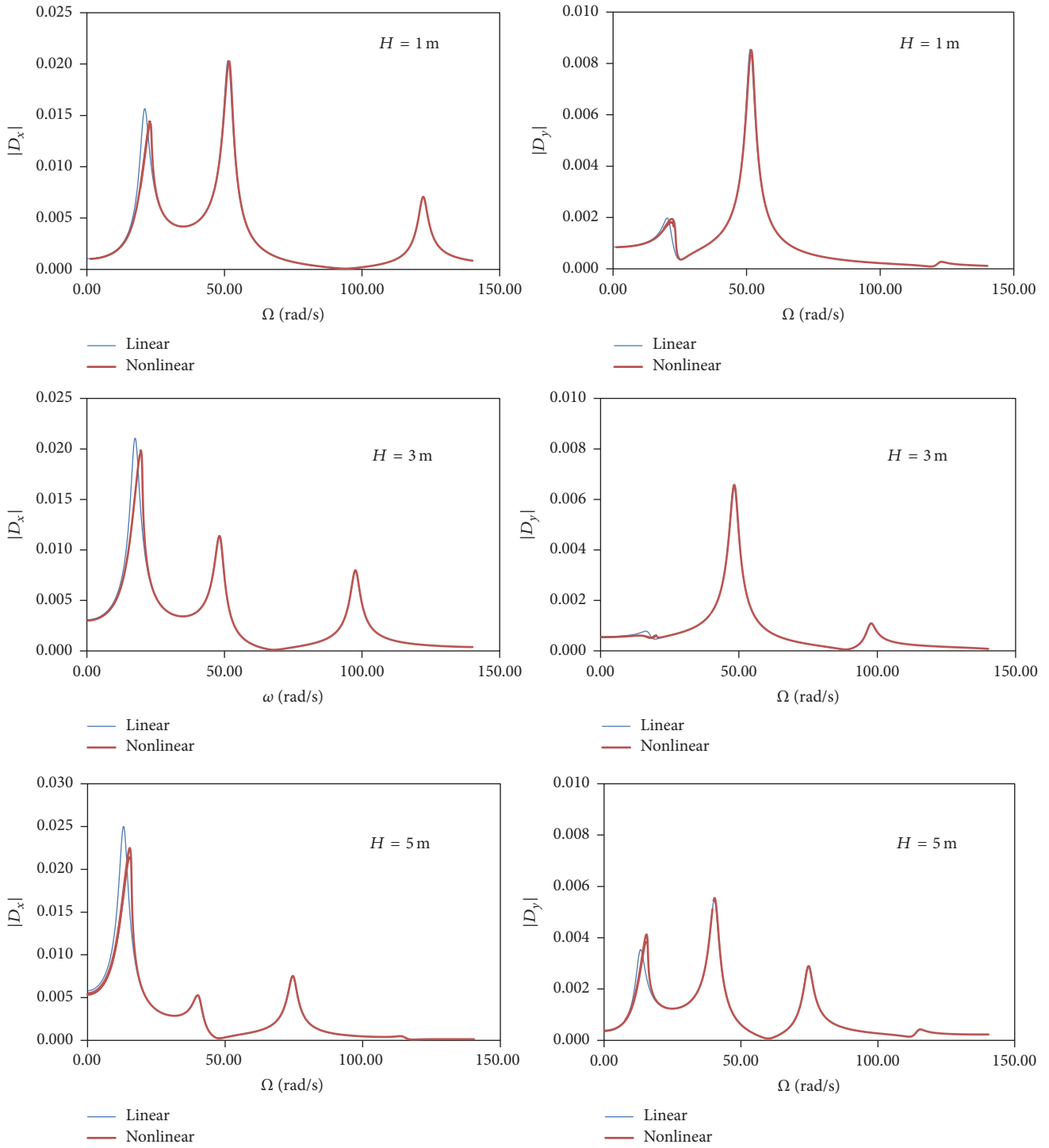


FIGURE 12: Variation of the norm of the vertical and horizontal vibration amplitudes at the roof top as a function of the excitation frequency for simultaneous vertical and horizontal excitation and three values of the roof height  $H$ .  $A_x = 0.8g$  and  $A_y = 0.667A_x$ .

Figure 12 shows the variation of the maximum horizontal ( $D_x$ ) and vertical displacements ( $D_y$ ) at the top of arch, considering both horizontal and vertical base excitations with  $A_y = 0.667A_x$  and  $A_x = 0.8g$ . In this case, all vibration modes are excited. The influence of the geometric nonlinearity is evident in the two first resonance regions, where

a hardening behavior leading to possible dynamic jumps is observed. As the roof height increases, the magnitude of  $D_x$  corresponding to the first resonant peak increases, while the magnitude of second peak decreases. The magnitude of vertical displacement  $D_y$  decreases in the two first resonance regions with the increase of the roof height.

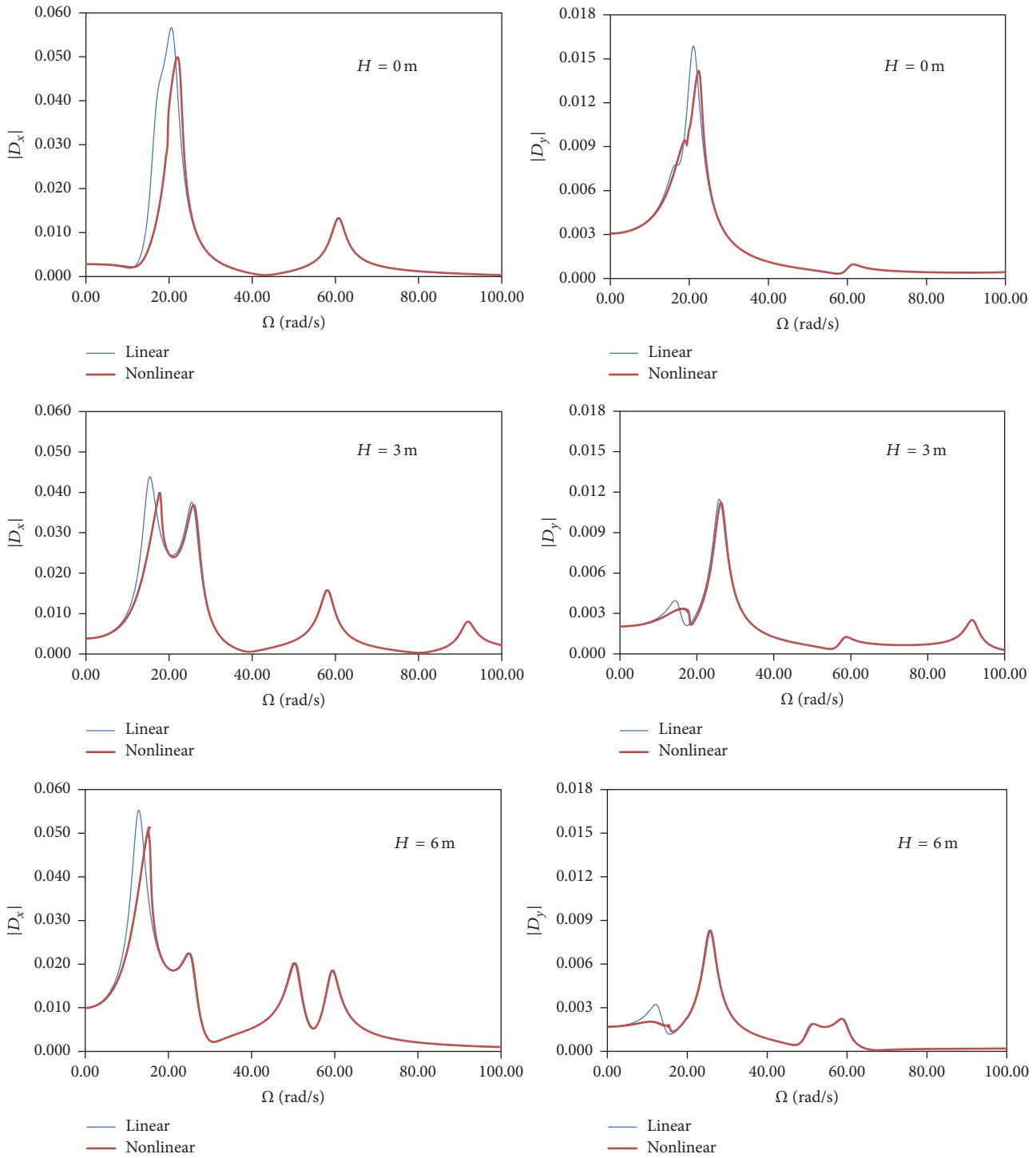


FIGURE 13: Influence of the roof height on the nonlinear response of the frame under horizontal and vertical excitation.  $A_x = 0.8g$  and  $A_y = 0.667A_x$ .

3.3.3. *Pitched-Roof Frame with a Long Span.* Now, the pitched roof is again analyzed considering a span length  $L = 16.0\text{ m}$ , increasing thus the frame’s slenderness. The other properties of the system are the same as those shown in Figure 5. Table 3 shows the first four natural frequencies for the three values of

the roof height. Compared with the results in Table 1, a strong decrease in the natural frequencies is observed.

Figure 13 shows the resonance curves of the horizontal ( $A_x$ ) and vertical ( $A_y$ ) displacement at the top of the frame considering vertical and horizontal harmonic base excitation

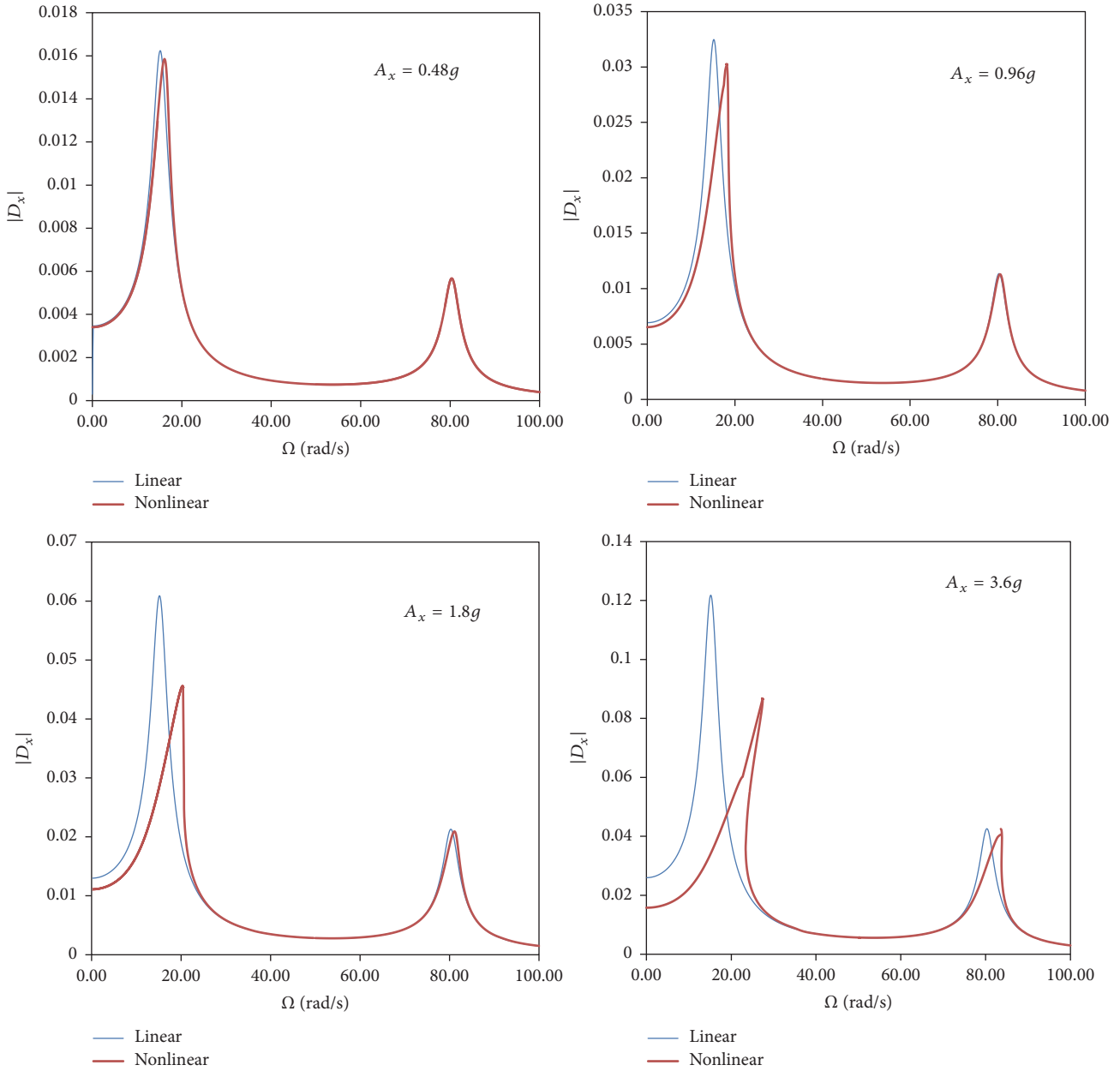


FIGURE 14: Influence of increasing magnitude  $A_x$  on the nonlinear response of the frame under horizontal excitation. Norm of the horizontal displacement at top of pitched-roof as a function of the forcing frequency.  $L = 10$  and  $H = 6$  m.

acting simultaneously with amplitude of the horizontal acceleration of  $A_x = 0.8g$  and vertical acceleration of  $A_y = 0.66A_x$ . The nonlinear effects are visible in the two first resonance regions, similar to the frame with  $L = 10$  m. However, the two first natural frequencies are close, especially for  $H = 0$  m, leading to modal interaction between the two first modes and a large excitation region, where large-amplitude vibrations occur. Compared with the results in Figure 6, for  $L = 10$  m, a marked increase in the lateral and vertical displacements is observed. The vertical displacements are particularly large around the second vibration frequency.

**3.3.4. Strong Base Motion.** Now, the effect of strong base motion on the nonlinear dynamics of the pitched-roof frame (Section 3.3.1), arched-roof (Section 3.3.2) frame, and pitched-roof frame with long span (Section 3.3.3) is assessed. For this, a parametric study considering the variation of the ground acceleration magnitude is presented. A maximum acceleration peak of  $3.6g$  for a single direction excitation and of  $3.0g$  for horizontal and vertical excitations acting simultaneously is adopted.

Figure 14 shows the variation of the maximum horizontal displacement at top of the pitched-roof frame (Figure 5) as a function of the forcing frequency for increasing base

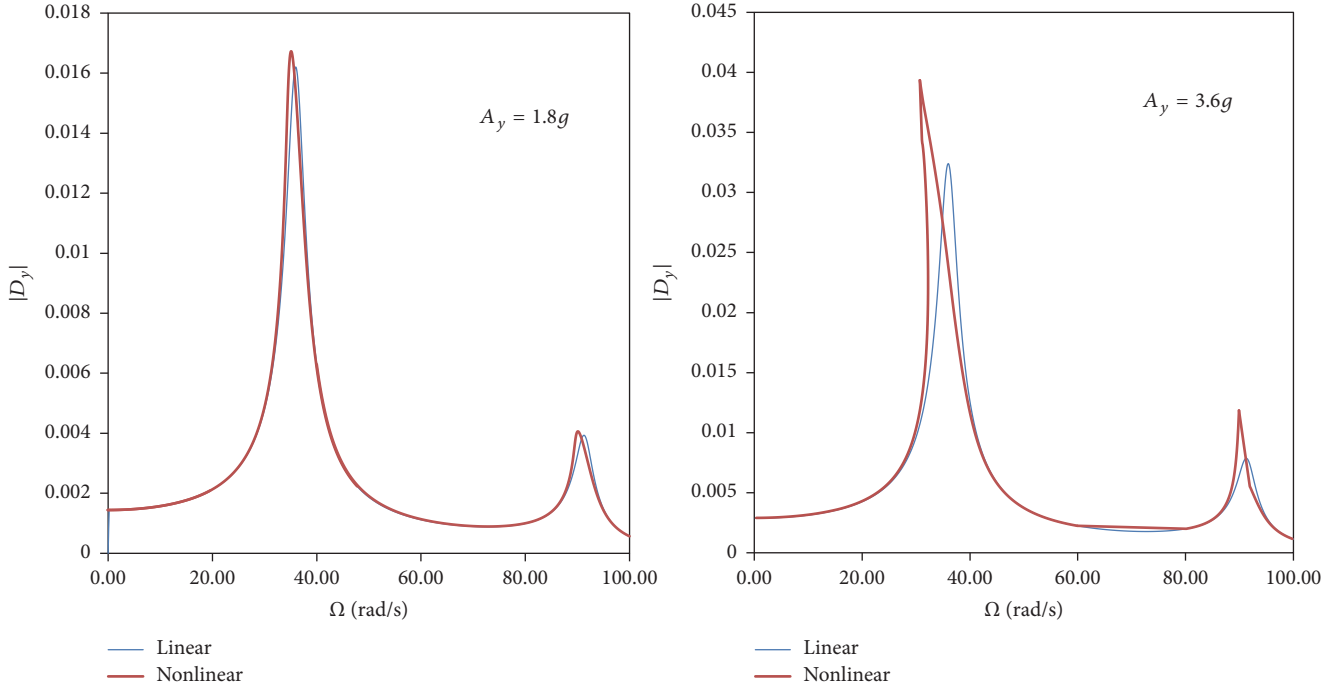


FIGURE 15: Influence of increasing base motion  $A_x$  on the nonlinear response of the frame under vertical excitation. Norm of the vertical displacement at top of pitched roof as a function of the forcing frequency.  $L = 10$  m and  $H = 6$  m.

TABLE 3: Natural vibration frequency of pitched-roof frame.

$H$ (m)	Natural frequency of vibration (rad/s)			
	1st mode	2nd mode	3rd mode	4th mode
0.0	16.60	21.09	60.68	117.35
3.0	15.52	25.58	58.03	91.95
6.0	12.93	24.82	50.24	59.47

excitation magnitude. A sharp increase in the vibration amplitude and the hardening nonlinearity of the response in the first resonance region is observed. For strong base motions, the effect of the nonlinearity in the vicinity of the third vibration frequency begins to appear, being also of the hardening type. The second mode is not excited.

Figure 15 shows the frame response due to vertical harmonic acceleration, considering  $A_x = 1.8g$  and  $A_x = 3.6g$ . The effect of the geometric nonlinearity is observed in the resonance regions associated with the second and fourth vibration modes, exhibiting softening behavior. The softening behavior is due to quadratic nonlinearities and is connected with the interaction between axial and transversal beam displacements. In such cases, the linear analysis underestimates the maximum vibration response. The softening effect due to negative quadratic nonlinearity can be observed in other slender structures under compressive loads like shallow arches and arises from the interaction between in-plane compressive forces and bending [25].

Figure 16 shows the horizontal and vertical components of vibration as function of forcing frequency at top of

pitched-roof frame ( $L = 10$  m and  $H = 6$  m), considering harmonic horizontal and vertical base excitations acting simultaneously and considering  $A_y = 0.667A_x$  and two values of the acceleration amplitude:  $A_x = 1.5g$  and  $A_x = 3.0g$ . The nonlinear effect is present in all resonance regions for the two displacement components. A strong difference between the linear and nonlinear responses is particularly observed in the first resonance region.

Finally, Figure 17 shows the horizontal and vertical displacement components at top of pitched-roof frame as a function of forcing frequency for the frame with  $L = 16$  m and  $H = 6$  m, considering harmonic horizontal and vertical base excitations acting simultaneously with  $A_y = 0.667A_x$ , for two values of  $A_x$ :  $1.5g$  and  $3.0g$ . Again, the strong base motion leads to a highly nonlinear response.

In all cases analyzed here, the resonance curves for the linear and nonlinear cases were easily obtained by the proposed numerical methodology, which can be easily applied to any structural system discretized by the FEM.

## 4. Conclusions

In this work, an incremental technique for the direct calculation of the nonlinear resonance curves of plane frames discretized by the finite element method and subjected to a base excitation is proposed. The transformation of discretized equations of motion, in the finite element method context, to the frequency domain is accomplished here through the classical harmonic balance method together with the Galerkin method. The resulting system of nonlinear equations in terms

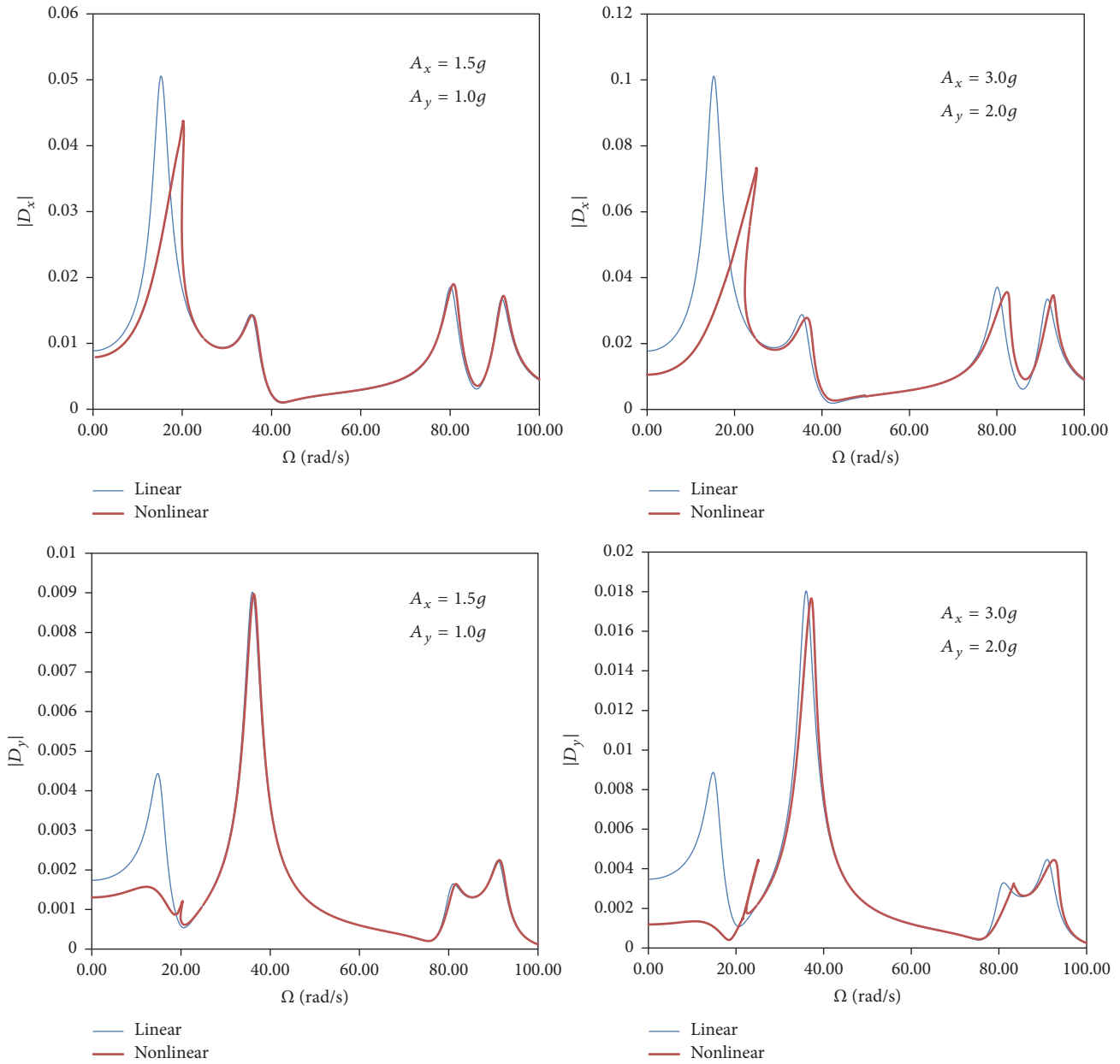


FIGURE 16: Horizontal and vertical displacements at top of the frame as a function of the forcing frequency due to simultaneous horizontal and vertical forcing.  $L = 10$  m and  $H = 6$  m.

of the modal amplitudes and forcing frequency is solved by the Newton-Raphson method together with an arc-length procedure to obtain the nonlinear resonance curves. The formulation of the proposed method is validated comparing the present results with time domain simulations showing coherence and precision. The algorithm is able to map regions with coexisting stable and unstable solutions. A pitched-roof frame and an arched-roof frame under horizontal and vertical base excitation with varying roof height and spans are studied to illustrate the influence of the nonlinearity on the four first resonance regions. Horizontal base motion

excites only the odd modes, while vertical base motion excites only the even modes. Under simultaneous vertical and horizontal excitation, all modes are excited. The roof height has a strong influence on the resonant peaks and degree of nonlinearity. The results also show the influence of increasing base excitation on the nonlinear behavior. Depending on the excitation magnitude, hardening or softening behavior can be observed. The proposed method is shown to be a useful method for the analysis of slender frame structures in frequency domain, since it is able to obtain the resonance curves with precision and small computational effort. This

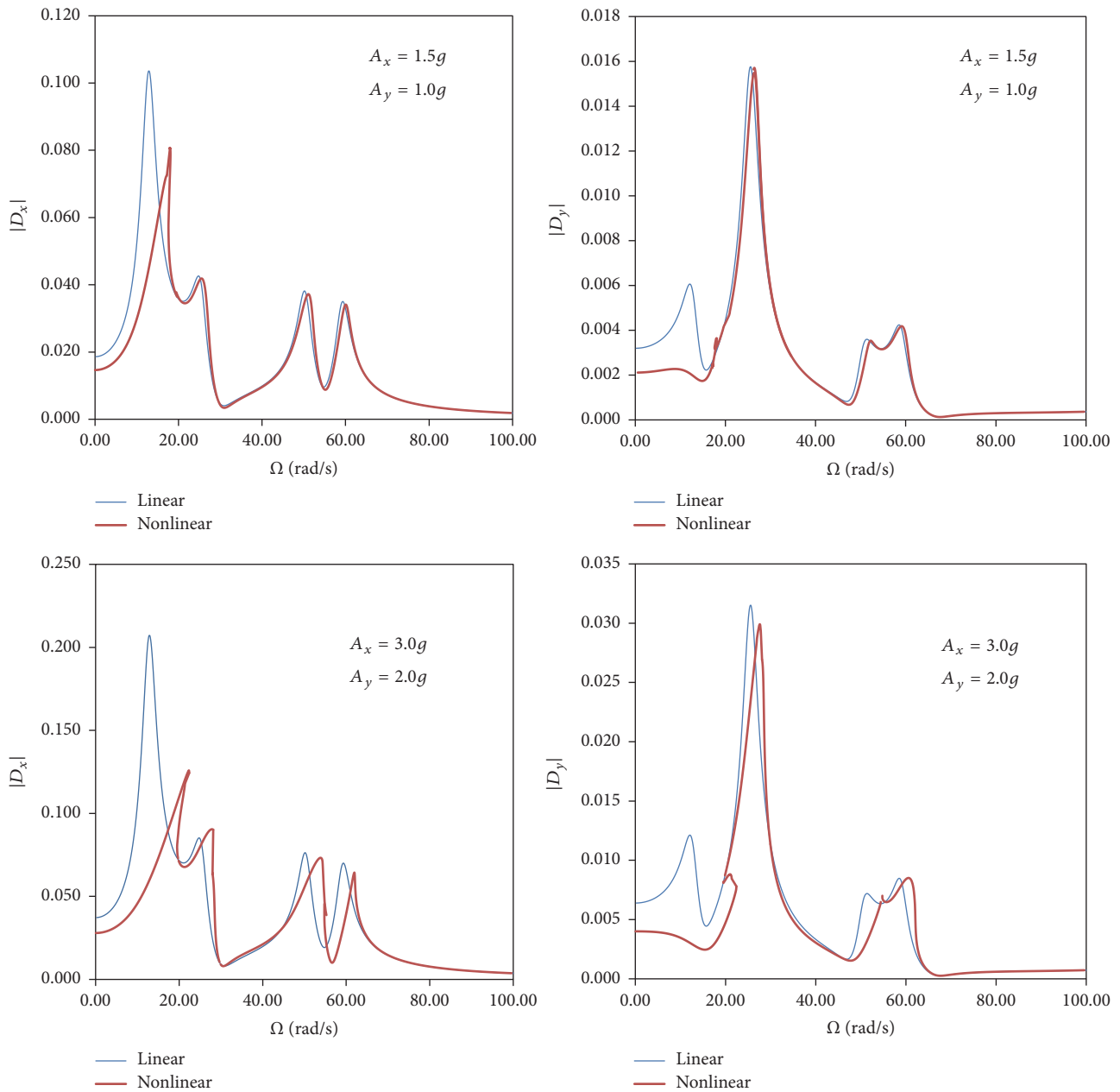


FIGURE 17: Horizontal and vertical displacements at the top of the frame as a function of the forcing frequency due to simultaneous horizontal and vertical forcing.  $L = 16$  m and  $H = 6$  m.

can be used as a preliminary design tool for frames under seismic and other types of base excitation, leading to a safer design.

### Conflicts of Interest

The authors declare that there are no conflicts of interest regarding the publication of this paper.

### References

- [1] W. T. Koiter, "Post-buckling analysis of simple two-bar frame," in *Recent Progress in Applied Mechanics*, B. Broberg, J. Hult, and F. Niordson, Eds., pp. 337–354, 1967.
- [2] J. Roorda, *The instability of imperfect elastic structures [Ph.D. thesis]*, University College London, London, UK, 1965.
- [3] Z. Bazant and L. Cedolin, *Stability of Structures*, Oxford University Press, Oxford, UK, 1991.
- [4] T. V. Galambos, *Guide to Stability Design Criteria for Metal Structures*, John Wiley & Sons, 1998.
- [5] N. Silvestre and D. Camotim, "Asymptotic-numerical method to analyze the postbuckling behavior, imperfection-sensitivity, and mode interaction in frames," *Journal of Engineering Mechanics*, vol. 131, no. 6, pp. 617–632, 2005.
- [6] N. Silvestre and D. Camotim, "Elastic buckling and second-order behaviour of pitched-roof steel frames," *Journal of Constructional Steel Research*, vol. 63, no. 6, pp. 804–818, 2007.

- [7] A. S. Galvão, P. B. Gonçalves, and R. A. M. Silveira, "Post-buckling behavior and imperfection sensitivity of L-frames," *International Journal of Structural Stability and Dynamics*, vol. 5, no. 1, pp. 19–35, 2005.
- [8] G. J. Simitses, "Effect of static preloading on the dynamic stability of structures," *AIAA Journal*, vol. 21, no. 8, pp. 1174–1180, 1983.
- [9] S. L. Chan and G. W. M. Ho, "Nonlinear vibration analysis of steel frames with semirigid connections," *Journal of Structural Engineering*, vol. 120, no. 4, pp. 1075–1087, 1994.
- [10] C. E. N. Mazzilli and R. M. L. R. F. Brasil, "Effect of static loading on the nonlinear vibrations of a three-time redundant portal frame: analytical and numerical studies," *Nonlinear Dynamics*, vol. 8, no. 3, pp. 347–366, 1995.
- [11] M. E. S. Soares and C. E. N. Mazzilli, "Nonlinear normal modes of planar frames discretized by the finite element method," *Computers and Structures*, vol. 77, no. 5, pp. 485–493, 2000.
- [12] S. L. Chan and P. T. Chui, Eds., *Non-Linear Static and Cyclic Analysis of Steel Frames with Semi-Rigid Connections*, Elsevier, 2000.
- [13] M. I. McEwan, J. R. Wright, J. E. Cooper, and A. Y. T. Leung, "A combined modal/finite element analysis technique for the dynamic response of a non-linear beam to harmonic excitation," *Journal of Sound and Vibration*, vol. 243, no. 4, pp. 601–624, 2001.
- [14] P. Ribeiro, "Hierarchical finite element analyses of geometrically non-linear vibration of beams and plane frames," *Journal of Sound and Vibration*, vol. 246, no. 2, pp. 225–244, 2001.
- [15] J. G. S. Da Silva, L. R. O. De Lima, P. D. S. Vellasco, S. De Andrade, and R. A. De Castro, "Nonlinear dynamic analysis of steel portal frames with semi-rigid connections," *Engineering Structures*, vol. 30, no. 9, pp. 2566–2579, 2008.
- [16] A. S. Galvão, A. R. D. Silva, R. A. M. Silveira, and P. B. Gonçalves, "Nonlinear dynamic behavior and instability of slender frames with semi-rigid connections," *International Journal of Mechanical Sciences*, vol. 52, no. 12, pp. 1547–1562, 2010.
- [17] W. Su and C. E. S. Cesnik, "Strain-based geometrically non-linear beam formulation for modeling very flexible aircraft," *International Journal of Solids and Structures*, vol. 48, no. 16-17, pp. 2349–2360, 2011.
- [18] P. B. Gonçalves, D. L. B. R. Jurjo, C. Magluta, and N. Roitman, "Experimental investigation of the large amplitude vibrations of a thin-walled column under self-weight," *Structural Engineering and Mechanics*, vol. 46, no. 6, pp. 869–886, 2013.
- [19] A. R. Masoodi and S. H. Moghaddam, "Nonlinear dynamic analysis and natural frequencies of gabled frame having flexible restraints and connections," *KSCCE Journal of Civil Engineering*, vol. 19, no. 6, pp. 1819–1824, 2015.
- [20] J. L. Palacios Felix, J. M. Balthazar, and R. M. L. R. F. Brasil, "On saturation control of a non-ideal vibrating portal frame foundation type shear-building," *Journal of Vibration and Control*, vol. 11, no. 1, pp. 121–136, 2005.
- [21] T. S. Parker and L. O. Chua, *Practical Numerical Algorithms for Chaotic Systems*, Springer, New York, NY, USA, 1989.
- [22] M. S. Nakhla and J. Vlach, "A piecewise harmonic balance technique for determination of periodic response of nonlinear systems," *IEEE Transactions on Circuits and Systems*, vol. 23, no. 2, pp. 85–91, 1976.
- [23] S. L. Lau, Y. K. Cheung, and S. Y. Wu, "Incremental harmonic balance method with multiple time scales for aperiodic vibration of nonlinear systems," *ASME Journal of Applied Mechanics*, vol. 50, no. 4, pp. 871–876, 1983.
- [24] Y. K. Cheung and S. H. Chen, "Application of the incremental harmonic balance method to cubic non-linearity systems," *Journal of Sound and Vibration*, vol. 140, no. 2, pp. 273–286, 1990.
- [25] S. H. Chen, Y. K. Cheung, and H. X. Xing, "Nonlinear vibration of plane structures by finite element and incremental harmonic balance method," *Nonlinear Dynamics*, vol. 26, no. 1, pp. 87–104, 2001.
- [26] A. Grolet and F. Thouverez, "Computing multiple periodic solutions of nonlinear vibration problems using the harmonic balance method and Groebner bases," *Mechanical Systems and Signal Processing*, vol. 52-53, no. 1, pp. 529–547, 2015.
- [27] P. Ribeiro and M. Petyt, "Geometrical non-linear, steady state, forced, periodic vibration of plates, part I: model and convergence studies," *Journal of Sound and Vibration*, vol. 226, no. 5, pp. 955–983, 1999.
- [28] G. Von Groll and D. J. Ewins, "The harmonic balance method with arc-length continuation in rotor/stator contact problems," *Journal of Sound and Vibration*, vol. 241, no. 2, pp. 223–233, 2001.
- [29] J. V. Ferreira and A. L. Serpa, "Application of the arc-length method in nonlinear frequency response," *Journal of Sound and Vibration*, vol. 284, no. 1-2, pp. 133–149, 2005.
- [30] J. M. Londoño, S. A. Neild, and J. E. Cooper, "Identification of backbone curves of nonlinear systems from resonance decay responses," *Journal of Sound and Vibration*, vol. 348, pp. 224–238, 2015.
- [31] L. Renson, G. Kerschen, and B. Cochelin, "Numerical computation of nonlinear normal modes in mechanical engineering," *Journal of Sound and Vibration*, vol. 364, pp. 177–206, 2016.
- [32] S. Stoykov and P. Ribeiro, "Nonlinear free vibrations of beams in space due to internal resonance," *Journal of Sound and Vibration*, vol. 330, no. 18-19, pp. 4574–4595, 2011.
- [33] S. Stoykov and P. Ribeiro, "Stability of nonlinear periodic vibrations of 3D beams," *Nonlinear Dynamics*, vol. 66, no. 3, pp. 335–353, 2011.
- [34] G. Formica, A. Arena, W. Lacarbonara, and H. Dankowicz, "Coupling FEM with parameter continuation for analysis of bifurcations of periodic responses in nonlinear structures," *Journal of Computational and Nonlinear Dynamics*, vol. 8, no. 2, Article ID 021013, 2013.
- [35] L. F. Paulo Muñoz, P. B. Gonçalves, R. A. M. Silveira, and A. R. D. Silva, "Non-linear dynamic analysis of plane frame structures under seismic load in frequency domain," in *Proceedings of the International Conference on Engineering Vibration*, Ljubljana, Slovenia, September 2016.
- [36] [https://en.wikipedia.org/wiki/Peak\\_ground\\_acceleration](https://en.wikipedia.org/wiki/Peak_ground_acceleration).
- [37] J. Douglas, "Earthquake ground motion estimation using strong-motion records: a review of equations for the estimation of peak ground acceleration and response spectral ordinates," *Earth-Science Reviews*, vol. 61, no. 1, pp. 43–104, 2003.
- [38] E. I. Katsanos, A. G. Sextos, and G. D. Manolis, "Selection of earthquake ground motion records: a state-of-the-art review from a structural engineering perspective," *Soil Dynamics and Earthquake Engineering*, vol. 30, no. 4, pp. 157–169, 2010.
- [39] A. H. Nayfeh and D. T. Mook, *Nonlinear Oscillations*, John Wiley & Sons, 2008.
- [40] R. Bouc, "Sur la méthode de Galerkin-Urabe pour les systèmes différentiels périodiques," *International Journal of Non-Linear Mechanics*, vol. 7, no. 2, pp. 175–188, 1972.
- [41] M. A. Crisfield, "A fast incremental/iterative solution procedure that handles 'snap-through'," *Computers and Structures*, vol. 13, no. 1–3, pp. 55–62, 1981.

- [42] E. Ramm, "Strategies for tracing the non-linear response near limit-points," in *Nonlinear Finite Element Analysis in Structural Mechanics*, W. Wunderlich, E. Stein, and K. J. Bathe, Eds., pp. 63–89, Springer, Berlin, Germany, 1981.
- [43] V. C. Ministério, *RNE E030: Norma de Diseño Sismorresistente*, Reglamento Nacional de Construcciones, Lima, Peru, 2007.

## Research Article

# Flexoelectric Effect on Vibration of Piezoelectric Microbeams Based on a Modified Couple Stress Theory

**Xingjia Li and Ying Luo**

*Faculty of Civil Engineering and Mechanics, Jiangsu University, Zhenjiang 212013, China*

Correspondence should be addressed to Ying Luo; [luoying@ujs.edu.cn](mailto:luoying@ujs.edu.cn)

Received 12 October 2016; Accepted 12 February 2017; Published 16 March 2017

Academic Editor: Paulo B. Gonçalves

Copyright © 2017 Xingjia Li and Ying Luo. This is an open access article distributed under the Creative Commons Attribution License, which permits unrestricted use, distribution, and reproduction in any medium, provided the original work is properly cited.

A novel electric Gibbs function was proposed for the piezoelectric microbeams (PMBs) by employing a modified couple stress theory. Based on the new Gibbs function and the Euler-Bernoulli beam theory, the governing equations which incorporate the effects of couple stress, flexoelectricity, and piezoelectricity were derived for the mechanics of PMBs. The analysis of the effective bending rigidity shows the effects of size and flexoelectricity can greatly increase the stiffness of PMBs so that the natural frequency increases significantly compared with the Euler-Bernoulli beam, and then the mechanical and electrical properties of PMBs are enhanced compared to the classical beam. This study can guide the design of microscale piezoelectric/flexoelectric structures which may find potential applications in the microelectromechanical systems (MEMS).

## 1. Introduction

Piezoelectricity is a well-studied electromechanical coupling effect in which the mechanical strain leads to electric polarization in piezoelectric crystals, or vice versa. Due to the excellent electromechanical characteristics at microscale [1], piezoelectric based microstructures have found a wide range of applications in microtechnology, like microtransducers, microgenerators, microresonators, and so forth [2, 3]. Particularly, these above microstructures are quasi one-dimensional structures which can be efficiently characterized by simple Euler-Bernoulli beam theory. Flexoelectricity [4–7] is, however, the coupling between the mechanical strain gradient and the electric polarization, and it is a universal electromechanical mechanism in all insulators including piezoelectric materials [8–11]. Shen and Hu [12, 13] introduced an electric Gibbs function to consider both of the piezoelectricity and flexoelectricity and derived the governing equations for dielectric materials. Flexoelectricity has also been found to be useful when it is used for sensing purpose [14, 15]. Moreover, the flexoelectric structures are theoretically predicted to be more sensitive when scaled down to microdomains [16, 17], yet their work did not take the size effect at microscale into account.

At microscale, size effect may be significant and even dominate the behavior of structures. Several strain gradient theories were dedicated to investigating the size effect [18–21]. Among these works, Yang et al. [20] developed a modified couple stress theory with only one high-order material constant to account for the size effect on the microscale structures which makes the size effect more convenient to express. Afterwards, many efforts were devoted to studying the size effect on the mechanical behaviors of microbeams using the modified couple stress theory [22–25]. Among these, Park and Gao [22] developed a new model for the bending of a Bernoulli-Euler beam. Ma et al. [23] employed the Timoshenko beam model to study the size-dependence of static bending and vibration behaviors. Reddy [24] modified Euler-Bernoulli and Timoshenko models for functionally graded beams and studied the size-dependence of the deflection, vibration, and buckling behaviors for beam models. In these studies, the modified couple stress theory was used for elastic beams whereas the electromechanical coupling effects, for example, piezoelectric effect and flexoelectric effect, were not considered. Recently, the modified couple stress theory was utilized by Ansari et al. [25] for discussing the vibration characteristics of microbeams with piezoelectricity; however, flexoelectricity was not taken into account. Li et al. [26]

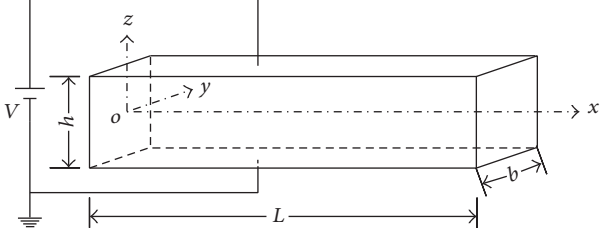


FIGURE 1: The schematic of the PMB whose cross section is a rectangle with width  $b$  and height  $h$ . The origin of  $x$ ,  $y$ , and  $z$  coordinate system is located at the geometric centre of the left end. Herein an electric field is applied between the top ( $z = h/2$ ) and bottom ( $z = -h/2$ ) surfaces. The bottom surface is grounded.

reformulated a flexoelectric theory to study the bending behavior of PMBs with flexoelectricity. However, the vibration behaviors of PMBs with flexoelectricity have not been reported to date, which may be as important as the bending behavior in MEMS.

The goal of this paper is to study the natural frequency of PMBs with considering the size effect, piezoelectricity, and flexoelectricity. To achieve this goal, together with the Euler-Bernoulli beam theory, a new Gibbs function needs to be defined by employing a modified couple stress theory to derive the governing equations for the PMBs. The proposed study can be fundamental for the vibration behaviors of PMBs which may have potential application in the microelectromechanical systems (MEMS).

This paper is organized as follows. After introduction, Section 2 presents an electric Gibbs function based on the flexoelectricity theory and the modified couple stress theory. The dynamics equation and boundary conditions of piezoelectric beams were then derived by using the new Gibbs function and the Euler-Bernoulli beam model. Afterwards, the first-order natural frequencies under different boundary conditions of the current model and the traditional Euler-Bernoulli model were displayed. In particular, the natural frequency of simply supported PMBs subjected to a voltage across the thickness is solved as an example. Then the relationship between the frequency and the effective bending stiffness was discussed and employed to study the effects of couple stress, piezoelectricity, and flexoelectricity in Section 3. The new findings were summarized in Section 4.

## 2. Dynamics Equation of Piezoelectric Microbeams with Flexoelectricity

An Euler-Bernoulli beam in Figure 1 is considered:

$$\begin{aligned} u_x &= -\frac{\partial w(x,t)}{\partial x} z, \\ u_y &= 0, \\ u_z &= w(x,t). \end{aligned} \quad (1)$$

To account for the piezoelectric effect, flexoelectric effect, and nonlocal mechanical and electrical effects, an electric Gibbs energy density  $G_b$  including the energy of elasticity,

piezoelectricity, flexoelectricity, and couple stress was proposed by

$$\begin{aligned} G_b &= -\frac{1}{2} (k_{ij} E_i E_j + b_{ijkl} E_{i,j} E_{k,l} - C_{ijkl} \varepsilon_{ij} \varepsilon_{kl}) \\ &\quad - e_{ijk} E_i \varepsilon_{jk} - \mu_{ijkl} (E_k \varepsilon_{ij,l} - \varepsilon_{ij} E_{k,l}) + \frac{1}{2} m_{ij} \chi_{ij}, \end{aligned} \quad (2)$$

where  $k_{ij}$  is dielectric constant tensor,  $E_i$  and  $E_j$  are electric field vectors,  $b_{ijkl}$  is the nonlocal electrical coupling coefficient tensor,  $C_{ijkl}$  is elastic stiffness tensor,  $\varepsilon_{kl}$  is strain tensor,  $e_{ijk}$  is piezoelectric coefficient tensor,  $\mu_{ijkl}$  is a fourth-order tensor of the flexoelectric coefficient, and  $\varepsilon_{kl,j}$  and  $E_{k,l}$  are the gradients of strain and electric field.  $m_{ij}$  is deviator part of couple stress tensor and  $\chi_{ij}$  is the symmetric part of curvature tensor, which, using the modified couple stress theory [20, 22], are defined as

$$\begin{aligned} m_{ij} &= 2l^2 \mu \chi_{ij}, \\ \chi_{ij} &= \frac{1}{2} (\theta_{i,j} + \theta_{j,i}), \\ \theta_i &= \frac{1}{2} e_{ijk} u_{k,l}, \end{aligned} \quad (3)$$

where  $\mu$  is Lamé's constants,  $l$  is the material length scale parameter,  $\theta_i$  is the rotation vector, and  $u_i$  is the gradient of displacement vector, respectively.

Thus the constitutive equations for piezoelectric Euler-Bernoulli beams can be derived as

$$\begin{aligned} \sigma_{xx} &= \frac{\partial G_b}{\partial \varepsilon_{xx}} = C_{11} \varepsilon_{xx} - e_{31} E_z + \mu_{31} E_{z,z}, \\ \tau_{xxz} &= \frac{\partial G_b}{\partial \varepsilon_{xx,z}} = -\mu_{31} E_z, \\ m_{xy} &= \frac{\partial G_b}{\partial \chi_{xy}} = 2l^2 \mu \chi_{kl}, \\ D_z &= \frac{\partial G_b}{\partial E_z} = k_{33} E_z + e_{31} \varepsilon_{xx} + \mu_{31} \varepsilon_{xx,z}, \\ Q_{zz} &= \frac{\partial G_b}{\partial E_{z,z}} = b_{33} E_{z,z} - \mu_{31} \varepsilon_{xx}, \end{aligned} \quad (4)$$

where  $\tau_{xxz}$ ,  $D_z$ , and  $Q_{zz}$  denote the higher-order stress tensor, electric displacement vector, and electric quadrupole, respectively. In the absence of free charges, Gauss's law requires

$$-\frac{\partial^2 Q_{zz}}{\partial z^2} + \frac{\partial D_z}{\partial z} = 0. \quad (5)$$

Substituting (4) into (5) leads to

$$k_{33} E_{z,z} + e_{31} \varepsilon_{xx,z} + \mu_{31} \varepsilon_{xx,zz} - b_{33} E_{z,zz} = 0. \quad (6)$$

The electrical boundary conditions are given by

$$\begin{aligned} \Phi \left( -\frac{h}{2} \right) &= 0, \\ \Phi \left( \frac{h}{2} \right) &= V, \end{aligned} \quad (7)$$

where  $\Phi$  is the electric potential. Combining  $E_z = -\partial\Phi/\partial z$  with (4)–(7) yields

$$\begin{aligned} \Phi = & \frac{V}{2} + \frac{V}{h}z + \frac{e_{31}}{2k_{33}} \left( \frac{h^2}{4} - z^2 \right) \left( \frac{\partial^2 w}{\partial x^2} \right) \\ & - \frac{\mu_{31}}{2k_{33}} \left( \frac{\partial^2 w}{\partial x^2} \right) z + \frac{e_{31}}{\eta^2 k_{33}} \frac{e^{\eta z} + e^{-\eta z}}{e^{\eta h/2} + e^{-\eta h/2}} \left( \frac{\partial^2 w}{\partial x^2} \right) \\ & + \frac{\mu_{31}h}{4\eta^2 k_{33}} \frac{e^{\eta z} - e^{-\eta z}}{e^{\eta h/2} - e^{-\eta h/2}} \frac{e^{\eta z} + e^{-\eta z}}{e^{\eta h/2} + e^{-\eta h/2}} \end{aligned} \quad (8)$$

with  $\eta = \sqrt{k_{33}/b_{33}}$ . Neglecting the high-order nonlocal electric effect in (8) by assuming  $b_{33} = 0$  yields the following equations [27, 28]:

$$\begin{aligned} \Phi = & \frac{V}{2} + \frac{V}{h}z + \frac{e_{31}}{2k_{33}} \left( \frac{h^2}{4} - z^2 \right) \left( \frac{\partial^2 w}{\partial x^2} \right) \\ & - \frac{\mu_{31}}{2k_{33}} \left( \frac{\partial^2 w}{\partial x^2} \right) z, \\ E_z = & \left( \frac{e_{31}}{k_{33}}z - \frac{\mu_{31}}{2k_{33}} \right) \frac{\partial^2 w}{\partial x^2} - \frac{V}{h}, \\ E_{z,z} = & \frac{e_{31}}{k_{33}} \left( \frac{\partial^2 w}{\partial x^2} \right), \\ \sigma_{xx} = & -C_{11} \left( \frac{\partial^2 w}{\partial x^2} \right) z - \frac{e_{31}^2}{k_{33}} \left( \frac{\partial^2 w}{\partial x^2} \right) z \\ & + \frac{e_{31}\mu_{31}}{2k_{33}} \left( \frac{\partial^2 w}{\partial x^2} \right) + e_{31} \frac{V}{h}, \\ \tau_{xxz} = & -\frac{e_{31}\mu_{31}}{k_{33}} \left( \frac{\partial^2 w}{\partial x^2} \right) z - \frac{\mu_{31}^2}{2k_{33}} \left( \frac{\partial^2 w}{\partial x^2} \right) + \frac{\mu_{31}V}{h}. \end{aligned} \quad (9)$$

The elastic energy  $U$ , kinetic energy  $T$ , and external work  $W$  are calculated by the following equations:

$$\begin{aligned} U = & \frac{1}{2} \int_0^l \int_A \left( \sigma_{xx} \varepsilon_{xx} + 2m_{xy} \chi_{xy} + \tau_{xxz} \varepsilon_{xx,z} \right) dA dx, \\ T = & \frac{1}{2} \int_0^l \int_A \rho \left( \frac{\partial u_z}{\partial t} \right)^2 dA dx, \\ W = & -\frac{1}{2} \int_0^l N_{xx} \left( \frac{\partial w}{\partial x} \right)^2 dx, \\ N_{xx} = & \int_A \sigma_{xx} dA. \end{aligned} \quad (10)$$

Hamilton's principle reads

$$\int_{t_1}^{t_2} (\delta T - \delta U + \delta W) dt = 0. \quad (11)$$

Then the governing equation for their transverse vibration can be derived by the vibrational principle

$$-\rho A \frac{\partial^2 w}{\partial t^2} = (EI)_{\text{eff}} \frac{\partial^4 w}{\partial x^4} - P_{\text{eff}} \frac{\partial^2 w}{\partial x^2}, \quad (12)$$

where

$$(EI)_{\text{eff}} = C_{11}I + \frac{e_{31}^2 I}{k_{33}} + A\mu^2 + \frac{\mu_{31}^2 A}{2k_{33}}, \quad (13)$$

$$P_{\text{eff}} = e_{31}Vb.$$

For facilitating, make the substitution of  $(EI)_e = C_{11}I$ ,  $(EI)_p = e_{31}^2 I/k_{33}$ ,  $(EI)_c = A\mu^2$ , and  $(EI)_f = \mu_{31}^2 A/2k_{33}$ , and then we have

$$(EI)_{\text{eff}} = (EI)_e + (EI)_p + (EI)_c + (EI)_f, \quad (14)$$

$$P_{\text{eff}} = e_{31}Vb.$$

If the flexoelectric effect is neglected, the effective bending rigidity can be reduced to

$$(EI)_{\text{eff}}^p = (\lambda + 2\mu)I + \frac{e_{31}^2 I}{k_{33}} + A\mu^2, \quad (15)$$

$$P_{\text{eff}}^p = e_{31}Vb.$$

If the working temperature of PMBs is higher than Curie's point, the piezoelectric effect will disappear and then the effective bending rigidity can be rewritten as

$$(EI)_{\text{eff}}^f = (\lambda + 2\mu)I + \frac{\mu_{31}^2 A}{2k_{33}} + A\mu^2, \quad (16)$$

$$P_{\text{eff}}^f = 0.$$

The geometric parameters are defined as

$$\int_A (1, z, z^2) dA = (A, 0, I) \quad (17)$$

with  $A$  and  $I$  being the cross section area and inertia moment of beams. The natural frequencies for PMBs with different boundary conditions, such as simply supported (S-S), cantilever (C-F), and clamped-clamped (C-C) types, can be calculated based on the following characteristic equations:

$$\begin{aligned} \sin(s_2 L) = 0 \quad (\text{S-S}), \\ s_1^4 + s_2^4 + s_1 s_2 (s_2^2 - s_1^2) \sinh(s_1 L) \sin(s_2 L) \\ + 2s_1^2 s_2^2 \cosh(s_1 L) \cos(s_2 L) = 0 \quad (\text{C-F}), \\ 2s_1 s_2 - 2s_1 s_2 \cosh(s_1 L) \cos(s_2 L) \\ + (s_1^2 - s_2^2) \sinh(s_1 L) \sin(s_2 L) = 0 \quad (\text{C-C}), \end{aligned} \quad (18)$$

where

$$\begin{aligned} s_1 = & \left( \frac{P_{\text{eff}} + \sqrt{P_{\text{eff}}^2 + 4\rho A \omega^2 (EI)_{\text{eff}}}}{2(EI)_{\text{eff}}} \right)^{1/2}, \\ s_2 = & \left( \frac{-P_{\text{eff}} + \sqrt{P_{\text{eff}}^2 + 4\rho A \omega^2 (EI)_{\text{eff}}}}{2(EI)_{\text{eff}}} \right)^{1/2} \end{aligned} \quad (19)$$

with  $\omega$  representing the angular resonant frequency.

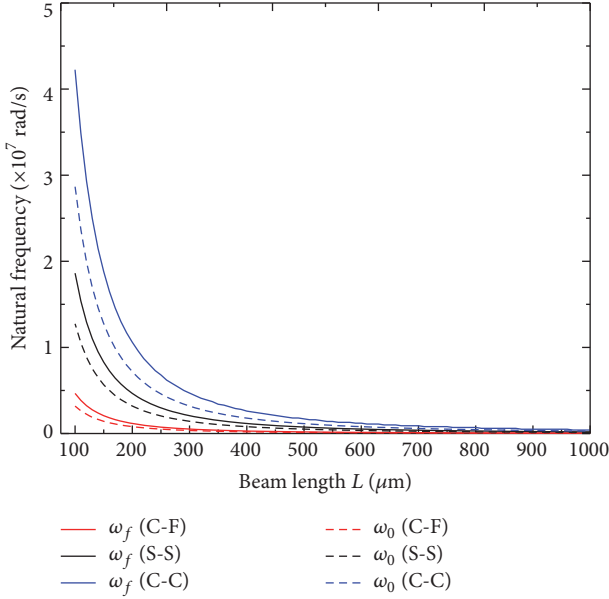


FIGURE 2: The first natural frequency of the present beam model ( $\omega_f$ ) without voltage and the traditional Euler-Bernoulli beam model ( $\omega_0$ ) versus beam length with different boundary conditions.

TABLE 1: Material constants of the piezoelectric microbeam [8–11].

$E$	$\nu$	$\rho$	$e_{31}$	$\mu_{31}$	$\epsilon_r$
150 GPa	0.33	$7.5 \times 10^3 \text{ Kg/m}^3$	$-4.35 \text{ C/m}^2$	$10 \mu\text{C/m}$	2300

$E$  is Young's modulus,  $\nu$  is Poisson's ratio,  $\rho$  is mass density,  $e_{31}$  is piezoelectric constant,  $\mu_{31}$  is flexoelectric constant,  $\epsilon_r$  is relative dielectric constant, and the vacuum dielectric constant  $\epsilon_0 = 8.85 \times 10^{-12} \text{ F/m}$ .

### 3. Results and Discussion

In this section the formulae derived in Section 2 will be used to study the fundamental vibration of the PMBs. The emphasis is on the effects of size, piezoelectricity, and flexoelectricity. To this end, BaTiO<sub>3</sub> was chosen as the material of the PMBs where the material constants are listed in Table 1. The cross section of BaTiO<sub>3</sub> beam is assumed to be square; that is,  $b = h$ .

Employing (13), (18), and (19) and the material constants in Table 1, we can easily get the first-order natural frequency of the PMBs  $\omega_f$ . Moreover, the first natural frequency of traditional Euler-Bernoulli beam model  $\omega_0 = (i\pi/L)^2 \sqrt{EI/\rho A}$  ( $i = 0.5$  for C-F type,  $i = 1$  for S-S type, and  $i = 1.5$  for C-C type) is employed for comparison. Here  $\omega_f$  denotes the natural frequency of the present model; that is, both effects of piezoelectricity and flexoelectricity are taken into consideration. Correspondingly,  $\omega_p$  represents the natural frequency when only piezoelectric effect is considered. The difference between the present model and the traditional model can be seen in Figure 2. Hereby PMBs have  $h = 10 \mu\text{m}$  and  $l = 5 \mu\text{m}$ .

From Figure 2 we can see that the differences in the frequencies between the present model and the traditional

model increase significantly when the beam length decreases to less than  $400 \mu\text{m}$  and then turn to be nearly the same when the beam length increases to more than  $800 \mu\text{m}$ . In general, the trends in the frequencies of the present model resemble that of the traditional model because the frequency equation of  $\omega_f|_{V=0} = (i\pi/L)^2 \sqrt{(EI)_{\text{eff}}/\rho A}$  and  $\omega_0$  are very alike with small difference between the bending stiffness  $(EI)_{\text{eff}}$  and  $(EI)$ .

**3.1. Effect of Piezoelectricity and Flexoelectricity.** Throughout the following sections of this work we will calculate the first normalized natural frequencies  $\bar{\omega}_p = \omega_p/\omega_0$  and  $\bar{\omega}_f = \omega_f/\omega_0$ , and, for facilitating the discussion, the simply supported (S-S) boundary condition was chosen as a representative. The normalized frequencies are shown in Figure 3 for PMBs where length-to-thickness ratio  $L/h$  is fixed at 20 and the length  $L$  increases from  $20 \mu\text{m}$  to  $1000 \mu\text{m}$ . Accordingly the thickness  $h$  grows from  $1 \mu\text{m}$  to  $50 \mu\text{m}$  and the material length scale parameter  $l$  is defined by  $l = h/2$  as others do in [25, 26] which increases from  $0.5 \mu\text{m}$  to  $25 \mu\text{m}$ . In addition, the voltage  $V = -2 \text{ V}$ ,  $0$ , and  $2 \text{ V}$  are applied to reveal the effects of piezoelectricity and flexoelectricity.

In Figure 3(a), where only piezoelectric effect is considered (i.e., without flexoelectricity),  $\bar{\omega}_p = 1.461$  is obtained at  $V = 0$  showing that the size effect increases by 46.1% for all PMBs of different length  $L$  and length scale parameter  $l$ . Equations (13) and (14) show the contribution of the size effect  $(EI)_c$  on the effective bending stiffness  $(EI)_{\text{eff}}$  of the PMBs. At  $L = 20 \mu\text{m}$ ,  $\bar{\omega}_p$  increases to 1.465 when  $V = -2 \text{ V}$  is applied whereas it decreases to 1.457 at  $V = 2 \text{ V}$ . This result shows that the external voltage leads to the increase (or decrease) of the frequency of PMBs in the presence of a negative (or positive) voltage. A 4 V external voltage can tune the frequency of PMBs by 0.55%, and the tuning of frequency can be greater under greater external voltage. Such a piezoelectric effect can be explained by the electromechanical coupling term  $(EI)_p$  in  $(EI)_{\text{eff}}$  and the extra-axial force  $P_{\text{eff}}$  in (13) and (14). Specifically, such a piezoelectric effect decreases monotonically with rising length  $L$  and shows significant length-dependence. As a result  $\bar{\omega}_p$  with  $V = -2 \text{ V}$  or  $2 \text{ V}$  approaches  $\bar{\omega}_f = 1.461$  when the length  $L$  is sufficiently large; for example,  $L > 900 \mu\text{m}$ . In this case the piezoelectric effect turns out to be negligible.

Different from Figure 3(a), both effects of piezoelectricity and flexoelectricity are considered in Figure 3(b) for the normalized frequency  $\bar{\omega}_f$ . Thus the difference between the results in Figures 3(a) and 3(b) [i.e.,  $(\bar{\omega}_f - \bar{\omega}_p)$ ] reveals the effect of flexoelectricity on the normalized fundamental frequency. First it is noted in Figure 3(b) that, at  $V = 0$ ,  $\bar{\omega}_f$  becomes length-dependent, which is in contrast to the length-independent  $\bar{\omega}_p$  in Figure 3(a). At  $L = 20 \mu\text{m}$  flexoelectric effect slightly increases the normalized frequency by 0.73% relative to  $\bar{\omega}_p$ . The relative increment then decreases with rising  $L$  and becomes negligible for long and thick PMBs. Qualitatively similar trend is observed for the flexoelectric effect at  $V = -2 \text{ V}$ , which raises the normalized frequency by 0.26% at  $L = 20 \mu\text{m}$ . The increase of the frequency decreases with rising  $L$  and almost vanishes at  $L = 1000 \mu\text{m}$ . On the other hand, when positive voltage  $2 \text{ V}$  is applied, it is

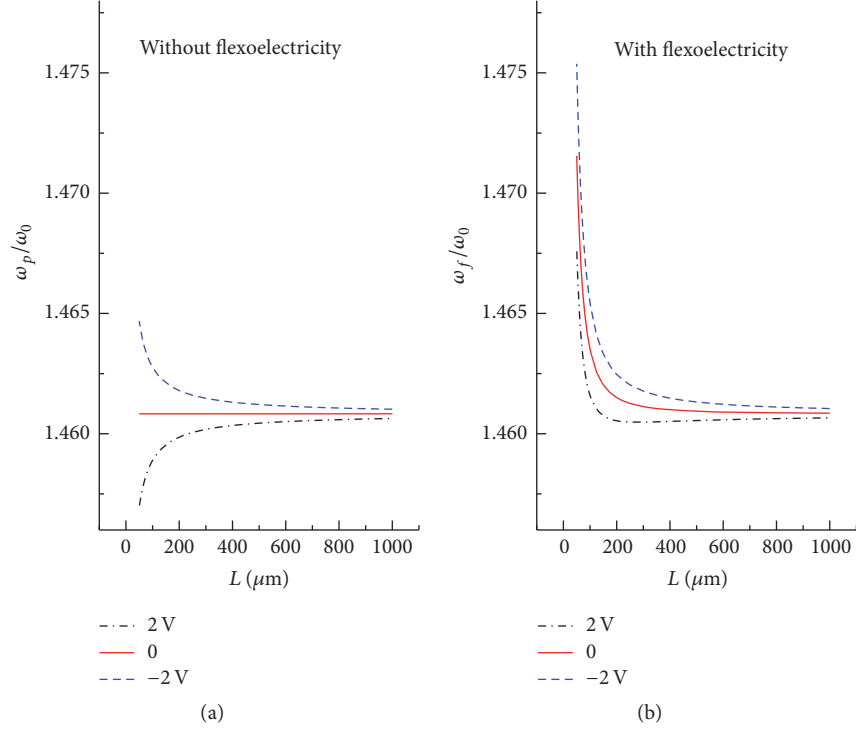


FIGURE 3: Length-dependence of the normalized fundamental frequency calculated for (a)  $\omega_p/\omega_0$  of PMBs with only piezoelectric effect and (b)  $\omega_f/\omega_0$  with both effects of piezoelectricity and flexoelectricity.

noted in Figure 3(b) that  $\bar{\omega}_f$  first decreases with rising  $L$  and reaches the lowest value at  $L = 302 \mu\text{m}$ . It then increases with increase of  $L$  and reaches close to  $\bar{\omega}_f = 1.461$  when the length is greater than  $900 \mu\text{m}$ . This behavior of  $\bar{\omega}_f$  at  $2 \text{ V}$  is qualitatively different from the corresponding  $L$ -dependence of  $\bar{\omega}_p$  in Figure 3(a) and can be attributed to the competition between the reversed effects of piezoelectricity (with positive voltage) and the flexoelectricity on the normalized frequency. Here it is noted that considering flexoelectricity always leads to the increase of the frequency independent of the voltage applied. This behavior can be attributed to the fact that flexoelectricity influences the frequency via the electromechanical coupling term  $(EI)_f$  in  $(EI)_{\text{eff}}$  found in (14), which always greathens the effective bending stiffness and also makes the natural frequency size-dependent. Though it can be seen from Figure 3(a) the positive voltage decreases the natural frequency with decreasing  $L$ , when  $L$  is shorter than  $302 \mu\text{m}$  flexoelectric effect dominates the electromechanical behaviors resulting in a significant rise in the natural frequency.

**3.2. Size Effect on the Electromechanical Coupling in Vibration.** After investigating the effects of piezoelectricity and flexoelectricity, we would like to further reveal the influence of the size effect of piezoelectricity and flexoelectricity. Here we first calculated the  $l$ -dependence of  $\bar{\omega}_p$  (without flexoelectricity) in Figure 4 for PMBs subjected to a voltage of  $-2 \text{ V}$ ,  $0$ , and  $2 \text{ V}$ , respectively. In the calculations two groups of PMBs are considered, which have an aspect ratio  $L/h = 20$  and  $40$ , respectively. In addition the scale material constant  $l$  is

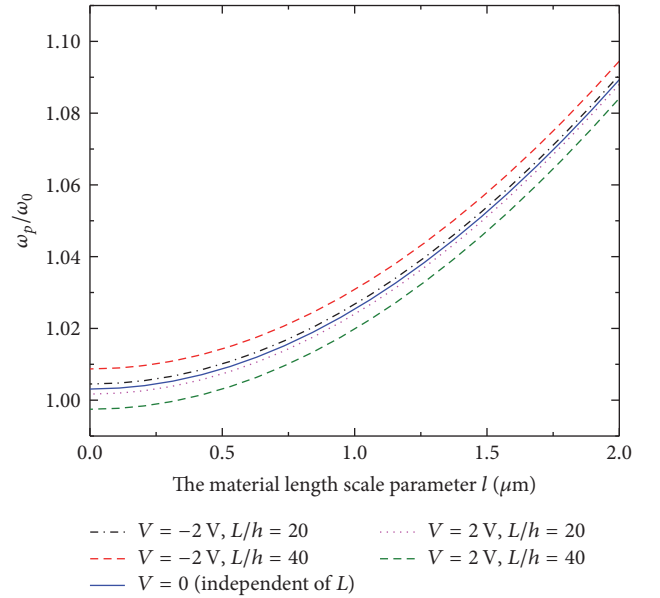


FIGURE 4:  $l$ -dependence of  $\omega_p/\omega_0$  obtained for PMBs where the effect of piezoelectricity is considered but the effect of flexoelectricity is ignored. Here PMBs have  $h = 10 \mu\text{m}$  and  $L/h = 20$  and  $40$ , respectively.

assumed to be a constant and increases from  $0$  (classical theory) to  $2 \mu\text{m}$ . Figure 4 shows that in general  $\bar{\omega}_p$  increases with growing  $l$  for all the PMBs under a given voltage. It is

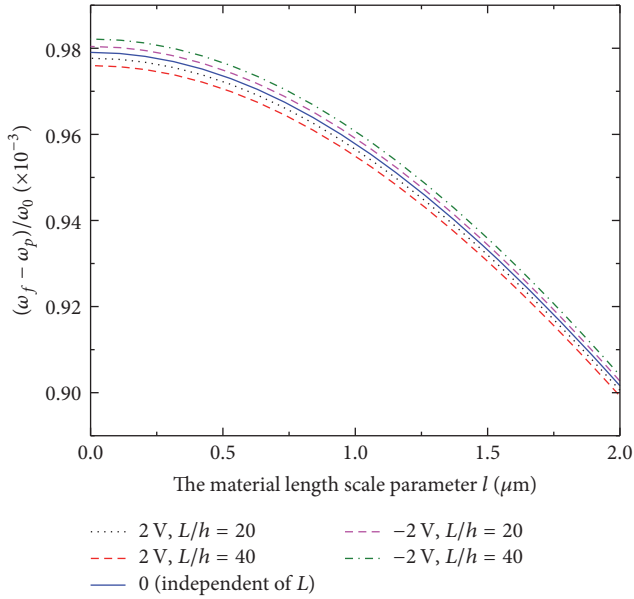


FIGURE 5:  $l$ -dependence of  $(\omega_f - \omega_p)/\omega_0$  obtained for PMBs where  $h$  is fixed at  $10 \mu\text{m}$  and  $L/h$  is equal to 20 and 40, respectively.

worth mentioning that at  $V = 0$  the results remain unchanged no matter what aspect ratio  $L/h$  is considered. Specifically, the curves associated with different nonzero voltages are almost parallel with one another. These results indicate that the change in normalized frequency, that is,  $(\bar{\omega}_p|_{V \neq 0} - \bar{\omega}_p|_{V=0})$  due to piezoelectric effect, is not very sensitive to the variation of the scale parameter  $l$  (the subscript shows the voltage applied). On the other hand, as  $\bar{\omega}_p|_{V=0}$  rises with rising  $l$ , the relative change  $(\bar{\omega}_p|_{V \neq 0} - \bar{\omega}_p|_{V=0})/\bar{\omega}_p|_{V=0}$  due to piezoelectric effect decreases significantly with increasing  $l$  (the subscript shows the voltage considered). For example, at  $l = 0$  relative change due to  $V = -2 \text{ V}$  ( $V = -2 \text{ V}$ ) is  $0.56\%$  ( $-0.56\%$ ) for PMBs with  $L = 40 \text{ h}$ . However, at  $l = 2 \mu\text{m}$  such a relative change decreases to  $0.47\%$  at  $V = -2 \text{ V}$  and  $-0.48\%$  at  $V = 2 \text{ V}$ . In addition it is also noticed that for a constant  $l$  the piezoelectric effect is less pronounced for shorter PMBs with greater  $L/h = 20$ .

Next we shall further exam the influence of the size effect on the effect of flexoelectricity by calculating the  $l$ -dependence of  $\bar{\omega}_{f-p} = \bar{\omega}_f - \bar{\omega}_p$  in Figure 5. It is easy to understand that  $\bar{\omega}_{f-p}$  reflects the pure effect of flexoelectricity. Figure 5 shows that, at  $V = 0$ ,  $\bar{\omega}_{f-p}$  decreases from around  $0.98 \times 10^{-3}$  to  $0.90 \times 10^{-3}$  when  $l$  increases from 0 to  $2.0 \mu\text{m}$ . These results indicate that the flexoelectricity increases the frequency of PMBs by less than 0.1%, and such an effect is found to be even smaller for greater  $l$  or larger size effect. In addition, at  $V = -2 \text{ V}$  (or  $2 \text{ V}$ ) the effect of flexoelectricity on PMB increases (decreases) slightly but the influence of voltage becomes smaller for greater  $l$ . Indeed it is seen from Figure 5 that, in terms of  $L/h = 40$  when  $l = 0$ ,  $\bar{\omega}_{f-p}|_{V=-2 \text{ V}}$  is  $0.32\%$  higher than  $\bar{\omega}_{f-p}|_{V=0}$  but it declines to  $0.27\%$  when  $l = 2 \mu\text{m}$ . In other words, by increasing  $l$  the effective bending stiffness by flexoelectricity increases; nevertheless

the frequency difference of  $\bar{\omega}_{f-p}$  between existing external voltage and no external voltage diminishes.

#### 4. Conclusions

A novel electric Gibbs function was proposed to describe the size effect on the electromechanical coupling behaviors of PMBs by incorporating a modified couple stress theory into Euler-Bernoulli beam model. Based on the obtained model, the effects of piezoelectricity and flexoelectricity and the size effect were examined for the vibration behavior of PMBs. It is found that, at the microscale, the size effect can raise the effective stiffness of the structure and thus increases the natural frequency. With the assumed value of the material length scale parameter  $l$ , the couple stress dominates the mechanical behavior of the PMBs and increases with rising  $l$ . Piezoelectric effect is achieved, which can increase or decrease the frequency depending on the axial force induced by external voltage. In particular, the contribution of piezoelectric effect to the natural frequency was found to be decreasing with rising  $l$  or geometric size of PMBs. In the meantime, the flexoelectricity can also raise the structural stiffness via an electromechanical coupling term, which is relatively small but detectable and always increases the frequency of PMBs. With the development of material science, the higher performance of flexoelectric materials might play an more important role in MEMS.

#### Conflicts of Interest

The authors declare that there are no conflicts of interest regarding the publication of this paper.

#### Acknowledgments

The research reported herein was supported under NSFC (no. 11272138) and Specialized Research Fund for the Doctoral Program of Higher Education of China (no. 20123227130002).

#### References

- [1] E. S. Hung and S. D. Senturia, "Extending the travel range of analog-tuned electrostatic actuators," *Journal of Microelectromechanical Systems*, vol. 8, no. 4, pp. 497–505, 1999.
- [2] X. Li, B. Bhushan, K. Takashima, C.-W. Baek, and Y.-K. Kim, "Mechanical characterization of micro/nanoscale structures for MEMS/NEMS applications using nanoindentation techniques," *Ultramicroscopy*, vol. 97, no. 1–4, pp. 481–494, 2003.
- [3] Y. Moser and M. A. M. Gijs, "Miniaturized flexible temperature sensor," *Journal of Microelectromechanical Systems*, vol. 16, no. 6, pp. 1349–1354, 2007.
- [4] A. K. Tagantsev, "Piezoelectricity and flexoelectricity in crystalline dielectrics," *Physical Review B*, vol. 34, no. 8, pp. 5883–5889, 1986.
- [5] L. E. Cross, "Flexoelectric effects: charge separation in insulating solids subjected to elastic strain gradients," *Journal of Materials Science*, vol. 41, no. 1, pp. 53–63, 2006.
- [6] P. Zubko, G. Catalan, A. Buckley, P. R. L. Welche, and J. F. Scott, "Strain-gradient-induced polarization in  $\text{SrTiO}_3$  single

- crystals,” *Physical Review Letters*, vol. 99, no. 16, Article ID 167601, 4 pages, 2007.
- [7] N. D. Sharma, R. Maranganti, and P. Sharma, “On the possibility of piezoelectric nanocomposites without using piezoelectric materials,” *Journal of the Mechanics and Physics of Solids*, vol. 55, no. 11, pp. 2328–2350, 2007.
- [8] W. Ma and L. E. Cross, “Observation of the flexoelectric effect in relaxor  $\text{Pb}(\text{Mg}_{1/3}\text{Nb}_{2/3})\text{O}_3$  ceramics,” *Applied Physics Letters*, vol. 78, no. 19, pp. 2920–2921, 2001.
- [9] W. Ma and L. E. Cross, “Flexoelectric polarization of barium strontium titanate in the paraelectric state,” *Applied Physics Letters*, vol. 81, no. 18, pp. 3440–3442, 2002.
- [10] W. Ma and L. E. Cross, “Flexoelectric effect in ceramic lead zirconate titanate,” *Applied Physics Letters*, vol. 86, no. 7, Article ID 072905, 2005.
- [11] W. Ma and L. E. Cross, “Flexoelectricity of barium titanate,” *Applied Physics Letters*, vol. 88, no. 23, Article ID 232902, 2006.
- [12] S. Shen and S. Hu, “A theory of flexoelectricity with surface effect for elastic dielectrics,” *Journal of the Mechanics and Physics of Solids*, vol. 58, no. 5, pp. 665–677, 2010.
- [13] S. Hu and S. Shen, “Variational principles and governing equations in nano-dielectrics with the flexoelectric effect,” *Science China Physics, Mechanics and Astronomy*, vol. 53, no. 8, pp. 1497–1504, 2010.
- [14] X. Yan, W. Huang, S. Ryung Kwon, S. Yang, X. Jiang, and F.-G. Yuan, “A sensor for the direct measurement of curvature based on flexoelectricity,” *Smart Materials and Structures*, vol. 22, no. 8, Article ID 085016, 2013.
- [15] W. Huang, X. Yan, S. R. Kwon, S. Zhang, F.-G. Yuan, and X. Jiang, “Flexoelectric strain gradient detection using  $\text{Ba}_{0.64}\text{Sr}_{0.36}\text{TiO}_3$  for sensing,” *Applied Physics Letters*, vol. 101, no. 25, Article ID 252903, 2012.
- [16] S. R. Kwon, W. B. Huang, S. J. Zhang, F. G. Yuan, and X. N. Jiang, “Flexoelectric sensing using a multilayered barium strontium titanate structure,” *Smart Materials and Structures*, vol. 22, no. 11, Article ID 115017, 2013.
- [17] S. R. Kwon, W. Huang, L. Shu, F.-G. Yuan, J.-P. Maria, and X. Jiang, “Flexoelectricity in barium strontium titanate thin film,” *Applied Physics Letters*, vol. 105, no. 14, Article ID 142904, 2014.
- [18] R. D. Mindlin and N. N. Eshel, “On first strain-gradient theories in linear elasticity,” *International Journal of Solids and Structures*, vol. 4, no. 1, pp. 109–124, 1968.
- [19] R. A. Toupin, “Theories of elasticity with couple-stress,” *Archive for Rational Mechanics and Analysis*, vol. 17, pp. 85–112, 1964.
- [20] F. Yang, A. C. M. Chong, D. C. C. Lam, and P. Tong, “Couple stress based strain gradient theory for elasticity,” *International Journal of Solids and Structures*, vol. 39, no. 10, pp. 2731–2743, 2002.
- [21] D. C. C. Lam, F. Yang, A. C. M. Chong, J. Wang, and P. Tong, “Experiments and theory in strain gradient elasticity,” *Journal of the Mechanics and Physics of Solids*, vol. 51, no. 8, pp. 1477–1508, 2003.
- [22] S. K. Park and X.-L. Gao, “Bernoulli-Euler beam model based on a modified couple stress theory,” *Journal of Micromechanics and Microengineering*, vol. 16, no. 11, pp. 2355–2359, 2006.
- [23] H. M. Ma, X.-L. Gao, and J. N. Reddy, “A microstructure-dependent Timoshenko beam model based on a modified couple stress theory,” *Journal of the Mechanics and Physics of Solids*, vol. 56, no. 12, pp. 3379–3391, 2008.
- [24] J. N. Reddy, “Microstructure-dependent couple stress theories of functionally graded beams,” *Journal of the Mechanics and Physics of Solids*, vol. 59, no. 11, pp. 2382–2399, 2011.
- [25] R. Ansari, M. A. Ashrafi, and S. Hosseinzadeh, “Vibration characteristics of piezoelectric microbeams based on the modified couple stress theory,” *Shock and Vibration*, vol. 2014, Article ID 598292, 12 pages, 2014.
- [26] A. Li, S. Zhou, L. Qi, and X. Chen, “A reformulated flexoelectric theory for isotropic dielectrics,” *Journal of Physics D: Applied Physics*, vol. 48, no. 46, Article ID 465502, 2015.
- [27] L. Shu, F. Li, W. Huang, X. Wei, X. Yao, and X. Jiang, “Relationship between direct and converse flexoelectric coefficients,” *Journal of Applied Physics*, vol. 116, no. 14, Article ID 144105, 2014.
- [28] X. Liang, S. Hu, and S. Shen, “Size-dependent buckling and vibration behaviors of piezoelectric nanostructures due to flexoelectricity,” *Smart Materials and Structures*, vol. 24, no. 10, Article ID 105012, 2015.

## Research Article

# Longitudinal Seismic Behavior of a Single-Tower Cable-Stayed Bridge Subjected to Near-Field Earthquakes

**J. Yi and J. Li**

*Department of Bridge Engineering, Tongji University, Shanghai, China*

Correspondence should be addressed to J. Li; [lijianzh@tongji.edu.cn](mailto:lijianzh@tongji.edu.cn)

Received 21 December 2016; Accepted 20 February 2017; Published 13 March 2017

Academic Editor: Paulo B. Gonçalves

Copyright © 2017 J. Yi and J. Li. This is an open access article distributed under the Creative Commons Attribution License, which permits unrestricted use, distribution, and reproduction in any medium, provided the original work is properly cited.

Cable-stayed bridges are quite sensitive to large amplitude oscillations from earthquakes and seismic damage was observed for Shipshaw Bridge and Chi-Lu Bridge during past earthquakes. In order to investigate seismic damage of cable-stayed bridges, a 1 : 20 scale model of a single-tower cable-stayed bridge with A-shaped tower was designed, constructed, and tested on shake tables at Tongji University, China. One typical near-field ground motion was used to excite the model from low to high intensity. Test result showed that severe structural damage occurred at the tower of the model including parallel concrete cracks from bottom to nearly half height of the tower, concrete spalling, and exposed bars at top tower 0.2 m above the section where two skewed legs intersect. Posttest analysis was conducted and compared with test results. It is revealed that the numerical model was able to simulate the seismic damage of the test model by modeling nonlinearity of different components for cable-stayed bridges, namely, the tower, bents, superstructure, cables, and bearings. Numerical analysis also revealed that cable relaxation, which was detected during the test, had limited influence on the overall seismic response of the bridge with maximum error of 12%.

## 1. Introduction

In recent decades, cable-stayed bridges have become popular worldwide due to their aesthetical appearance, structural efficiency, and short construction period. This type of structure, usually representing key points of the transportation networks, is normally required to remain nearly elastic under the design seismic action, as recommended in Chinese Code [1]. However, due to low structural damping, cable-stayed bridges are quite sensitive to large amplitude oscillations from earthquakes and nonlinear seismic response is anticipated. For example, during Great East Japan Earthquake (2011), the Yokohama Bay Bridge went through much nonlinearity of the response as evidenced by variations in natural frequencies and mode shapes [2]. Even worse, some structural damage was observed during past earthquakes. The first reported seismic damage of cable-stayed bridges is Shipshaw cable-stayed bridge in 1988 Saguenay Earthquake [3, 4]. An anchorage plate underneath the deck failed due to stress increments during earthquake and the abutment concrete was damaged from pounding of deck against the abutment. During 1999 Chi-Chi Earthquake, much more severe damage

was observed at Chi-Lu cable-stayed bridge [5, 6]. The damage included (1) bending failure of the superstructure at the superstructure pylon connection, (2) bending failure of the pylon above the pile cap and above the superstructure to pylon connection with concrete spalling, (3) pounding damage at the end span supports, and (4) anchorage failure of a cable stay.

Upon the nonlinear response and structural damage observed during earthquakes, some cable-stayed bridges have permitted controllable damage at tower legs under extreme seismic event, like Rion-Antirion bridge in Greece [7] and Stonecutters in Hong Kong, China [8]. In Japanese code [9], the main tower of cable-stayed bridge is allowed with plastic behavior by carefully investigating and designing its plastic ranges. Meanwhile, several studies have been conducted in an attempt to reveal elastic-plastic seismic response of cable-stayed bridges. Camara and Astiz [10] proposed coupled pushover analysis to estimate the complex inelastic response of cable-stayed bridges and revealed the contribution of higher modes (approximately between 1 Hz and 25 Hz) is significant in seismic response. Li et al. [11] conducted damage analysis of a three-tower cable-stayed bridge with

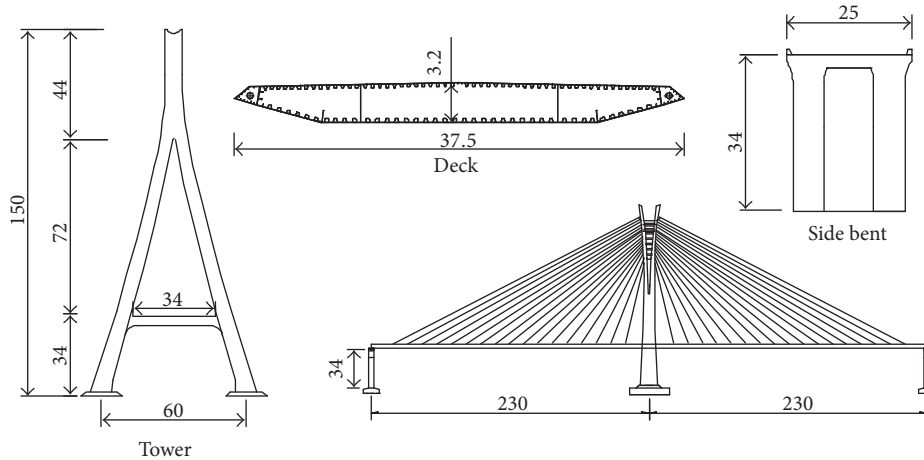


FIGURE 1: Schematic of the Puqian cable-stayed Bridge [m].

rigid system, floating system, and passive energy dissipation system, revealing that plastic hinge may form at either the bottom of middle tower or side tower, depending on different systems. However, as highlighted by the damage of Chi-Lu Bridge [5, 6], all composing parts of cable-stayed bridges, namely, the tower, deck, cables, and bearings, might go through nonlinear stage while current studies mainly focused on one or two parts of the cable-stayed bridges.

On the other hand, near-field ground motions exert a large influence on cable-stayed bridges which have a number of long-period modes [12]. In recent decades, several near-field ground motions have been recorded during past earthquakes as Parkfield (1966), San Fernando (1971), Kobe (1995), Chi-Chi (1999), and South Napa (2014) [13] events. Comparing to typical far-field ground motions, near-field ground motions usually contained long-duration pulses and high peak ground velocities [14]. Cable-stayed bridges are quite sensitive to near-field ground motions since large amplitude spectral acceleration of near-field ground motions usually occurred at long periods where many cable-stayed bridges have significant structural response modes. For instance, it was speculated that damage of Chi-Lu bridges was likely caused by ground motion pulses from the near-field ground motion at the bridge site [6].

To recognize all nonlinear response of cable-stayed bridges subjected to near-field ground motions, one of the most obvious and effective ways is through shake table tests. Shake table tests can excite structures in such a way that they are subjected to conditions representing true earthquake ground motions and verify the analysis results from different numerical methods, as the case of Jindo Bridge [15] and Taizhou Changjiang Bridge [16]. Several shake table tests have been conducted regarding structural damage of cable-stayed bridges under earthquakes. Duan [17] firstly conducted a 1/20 scale tower model of a cable-stayed bridge. Test results showed that (1) several cracks appeared and extended at the bottom of tower legs and at the middle of tower legs near the lower strut and (2) the bottom of the tower was seriously damaged with concrete spalling and steel bars fractured and exposed approximately 30 cm of the plastic region. But with

lack of corresponding cable and deck systems in the model, the applicability of the test results needed to be further verified. So a 1/20 scale full cable-stayed bridge model was designed and tested on shake tables by Wang et al. [18]. By exciting the model transversely, the test result showed the damage characteristics of a cable-stayed bridge with H-shaped tower in transverse direction including: (1) severe damage at the upper strut with several steel bars fractured at both ends, (2) repairable damage at the bottom and middle part of tower legs with concrete cover spalling and exposure of steel bars, and (3) minimal damage at the lower strut with slight concrete spalling.

This paper introduced another 1:20 full-scale model of a single-tower cable-stayed bridge which was excited longitudinally on shake tables at Tongji University, China. The design details of test model were described and the validation of the test model was conducted. One typical near-field ground motion was used to excite the model from low to high intensity and the observed damage and test results were presented. Posttest model was conducted and analyses results were compared with test results so as to check the adequacy of existing nonlinear analytical techniques in estimating seismic response of cable-stayed bridges under near-field ground motions. The influence of cable relaxation which was detected during the test was also studied. The objective of this test is to study structural damage of cable-stayed bridges under longitudinally excited earthquakes.

## 2. Bridge Model

*2.1. Prototype Bridge.* The prototype bridge, Puqian Bridge, spans Puqian sea area which lies in the northeast of Hainan province, China. It is a symmetric single-tower cable-stayed bridge with two 230 spans, as is shown in Figure 1. The concrete A-shape tower is 150 m high from bottom to tower top and 60 m wide at the foundation level. The rectangular crossbeam of the tower is at elevation 34 m and two skewed legs intersect at elevation 106 m. The deck is composed by a closed steel box, which is 37.5 m wide and 3.2 m high at

TABLE 1: Material properties of Puqian Bridge.

Structural components	Material	Elastic modulus (GPa)	Yield stress (MPa)	Density (kg/m <sup>3</sup> )
Tower and bents	Concrete	34.5	32.5	2600
	Steel bar	210	400	7850
Deck	Steel plate	210	345	7850
Cables	Steel strand	195	1860	7850

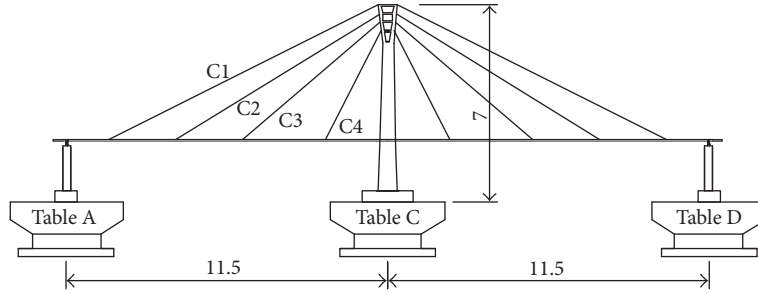


FIGURE 2: Bridge model and arrangement of shake tables [m].

TABLE 2: Self-weight and additional masses of the model.

Components	Self-weight (kg)	Additional mass (kg)	Total mass (kg)
Tower	3336	15200	18536
Deck	2453	6216	8669
Bents	1440	4200	5640
Cables	26	—	26

middle span. The stay cable arrangement is a two-vertical-plane system and totally 68 cable strands are used to support the deck. The concrete side bent is a portal frame which is 34 m high and 25 m wide. The deck of the bridge was vertically supported on bents and towers through spherical steel bearings which can slide longitudinally, while transversely being fixed to the side bents and towers by shear keys. Table 1 lists the material properties of prototype bridge.

## 2.2. Test Model

**2.2.1. Scale Factors.** According to the available testing system and the prototype of the bridge, the shake table bridge model is designed as a 1:20 scale geometric model of prototype. With this scale, the total height of the model from the base of the footing to the tower top was 7 m, and the total length was 23 m. Three shake tables, Tables A, C, and D, were used to support the test model, as shown in Figure 2. The payloads of Tables A and D are 30 t and those of Tables C are 70 t. All the tables have the dimension of 6 \* 4 m and maximum acceleration of 1.0 g.

In order to simulate the gravity effect, the acceleration scale factor was set to 1. Therefore, additional mass is added to increase the density of the structure and to produce a realistic dead load and inertial force. Table 2 lists the self-weight and the additional mass attached to the model. In total, the test

TABLE 3: Test results of microconcrete specimens.

Elastic modulus (GPa)	Specimen 1	Specimen 2	Specimen 3	Average
	12.80	10.59	11.25	11.6
Compressive stress (MPa)	Specimen 1	Specimen 2	Specimen 3	Average
	13.3	13.8	13.2	13.4

model has a weight of 32871 kg, including 7255 kg self-weight and 25616 kg additional mass.

**2.2.2. Tower and Bents Design.** Buckingham  $\pi$  theorem of dimensional analysis [19] was performed to design the model. Basically, the bridge model should provide a realistic representation of the prototype bridge response. However, if strictly following geometric scaling factor of 1/20, the minimum thickness of tower plate would be 40 mm, making it too difficult to manufacture the model. To solve the construction problem, the thickness of the tower and bents was enlarged to 80 mm while strictly following the scaling factor of flexural stiffness. Meanwhile, in order to reduce the total weight of the model [15], microconcrete was used to substitute the prototype concrete and its elastic modulus was designed to be 1/3 of the prototype material. Available rebar with the minimum diameter of 6 mm in Chinese commercial market was used to substitute 36 mm rebar of the prototype. The number and arrangement of rebars were properly designed so that the towers and bent columns of the test model would have the same shear and bending capacity exactly scaling down from the prototype bridge. Details of designed tower and bents are shown in Figure 3.

Before shake table tests, material tests for microconcrete were conducted through static modulus of elasticity in compression. Table 3 lists the test results of microconcrete specimens. The testing elastic modulus was 11.6 GPa, almost equal to 1/3 of elastic modulus of the prototype material

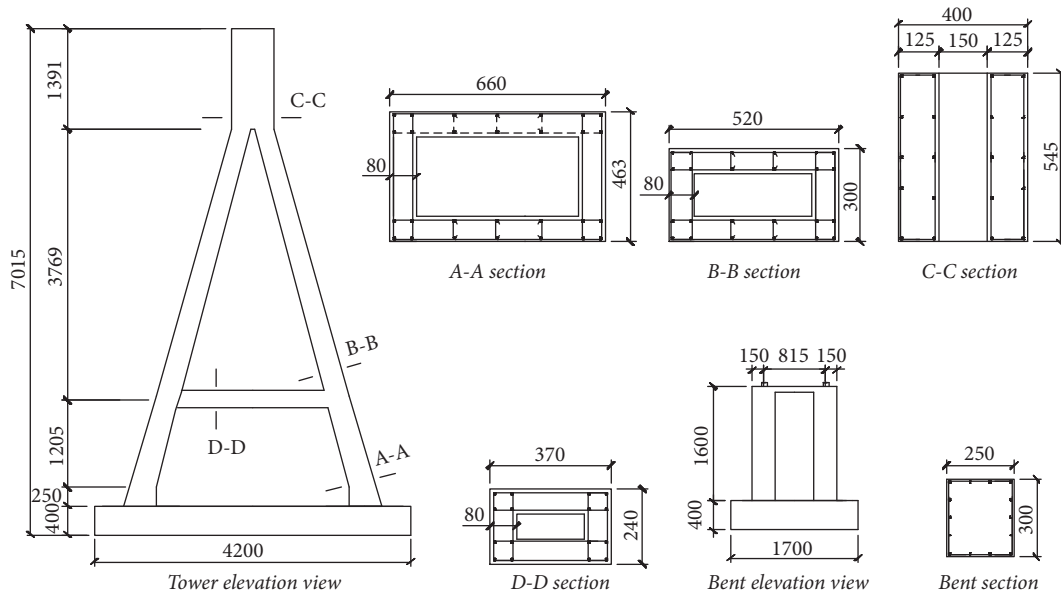


FIGURE 3: Details of the tower and bents design [mm].

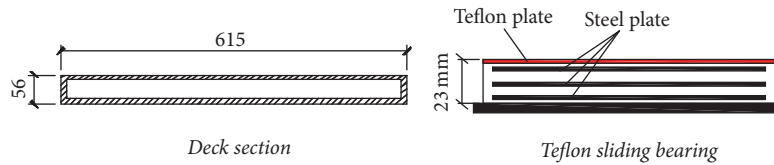


FIGURE 4: Details of the deck and sliding bearing design [mm].

as designed, and the average compressive strength of the microconcrete was 13.4 MPa.

**2.2.3. Deck and Cable Design.** To simplify construction, a regular box section composed of 10 mm thick steel plate was designed to substitute the streamlined, flat, thin-walled steel box, as shown in Figure 4. The model steel box had the exact scaling bending moment of inertia about both strong and weak axes from the prototype box. Six Teflon sliding bearings, as also shown in Figure 4, were distributed to the tower and bents to support the deck.

High-strength stainless steel wires were used for cables of test model. In order to simplify the construction, 68 cables from the prototype bridge were condensed to 16 cables for the test model. According to the principles of equivalent cable forces and dynamic characteristics from the prototype, each cable had a cross-sectional area of  $7.85 \times 10^{-5} \text{ mm}^2$ .

**2.2.4. Assembled Bridge Model.** The assembled bridge model is shown in Figure 5. Out of safety consideration, a gate-style frame was used above each transition pier to restrain vertical movement at deck end so that end span uplift effect is prevented [5].



FIGURE 5: Assembled bridge model.

### 3. Testing Protocol

In order to study the near-fault effects on the seismic damage of cable-stayed bridges, one typical near-fault ground motion, TCU052 from the 1999 Chi-Chi Earthquake [20], was used to excite the test model. To account for the scale effect of the test model, the time axis of the prototype motion was compressed by 0.2236 ( $1/\sqrt{20}$ ). Figure 6 shows the input records with a compressed time axis and scaled amplitude

TABLE 4: Comparison of target and achieved peak ground acceleration.

Cases	Target PGA (g)	Achieved PGA (g)	Ratios
Case 1	0.05	0.051	1.02
Case 2	0.1	0.103	1.03
Case 3	0.15	0.164	1.09
Case 4	0.2	0.212	1.06
Case 5	0.25	0.265	1.06
Case 6	0.3	0.31	1.03
Case 7	0.35	0.364	1.04
Case 8	0.4	0.418	1.05
Case 9	0.45	0.464	1.03
Case 10	0.5	0.506	1.01
Case 11	0.55	0.547	0.99
Case 12	0.6	0.594	0.99
Case 13	0.65	0.648	1.00
Case 14	0.7	0.728	1.04
Case 15	0.75	0.78	1.04
Case 16	0.8	0.812	1.02

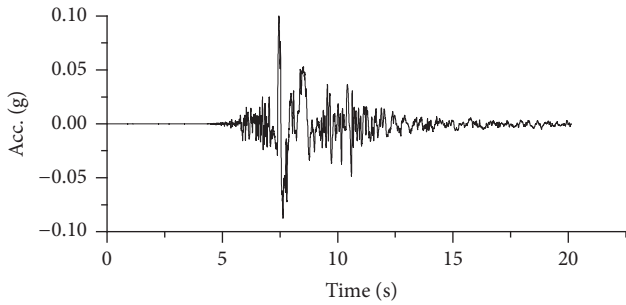


FIGURE 6: Input motions with compressed time axis and scaled amplitude.

(PGA = 0.1g). During the test, the TCU052 waves were applied with the increasing PGA from 0.05 to 0.80 g in the longitudinal direction. In order to determine changes in structural period so as to evaluate the stiffness degradation of the model, white noise excitation was applied at the beginning of the test and between each earthquake test after PGA > 0.25 g.

To check the relevance between actual shake table motions and target motions, achieved PGAs were compared with the target ones. Target and achieved PGAs and the ratios of the achieved PGAs to target ones were listed in Table 4. One can see that the ratios were within 0.99~1.09 for all cases, indicating that the achieved and target values are quite matched.

#### 4. Validation of Test Model against Prototype

The test model is assumed to provide a realistic representation of the prototype bridge response. However, to simplify the construction, several adjustments were made to the test model comparing to theoretical model which is exactly scaling down from the prototype bridge structure. These

adjustments included the following: (1) the plate thickness of the tower was enlarged to 80 mm; (2) the deck was a regular box section with 10 mm thick steel plate to substitute the streamlined, flat, thin-walled steel box, following the scale factors of flexural stiffness; (3) the number of cables was condensed from 68 to 16 to simplify the construction. Therefore, preliminary linear analysis was performed to check the accuracy of the test model representing theoretical model at linear stage.

Two analytical models were conducted for preliminary analysis based on OpenSees (open system for earthquake engineering simulation) [21]: Model A, analytical model for test model, and Model B for theoretical model. For both models, the tower, piers, and the deck were modeled using linear-elastic element with P-Delta effects included. The stay cables were modeled using truss elements and sag effect was accounted for based on Ernst's equivalent elastic modulus concept [22]. Connections of deck-piers and deck-tower are free for longitudinal floating system while being restrained for transverse direction. Since the tower and bents of the test model were fixed on the shake tables and the soil-structure interaction effect was neglected, fixed constraint was set to the tower and the bents for two models.

Table 5 lists comparisons between theoretical model and test model with 1st and 2nd longitudinal modal periods and time-history analysis results. In Table 5, the 1st mode for two models was longitudinal vibration of the deck while 2nd mode was longitudinal vibration of the tower, and the input ground motion used for time-history analysis was Case 2 from Table 4. From Table 5, one can see that the maximum error of the natural period between the test model and the theoretical model was within 15% and the maximum error of seismic response was within 10%.

## 5. Test Results

**5.1. Observed Damaged.** The observed damage was mainly from the concrete cracks and concrete spalling of the tower while the deck, cables, and bents were visually undamaged. The development of observed cracks at RC tower sections subjected to increasing PGA was shown in Table 6 and Figure 7. One can see that severe structural damage occurred at the tower of the model including parallel concrete cracks from the bottom to nearly half height of the tower, concrete spalling, and exposed bars at top tower 0.2m above the section where two skewed legs intersect. When PGA reached 0.8 g, sudden large noise was produced at the time that the concrete spalls and large permanent rotation was observed at top tower after the test. Out of safety consideration and to prevent collapse of the model, no TCU052 waves with larger PGA were applied to the test model after PGA = 0.8 g.

An immediate survey was conducted concerning the cause of concrete spalling at Section C-C as PGA = 0.8 g. It was due to abrupt change of cross section at Section C-C where stress concentration was induced, as shown in Figure 8.

**5.2. Model Period.** Along with damage observation, model period shift of the test model was also detected during the

TABLE 5: Comparison of the test model and theoretical model.

Items	Theoretical model	Test model	errors
Modal analysis			
1st longitudinal model period (s)	1.335	1.149	-13.9%
2nd longitudinal model period (s)	0.630	0.545	-13.5%
Time history analysis			
Peak displacement at tower top (m)	0.0273	0.0284	4.0%
Peak displacement at deck end (m)	0.0368	0.0331	-10.0%
Peak bending moment at tower bottom (kN·m)	52.87	56.5	6.8%

TABLE 6: Observed damage during the test.

PGA	Damage height	description
0-0.25 g	—	No damage.
0.30 g	$H = 0.65$ m	First crack appeared at the bottom of tower leg.
0.30~0.50 g	$H = 0.65$ m	First crack extended to gradually form a circle.
0.50 g~0.60 g	$H = 0.80\sim 1.20$ m	Several parallel cracks appeared just above the first crack.
0.6~0.70 g	$H = 0.80\sim 1.20$ m	Cracks extended horizontally.
0.6~0.70 g	$H = 1.4$ m~3.5 m	Several parallel cracks appeared and were distributed in parallel at a nearly equal distance of tower width (around 0.35 m).
0.75 g	$H = 5.8$ m	Cracks appeared at top tower 0.2 m above the section where two skewed legs intersect (Section C-C in Figure 3).
0.75 g	$H = 5.8$ m	Cracks extended and penetrated Section C-C.
0.80 g	$H = 5.8$ m	Considerable concrete spalling and exposed longitudinal bars were observed at Section C-C.

test. The stiffness of concrete structure decreased as structural damage occurred and developed. Therefore, modal periods, related to structural stiffness, can be used as a stiffness degradation index of the tested model due to structural damage under earthquake excitation. Based on white noise excitation results, modal periods were determined from plots of the Fast Fourier Transform (FFT) utilizing acceleration at tower top and table acceleration.

Figure 9 shows the changes of the first and second modal period of the test model after applying TCU052 waves with varying PGA. Based on FFT results, the first mode of the test model is longitudinal vibration of the deck and the second mode is longitudinal vibration of the tower coupled with vertical vibration of the deck. From Figure 9, the second modal period gradually increased three times, namely, at  $PGA = 0.45$  g, 0.7 g, and 0.75 g, which fit in with the observed damage in Table 6. The first modal period slightly increased only when penetrating cracks occurred at Section C-C at  $PGA = 0.75$  g. After the test, the period for the first and second longitudinal mode was 1.06 s and 0.70 s, 3% and 10% longer than that before the test, respectively. The increased modal periods reflected stiffness degradation of the model as damage of tower occurred and accumulated during the test.

**5.3. Acceleration and Displacement Response.** Figure 10 presents measured maximum longitudinal acceleration and displacement at tower top and at deck end. From Figure 10(a), acceleration at tower top and that at deck end both increased linearly as PGA increased for most cases. From Figure 10(b),

the displacement at tower top increased almost linearly with increasing PGA when  $PGA \leq 0.70$  g. But when concrete spalling appeared at  $PGA = 0.8$  g, the tower top suddenly went through large displacement response, almost twice that at  $PGA = 0.75$  g. Deck displacement linearly increased with increasing PGA, revealing that cracks or concrete spalling of the tower negligibly influenced deck displacement response.

**5.4. Cable Response.** Figure 11 shows tension force envelope of C1~C4. When  $PGA < 0.70$  g, the maximum and minimum tension forces of C1~C4 changed in a linear manner as PGA increased. However, when  $PGA = 0.7$  g, the minimum tension force of C3 and C4 almost reached 0 and no longer decreased as PGA increased. As cable forces dropped to 0, the cables provided no stiffness to support the deck, reflecting that cable relaxation occurred for C3 and C4 during the test. When  $PGA > 0.7$  g, little change was observed as PGA increased for the minimum tension force of C1 and C2 and maximum tension force of all cables, clearly indicating influence of cable relaxation on cable force response. When  $PGA = 0.8$  g, the maximum tension force of C1, C3, and C4 reached about twice the initial cable force, showing large variation of cable forces during the test.

## 6. Posttest Analysis Results

**6.1. Analytical Model for Posttest Analyses.** To determine the adequacy of existing nonlinear analytical techniques in estimating the seismic response of cable-stayed bridges,

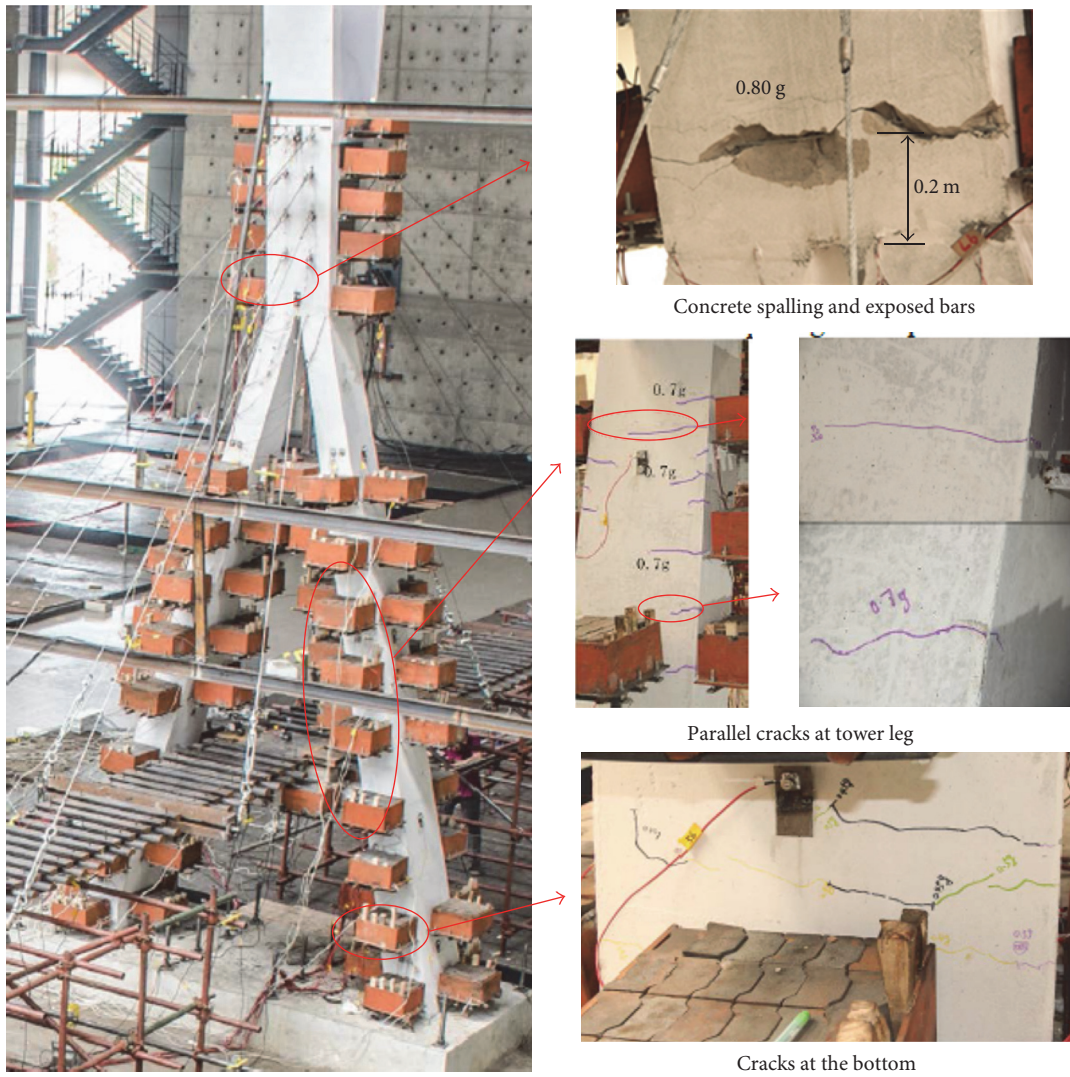


FIGURE 7: Observed seismic damage of the bridge model.

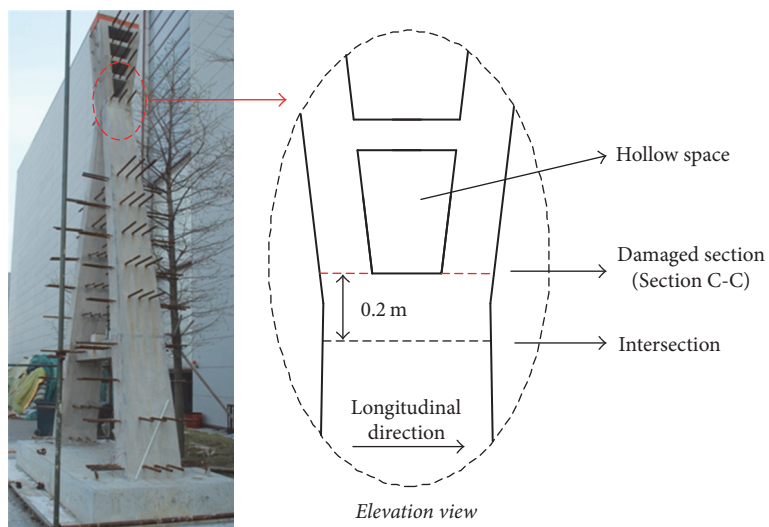


FIGURE 8: Configuration of Section C-C.

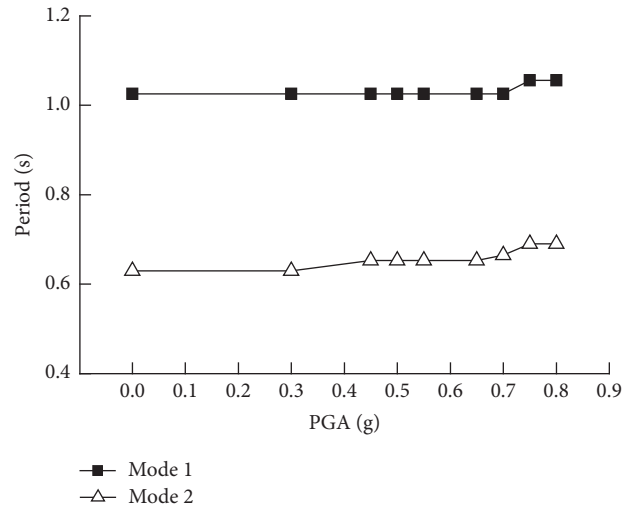


FIGURE 9: Period shifts of first and second longitudinal modes.

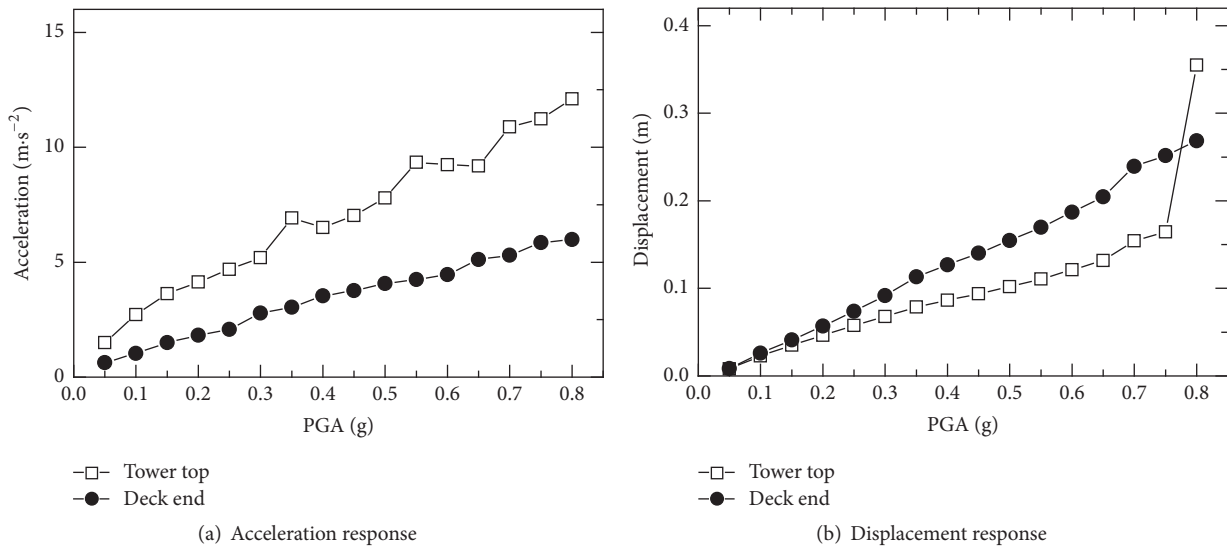


FIGURE 10: Measured peak acceleration and displacement response of the model.

one sophisticated model, Model C, was conducted for the test model based on OpenSees. Both Nazmy and Abdel-Ghaffar [23] and Ren and Obata [24] recommended the following nonlinear characteristics when modeling large long cable-stayed bridges for seismic analyses: (1) sag effect of inclined cables, (2) combined axial load and bending moment interaction effect of towers and deck, (3) large displacement effect of the structure, and (4) material nonlinearity. These nonlinearities were modeled in Model C. Besides, cable relaxation, detected in the experiments, was also considered. Similar to Model A, fixed constraint was set to the tower and the bents for two models, ignoring the soil-structure interaction. The following shows the modeling details of different parts of the model, namely, tower and bents, superstructure, cables, and bearings.

**6.1.1. Tower and Bents Model.** To account for material nonlinearity and axial force-moment interaction effect, the tower and bents were modeled using nonlinear beam-column elements whose cross section was discretized into unidirectional confined concrete, unconfined concrete, and steel fibers. Both confined and unconfined concrete fibers were represented using the uniaxial Kent-Scott-Park model [25] with degraded linear unloading/reloading stiffness. The steel fibers were represented using a bilinear hysteretic model with kinematic strain hardening. The concrete fibers were at a rectangular patch. As an example, Section A-A contained 1, 536 concrete fibers and 28 longitudinal bar fibers.

**6.1.2. Superstructure Model.** During the test, no damage occurred at superstructure. Therefore, the superstructure is

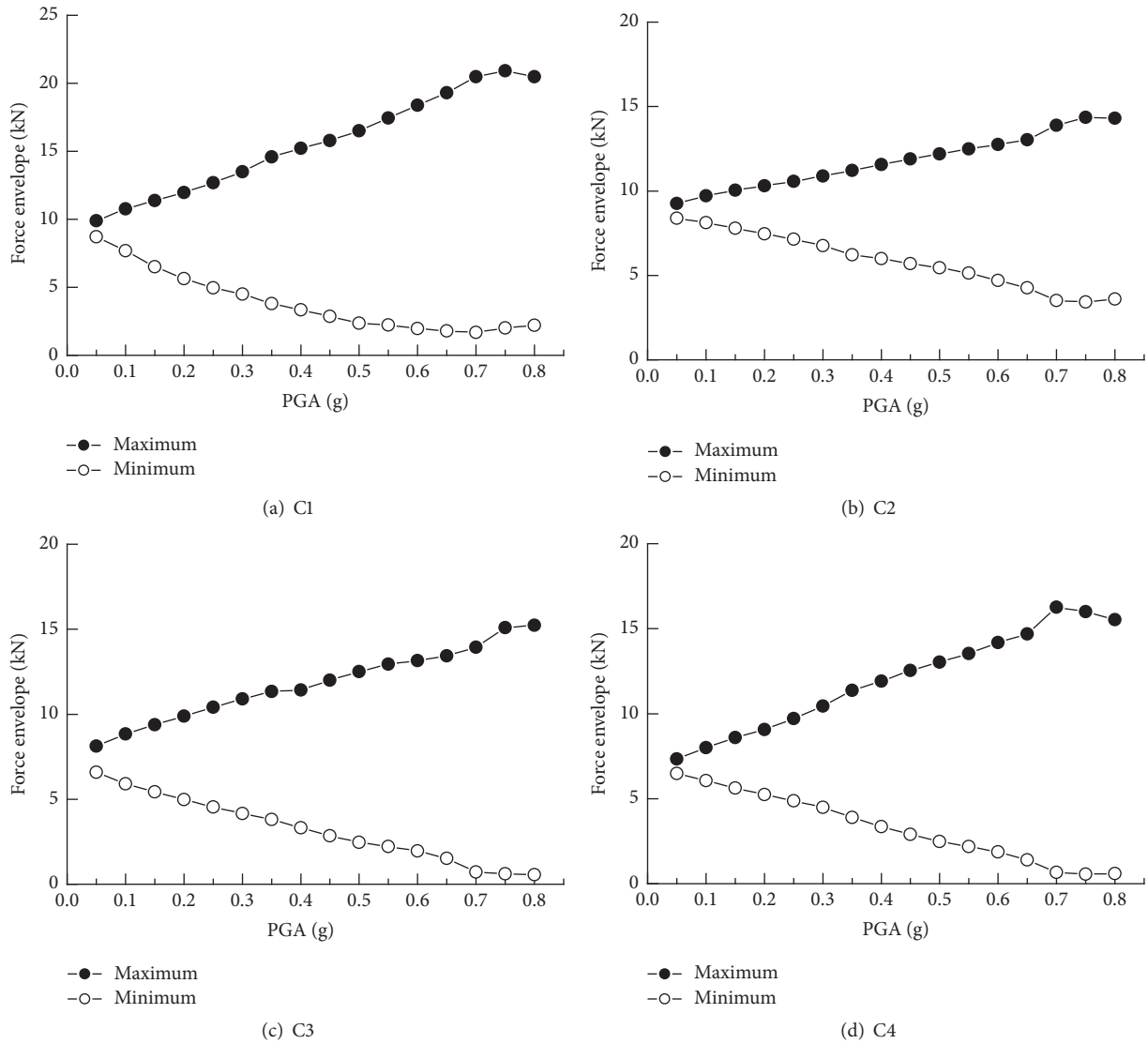


FIGURE 11: Cable force envelope of test results.

expected to remain linear during earthquake and was modeled using linear-elastic element. However, its axial force-moment interaction and large displacement effect were taken into account.

6.1.3. *Cable Model.* Two sources of nonlinearity were included in the cable modeling: sag effects and cable relaxation. Sag effects were approximately taken into account based on Ernst's equivalent elastic modulus [22]. In fact, elastic modulus of cables changes with varying cable force during the excitation. However, constant elastic modulus from dead loads was adopted instead since changing cable force had limited influence on the cable stiffness, as indicated by Zárate and Caicedo's work [26]. Cable relaxation was considered using no-compression material so that cables function only in tension state. Besides, cables are prestressed under dead-load state, which is considered by applying initial strain to cable material so that the cable force resists at prestressed value at zero applied force.

6.1.4. *Bearing Model.* Longitudinal sliding bearings were used to connect the deck to the tower and piers. In longitudinal direction, friction effects of sliding bearings were modeled with an elastic-plastic material and the initial stiffness was calculated as  $K = 267 \text{ kN/m}$  based on the geometry of the bearing. In transverse and vertical direction, the connections between deck-pier and deck-tower were set fixed since transverse displacement of the deck was restrained by the restrainers and vertical movement of deck end at piers was restrained by gate-style frames (see Figure 5).

6.1.5. *Completed Model.* Figure 12 shows general configuration of Model C. After modeling, Model C had totally 278 nodes, 108 nonlinear beam-column elements, 109 linear-elastic beam-column elements, and 16 cable elements. Before nonlinear seismic analysis, dead load was applied to the three FEM models prior to nonlinear dynamic analysis so that nonlinear seismic analysis starts from the equilibrium

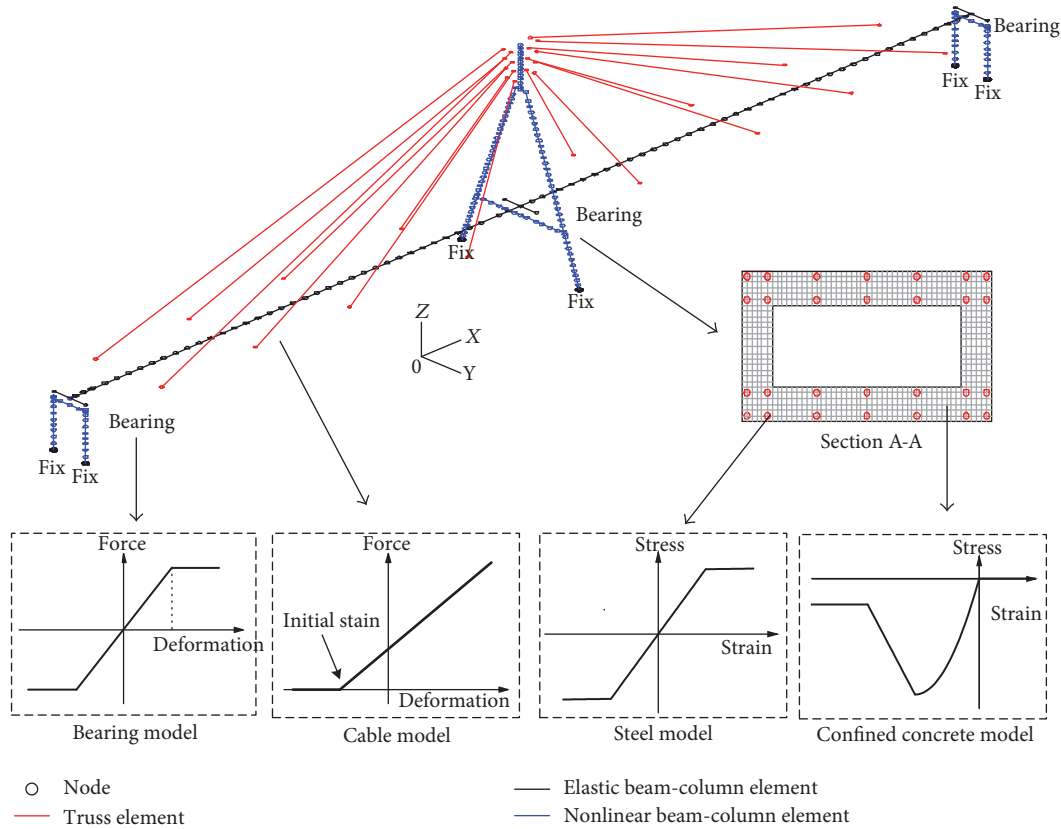


FIGURE 12: FEM model of Model C.

configuration of dead loads [23, 24]. 5% inherent damping was accounted for using Rayleigh damping based on 1st and 2nd longitudinal vibration period.

6.2. Validation of Model C

6.2.1. Acceleration and Displacement Response. OpenSees analysis of Model C was conducted to evaluate its ability to reproduce the measured test results. Figures 13 and 14 show comparison of acceleration and displacement histories at tower top and at deck end between measured and numerical result, respectively. In addition, Table 7 shows the comparisons of peak displacement results between measured and numerical results.

From Figures 13 and 14, it can be seen that though numerical results of Model C slightly deviated from the test results, numerical results catch the main features of the measured results and the shapes of the time histories fit in well for  $PGA < 0.8\text{ g}$ . When  $PGA = 0.8\text{ g}$ , numerical acceleration histories agreed with test results while numerical displacement histories failed to catch tower permanent displacement at  $t = 9\text{ s}$  when concrete spalling occurred of test model.

As seen in Table 7, for deck displacement, the correlation between measured and numerical results was good with maximum error less than 10%. For tower displacement, numerical results and measured results agreed quite well at low PGA levels ( $PGA < 0.15\text{ g}$ ) with maximum error less

than 10%, but numerical results were slightly overestimated as PGA increased ( $0.2\text{ g} \leq PGA \leq 0.75\text{ g}$ ) with maximum error up to 46%. And when  $PGA = 0.8\text{ g}$ , numerical results failed to catch the suddenly increased tower displacement of measured results.

The disagreement between measured and numerical results may be from the fact that the concrete model used in the numerical model might deviate from the actual stress-strain relationship of microconcrete. But based on the overall satisfactory correlation between the measured and calculated results, it was concluded that Model C adequately simulated the acceleration and displacement response of the test model.

6.2.2. Cable Force Response. Figure 15 shows a representative sample of measured and numerical cable force histories for C3 which went through cable relaxation during the test. Table 8 shows comparison of maximum and minimum cable force between measured and numerical results. In Figure 15 and Table 8, the cable forces were normalized by the pretension value at completed state of C3 (8.75 kN). From Figure 14, it can be seen that the numerical results clearly catch the cable relaxation at  $PGA = 0.8\text{ g}$  when minimum cable force drops to zero. And as seen in Table 8, the numerical results agreed with measured maximum cable force for all PGA levels with maximum difference less than 15%, while the difference of minimum tension force was slightly larger between test results and numerical results, with

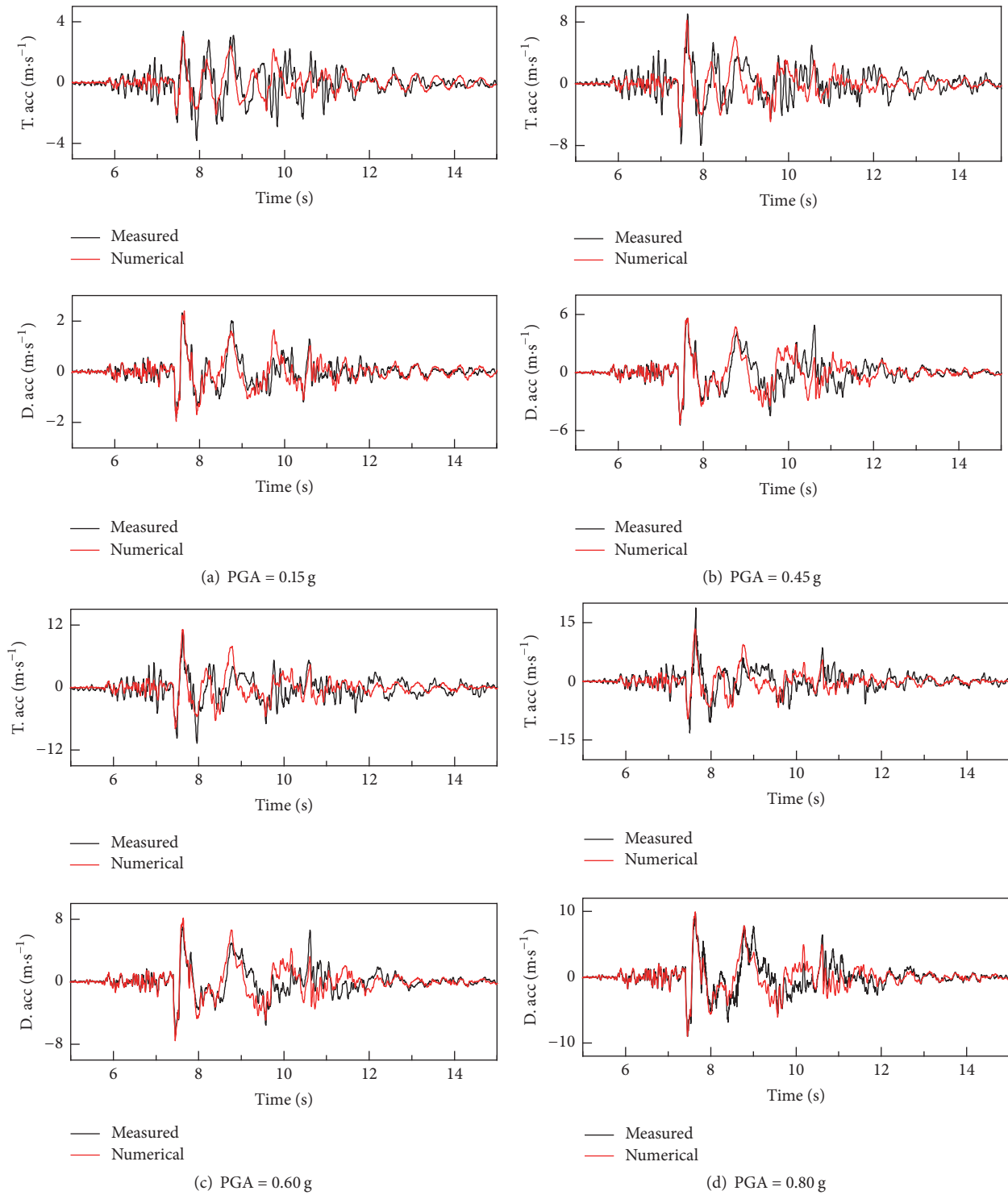


FIGURE 13: Comparisons between measured and numerical results of acceleration histories at tower top and deck end.

maximum difference around 25%. Based on the comparison, the numerical model was able to capture large variation of cable tension force and cable relaxation.

6.2.3. *Steel Strain Response.* Figure 16 shows measured and numerical results of maximum steel strain response for the

tower in order to verify that numerical model duplicates the observed damage of the test model. For the test model, steel strain gauges were placed only at Sections A-A and B-B and no strain gauges were available at Section C-C. Thus, only measured steel strain at Sections A-A and B-B was provided in Figure 16.

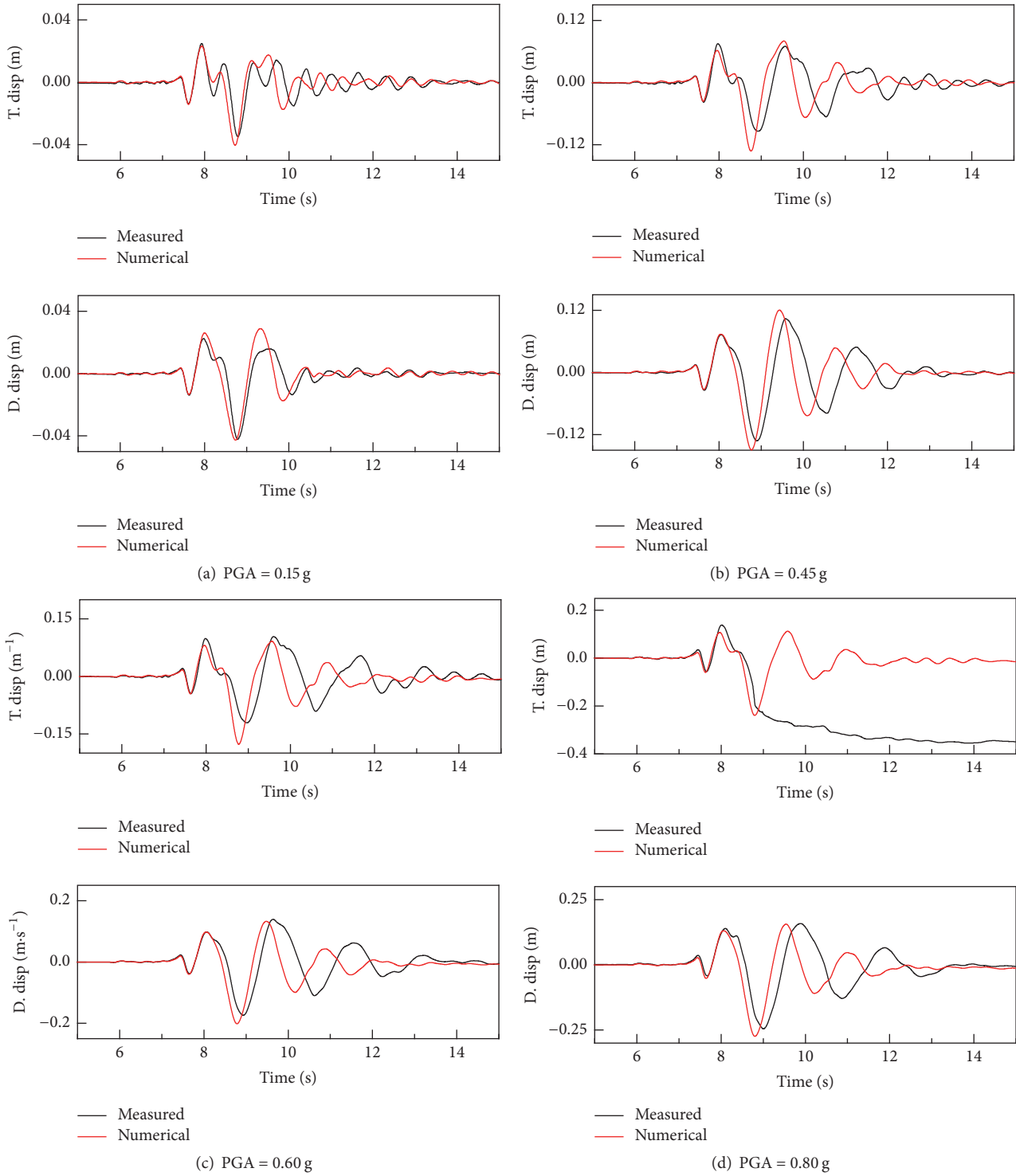


FIGURE 14: Comparisons between measured and numerical results of displacement histories at tower top and deck end.

From Figure 16, it can be seen from numerical steel stain envelop that before longitudinal steel yielded (PGA < 0.4 g), the maximum strain occurred at tower bottom, which agreed with observation during the test that the first cracks occurred at this section. The longitudinal steel first yielded when PGA

= 0.4 g at Section A-A (height = 0.65 m) and Section B-B (height = 2 m). At this PGA level, steel stains at lower tower almost reached yield limit. After steel first yielded (PGA > 0.4 g), steel strain at lower tower and middle tower increased almost linearly as PGA increased at a controllable

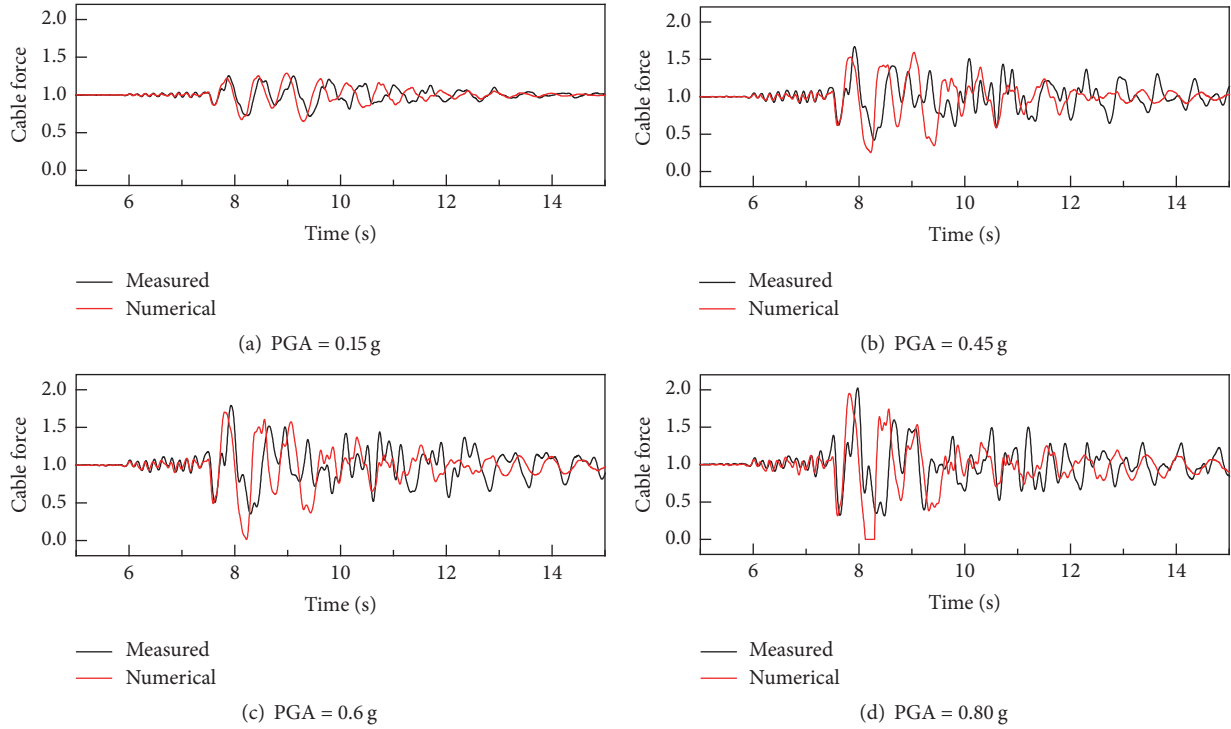


FIGURE 15: Comparisons of normalized cable force histories between measured and numerical results (C3).

TABLE 7: Comparisons of maximum displacement between measured and numerical results.

PGA	Tower top displacement (m)			Deck end displacement (m)		
	Test results	Numericalresults	Error	Test results	Numericalresults	Error
0.05	0.0082	0.008931	8.91%	0.0085	0.007804	-8.19%
0.1	0.0228	0.02586	13.42%	0.0261	0.027044	3.62%
0.15	0.035	0.043353	23.87%	0.0413	0.047237	14.38%
0.2	0.0465	0.059795	28.59%	0.0568	0.066117	16.40%
0.25	0.0576	0.077512	34.57%	0.0737	0.086395	17.23%
0.3	0.0679	0.091692	35.04%	0.0917	0.10319	12.53%
0.35	0.0787	0.10177	29.31%	0.1133	0.113957	0.58%
0.4	0.0865	0.11591	34.00%	0.1269	0.130522	2.85%
0.45	0.0937	0.12882	37.48%	0.1403	0.145473	3.69%
0.5	0.1019	0.14146	38.82%	0.1547	0.160204	3.56%
0.55	0.1108	0.15357	38.60%	0.1698	0.174496	2.77%
0.6	0.1212	0.17336	43.04%	0.1871	0.197462	5.54%
0.65	0.1318	0.18981	44.01%	0.2044	0.216463	5.90%
0.7	0.1542	0.21695	40.69%	0.2393	0.248249	3.74%
0.75	0.1644	0.228	38.69%	0.2517	0.261367	3.84%
0.8	0.355	0.23537	-33.70%	0.2687	0.269654	0.36%

range. For example, the maximum steel strain of Sections A-A and B-B was about 3 times the yield strain when  $PGA = 0.8g$ . Meanwhile, the yielding sections at middle tower extended to higher height as  $PGA$  increased, showing related damage process of the test model. When  $PGA = 0.8G$ , the highest section with yielding steel at middle tower was at 3.4 m, almost at half height of the tower, agreeing with observation during the test. At top tower, the yielding section

only occurred at Section C-C where cross section changed abruptly and its steel stain increased substantially after first yielding at  $PGA = 0.4g$ . The maximum steel strain was 15 times the yield stain when  $PGA = 0.8g$ , which accordingly depicted concrete spalling at this section.

For Sections A-A and B-B, numerical steel stain agreed quite well with measured results when  $PGA < 0.35g$ . However, after steel yielded at  $PGA = 0.4g$ , discrepancy of

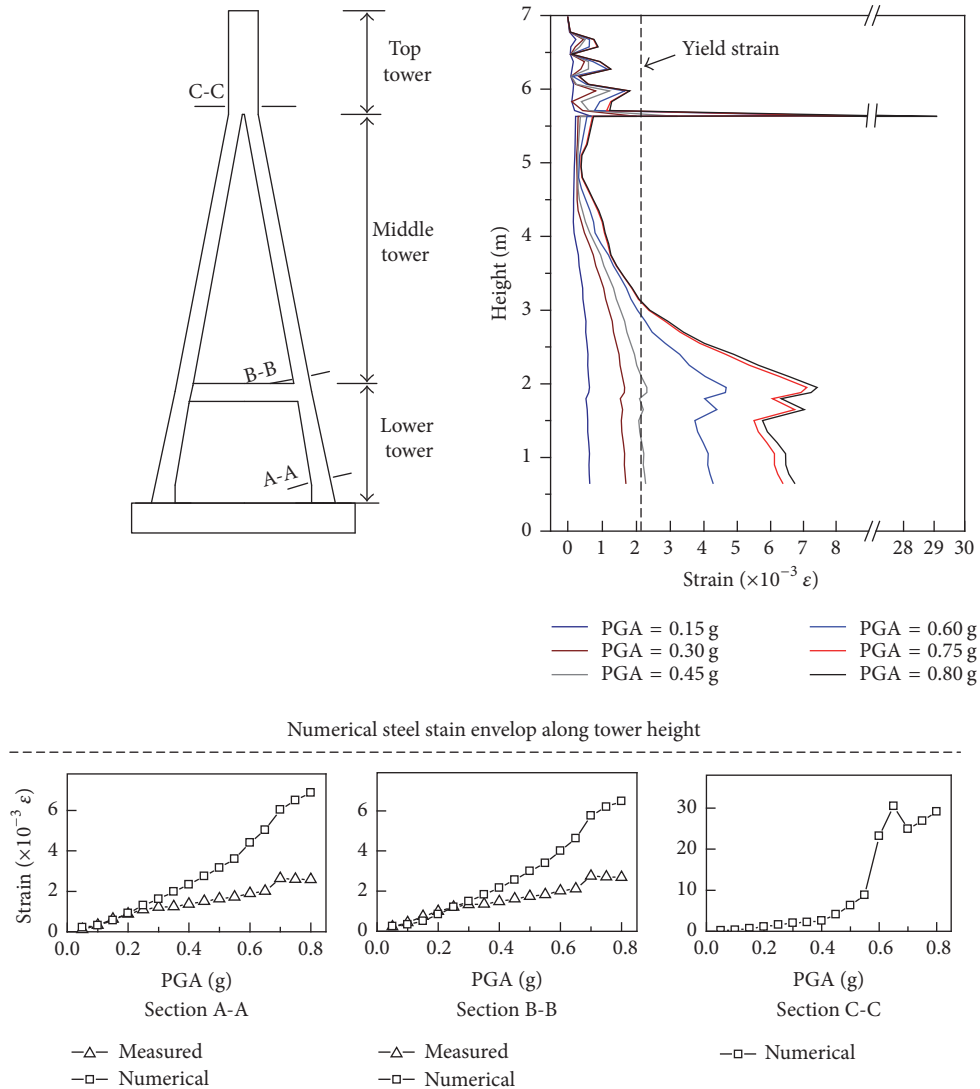


FIGURE 16: Measured and numerical results of maximum longitudinal steel strain response for the tower.

numerical and measured results was observed since steel stain gauges of the test model lose proper function at high strains ( $>2 \times 10^{-3} \epsilon$ ).

From the above discussion, Model C overall reflected test model of the measured acceleration and displacement response, cable tension force, and the observed damage with good agreement. It is concluded that, by modeling several nonlinearities of different elements of cable-stayed bridges, Model C is able to simulate the elastic-plastic behavior of the cable-stayed bridge.

**6.3. Cable Relaxation Effects.** In order to study the cable relaxation effects on the seismic response of cable-stayed bridges, a companion model of Model C, Model D, was conducted. Model D is similar to Model C except that cable relaxation was neglected by applying elastic material to cable models with elastic modulus the same as Model C at tension state. For Model D, cable elements were able to suspend compression force despite the fact that it was against the

actual material properties of the cables. In this way, Model D should have the same seismic response as Model C until any of cable relaxations occurred. Figure 17 shows the peak response of Model D including deck and tower displacement, tension force of C3, and bending moment at tower bottom. In Figure 17, for comparing purpose, all the responses were normalized by that of Model C.

From Figure 17, the response of Model D, as expected, is exact to that of Model C before cable relaxation first occurred at PGA = 0.45 g. After cable relaxation (PGA  $\geq$  0.45 g), one can see that Model D experienced slightly larger seismic response than Model C and it becomes more obvious as PGA increased. For tower displacement, tower bending moment, and deck displacement, the maximum difference between two models was less than 4% for all PGA levels while it was less than 12% for maximum cable force of C4. It is concluded that cable relaxation slightly enlarged the seismic response of cable-stayed bridges like tower displacement, bending moment at tower bottom, and deck displacement

TABLE 8: Comparisons of normalized maximum and minimum cable forces between measured and numerical results.

PGA	Maximum tension force			PGA	Minimum tension force		
	Test results	Numerical results	Difference		Test results	Numerical results	Difference
0.05	1.092	1.098	0.5%	0.05	0.886	0.903	1.7%
0.10	1.189	1.206	1.7%	0.10	0.793	0.771	-2.2%
0.15	1.260	1.285	2.5%	0.15	0.731	0.666	-6.5%
0.20	1.330	1.350	2.0%	0.20	0.670	0.585	-8.5%
0.25	1.398	1.413	1.5%	0.25	0.611	0.508	-10.3%
0.30	1.465	1.451	-1.4%	0.30	0.559	0.454	-10.5%
0.35	1.523	1.505	-1.7%	0.35	0.511	0.393	-11.8%
0.40	1.536	1.568	3.2%	0.40	0.445	0.320	-12.5%
0.45	1.614	1.592	-2.2%	0.45	0.383	0.253	-13.0%
0.50	1.681	1.582	-9.9%	0.50	0.332	0.181	-15.1%
0.55	1.739	1.617	-12.1%	0.55	0.299	0.118	-18.1%
0.60	1.769	1.695	-7.3%	0.60	0.262	0.011	-25.1%
0.65	1.805	1.763	-4.2%	0.65	0.205	0.000	-20.5%
0.70	1.873	1.868	-0.5%	0.70	0.097	0.000	-9.7%
0.75	2.028	1.920	-10.8%	0.75	0.082	0.000	-8.2%
0.80	2.048	1.947	-10.1%	0.80	0.074	0.000	-7.4%

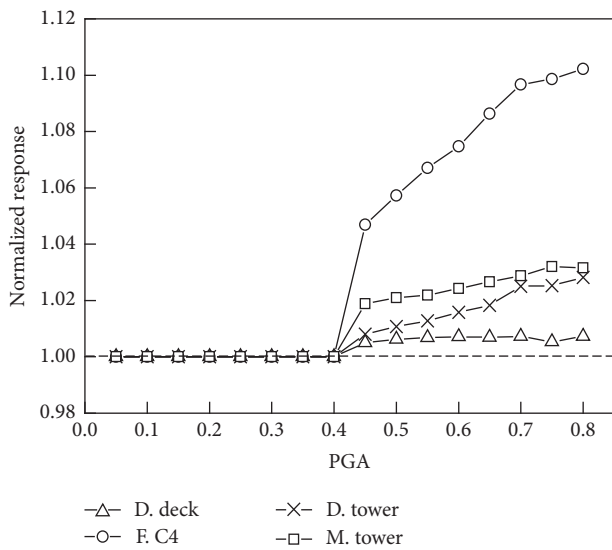


FIGURE 17: Normalized seismic response of Model D. Note: D. deck, deck displacement at deck end; D. tower, tower displacement at tower top; F. C4, maximum cable force of C4; M. tower, bending moment at tower bottom.

and maximum cable force, but its influence is quite small with maximum error less than 12%.

## 7. Conclusion

The main objective of this paper was to describe experimental and analytical studies on seismic damage of cable-stayed bridges in longitudinal direction. From the set of results presented, the following conclusion can be drawn:

- (1) The observed damage of the test model mainly concentrated at the tower including (1) several cracks at the bottom region of the tower leg when  $\text{PGA} = 0.3\sim 0.5$  g, (2) parallel horizontal cracks from the bottom to nearly half height of the tower leg distributed at a nearly equal distance when  $\text{PGA} = 0.5\sim 0.7$  g, and (3) concrete spalling and exposed longitudinal bars at top tower 0.2 m above the section where two skewed legs intersect.
- (2) The stiffness of the bridge decreased as damage of the tower occurred and accumulated, leading to gradual elongation of natural period of the model.
- (3) By modeling nonlinearity for different components of cable-stayed bridges, numerical model reflected test model of the measured acceleration and displacement response, cable tension force, and the observed damage with good agreement. It is thus concluded that nonlinear analytical techniques were able to simulate the elastic-plastic response of the cable-stayed bridge.
- (4) Cable experienced large variation of tension force during the test, and cable relaxation was detected. Based on the numerical study, cable relaxation enlarged the seismic response of cable-stayed bridges like tower displacement, bending moment at tower bottom, deck displacement, and maximum cable force, but its influence is quite small with maximum error less than 12%.

## Conflicts of Interest

The authors declare that they have no conflicts of interest.

## Acknowledgments

This research is supported by the National Basic Research Program of China (no. 2013CB036302) and Strategic Study on the Technology Development of Marine Bridge Engineering. The support is gratefully acknowledged.

## References

- [1] MCPRC, *Guidelines for Seismic Design of Highway Bridges*, Ministry of Communications of the People's Republic of China, Beijing, China, 2008 (Chinese).
- [2] D. M. Siringoringo, Y. Fujino, and K. Namikawa, "Seismic response analyses of the Yokohama Bay cable-stayed bridge in the 2011 great East Japan Earthquake," *Journal of Bridge Engineering*, vol. 19, no. 8, Article ID A4014006, 2011.
- [3] A. Filiatrault, R. Tinawi, and B. Massicotte, "Damage to cable-stayed bridge during 1988 saguenay earthquake. I: pseudostatic analysis," *Journal of Structural Engineering (United States)*, vol. 119, no. 5, pp. 1432–1449, 1993.
- [4] A. Filiatrault, R. Tinawi, and B. Massicotte, "Damage to cable-stayed bridge during 1988 Saguenay earthquake. II: dynamic analysis," *Journal of Structural Engineering*, vol. 119, no. 5, pp. 1450–1463, 1993.
- [5] K. C. Chang, Y. L. Mo, C. C. Chen, L. C. Lai, and C. C. Chou, "Lessons learned from the damaged Chi-Lu cable-stayed bridge," *Journal of Bridge Engineering*, vol. 9, no. 4, pp. 343–352, 2004.
- [6] C. B. Chadwell and G. L. Fennes, "Near source earthquake effects on the Jilu cable-stayed bridge in the 21 September 1999 chi-chi taiwan earthquake," in *Proceedings of the Community Workshop On Computational Simulation and Visualization Environment for NEES*, W. M. Kim Roddis, Ed., National Science Foundation, University of Kansas, Lawrence, Kan, USA, 2003.
- [7] J. Combault and J. P. Teyssandier, "The Rion-Antirion bridge: concept, design and construction," in *Proceedings of the Structures Congress and the 2005 Forensic Engineering Symposium*, pp. 1539–1550, New York, NY, USA, April 2005.
- [8] S. Kite, K. Falbe-Hansen, T. Vejrum et al., "Stonecutters bridge—design for extreme events," in *Proceedings of the IABSE Symposium Report, International Association for Bridge and Structural Engineering*, vol. 90, no. 2, pp. 27–34, Lisbon, Portugal, 2005.
- [9] Japan Road Association, *Specifications for Highway Bridges*, Maruzen, Tokyo, Japan, 2002.
- [10] A. Camara and M. A. Astiz, "Pushover analysis for the seismic response prediction of cable-stayed bridges under multi-directional excitation," *Engineering Structures*, vol. 41, no. 3, pp. 444–455, 2012.
- [11] H. Li, J. Liu, and J. Ou, "Investigation of seismic damage of cable-stayed bridges with different connection configuration," *Journal of Earthquake and Tsunami*, vol. 3, no. 3, pp. 227–247, 2009.
- [12] M. J. Wesolowsky and J. C. Wilson, "Seismic isolation of cable-stayed bridges for near-field ground motions," *Earthquake Engineering and Structural Dynamics*, vol. 32, no. 13, pp. 2107–2126, 2003.
- [13] C. Ji, R. J. Archuleta, and C. Twardzik, "Rupture history of 2014 Mw 6.0 South Napa earthquake inferred from near-fault strong motion data and its impact to the practice of ground strong motion prediction," *Geophysical Research Letters*, vol. 42, no. 7, pp. 2149–2156, 2015.
- [14] R. S. Jangid and J. M. Kelly, "Base isolation for near-fault motions," *Earthquake Engineering and Structural Dynamics*, vol. 30, no. 5, pp. 691–707, 2001.
- [15] M. A. Garevski, J. M. W. Brownjohn, A. Blakeborough, and R. T. Severn, "Resonance-search tests on a small-scale model of a cable-stayed bridge," *Engineering Structures*, vol. 13, no. 1, pp. 59–66, 1991.
- [16] J. Li, J. Yan, T. Peng, and L. Han, "Shake table studies of seismic structural systems of a Taizhou Changjiang Highway Bridge model," *Journal of Bridge Engineering*, vol. 20, no. 3, 2015.
- [17] X. Duan, *Experimental Study on Seismic Performance of Cable-Stayed Bridge Tower Subjected to Longitudinal Strong Ground Motions*, Tongji University, Shanghai, China, 2012 (Chinese).
- [18] R. Wang, Y. Xu, and J. Li, "Transverse seismic behavior studies of a medium span cable-stayed bridge model with two concrete towers," *Journal of Earthquake Engineering*, vol. 21, no. 1, pp. 151–168, 2017.
- [19] P. D. Moncarz and H. Krawinkler, *Theory and Application of Experimental Model Analysis in Earthquake Engineering*, Stanford University, 1981.
- [20] G. P. Mavroeidis and A. S. Papageorgiou, "A mathematical representation of near-fault ground motions," *Bulletin of the Seismological Society of America*, vol. 93, no. 3, pp. 1099–1131, 2003.
- [21] S. Mazzoni, F. McKenna, M. H. Scott et al., *OpenSees Command Language Manual*, Pacific Earthquake Engineering Research (PEER) Center, 2006.
- [22] H. J. Ernst, "Der E-modul von seilen unter berucksichtigung des durchchanges," *Der Bauingenieur, Berlin*, vol. 40, no. 2, pp. 52–55, 1965 (German).
- [23] A. S. Nazmy and A. M. Abdel-Ghaffar, "Non-linear earthquake-response analysis of long-span cable-stayed bridges: theory," *Earthquake Engineering & Structural Dynamics*, vol. 19, no. 1, pp. 45–62, 1990.
- [24] W.-X. Ren and M. Obata, "Elastic-plastic seismic behavior of long span cable-stayed bridges," *Journal of Bridge Engineering*, vol. 4, no. 3, pp. 194–203, 1999.
- [25] D. C. Kent and R. Park, "Flexural members with confined concrete," *Journal of the Structural Division*, vol. 97, pp. 1969–1990, 1971.
- [26] B. A. Zárate and J. M. Caicedo, "Effects of cable dynamics in the modeling of cable-stayed bridges under seismic excitation," *International Journal of Structural Stability and Dynamics*, vol. 15, no. 4, Article ID 1450061, 2015.

## Research Article

# Fatigue Properties of Plain Concrete under Triaxial Tension-Compression-Compression Cyclic Loading

Dongfu Zhao,<sup>1,2</sup> Haijing Gao,<sup>2</sup> Huixuan Liu,<sup>2</sup> Penghe Jia,<sup>2</sup> and Jianhui Yang<sup>3</sup>

<sup>1</sup>Beijing Higher Institution Engineering Research Center of Structural Engineering and New Materials, Beijing University of Civil Engineering and Architecture, Zhanlanguan Road No. 1, Beijing 100044, China

<sup>2</sup>School of Civil and Transportation Engineering, Beijing University of Civil Engineering and Architecture, Zhanlanguan Road No. 1, Beijing 100044, China

<sup>3</sup>School of Civil Engineering, Henan Polytechnic University, No. 2001, Century Avenue, New District, Jiaozuo 454000, China

Correspondence should be addressed to Haijing Gao; baboon007@126.com

Received 10 November 2016; Revised 8 January 2017; Accepted 1 February 2017; Published 21 February 2017

Academic Editor: Paulo B. Gonçalves

Copyright © 2017 Dongfu Zhao et al. This is an open access article distributed under the Creative Commons Attribution License, which permits unrestricted use, distribution, and reproduction in any medium, provided the original work is properly cited.

Fatigue tests were performed on plain concrete under triaxial tension-compression-compression (T-C-C) cyclic loading with constant and variable amplitude using a large multiaxial machine. Experimental results show that, under constant amplitude fatigue loads, the development of residual strain in the fatigue loading direction depends mostly on the lateral compressive stress ratio and is nearly independent of stress level. Under variable amplitude fatigue loads, the fatigue residual strain is related to the relative fatigue cycle and lateral compressive stress ratio but has little relationship with the loading process. To model this system, the relative residual strain was defined as the damage variant. Damage evolutions for plain concrete were established. In addition, fatigue damage analysis and predictions of fatigue remaining life were conducted. This work provides a reference for multistage fatigue testing and fatigue damage evaluation of plain concrete under multiaxial loads.

## 1. Introduction

In practice, many concrete structures such as offshore platforms, nuclear reactor pressure containers, and bridges are subjected to repeated loading amplitudes in complex multiaxial stress states during normal use. Thus, it is important to understand fatigue damage accumulation in concrete under multiaxial variable amplitude stresses and various stress ratios. In the last few decades, many researches have been carried out to study the fatigue properties of plain concrete (PC) under uniaxial and multiaxial compressive loads. Because the development of multiaxial fatigue test system technology is difficult and with high cost and several key technical problems exist in the experiment, to date, a few works have been dedicated to investigating multiaxial tension and compression fatigue properties. Park et al. [1] used thin fire-damaged concrete discs to evaluate tensile strength and found that the tensile strength could be effectively estimated from the HNP without consideration of the

mix proportion. He et al. [2, 3] focused on the multiaxial mechanical properties of plain recycled aggregate concrete (RAC) and found that the ratio of triaxial fatigue strength to the corresponding uniaxial compressive strength for the three strength grades of RAC was higher than that of conventional concrete. Mun et al. [4] examined the fatigue stress-strain response of different concrete mixtures under compressive cyclic loadings with maximum and minimum stress levels. Shi et al. [5] reported that the tensile strength and secant modulus of large aggregate concrete under triaxial T-C-C increase with the increase of strain rate but decrease with the increase of lateral compressive stress. Subramaniam et al. [6] studied the fatigue behavior of concrete subjected to combined stresses in the T-C region of the biaxial stress space and found that the decrease in rotational stiffness at failure for the constant amplitude fatigue loading was comparable to the corresponding load in the postpeak part of the quasistatic response. Shiming and Yupu [7] studied on biaxial T-C strength and found that tensile compressive strength

increases with the increase of strain rate when the lateral tensile stress is constant and the tensile compressive strength decreases with the increase of lateral tensile stress. Yan et al. [8] tested the dynamic properties of concrete materials under both high strain rates and triaxial stress states. It was pointed out that the strain rate effects on maximum strength under triaxial stress states decrease with an increase in confining stress. Only Yang et al. [9] investigated the fatigue properties of concrete in tension under single and bilateral pressure of variable amplitude, determining fatigue life and residual strain. Based on the cyclic stress-strain curve, fatigue deformation modulus was defined. Accordingly, a damage model was established through the relationship between the ratios of fatigue deformation modulus and the number of cycles. Above all, we can see that the researches on plain concrete for fatigue properties under triaxial T-C-C loading are rare, so it has a realistic significance for us.

Fatigue cumulative damage is one of the main concerns when using PC, and the P-M linear fatigue cumulative damage criterion is still the most widely used model. On this basis, most studies have included research on the linear damage of PC. Studies have validated and discussed the damage variant  $D = \sum(n_i/N_i)$ . Subramaniam et al. [6] recommended that damage in concrete subjected to biaxial fatigue loading in the T-C region through torsion is localized, the damage localizes to a single crack, and the observed overall response is governed by crack growth. The load-deformation response obtained from quasistatic loading acts as the envelope failure curve for fatigue loading considering decrease in rotational stiffness. Peiyin et al. [10] discussed the laws and characteristics of fatigue residual strain, defined the damage variable, and carried out damage accumulation and evolution rules. In addition, a model of fatigue damage was established and verified using experimental results. These investigations focused on the nonlinear cumulative fatigue damage to concrete. The fatigue damage evolution equations were defined using other parameters such as strain, strength, and elastic modulus as part of the damage variant. Chen et al. [11] reported the effects of stress state on the dynamic compressive strength and the dynamic damage evolution process of concrete using a split Hopkinson pressure bar and ultrasonic technique. Results showed that dynamic damage evolutions are accelerated with an increase in strain rate and are delayed significantly under confined pressure. Byung [12] introduced the cumulative damage theory of concrete under variable amplitude fatigue loading condition. Yang et al. [9] investigated the properties of concrete in tension under single and bilateral pressure of variable amplitude fatigue, working out fatigue life and residual strain. Based on the cyclic stress-strain curve, fatigue deformation modulus was defined. Accordingly, a damage model was established through the relationship between the ratios of fatigue deformation modulus and the number of cycles. Cao et al. [13] considered more than the fatigue residual strain of concrete when determining the damage variant. Steady deformations and smaller discreteness at the ultimate residual strain were observed when considering residual strain on the concrete fatigue loading direction. Thus, the unrecoverable degree of microplastic deformation and microcracks can be

determined. This model better reflects the properties of the material than the method of maximum strain for concrete in the fatigue loading direction.

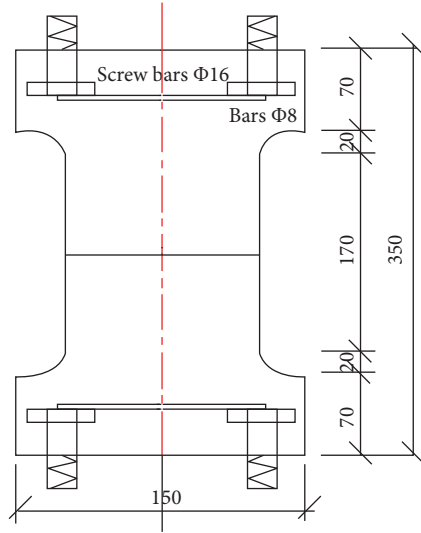
Testing of the triaxial T-C-C fatigue properties was performed using a triaxial testing machine capable of developing three independent compressive or tensile forces at Dalian University of Technology. Fatigue residual strain was recorded during both constant and varying amplitude fatigue processes. The relative residual strain was defined as the damage variant, updates were proposed to the corresponding fatigue damage equation, and the multistage fatigue damage model under triaxial T-C-C loading was established. This work provides a reference for multistage fatigue testing and fatigue damage evaluation of concrete under multiaxial loads.

## 2. Materials and Experimental Procedures

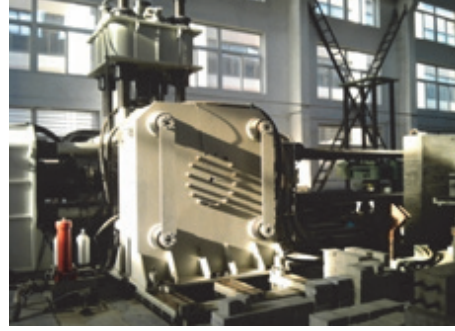
*2.1. Casting and Curing of Specimens.* The constituent proportions within the mix used experimentally were cement : sand : stone : water = 383 : 663 : 1154 : 193 (kg/m<sup>3</sup>). During testing, the ends of the specimen bulk and the testing machine load head were connected by tightening nuts. This transmitted the tensile strength of the machine through the screw, which was then passed to the specimen in order to test volatility in tension fatigue loading. Specimens were created by casting in wooden molds and compacted slightly by a vibrating table. After 24 hours, specimens were removed from molds and then cured at 20 ± 3°C and 95% relative humidity for 28 days covered with grass. Specimens were tested 90 days after cure by the test method of Chinese standard GB/T 17671-1999 [14].

Variable cross-section prism specimens were used for testing based on experimental requirements, fatigue performance, specimen installation, and references available at home and abroad. As shown in Figure 1, lateral pressure can be applied to two pairs of sides when testing a prism shaped specimen. The specimens tested measured 150 mm × 150 mm × 350 mm. In order to reduce stress concentrations, both ends of the specimen were embedded with four Φ16 steel screws, and the end of the screw was embedded within the specimen by Φ8 steel welded connections. The same batch of concrete was used to create six or more 150 mm × 150 mm × 150 mm standard cubes, which were used to measure the strength for multiaxial tests and determine strength class [15].

*2.2. Testing Load Patterns.* Fatigue tests were performed on plain concrete subjected to constant and variable amplitude triaxial T-C-C cyclic loading, and the lateral pressure stresses  $S_{\max}$  are 0.25 $f_t$  and 0.50 $f_t$ .  $S$  is the stress level of fatigue,  $S_{\max} = \sigma_{\max}/f_t$ ,  $S_{\min} = \sigma_{\min}/f_t = 0.10$ , and  $f_t$  is the uniaxial tensile strength of 150 mm × 150 mm × 300 mm prism. Constant amplitude fatigue of maximum stress was varied from 0.25 $f_t$  to 0.75 $f_t$ , and variable amplitude fatigue procedures included tests with two and three stages. The loading mode is shown in Figure 2, where loading frequency was 5 Hz. Cyclic loading was applied using a sine wave waveform and the minimum stress level. Load patterns are shown in Table 1.



(a) Specimen size and shape



(b) The large-scale static and dynamic multiaxial testing machine



(c) Specimens under multiaxial loads

FIGURE 1: Machine and specimen.

TABLE 1: Test results for constant-amplitude cyclic loading.

Lateral stress ratio		$S_{\max}$	Fatigue life					
$\sigma_2/f_c$	$\sigma_3/f_c$		$N_f$			$\bar{N}_f$		
0.25	0.25	0.75	210	121	89	75	43	108
		0.65	16188	8903	5117	1547	369	6425
		0.55	950477	783912	361760	137334	32729	453242
0.25	0.50	0.60	171	102	72	46	21	82
		0.50	20387	9753	7415	1110	336	7800
		0.40	1453275	1150119	785733			1129709
0.50	0.50	0.45	1276	871	625	389	207	674
		0.35	348663	150744	98146	51405	17592	133310
		0.25						

Note.  $\bar{N}_f$  is the average fatigue life.

**2.3. Testing Methods.** Deformation of the specimen was recorded within a range of  $\pm 5$  mm using displacement sensors. Three layers of plastic membrane with Mobil lubricants were placed between the compressive loading plate and the specimen as friction-reducing pads [2, 3]. After the specimen was placed in the appropriate position, first execute visual

alignment and preload 10 kN static load in the vertical direction. Moreover, a larger static load was applied on specimens to complete the horizontal direction centering controlling. Then, preload the same proportion more than three times repeatedly in three directions, so that specimen with the loading plate contact surface compaction and load

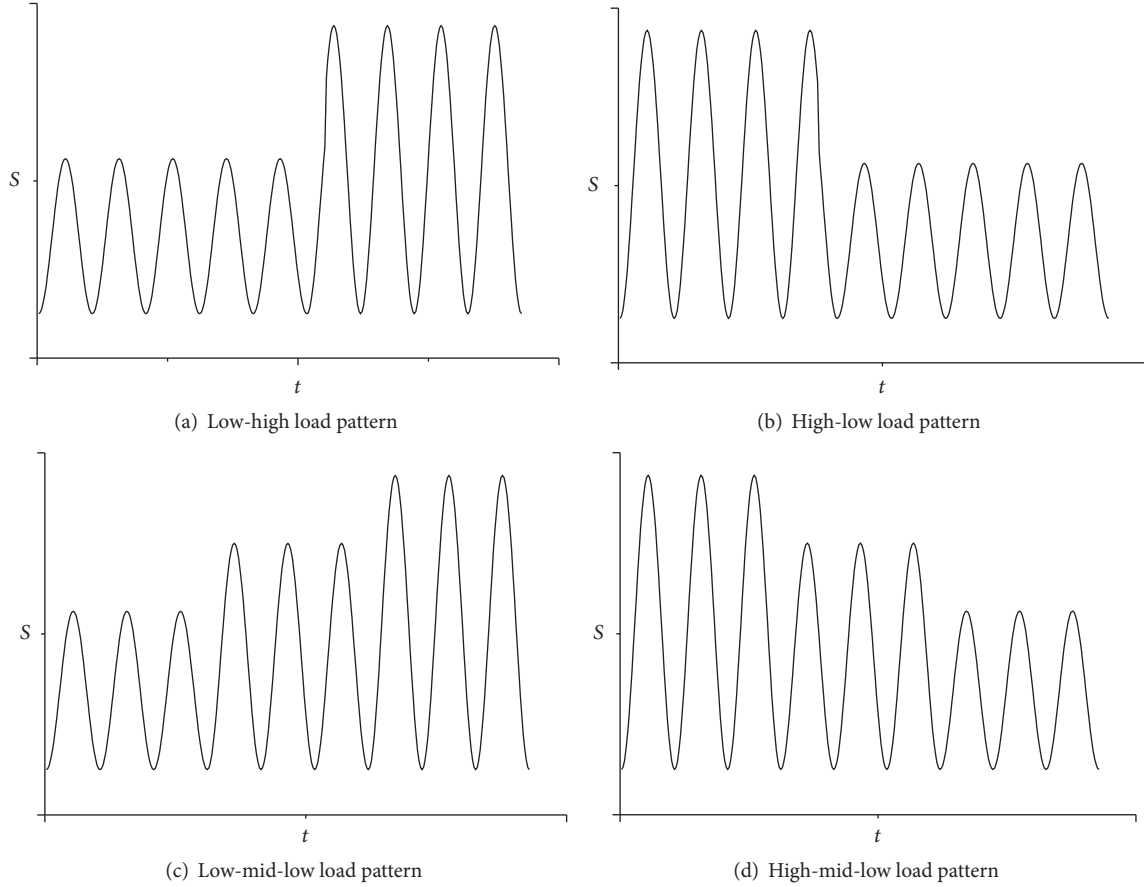


FIGURE 2: Load patterns of variable amplitude multistage fatigue tests.

can be appropriately increased to 20~30 kN. Complete the specimen in the geometric centering controlling and fix it with moderate force, gradually tightening evenly eight screws at the upper and lower edges of the specimen. Finally, use a small hammer to tap specimen or load head, through the rotation of globe hinge to adjust mechanical alignment of specimen [16].

### 3. Test Results and Discussions

**3.1. Fatigue Life.** Fatigue life was measured on plain concrete and results are shown in Tables 1 and 2. A large number of studies have shown that the fatigue strength of concrete is usually attributed to the establishment of  $S-N$  curve equation (also known as Wöhler equation). The  $S-N$  curve quantitatively describes the relationship between stress level  $S$  and fatigue life  $N$ , and the mathematical expression is

$$S_{\max} = A - B \lg N, \quad (1a)$$

where  $A$  and  $B$  are coefficients. And fatigue  $S-N$  equations under T-C-C constant amplitude loading at various lateral

pressures were analyzed using the linear regression method proposed below:

$$S_{\max} = -0.0519 \lg N + 0.8388 \quad \left( \frac{\sigma_2}{f_c} = 0.25; \frac{\sigma_3}{f_c} = 0.25 \right), \quad (1b)$$

$$S_{\max} = -0.0427 \lg N + 0.6642 \quad \left( \frac{\sigma_2}{f_c} = 0.25; \frac{\sigma_3}{f_c} = 0.50 \right), \quad (1c)$$

$$S_{\max} = -0.0412 \lg N + 0.5582 \quad \left( \frac{\sigma_2}{f_c} = 0.50; \frac{\sigma_3}{f_c} = 0.50 \right), \quad (1d)$$

where  $S_{\max}$  is the maximum stress level of fatigue,  $N$  is fatigue life,  $f_c$  is uniaxial compressive strength of a concrete prism,  $\sigma_1$  is the cyclic tensile stress,  $\sigma_2$  and  $\sigma_3$  are lateral compressive stresses,  $\sigma_3 < \sigma_2 < \sigma_1$ , and the compressive stress is negative but tensile stress is positive. The correlation coefficients  $R^2$  of the above equations are 0.945, 0.965, and 0.948, respectively. Figure 3 shows the corresponding  $S-N$  scattergram.

TABLE 2: Test data of fatigue for variable amplitude.

Specimen number	Fatigue life		$D$	$\epsilon_0$ $\mu\epsilon$	Specimen number	Fatigue life			$D$	$\epsilon_0$ $\mu\epsilon$
	$n_1$	$n_2$				$n_1$	$n_2$	$n_3$		
25250101	52203	24	0.45	215	25250301	52203	1004	121	1.79	255
25250102	52203	308	3.48	234	25250302	52203	1004	75	1.30	248
25250103	52203	272	3.09	238	25250303	52203	1004	13	0.64	192
25250104	52203	43	0.66	247	25250304	52203	1004	360	4.33	244
25250105	52203	640	7.01	204	25250305	52203	1004	29	0.81	232
25250201	19	816980	3.33	217	25250401	19	1004	1498232	6.24	234
25250202	19	185321	0.91	213	25250402	19	1004	300168	1.65	229
25250203	19	114847	0.64	225	25250403	19	1004	70474	0.77	203
25250204	19	91356	0.55	199	25250404	19	1004	49593	0.69	237
25250205	19	1934129	7.61	243	25250405	19	1004	109627	0.92	226
25500101	304705	110	1.86	327	25500301	304705	1060	67	1.52	308
25500102	304705	17	0.45	319	25500302	304705	1060	315	5.27	314
25500103	304705	43	0.85	313	25500303	304705	1060	16	0.74	301
25500104	304705	233	3.73	306	25500304	304705	1060	32	0.99	335
25500105	304705	59	1.09	286	25500305	304705	1060	143	2.67	327
25500201	13	2559519	1.88	310	25500401	13	1060	594174	0.89	334
25500202	13	700821	0.66	302	25500402	13	1060	1218818	130	305
25500203	13	594174	0.59	275	25500403	13	1060	289469	0.69	307
25500204	13	1767287	1.36	293	25500404	13	1060	319940	0.71	320
25500205	13	>2500000	>1.88	319	25500405	13	1060	>2500000	>2.14	261
50500101	17171	1057	2.08		50500201	112		340844	4.17	400

Note.  $D = \sum(n_i/N_i)$ ,  $\epsilon_0$  is the ultimate strain of specimen damage. Specimen numbering methods xxyzztt: xxyy means the two directions of lateral compressive stress ratio, where 2550 indicates that one direction of lateral compressive stress ratio  $\sigma_2/f_c$  is 0.25, another  $\sigma_3/f_c$  is 0.50; zz represents the amplitude loading condition; 01, 02, 03, and 04 are four testing loading conditions for low-high, high-low, low-medium-high, and high-medium-low, respectively; tt represents the sample number to each operating mode.

3.2. *Linear Fatigue Damage Analysis.* Miner [17] performed pioneering work on the amplitude fatigue linear cumulative damage rule, the P-M criterion as shown below:

$$D = \sum_{i=1}^k D_i = \sum_{i=1}^k \frac{n_i}{N_i} = 1. \quad (2)$$

In this paper, Miner experimentally verified the P-M criterion. Table 3 shows the values obtained by this work.

As shown in Table 3, our experimental result for the value of  $D$  is higher than predicted. However, considering factors that influence multiaxial fatigue, the values of  $D$  obtained can be considered within the normal range. Moreover, results indicate that the P-M criterion for multiaxial amplitude fatigue has certain limitations. These limitations are mainly caused by difficulty in satisfying the prerequisites of the principle, which are as follows: each cycle of the energy dissipation is equal under constant amplitude stress level, cumulative damage cannot be influenced by the past loading process, and the fatigue life of concrete would not be affected by variable amplitude loading order.

## 4. Nonlinear Damage Analysis

4.1. *Residual Strain.* Residual strains were measured during strain development along the fatigue loading direction, and

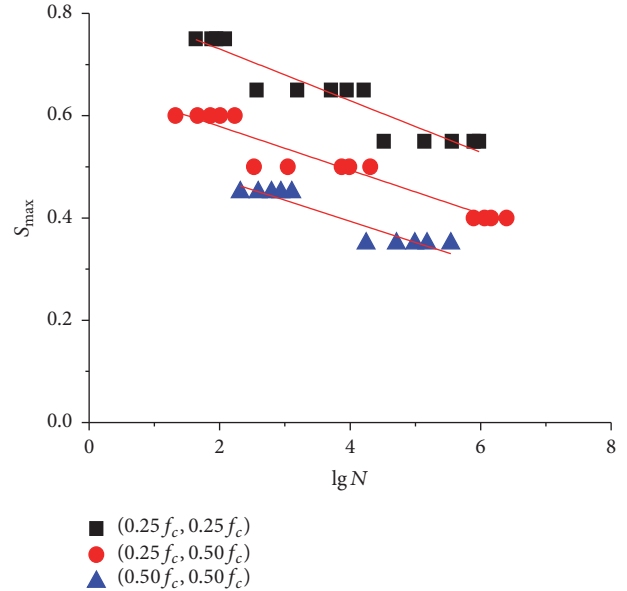


FIGURE 3: S-N Scatter-gram.

results are shown in Figures 4 and 5. As shown, under triaxial T-C-C constant amplitude cyclic loading, the development of residual strain of plain concrete in the fatigue

TABLE 3: Value  $D$ .

	[10]	[20]	[21]	[12]	This paper
Max	2.94	95.72	1.11	3.26	7.61
Min	0.36	0.01	0.21	0.38	0.31
Avg.	1.20	8.32	0.53	1.27	1.87

direction depends mainly on lateral compressive stress and is not significantly related to the stress level. The maximum strain development of constant amplitude fatigue follows an obvious three-stage rule, which is defined by the crack initiation, crack stable expansion, and crack propagation. The ratio of these three stages has a great correlation with the lateral pressure level, especially at a high lateral pressure, and the second stage of the maximum strain development is obviously longer, while the third stage becomes shorter and the specimen rapidly deteriorates. The strain development law [18, 19] follows the same pattern for uniaxial fatigue residual strain, but the value of the fatigue residual strain is larger than uniaxial. Under variable amplitude fatigue loads, the fatigue residual strain is not associated with the loading process. Development of fatigue residual strain is stable whether under variable amplitude loading or constant amplitude loading. The same is true for specimens loaded in the uniaxial direction.

Based on Figure 4, regression equations under different lateral stress ratios were analyzed using a nonlinear regression method for residual strain  $\varepsilon_r$  and relative fatigue cycle  $n/N$  as shown:

$$\varepsilon_r = 109.0 \left(\frac{n}{N}\right)^3 - 220.0 \left(\frac{n}{N}\right)^2 + 164.6 \left(\frac{n}{N}\right) \quad (3a)$$

$$\frac{\sigma_2}{f_c} = 0.25, \quad \frac{\sigma_3}{f_c} = 0.25,$$

$$\varepsilon_r = 173.9 \left(\frac{n}{N}\right)^3 - 328.1 \left(\frac{n}{N}\right)^2 + 236.0 \left(\frac{n}{N}\right) \quad (3b)$$

$$\frac{\sigma_2}{f_c} = 0.25, \quad \frac{\sigma_3}{f_c} = 0.50,$$

$$\varepsilon_r = 246.7 \left(\frac{n}{N}\right)^3 - 442.9 \left(\frac{n}{N}\right)^2 + 302.7 \left(\frac{n}{N}\right) \quad (3c)$$

$$\frac{\sigma_2}{f_c} = 0.50, \quad \frac{\sigma_3}{f_c} = 0.50.$$

Correlation coefficients  $R^2$  of the above equations are, respectively, 0.976, 0.976, and 0.943, all the values of  $R^2$  are greater than 0.90, and it indicates that Formulas (3a), (3b), and (3c) are suitable to express the fatigue T-C-C failure criterion. If relative fatigue cycle  $n/N = 1$ , the extreme fatigue residual strain  $\varepsilon_r^0$  of concrete is, respectively,  $53.6\mu$ ,  $81.8\mu$ , and  $106.5\mu$ . The extreme residual strain  $\varepsilon_r^0$  can be used as a criterion to judge the fatigue damage of plain concrete in corresponding lateral stress ratio.

**4.2. Fatigue Damage Model and Validation.** According to the basic concepts of damage mechanics and the development

laws of residual strain on PC under T-C-C and uniaxial fatigue loading, the fatigue damage was defined as the ratio between the residual strain of concrete  $\varepsilon_r$  and the extreme fatigue residual strain  $\varepsilon_r^0$ ,  $\varepsilon_r/\varepsilon_r^0$ . The damage equation is given by

$$D = \frac{\varepsilon_r}{\varepsilon_r^0} = a \left(\frac{n}{N}\right)^3 + b \left(\frac{n}{N}\right)^2 + c \left(\frac{n}{N}\right), \quad (4)$$

where  $a$ ,  $b$ ,  $c$  are coefficients of the damage equation and relate to fatigue loading method and extreme fatigue residual strain. The relationships between the fatigue damage  $D$  and relative number  $n/N$  of plain concrete under T-C-C loading are shown in Figure 6. Above all, the proposed fatigue damage model can be used for multistage fatigue cumulative damage analysis of plain concrete in uniaxial and T-C-C loading. This analysis can also be used to predict remaining fatigue life of the sample.

The equivalent damage value  $D_e$  and residual fatigue life prediction value  $N_{2e}$  or  $N_{3e}$  of PC at the lateral compressive stress ratio of 0.50 under T-C-C loading are shown in Table 4;  $n_{20}$  is the fatigue life of the residual strain under two-stage loading;  $n_{10}/N_{1e}$  and  $n_{20}/N_{2e}$  are the corresponding relatively equivalent fatigue life of  $\varepsilon_{r1}$  and  $\varepsilon_{r2}$ ;  $N_{2e}$  ( $N_{3e}$ ) is the remaining fatigue life prediction value (including  $n_{20}$ );  $D_e$  is the equivalent damage value,  $D_e = n_1/N_{1e} + n_2/N_{2e}$  is the remaining fatigue life.

As shown in Table 4, samples tested with variable amplitude fatigue loading had a maximum equivalent damage value  $D_e$  of 1.92, a minimum of 0.65, and an average of 1.08. In comparison, the maximum damage value  $D$  of the P-M criterion (Table 3) is 7.61, the minimum is 0.31, and the average is 1.87 (not including the residual fatigue life of specimens with more than 2.5 million cycles). Meanwhile, the remaining fatigue life prediction values  $N_{2e}$  (two-grade fatigue) or  $N_{3e}$  (three-grade fatigue) are relatively close to the actual remaining fatigue life  $n_2$  or  $n_3$  in Table 2. Figure 7 takes  $N_{2e}$ ,  $N_{3e}$  and  $n_2$ ,  $n_3$  logarithmic, makes  $\lg N_{2e}(\lg N_{3e})$  ordinate, makes  $\lg n_2(\lg n_3)$  an abscissa, and converts the remaining fatigue life prediction values and the corresponding actual values into a scatter plot. If the scatter points are near the diagonal line on both sides, the forecast and experiment values of theory are satisfactory. As shown, the damage model proposed here is sufficiently accurate.

Based on the residual strain  $\varepsilon_r$  and relative fatigue cycles  $n/N$  of (3a), (3b), and (3c), the regression equation under

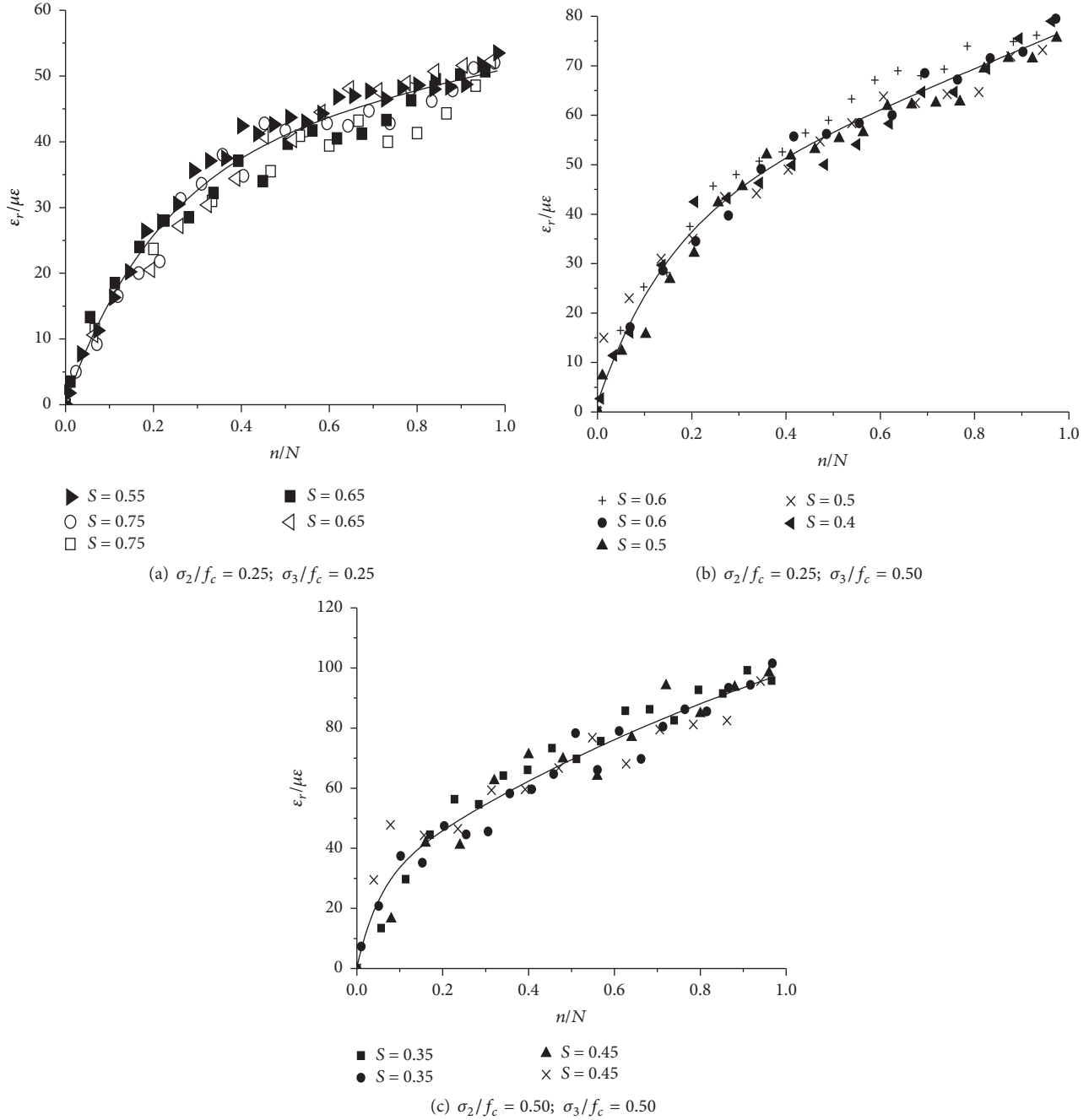


FIGURE 4: Relationship of residual strain and relative fatigue cycle in T-C-C constant amplitude loading.

different lateral stress ratios was analyzed using nonlinear regression as shown below:

$$\begin{aligned}
 D = & \left\{ \left( -\frac{1.24\sigma_2}{f_c} + \frac{0.04\sigma_3}{f_c} + 2.60 \right) \left( \frac{n}{N} \right)^3 \right. \\
 & + \left( \frac{1.82\sigma_2}{f_c} + \frac{1.34\sigma_3}{f_c} - 5.32 \right) \left( \frac{n}{N} \right)^2 \\
 & \left. + \left( -\frac{0.58\sigma_2}{f_c} - \frac{1.39\sigma_3}{f_c} + 3.72 \right) \left( \frac{n}{N} \right) \right\}. \quad (5)
 \end{aligned}$$

Using (5), Figure 8 shows the relationships between the damage variable  $D$  and lateral compressive stress of  $\sigma_2/f_c$ ,  $\sigma_3/f_c$  as well as the spatial relationships in different relative cycle ratios of fatigue ( $n/N = 0.2, 0.4, 0.6, 0.8$ ). The figure axes are the damage variable  $D$  and the lateral compressive stress ratios  $\sigma_2/f_c$ ,  $\sigma_3/f_c$ , respectively.

## 5. Discussion

So far, there have been a lot of researches on uniaxial and multiaxial fatigue of concrete subjected to variable amplitude

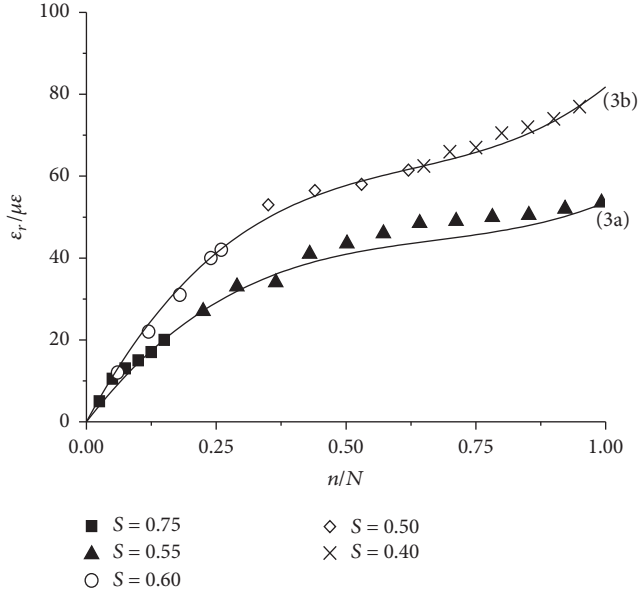


FIGURE 5: Relationship of residual strain and relative fatigue cycle in T-C-C variable amplitude loading.

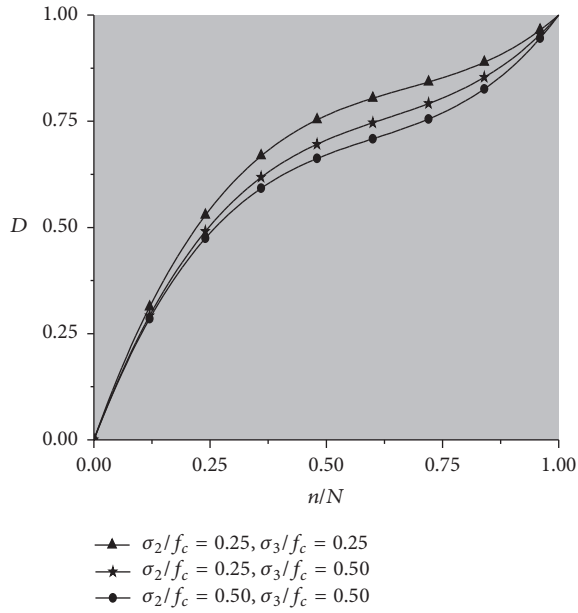


FIGURE 6: Relationship between damage and relative fatigue cycles  $n/N$  in T-C-C loading case.

compression, while little attention has been paid to biaxial and triaxial tension and compression fatigue. The main reason is that the concrete specimen is difficult to achieve repeated tension-compression loading, and the testing key technology is not complete.

- (1) For the multiaxial fatigue test, the physical centering of the sample is very important in the process of installation and testing and is more difficult than in a triaxial fatigue test. Poor alignment will result

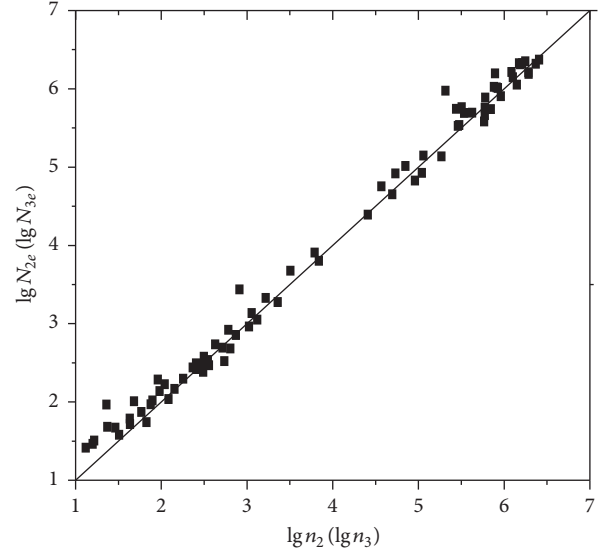


FIGURE 7: Comparison between predicted residual fatigue life and observed ones.

TABLE 4: Variable amplitude fatigue life of prediction.

Specimen number	$D_e$	$N_{2e}$	Specimen number	$D_e$	$N_{3e}$
25250101	0.88	48	25250301	1.44	109
25250102	1.37	241	25250302	0.94	93
25250103	0.88	303	25250303	0.93	26
25250104	0.91	52	25250304	1.29	293
25250105	1.09	479	25250305	1.06	47
25250201	0.89	1037225	25250401	1.51	2113472
25250202	0.91	136286	25250402	0.76	343910
25250203	0.87	140203	25250403	1.11	102601
25250204	1.01	67159	25250404	1.00	44838
25250205	1.36	1548276	25250405	0.72	84152
25500101	0.80	168	25250301	0.84	55
25500102	0.91	32	25250302	1.27	376
25500103	0.98	61	25250303	1.53	29
25500104	1.29	274	25250304	0.85	38
25500105	0.82	74	25250305	1.28	146
25500201	0.97	2350852	25250401	1.09	572043
25500202	1.13	549963	25250402	1.45	1635711
25500203	0.78	458977	25250403	1.22	335639
25500204	1.33	2245031	25250404	0.97	579068
25500205			25250405		
50500101	1.55	916	50500201	0.98	490733
50500102	1.76	330	50500201	1.92	382615
50500103	0.67	137	50500201	1.35	24700
50500104	0.65	542	50500201	0.77	82501
50500105	1.04	2134	50500201	0.63	56662

Note.  $D_e$  is equivalent damage value;  $N_{2e}/N_{3e}$  is the residual fatigue life prediction values.

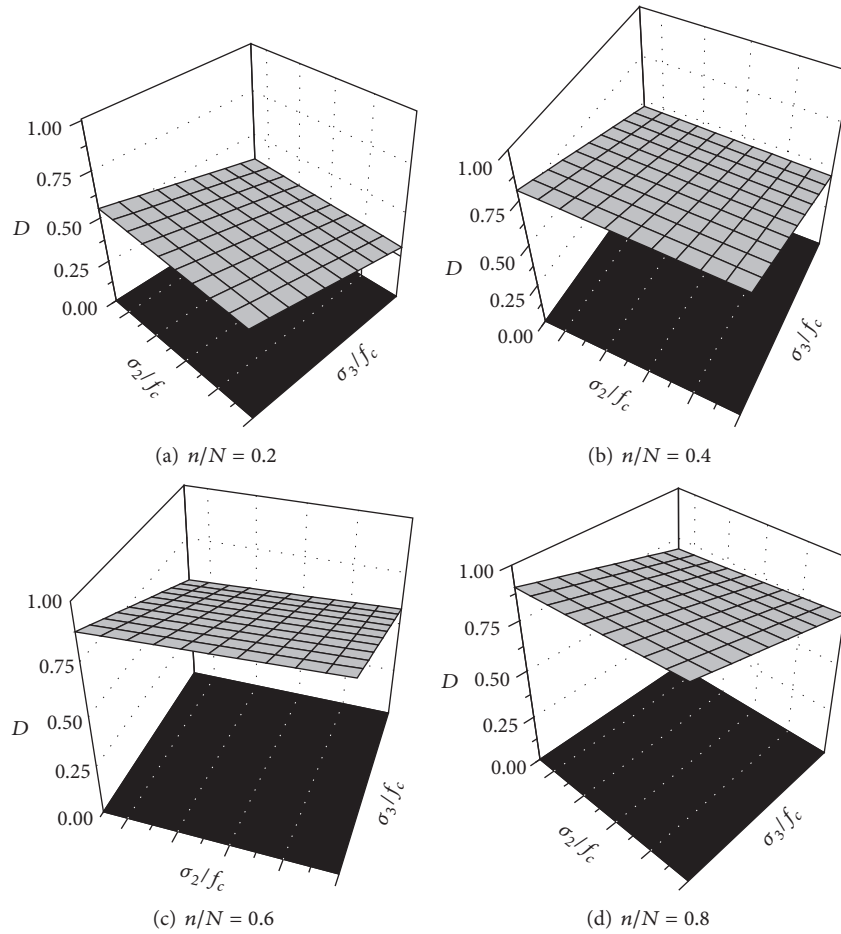


FIGURE 8: Relationship between damage  $D$  and  $\sigma_2/f_c$ ,  $\sigma_3/f_c$ .

in specimen failure and consequently failure of the experiment. During testing, specimens were placed in the appropriate position and visually aligned before applying a 10 kN static preload in the vertical direction. Moreover, a larger static load was applied to the specimens to center the samples horizontally. Finally, the sample was preloaded in the same proportions more than three times in three directions to verify centering in the test apparatus. Preload levels were then increased to 20~30 kN to ensure contact between the loading plate and the specimen. Next, specimens were held in this centered position by gradually and evenly tightening eight screws at the upper and lower edges of the specimen. Fatigue tests were suspended after a dozen cyclic loads, to analyze the output of the deformation data in each direction and verify consistency. Finally, a small hammer was used to tap specimens or load heads as needed to adjust mechanical alignment through rotation of the globe hinge of the specimen in order to obtain valid data.

- (2) As the testing system uses electrohydraulic servo control technology, the system is easily self-excited. Even the original MTS single-axis fatigue testing machine can appear self-excited during testing. Here,

self-excitation refers to the system suddenly operating at a different frequency compared to the load frequency during normal operation or the ability to adjust the loading frequency to produce substantial vibration. To avoid mechanical resonance, the experiment should begin at a lower frequency running for a period of time, so that the direction of the installation of the specimen can be verified. The frequency can be smoothly increased to the ideal test frequency. The system has load control and displacement control in two directions; thus, each direction should be treated similarly to avoid self-excitation. Finally, the test system must be completely independent of the power supply to eliminate interference with other electrical equipment.

## 6. Conclusions

Based on analysis of experimental results from the development of fatigue strain, the following conclusions can be drawn below.

- (1) The development of fatigue residual strain in the fatigue loading direction of PC under triaxial T-C-C

constant amplitude cyclic loading is mainly dependent on the lateral compressive stress ratio and is mostly independent of stress level. The fatigue residual strain under variable amplitude fatigue loading was found to be associated with the relative fatigue cycle and lateral compressive stress ratio but is independent of the loading process. Strain development is as stable as the constant loading amplitude.

- (2) The residual strain  $\varepsilon_r$  and fatigue relative cycle  $n/N$  were used to develop a nonlinear regression model. The ultimate residual strains  $\varepsilon_r^0$  of concrete fatigue damage are, respectively,  $53.6\mu$ ,  $81.8\mu$ , and  $106.5\mu$ . This can be used as a criterion to judge the fatigue damage of plain concrete in corresponding lateral stress ratios.
- (3) Relative residual strain was defined as the damage variant, a damage evolution for plain concrete was proposed, and models for damage analysis and prediction of fatigue life were executed. The failure models developed can be used to predict the residual remaining life of plain concrete under multiaxial fatigue loads. Model predictions and the measured results are in good agreement.
- (4) It is proved that Miner's rule is not applicable to multiaxial loading of plain concrete and has certain limitations for calculating multiaxial amplitude fatigue.

## Competing Interests

The authors declare that they have no competing interests.

## Acknowledgments

The present work was supported by the National Natural Science Foundation of China (no. 51378045) and Open Research Fund Program of Engineering Structure and New Materials of Beijing University Engineering Research Center (Beijing University of Civil Engineering and Architecture). The authors acknowledge the mentioned financial support gratefully.

## References

- [1] S.-J. Park, G.-K. Park, H. J. Yim, and H.-G. Kwak, "Evaluation of residual tensile strength of fire-damaged concrete using a non-linear resonance vibration method," *Magazine of Concrete Research*, vol. 67, no. 5, pp. 235–246, 2015.
- [2] Z.-J. He, W.-L. Cao, J.-X. Zhang, and L. Wang, "Multiaxial mechanical properties of plain recycled aggregate concrete," *Magazine of Concrete Research*, vol. 67, no. 8, pp. 401–413, 2015.
- [3] Z.-J. He and J.-X. Zhang, "Strength characteristics and failure criterion of plain recycled aggregate concrete under triaxial stress states," *Construction and Building Materials*, vol. 54, pp. 354–362, 2014.
- [4] J. Mun, K. Yang, and S. Kim, "Tests on the compressive fatigue performance of various concretes," *Journal of Materials in Civil Engineering*, vol. 28, no. 10, 2016.
- [5] L. Shi, L. Wang, Y. Song, and L. Shen, "Dynamic properties of large aggregate concrete under triaxial loading," *Magazine of Concrete Research*, vol. 67, no. 6, pp. 282–293, 2015.
- [6] K. V. Subramaniam, J. S. Popovics, and S. R. Shah, "Fatigue response of concrete subjected to biaxial stresses in the compression-tension region," *ACI Materials Journal*, vol. 96, no. 6, pp. 663–669, 1999.
- [7] S. Shiming and S. Yupu, "Dynamic biaxial tensile-compressive strength and failure criterion of plain concrete," *Construction and Building Materials*, vol. 40, pp. 322–329, 2013.
- [8] D. Yan, G. Lin, and G. Chen, "Dynamic properties of plain concrete in triaxial stress state," *ACI Materials Journal*, vol. 106, no. 1, pp. 89–94, 2009.
- [9] J. H. Yang, D. F. Zhao, and Y. P. Song, "A study on variable-amplitude fatigue test and damage of concrete in tension and under multi-lateral pressures," *China Civil Engineering Journal*, vol. 38, no. 9, pp. 37–44, 2005 (Chinese).
- [10] L. Peiyin, L. Qingbin, and S. Yupu, "Behavior of concrete under nonproportional biaxial fatigue stresses with one constant," *ACI Materials Journal*, vol. 104, no. 1, pp. 3–12, 2007.
- [11] J. Y. Chen, Z. X. Zhang, H. W. Dong, and J. Zhu, "Experimental study on dynamic damage evolution of concrete under multiaxial stresses," *Engineering Failure Analysis*, vol. 18, no. 7, pp. 1784–1790, 2011.
- [12] H. O. Byung, "Cumulative damage theory of concrete under variable-amplitude fatigue loadings," *ACI Materials Journal*, vol. 88, no. 1, pp. 41–48, 1991.
- [13] W. Cao, Y.-P. Song, and H.-C. Liu, "Fatigue properties of plain concrete under triaxial variable-amplitude tension-compression cyclic loading," *Engineering Mechanics*, vol. 23, no. 3, pp. 31–117, 2006 (Chinese).
- [14] MTCDS, *GB/T 17671-1999: Standard for the Test Method on Cements for Determination of Strength*, MTCDS, Beijing, China, 1999 (Chinese).
- [15] NSCGPRC, "Standard for test method of mechanical properties on ordinary concrete," *GB/T 50081-2002*, NSCGPRC, Beijing, China, 2003 (Chinese).
- [16] D. Zhao, Y. Song, and M. Li, "Multiaxial fatigue experimental apparatus of concrete and relevant technics," *Chinese Journal of Rock Mechanics and Engineering*, vol. 23, no. 2, pp. 187–191, 2004.
- [17] M. A. Miner, "Cumulative damage in fatigue," *Transactions of the ASME*, vol. 67, pp. 159–164, 1945.
- [18] H.-S. Shang, S.-T. Yang, and X.-Y. Niu, "Mechanical behavior of different types of concrete under multiaxial tension-compression," *Construction and Building Materials*, vol. 73, pp. 764–770, 2014.
- [19] H.-S. Shang and G.-J. Ji, "Mechanical behaviour of different types of concrete under multiaxial compression," *Magazine of Concrete Research*, vol. 66, no. 17, pp. 870–876, 2014.
- [20] R. Tepfers, C. Friden, and L. Georgsson, "Study of the applicability to the fatigue of concrete of the palmgren-miner partial damage hypothesis," *Magazine of Concrete Research*, vol. 29, no. 100, pp. 123–130, 1977.
- [21] J. O. Holmen, "Fatigue of concrete by constant and variable amplitude tests," *ACI Journal*, vol. 75, no. 4, pp. 71–110, 1982.

## Research Article

# A Spectrum Detection Approach for Bearing Fault Signal Based on Spectral Kurtosis

Yunfeng Li, Liqin Wang, and Jian Guan

*School of Mechanical Engineering, Harbin Institute of Technology, Harbin, China*

Correspondence should be addressed to Liqin Wang; [lqwang@hit.edu.cn](mailto:lqwang@hit.edu.cn)

Received 2 August 2016; Revised 9 November 2016; Accepted 4 December 2016; Published 19 February 2017

Academic Editor: Angelo M. Tusset

Copyright © 2017 Yunfeng Li et al. This is an open access article distributed under the Creative Commons Attribution License, which permits unrestricted use, distribution, and reproduction in any medium, provided the original work is properly cited.

According to the similarity between Morlet wavelet and fault signal and the sensitive characteristics of spectral kurtosis for the impact signal, a new wavelet spectrum detection approach based on spectral kurtosis for bearing fault signal is proposed. This method decreased the band-pass filter range and reduced the wavelet window width significantly. As a consequence, the bearing fault signal was detected adaptively, and time-frequency characteristics of the fault signal can be extracted accurately. The validity of this method was verified by the identifications of simulated shock signal and test bearing fault signal. The method provides a new understanding of wavelet spectrum detection based on spectral kurtosis for rolling element bearing fault signal.

## 1. Introduction

The rolling element bearing is one of the most important parts in aircraft engines. Many bearing incidents in aircraft engines have indicated that the initial damage of bearing occurred on the surface and subsurface. This initial damage appears as the peeling and develops into spalls eventually [1]. During the performance and reliability testing, the vibration signal can reveal the failure state in time and frequency domain promptly. In order to obtain the fault characteristic parameters of the rolling bearing, a variety of signal processing methods are applied to process the rolling bearing vibration signal. Since wavelet transform has the property of time-frequency localization, it is utilized to detect the signal transients from the raw signal extensively [2–6]. The wavelet transform provides an analysis method both in time domain and in frequency domain, which becomes an important method in the nonstationary signal analysis. It is well known that the similarity exists between Morlet wavelet and the impact response of the attenuation components, and the Morlet wavelet is Gaussian in the frequency domain. In addition to the above factors, the time-frequency structure of the Morlet wavelet is optimal match with the typical transients. Therefore, the Morlet wavelet is more suitable for the extraction of rotating machinery fault signal and the rolling bearing fault diagnosis.

The purpose of wavelet transform is to select the proper frequency band of the correct faulty information and the best filter. Therefore, it is necessary and urgent to select the reasonable resonance frequency band for the demodulation technology. At the same time, an index unaffected by experimental conditions is needed to measure the transform result. Kurtosis is a normalized time domain statistics parameter, which is sensitive to the instantaneous signal. Thus, the spectral kurtosis (SK) is an effective tool to get the fault signals of rolling bearing and the reasonable bandwidth [7, 8]. SK is used to analyze the Gaussian components of the signal and locate these components in the frequency domain. It can be seen as a measurement of the energy distribution at each frequency. The peeling of the faulty bearing produces a non-gauss distribution signal, which can be described by the time averaging statistic. The final purpose of SK is to detect the fault signal characteristics in the filtering results [9–11].

The concept of SK was proposed by Dwyer firstly [12]. Then, it was successfully applied to the rolling bearing resonance peak and resonance band selection by Antoni and Randall [13]. Fast Kurtogram based on band-pass filter and short-time Fourier transform (STFT) has made SK a practical tool for the fault diagnosis [14]. Nevertheless, in order to obtain a maximum value of the spectral kurtosis, the STFT window must be shorter than the spacing between the pulses and longer than the individual pulses. The maximum spectral

kurtosis value corresponding to the band is not always the optimal band by the above method. In order to solve these problems, various kinds of improved algorithms based on spectral kurtosis and other signal processing technologies were presented, such as searching all the possible resonance frequency bands adaptively by shifting and expanding pre-determined Morlet wavelet [15].

In this paper, the Morlet wavelet and SK are combined. The spline curve function is utilized to obtain the optimal wavelet filter range, and different wavelet clusters are designed to detect the impact frequency. Firstly, a group of Morlet wavelet cluster with different quality factor  $Q$  is designed and the spectral kurtosis of the filtered signal is calculated, respectively. Then, the trend of spectral kurtosis is drawn by the spline curve based on a limited number of points. The signal detection range and filter bandwidth are gradually reduced. As a consequence, the accuracy of fault diagnosis is improved by the optimized filter.

## 2. Adaptive Spectral Kurtosis Filtering Based on Morlet Wavelet

**2.1. Morlet Wavelet.** The complex Morlet wavelet is the product of a complex exponential function multiplied by a Gaussian function. The expression of Morlet wavelet is

$$\text{Morl}(t) = \frac{\sigma}{\sqrt{\pi}} e^{-\sigma^2 t^2} e^{i2\pi f_0 t}. \quad (1)$$

Meanwhile, the shape of Gaussian window in the frequency domain can be derived as [16]

$$\text{Morl}(f) = \text{Morl}^*(f) = e^{-(\pi^2/\sigma^2)(f-f_0)^2}, \quad (2)$$

where  $\text{Morl}(f)$  is the fast Fourier transformation of  $\text{Morl}(t)$ . Since  $\text{Morl}(f)$  is real,  $\text{Morl}(f) = \text{Morl}^*(f)$ , and the superscript  $*$  denotes the complex conjugate.  $f_0$  is the center frequency of the wave and  $\sigma$  is waveform parameter that determines its width. For Morlet wavelet, the center frequency  $f_0$ , and shape factor  $\sigma$  affect the shape and location simultaneously. By (1), the corresponding wave shape of Morlet wavelet is shown in Figure 1.

In Figure 1,  $\text{Morl1}$  is the wave of the Gaussian function, and  $\text{Morl2}$  is the complex exponential wave function. They are expressed as

$$\text{Morl1} = e^{-t^2 \sigma^2}, \quad (3)$$

$$\text{Morl2} = e^{i2\pi f_0 t}.$$

According to the Euler formula,  $\text{Morl2}$  can be expressed as  $\text{Morl2} = \cos(2\pi f_0 t) + i \sin(2\pi f_0 t)$ , where  $\text{Re}(\text{Morl2}) = \cos(2\pi f_0 t)$ . If  $t_1$  is half a cycle of  $\text{Morl1}$  and  $t_2$  is a quarter period of  $\text{Re}(\text{Morl2})$ ,  $t_1$  and  $t_2$  can be deduced as

$$\begin{aligned} t_1 &= \frac{\sqrt{\ln m^{-1}}}{\sigma}, \\ t_2 &= \frac{\arccos(m)}{2\pi f_0}, \end{aligned} \quad (4)$$

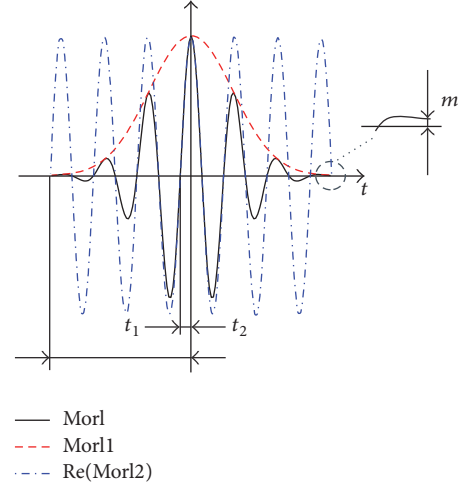


FIGURE 1: Structure of Morlet wavelet.

where  $m$  is the value of Morlet wave endpoint and it is infinitesimal (as shown in Figure 1). It is necessary to ensure that the Morlet wavelet is fluctuant enough and compactly supported. For  $\text{Morl1}$  and  $\text{Morl2}$ , the period ratio  $T_1/T_2$  is

$$\frac{T_1}{T_2} = \frac{2t_1}{4t_2} = \frac{Q\pi \sqrt{\ln m^{-1}}}{\arccos(m)} = k, \quad (5)$$

where  $Q$  is the quality factor,  $Q = f_0/\sigma$ . When  $k_1 \leq k \leq k_2$ , Morlet wavelet at most includes  $k_2 \text{Morl2}$  and at least  $k_1 \text{Morl2}$ . If (5) is introduced into  $k_1 \leq k \leq k_2$ , the expression of the quality coefficient  $Q$  can be obtained as follows:

$$\frac{k_1 \arccos(m)}{\pi \sqrt{\ln m^{-1}}} \leq Q \leq \frac{k_2 \arccos(m)}{\pi \sqrt{\ln m^{-1}}}. \quad (6)$$

The quality coefficient  $Q$  is proportional to the fluctuation of the Morlet wavelet. The larger the quality coefficient  $Q$  is, the smaller the volatility of the Morlet wavelet is and vice versa. Therefore, when  $0.5 \leq k \leq 2$  and  $m = 0.00001$ , the value range of  $Q$  is  $0.0217 \leq Q \leq 0.0869$ .

The corresponding family of wavelets consists of a series of son wavelets, which are generated by dilation and translation from the mother wavelet shown as follows:

$$\text{Morl}_{a,b}(t) = \frac{1}{\sqrt{a}} \text{Morl}\left(\frac{t-b}{a}\right), \quad (7)$$

where  $a$  is the scale factor and  $b$  is wavelet displacement factor (the constant  $1/\sqrt{a}$  is used for energy normalization). The wavelet transform coefficient is defined by the following equation:

$$\begin{aligned} \text{WT}_{(a,b)} &= \int_{-\infty}^{+\infty} x(t) \cdot \text{Morl}_{a,b}^*(t) \cdot dt \\ &= \langle x(t), \text{Morl}_{a,b}(t) \rangle, \end{aligned} \quad (8)$$

where  $\text{Morl}_{a,b}^*(t)$  is the conjugate complex numbers of  $\text{Morl}_{a,b}(t)$  and  $\langle \cdot \rangle$  represents solving convolution.

**2.2. Spline Curve Interpolation.** Since the SK values are not continuous, the spline curve is used to obtain the variation trend of SK on the basis of discrete points. It can provide the basis for optimizing the analysis range.

The function of spline curve interpolation is an approximation of piecewise three polynomials, but it is continuous. Its first- and second-order derivatives are both continuous. The value of  $x_j$  is  $y_j = f(x_j)$  ( $j = 0, 1, \dots, n$ ), spline curve interpolation function is  $S(x)$ , and its first-order derivative  $S'(x_j) = m_j$ .  $S(x)$  can be expressed as

$$S(x) = \sum_{j=0}^n [y_j \alpha_j(x) + m_j \beta_j(x)], \quad (9)$$

where  $\alpha_j(x)$  and  $\beta_j(x)$  are the interpolation function, expressed by

$$\alpha_j(x) = \begin{cases} \left( \frac{x - x_{j-1}}{x_j - x_{j-1}} \right)^2 \left( 1 + 2 \frac{x - x_j}{x_{j-1} - x_j} \right) & x_{j-1} \leq x \leq x_j \quad (j \neq 0) \\ \left( \frac{x - x_{j+1}}{x_j - x_{j+1}} \right)^2 \left( 1 + 2 \frac{x - x_j}{x_{j+1} - x_j} \right) & x_j \leq x \leq x_{j+1} \quad (j \neq n) \\ 0 & \text{Others,} \end{cases} \quad (10)$$

$$\beta_j(x) = \begin{cases} \left( \frac{x - x_{j-1}}{x_j - x_{j-1}} \right)^2 (x - x_j) & x_{j-1} \leq x \leq x_j \quad (j \neq 0) \\ \left( \frac{x - x_{j+1}}{x_j - x_{j+1}} \right)^2 (x - x_j) & x_j \leq x \leq x_{j+1} \quad (j \neq n) \\ 0 & \text{Others.} \end{cases}$$

Under the condition of corresponding boundary, the function  $S(x)$  can be calculated when the equations of  $m_j$  ( $j = 0, 1, \dots, n$ ) were obtained [17].

**2.3. Transient Signal Detection Based on SK.** The nonstationary signal is normally expressed by Wold-Cramér decomposition; that is,

$$Y(t) = \int_{-\infty}^{+\infty} e^{j2\pi ft} H(t, f) dX(f), \quad (11)$$

where the time-varying transfer function  $H(t, f)$  can be interpreted as the complex envelope or complex demodulate of process  $Y(t)$  at frequency  $f$ .

The signal characteristics information in  $H(t, f)$  can be described by the spectral moments, the expression of which is

$$S_{2nY}(f) \triangleq E \{ S_{2nY}(t, f) \} = \frac{E \{ |H(t, f) dX(f)|^{2n} \}}{df} \quad (12)$$

$$= E \{ |H(t, f)|^{2n} \} \cdot S_{2nX}.$$

Under the conditions of ergodicity and stationarity of  $H(t, f)$ , it is easy to prove that

$$S_{2nY}(f) = \langle S_{2nY}(t, f) \rangle_t. \quad (13)$$

The significant property of nonstationary processes is non-Gaussian. For a non-Gaussian process, spectrum accumulation that is greater than or equal to the fourth order is a nonzero value. Therefore, the fourth-order spectral accumulation is adopted, which is defined as

$$C_{4Y}(f) = S_{4Y}(f) - 2S_{2Y}^2(f). \quad (14)$$

The greater the degree of signal deviation from Gaussianity is, the greater its fourth-order spectral accumulation is. Therefore, the energy normalized fourth-order spectral accumulation can be used to measure the peak of the signal process probability density at the frequency  $f$ , that is, spectral kurtosis.

The wavelet coefficients can be obtained by calculating the signal convolution by each row of the filter. The higher value of the wavelet coefficient is, the more similar the wavelet function with the signal waveform will be. The values of the wavelet coefficients are equal to the square of energy. SK is used to measure the energy spectrum. Therefore, SK achieves the maximum value when the waveforms are most similar [16]. Equation (15) gives the value of spectral kurtosis for each filter [18]:

$$\text{kurtosis}(y) \triangleq \frac{C_{4Y}(f)}{S_{2Y}^2(f)} = \frac{S_{4Y}(f)}{S_{2Y}^2(f)} - 2$$

$$= \frac{\text{mean}(H^4(t, f))}{(\text{mean}(H^2(t, f)))^2} - 2. \quad (15)$$

**2.4. Construction of Wavelet Clusters.** Adaptive wavelet method uses spectral kurtosis as the evaluation index of Morlet wavelet filtered results. This method can optimize the latter filter parameters according to the calculation results in the previous step. Each step can improve the calculation accuracy and reduce the searching scope effectively. Compared with other bearing fault diagnosis method based on kurtosis, the accuracy of fault frequency identification and the detection bandwidth are both optimized.

During the construction of octave filter with complex translation Morlet wavelet, the number of filters that cover the entire analysis band is  $M = K \times N$ , where  $K$  is the number of the filters in each octave and  $N$  is the number of the octaves [19].

The central frequency of the filter is expressed as

$$f_{mk} = \frac{f_{\max} - f_{\min}}{(2^{1/K})^n} \quad (n = 1, 2, \dots, M), \quad (16)$$

where  $[f_{\min}, f_{\max}]$  is the frequency band range of the bearing characteristic frequencies in the operating mode. Bandwidth of each filter is expressed by

$$\sigma_{nK} = f_{nK} \cdot \frac{2}{K}. \quad (17)$$

The value of  $K$  and  $N$  and the frequency analysis range  $[f_{\min}, f_{\max}]$  containing all possible fault frequencies are initially set. The center frequencies and bandwidths can be

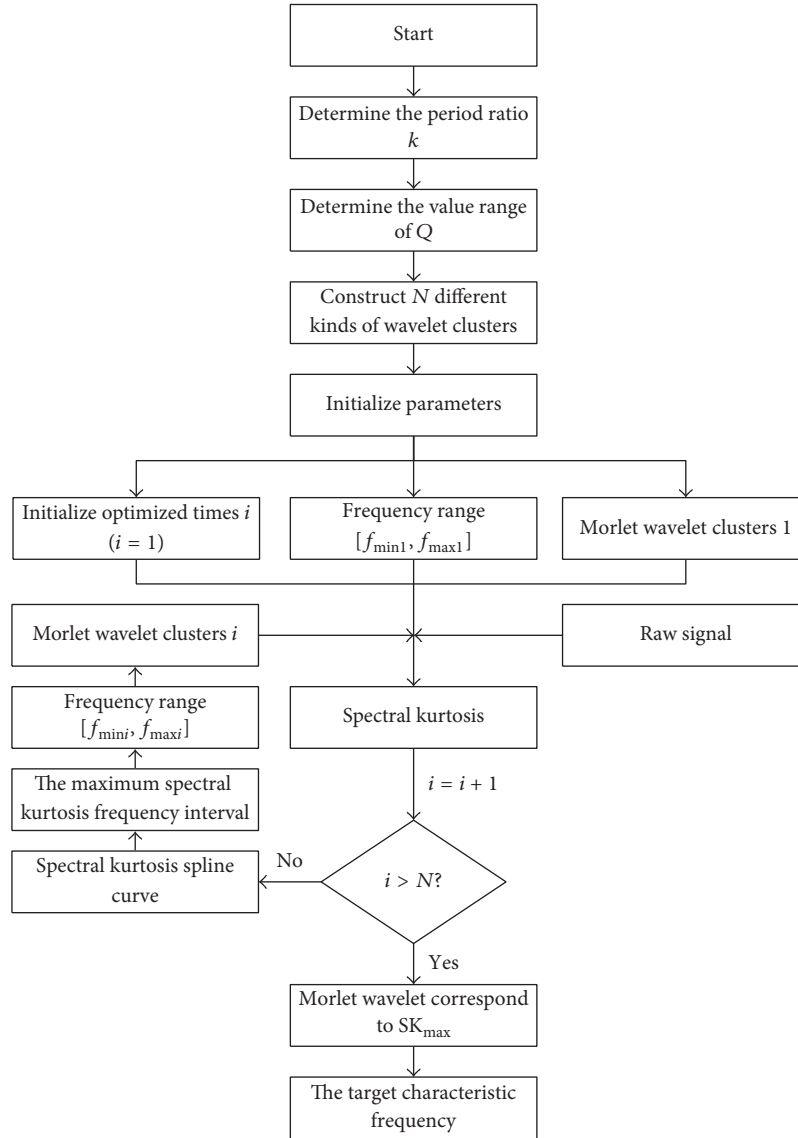


FIGURE 2: Program flow chart.

obtained by (16) and (17). The results are introduced into (1); then,  $N$  Morlet wavelet clusters for signal processing are obtained.

When the frequency analysis range is optimized by the spline curve, the same number of filters is allocated within a smaller frequency range. As a result, the fault center frequency is more accurate and the bandwidth of the filter is smaller.

**2.5. Adaptive Wavelet Method Based on Spectrum Diagnosis.** Obviously, the proportion of the impact component in each filter window is different and it directly influences the spectral kurtosis of the filtering results. The former one is large means that the latter one is also large. The value of the quality factor  $Q$  affects the shape of the wavelet clusters. Therefore, each quality factor corresponds to an optimization process. For a rolling element bearing, the signal components related to the

rotational speed usually cannot be extracted from the time-frequency representation directly. A new proposed method is presented to solve the above problems, as shown in Figure 2:

- (1) In the frequency band range containing the bearing characteristic frequencies  $[f_{\min 1}, f_{\max 1}]$ , it can calculate the spectral kurtosis of the filtered result and describe the spectral kurtosis by the spline curve interpolation along the frequency axis.
- (2) By solving the derivation of the spline curve, the peak containing maximum spectral kurtosis and the valley on both sides of the maximum spectral kurtosis could be obtained, respectively, which is the frequency range of the next optimizing calculation  $[f_{\min 2}, f_{\max 2}]$ .
- (3) The quality factor  $Q$  is changed and the range of Morlet wavelet is reduced to  $[f_{\min 2}, f_{\max 2}]$ ; the spectral

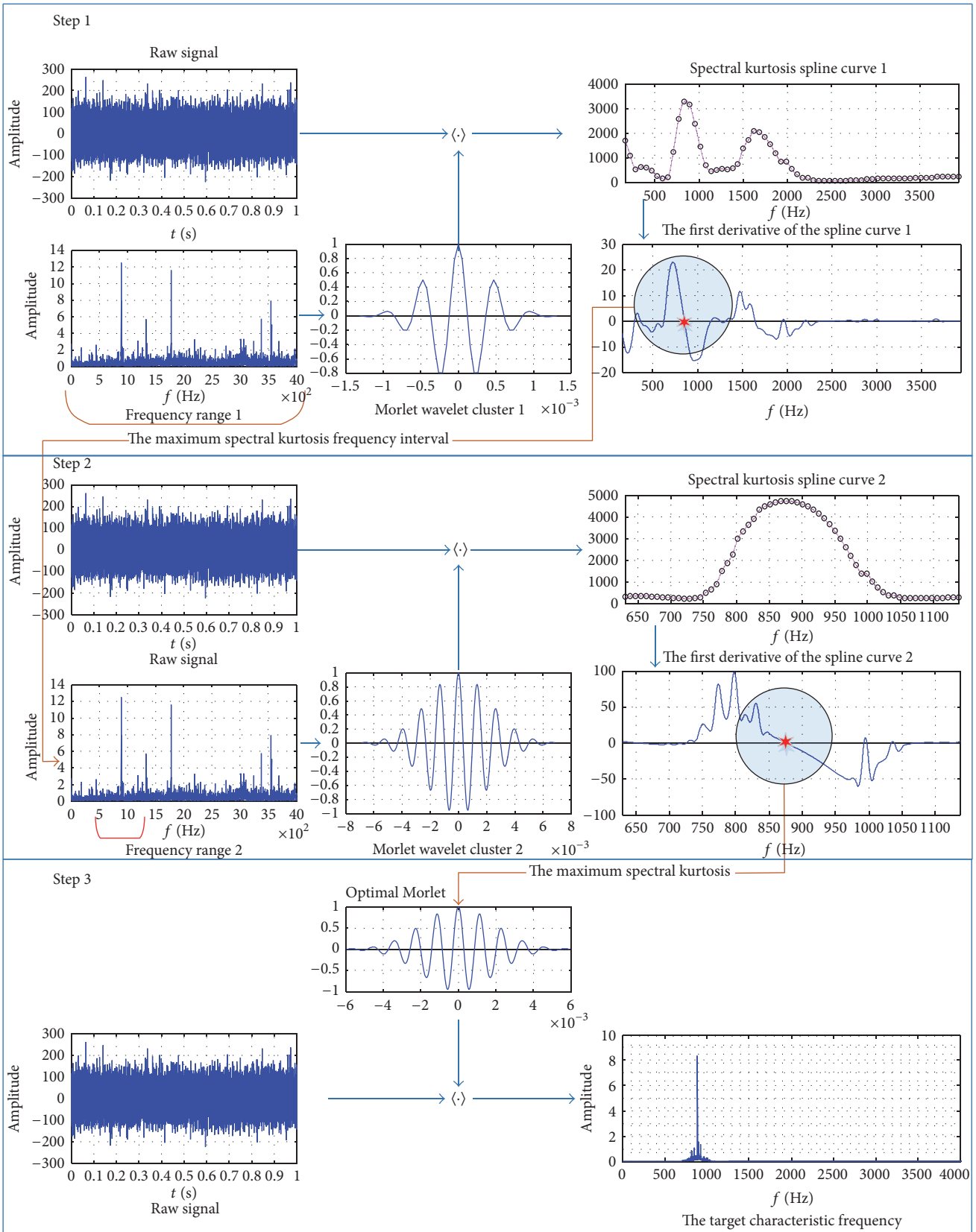


FIGURE 3: Quadratic optimization flow chart.

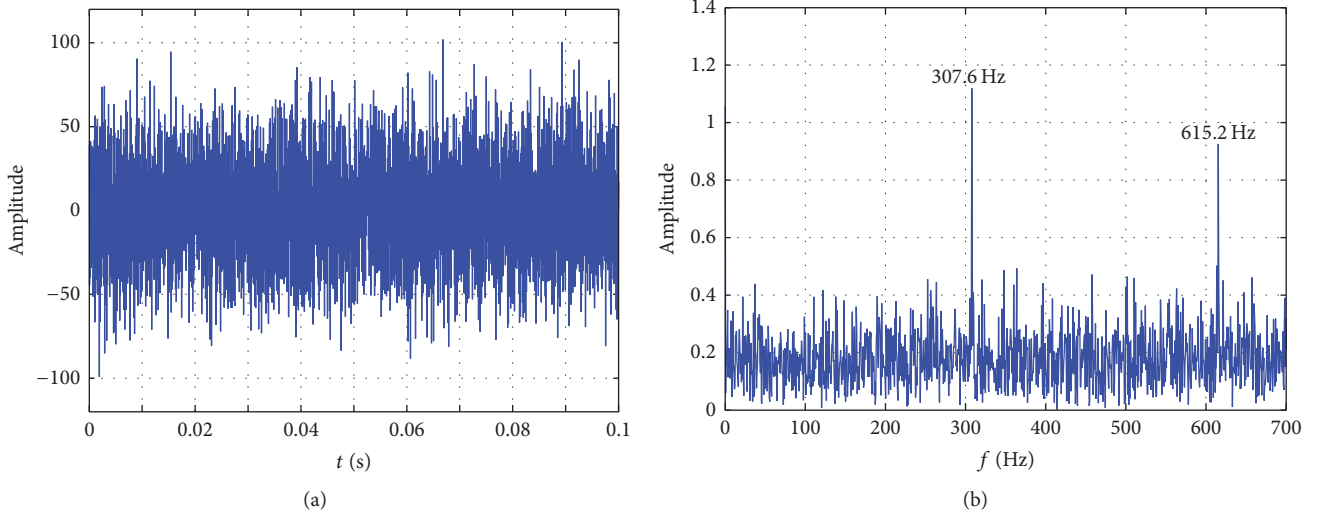


FIGURE 4: (a) Simulation signal in time domain and (b) simulation signal in frequency domain.

TABLE 1: The specific test data.

Parameter	Dimension of fault	Shaft rotation speed	Motor loads	Sampling frequency
Value	0.007 in	29.53 Hz	1 HP	12 kHz

kurtosis of the filter bandwidths can be calculated continually. The spline curve of the spectral kurtosis can be obtained by the spline curve interpolation. However, the bandwidth of the filter is smaller than the last step.

- (4) Steps (2) and (3) are repeated, until the characteristic frequency and its bandwidth are identified. The target can be achieved usually after several optimization calculations.

The calculation procedure of quadratic optimized filter is depicted iconically in Figure 3. The optimized result of Step 1 becomes the process object in Step 2. At the same time, the parameters of the Morlet wave are also adjusted. According to the result of Step 2, the fault signal was extracted in Step 3.

### 3. Methods Validation

**3.1. Simulation Analysis.** The validity of proposed method is verified by the bearing fault simulation signal under strong noise background. The fault simulation signal including a natural frequency of 7000 Hz and a fault signal frequency of 307.6 Hz is generated. A white Gaussian noise of 25 dB is added to the signal and the noise ratio is 5.49, as shown in Figure 4.

The bearing fault simulation signal is detected by the above method. First of all, the spectral kurtosis is calculated along the initial pass band. The impact frequency is 268.8 Hz, and  $SK_{\max} = 310.8$ , as shown in Figure 5(a). Then, the impact frequency is 297.5 Hz, and  $SK_{\max} = 682.1$  in the frequency range narrowed in the previous step, as shown in Figure 5(b). Thirdly, the frequency range is further reduced. The impact frequency is 307 Hz, and  $SK_{\max} = 5652$ , as shown in

TABLE 2: The bearing characteristic frequency.

Inner ring	Outer ring	Rolling element	Cage
159.93 Hz	105.73 Hz	139.21 Hz	11.76 Hz

Figure 5(c). The optimization is close to the impact frequency gradually and the bandwidth is gradually reduced at each time.

Finally, the bearing fault frequency is detected in 307.6 Hz and the bandwidth is about 200 Hz as shown in Figure 6(a). Figure 6(b) shows the result of STFT-based SK [14]. The maximum spectral kurtosis ( $K_{\max} = 0.3$ ) is at Leave 4.5, the center frequency  $f_c = 208.33$  Hz, and the bandwidth  $BW = 416.67$  Hz. The center frequency  $f_c$  does not match better with impact frequency and the bandwidth  $BW$  is too wide to cover the feature frequency band precisely compared with the proposed method.

**3.2. Experimental Tests.** This method is verified by detecting the test data of the Case Western Reserve University Bearing Data Center [20]. In the experiment process, the bearing (SKF6205) was seeded with faults by electrodischarge machining (EDM) previously. A 0.007-inch fault was introduced at the outer raceway of faulted bearings. Then, this bearing was reinstalled into the test motor. Vibration data was recorded for motor loads of 1 horsepower and motor speeds of 1772 RPM. The specific test data is shown in Table 1.

The bearing characteristic frequency under this condition is shown in Table 2. Therefore, the initial analysis band range is designed as [5,300] Hz. The recorded vibration signal is shown in Figure 7.

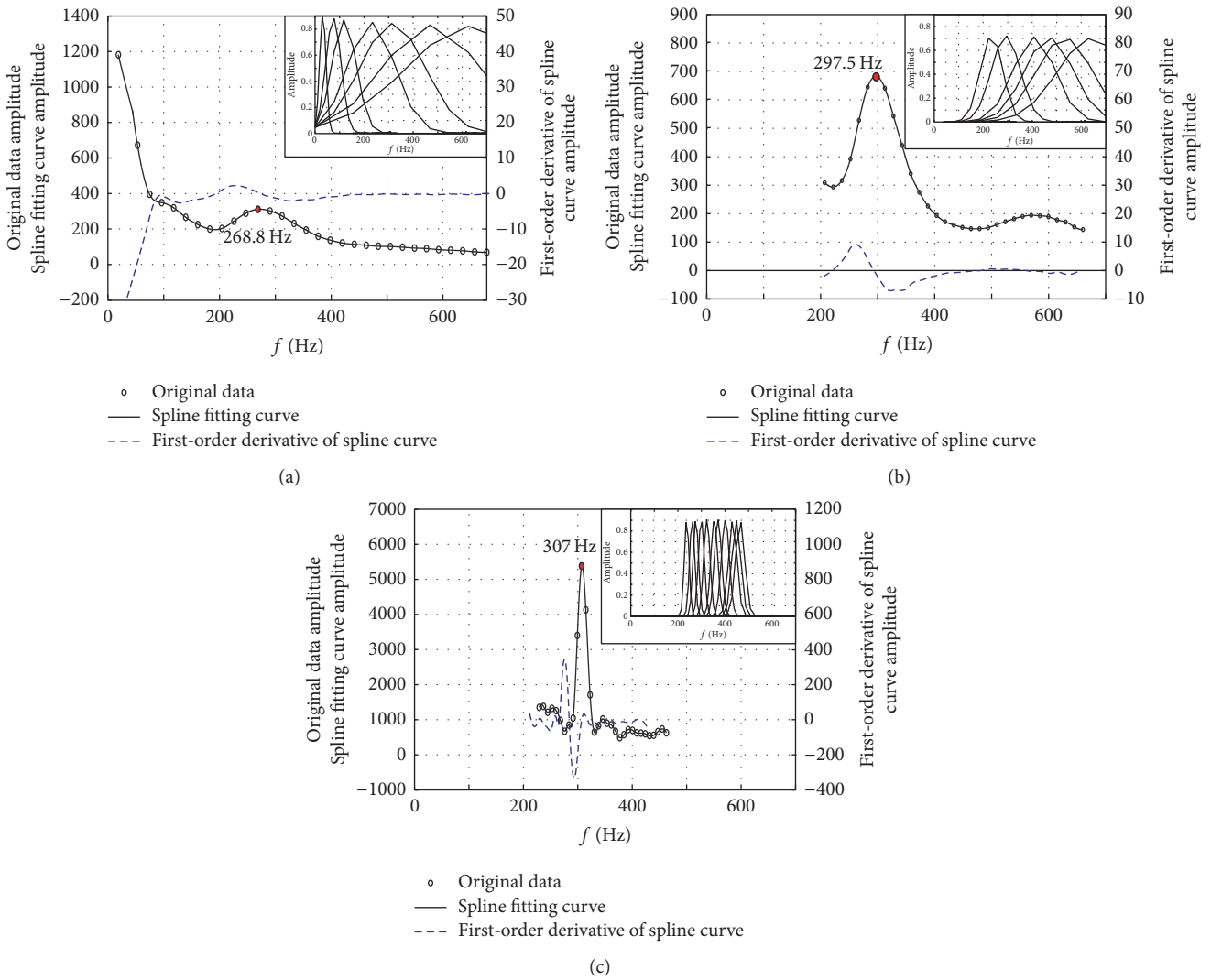


FIGURE 5: (a) The first optimization result of simulation signal. (b) The second optimization result of simulation signal. (c) The third optimization result of simulation signal.

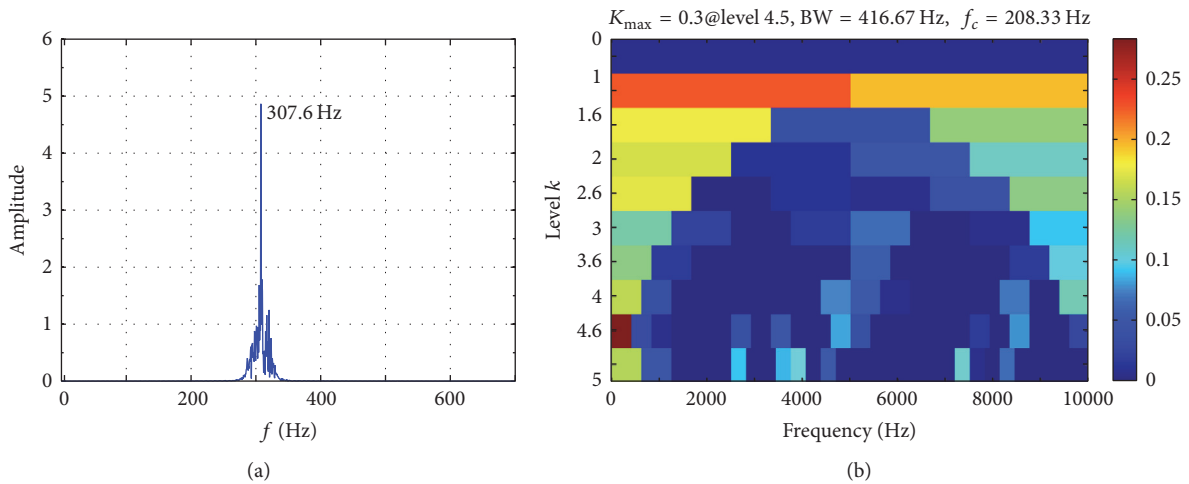


FIGURE 6: (a) Impact signal in frequency domain. (b) Fast Kurtogram of simulation signal verification.

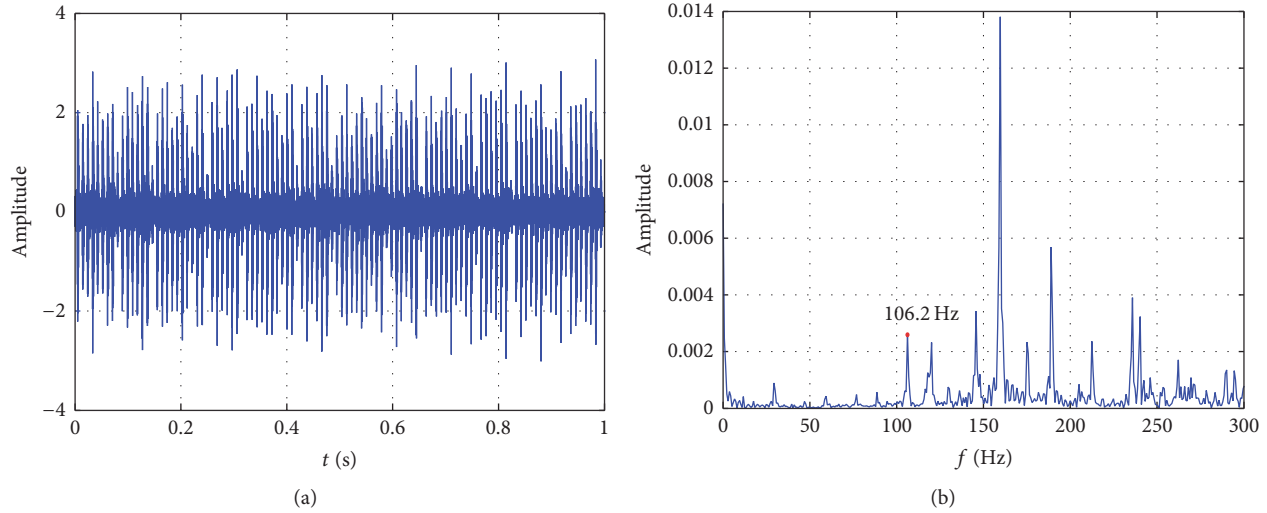


FIGURE 7: (a) The vibration signal in time domain. (b) The vibration signal in frequency domain.

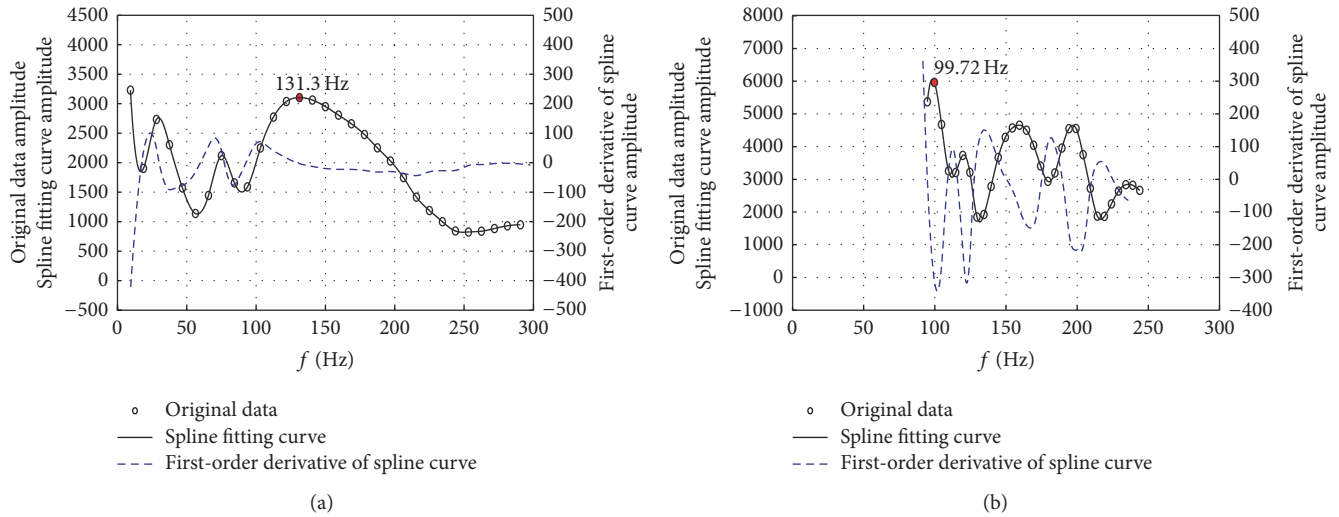


FIGURE 8: (a) The first optimization result of vibration signal. (b) The second optimization result of vibration signal.

The initial maximal spectral kurtosis and the impact frequency are 3104 and 131.3 Hz, respectively. Then, the spectral kurtosis is calculated in the optimized frequency band, and it can be extracted that the impact frequency is 99.72 Hz,  $SK_{\max} = 5959$  in Figure 8.

The fault frequency is 106.2 Hz and the fault signal can be identified clearly in the frequency domain and time domain as shown in Figure 9.

#### 4. Conclusion

The method was based on the similarity between Morlet wavelet and faulty impulse signal. The spectral kurtosis maximum principle was employed into wavelet spectrum detection method for rolling element bearing fault signal

as a criterion. At the initial filtering of the raw signal, the frequency range of the fault signal was found by the spline curve interpolation and its derivation. Different wavelet clusters that produced by the quality factor  $Q$  could optimize the searching range gradually and reduce the filter window width. The fault diagnosis ability of rolling bearing was improved. In conclusion, according to the treatment of the simulation signal and the bearing experimental test signal by the proposed method, it showed that the proposed method recognized the fault signal accurately and had better bearing fault time-frequency recognition feature.

#### Competing Interests

The authors declare that they have no competing interests.

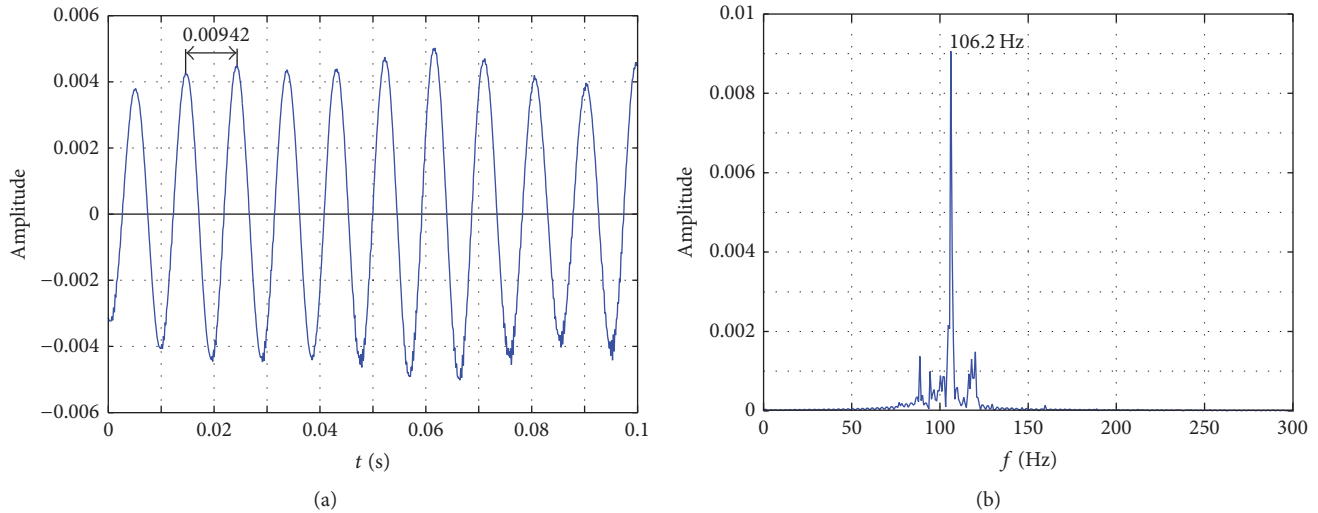


FIGURE 9: (a) Bearing fault signal in frequency domain. (b) Bearing fault signal in time domain.

## Acknowledgments

This research is supported by National Key Basic Research Program of China (973 Program) under Grant no. 2013CB632305 and the Foundation for Innovative Research Groups of the National Natural Science Foundation of China under Grant no. 51521003.

## References

- [1] I. El-Thalji and E. Jantunen, "Fault analysis of the wear fault development in rolling bearings," *Engineering Failure Analysis*, vol. 57, pp. 470–482, 2015.
- [2] S. Prabhakar, A. S. Sekhar, and A. R. Mohanty, "Detection and monitoring of cracks in a rotor-bearing system using wavelet transforms," *Mechanical Systems and Signal Processing*, vol. 15, no. 2, pp. 447–450, 2001.
- [3] Y. Lei, J. Lin, Z. He, and M. J. Zuo, "A review on empirical mode decomposition in fault diagnosis of rotating machinery," *Mechanical Systems and Signal Processing*, vol. 35, no. 1-2, pp. 108–126, 2013.
- [4] N. Tandon and A. Choudhury, "A review of vibration and acoustic measurement methods for the detection of defects in rolling element bearings," *Tribology International*, vol. 32, no. 8, pp. 469–480, 1999.
- [5] P. K. Kankar, S. C. Sharma, and S. P. Harsha, "Fault diagnosis of ball bearings using continuous wavelet transform," *Applied Soft Computing*, vol. 11, no. 2, pp. 2300–2312, 2011.
- [6] C. T. Yiakopoulos and I. A. Antoniadis, "Wavelet based demodulation of vibration signals generated by defects in rolling element bearings," *Shock and Vibration*, vol. 9, no. 6, pp. 293–306, 2002.
- [7] R. B. Randall and J. Antoni, "Rolling element bearing diagnostics—a tutorial," *Mechanical Systems and Signal Processing*, vol. 25, no. 2, pp. 485–520, 2011.
- [8] X. Zhang, J. Kang, L. Xiao, J. Zhao, and H. Teng, "A new improved Kurtogram and its application to bearing fault diagnosis," *Shock and Vibration*, vol. 2015, Article ID 385412, 22 pages, 2015.
- [9] H. Liu, W. Huang, S. Wang, and Z. Zhu, "Adaptive spectral kurtosis filtering based on Morlet wavelet and its application for signal transients detection," *Signal Processing*, vol. 96, pp. 118–124, 2014.
- [10] R. F. Dwyer, "A technique for improving detection and estimation of signals contaminated by under ice noise," *Journal of the Acoustical Society of America*, vol. 74, no. 1, pp. 124–130, 1983.
- [11] R. F. Dwyer, "Use of the kurtosis statistic in the frequency domain as an aid in detecting random signals," *IEEE Journal of Oceanic Engineering*, vol. 9, no. 2, pp. 85–92, 1984.
- [12] R. F. Dwyer, "Detection of non-Gaussian signals by frequency domain kurtosis estimation," in *Proceedings of the IEEE International Conference on Acoustics, Speech and Signal Processing (ICASSP '83)*, pp. 607–610, Boston, Mass, USA, 1983.
- [13] J. Antoni and R. B. Randall, "The spectral kurtosis: application to the vibratory surveillance and diagnostics of rotating machines," *Mechanical Systems and Signal Processing*, vol. 20, no. 2, pp. 308–331, 2006.
- [14] J. Antoni, "Fast computation of the kurtogram for the detection of transient faults," *Mechanical Systems and Signal Processing*, vol. 21, no. 1, pp. 108–124, 2007.
- [15] K. Ding, Z.-D. Huang, and H.-B. Lin, "A weak fault diagnosis method for rolling element bearings based on Morlet wavelet and spectral kurtosis," *Journal of Vibration Engineering*, vol. 27, no. 1, pp. 128–135, 2014.
- [16] N. Sawalhi and R. B. Randall, "Spectral kurtosis optimization for rolling element bearings," in *Proceedings of the 8th International Symposium on Signal Processing and Its Applications (ISSPA '05)*, vol. 2, pp. 839–842, IEEE, August 2005.
- [17] Q. Li and C. Wang, *Numerical Analysis*, Tsinghua University Press, Beijing, China, 4th edition, 2001.
- [18] J. Antoni, "The spectral kurtosis: a useful tool for characterising non-stationary signals," *Mechanical Systems and Signal Processing*, vol. 20, no. 2, pp. 282–307, 2006.
- [19] Y. Guo, H. Zheng, Y. Gao, and T. Wu, "The spectral envelope of rolling bearing analysis based on kurtosis," *Journal of Vibration, Measurement & Diagnosis*, no. 4, pp. 517–539, 2011.
- [20] W. A. Smith and R. B. Randall, "Rolling element bearing diagnostics using the Case Western Reserve University data: a benchmark study," *Mechanical Systems and Signal Processing*, vol. 64-65, pp. 100–131, 2015.

## Research Article

# A Reduced-Order Controller Considering High-Order Modal Information of High-Rise Buildings for AMD Control System with Time-Delay

Zuo-Hua Li,<sup>1</sup> Chao-Jun Chen,<sup>1</sup> Jun Teng,<sup>1</sup> Wei-Hua Hu,<sup>1</sup> Hou-Bing Xing,<sup>2</sup> and Ying Wang<sup>3</sup>

<sup>1</sup>School of Civil and Environment Engineering, Shenzhen Graduate School, Harbin Institute of Technology, Shenzhen 518055, China

<sup>2</sup>China Construction 4th Engineering Division Corp., Ltd., South China Branch, Guangzhou 510660, China

<sup>3</sup>Department of Civil and Environmental Engineering, University of Surrey, Guildford GU2 7XH, UK

Correspondence should be addressed to Jun Teng; [tengj@hit.edu.cn](mailto:tengj@hit.edu.cn)

Received 15 October 2016; Accepted 6 December 2016; Published 19 January 2017

Academic Editor: Paulo B. Gonçalves

Copyright © 2017 Zuo-Hua Li et al. This is an open access article distributed under the Creative Commons Attribution License, which permits unrestricted use, distribution, and reproduction in any medium, provided the original work is properly cited.

Time-delays of control force calculation, data acquisition, and actuator response will degrade the performance of Active Mass Damper (AMD) control systems. To reduce the influence, model reduction method is used to deal with the original controlled structure. However, during the procedure, the related hierarchy information of small eigenvalues will be directly discarded. As a result, the reduced-order model ignores the information of high-order mode, which will reduce the design accuracy of an AMD control system. In this paper, a new reduced-order controller based on the improved Balanced Truncation (BT) method is designed to reduce the calculation time and to retain the abandoned high-order modal information. It includes high-order natural frequency, damping ratio, and vibration modal information of the original structure. Then, a control gain design method based on Guaranteed Cost Control (GCC) algorithm is presented to eliminate the adverse effects of data acquisition and actuator response time-delays in the design process of the reduced-order controller. To verify its effectiveness, the proposed methodology is applied to a numerical example of a ten-storey frame and an experiment of a single-span four-storey steel frame. Both numerical and experimental results demonstrate that the reduced-order controller with GCC algorithm has an excellent control effect; meanwhile it can compensate time-delays effectively.

## 1. Introduction

Active Mass Damper (AMD) can be used to control the dynamic response of highly flexible building horizontally under strong wind or earthquake [1–4]. At present, several problems restrict the development of AMD control system, such as slow calculation speed and long time-delay [5, 6]. They mainly resulted from data acquisition, control force calculation, and actuator response.

Regarding high-rise building structures, the excessive number of degrees of freedom causes the fact that the order of the designed controller based on the original model will be extremely large, and the long control force calculation time induces the fact that the control force is too difficult to fulfill the requirement of real-time control. Hence, it is necessary to build a reduced-order controller to reduce calculation

workload and decrease time-delay [7]. Model reduction [8] is a process that a more complex model will be transformed for a low-order model that meets the requirements of engineering precision. For instance, a dynamic condensation method was proposed for high-rise buildings with Active Tuned Mass Damper (ATMD) control system; the analysis results showed the proposed method was efficient for the reduced-order modeling and reduced calculation time and workload [9]. The dynamic model reduction method was applied to obtain a reduced-order model of an experimental high-rise building with an AMD control system, and numerical simulations showed the low-order controller could be used available to mitigate the vibration [10]. Balanced Truncation (BT) method [11, 12] is more widely used to complete model reduction of high-rise buildings [9, 13]. According to eigenvalues' size of state vectors in a high-rise building, BT method will be used

to reorder these state vectors to form the internal equilibrium model. Partial state vectors that correspond to the small eigenvalues will be omitted. They include high-order modal information of the original structure. However, the omitted state vectors will decrease the accuracy of model reduction method and reduce the control effect of this controller. It is necessary to reconsider high-order modal information in the design process of a reduced-order controller.

In addition to control force calculation time-delay, the compensation design method of the time-delays of data acquisition and actuator response should be considered. Obviously, conventional methods of control include pole-assignment method and linear quadratic regulator cannot be used in time-delay systems. For instance, Linear Quadratic Regulator (LQR) [14] is a suitable control strategy for high-rise buildings, but it requires an accurate mathematical model. If parameter perturbation or time-delay exists in a closed-loop system, its stability is difficult to be guaranteed. Linear Matrix Inequality (LMI) [15] approach is widely used to analyze the stability of time-delay systems [16–19] and to design a feedback controller with compensation gain [20–23]. Although compensation gain needs to guarantee the performance of systems with time-delay, Guaranteed Cost Control (GCC) algorithm [24] is a special LQR control method that is widely used in the fields of electronics, aerospace, mechanical engineering, and automation, and it combines the performance and robustness of nonlinear systems with time-delay [25, 26]. In order to implement GCC for a high-rise building, a key step is to solve a positive-definite solution of Riccati matrix equations. Previously, this problem is based on the Riccati equation method, and several key parameters should be determined in advance. However, methods for searching for the optimal values of these parameters are still lacking. The only method of artificially determined parameters is conservative, and the Riccati equation is solved by iterative methods; it means that the convergence is not guaranteed [27–30]. Combined with LMI approach, the Riccati matrix equations could be solved easily. As a result, the time-delay compensation controller with GCC algorithm can be designed for high-rise buildings based on LMI approach.

In this paper, a low-order controller based on improved BT method is proposed and the structural high-order modal information is considered, and the influence of transfer functions and orders of a low-order model on the control system's performance is analyzed. As a result, the performance of this system can be guaranteed and the order of the controlled structure can be reduced in maximum extent. The design problem of a time-delay compensation control gain based on GCC algorithm can be expressed as a group of nonlinear matrix inequalities. It can be further transformed into a group of linear matrix inequalities (LMIs) through variable substitution method [31]. Finally, the design of the reduced-order controller with GCC algorithm for high-rise buildings is performed to compensate its long time-delay. A numerical example of ten-storey frame and an experiment of a single span four-storey steel frame will be presented to validate the effectiveness of the proposed method.

## 2. The Design Method of Reduced-Order Controller with GCC Algorithm

*2.1. Reduced-Order Controller Design by Improved BT Method.* The state-space equation of an AMD control systems is

$$\begin{aligned}\dot{Z}(t) &= AZ(t) + BU(t), \\ Y(t) &= CZ(t) + DU(t),\end{aligned}\quad (1)$$

where  $A$ ,  $B$ ,  $C$ , and  $D$  are the state matrix, the control matrix, the state output matrix, and the direct transmission matrix, respectively.  $Z$  and  $Y$  are the state vector and the output vector, respectively.  $U$  includes control force and input excitation.

When control force and input excitation are considered separately, (1) can be described as

$$\begin{aligned}\dot{Z}(t) &= AZ(t) + B_2u(t) + B_1w(t), \\ Y(t) &= CZ(t) + D_2u(t) + D_1w(t),\end{aligned}\quad (2)$$

where  $u$  and  $w$  are the control force and the input excitation, respectively.  $A$ ,  $B_1$ ,  $B_2$ ,  $C$ ,  $D_1$ , and  $D_2$  can be expressed as

$$\begin{aligned}A &= \begin{bmatrix} 0 & I \\ -M^{-1}K & -M^{-1}C \end{bmatrix}, \\ B_1 &= \begin{bmatrix} 0 \\ -M^{-1}B_w \end{bmatrix}, \\ B_2 &= \begin{bmatrix} 0 \\ -M^{-1}B_s \end{bmatrix}, \\ C &= \begin{bmatrix} I & 0 \\ 0 & I \\ -M^{-1}K & -M^{-1}C \\ 0 & 0 \end{bmatrix}, \\ D_1 &= \begin{bmatrix} 0 \\ 0 \\ -M^{-1}B_w \\ 0 \end{bmatrix}, \\ D_2 &= \begin{bmatrix} 0 \\ 0 \\ -M^{-1}B_s \\ 1 \end{bmatrix},\end{aligned}\quad (3)$$

where  $M$ ,  $C$ , and  $K$  are the mass, damping, and stiffness matrix of an AMD control system, respectively.  $B_s$  and  $B_w$  are the location matrices of control force and strong wind, respectively.

The balanced realization system can be obtained by transforming the state-space equation of the stable system by BT method. Define

$$Z(t) = TZ_b(t), \quad (4)$$

where  $T$  is the transform matrix.  $Z_b$  is the state vector of the balanced realization system.

By substituting (4) into (2), the state-space equation of the balanced realization system is

$$\begin{aligned}\dot{Z}_b(t) &= A_b Z_b(t) + B_{b2} u(t) + B_{b1} w(t), \\ Y_b(t) &= C_b Z_b(t) + D_{b2} u(t) + D_{b1} w(t),\end{aligned}\quad (5)$$

where  $A_b = T^{-1}AT$ ,  $B_{b2} = T^{-1}B_2$ ,  $B_{b1} = T^{-1}B_1$ ,  $C_b = CT$ ,  $D_{b2} = D_2$ , and  $D_{b1} = D_1$ .

According to [32], the transform matrix  $T$  can be calculated:

$$T = L_c V S^{-1/2}, \quad (6)$$

where  $V$  and  $S$  are the orthogonal and the positive diagonal matrices that can be obtained by applying the singular value decomposition technique for the matrix  $L_o^T L_c$ .  $L_c$  and  $L_o$  are the lower triangular matrix of the controllability and the observability matrices decomposed by Cholesky.

Then the matrix  $S$  can be described as

$$S = \text{diag}(\sigma_1, \sigma_2, \dots, \sigma_n), \quad (7)$$

where  $\sigma_i$  is the diagonal elements that reflect the controllability and observability of the state vector.

The diagonal elements  $\sigma_i$  were rearranged in descending order. When  $\sigma_{r+1} \ll \sigma_r$ ,  $r$  is the reserved order and is twice the number of the structure vibration modes; it means that the states  $Z_{r+1} \sim Z_n$  corresponding to the eigenvalues  $\sigma_{r+1} \sim \sigma_n$  have lower performance of controllability and observability. Only the states  $Z_1 \sim Z_r$  are retained in the balanced realization system. The state-space equation of this system is

$$\begin{aligned}\dot{Z}_{br}(t) &= A_{br} Z_{br}(t) + B_{br2} u(t) + B_{br1} w(t), \\ Y_{br}(t) &= C_{br} Z_{br}(t) + D_{br2} u(t) + D_{br1} w(t),\end{aligned}\quad (8)$$

where  $A_{br} = A_b(1:r, 1:r)$ ,  $B_{br2} = B_{b2}(1:r, :)$ ,  $B_{br1} = E_{b1}(:, 1:r)$ ,  $C_{br} = C_b(:, 1:r)$ ,  $D_{br2} = D_{b2}$ , and  $D_{br1} = D_{b1}$ .

Equation (8) can be described as block matrix:

$$\begin{aligned}\begin{Bmatrix} \dot{Z}_{br}(t) \\ \dot{Z}_{bl}(t) \end{Bmatrix} &= \begin{bmatrix} A_{br} & A_{b12} \\ A_{b21} & A_{b22} \end{bmatrix} \begin{Bmatrix} Z_{br}(t) \\ Z_{bl}(t) \end{Bmatrix} + \begin{Bmatrix} B_{br2} \\ B_{bl2} \end{Bmatrix} u(t) \\ &+ \begin{Bmatrix} B_{br1} \\ B_{bl1} \end{Bmatrix} w(t), \\ Y_b(t) &= [C_{br} \quad C_{bl}] \cdot \begin{Bmatrix} Z_{br}(t) \\ Z_{bl}(t) \end{Bmatrix} + D_{b2} u(t) \\ &+ D_{b1} w(t),\end{aligned}\quad (9)$$

where  $Z_{br}$  and  $Z_{bl}$  are the retained and abandoned state vectors of the balanced realization system, respectively.

Block matrix of (4) is

$$\begin{Bmatrix} Z_{br}(t) \\ Z_{bl}(t) \end{Bmatrix} = \begin{bmatrix} (T^{-1})_{11} & (T^{-1})_{12} \\ (T^{-1})_{21} & (T^{-1})_{22} \end{bmatrix} \begin{Bmatrix} Z_r(t) \\ Z_l(t) \end{Bmatrix}, \quad (10)$$

where  $Z_r$  and  $Z_l$  are the retained and abandoned state vectors corresponding to the original system.

Substituting (10) into (9) leads to

$$\begin{aligned}\begin{Bmatrix} \dot{Z}_{br}(t) \\ \dot{Z}_{bl}(t) \end{Bmatrix} &= \begin{bmatrix} A_1 & A_2 \\ A_3 & A_4 \end{bmatrix} \begin{Bmatrix} Z_r(t) \\ Z_l(t) \end{Bmatrix} + \begin{Bmatrix} B_{br2} \\ B_{bl2} \end{Bmatrix} u(t) \\ &+ \begin{Bmatrix} B_{br1} \\ B_{bl1} \end{Bmatrix} w(t), \\ Y_b(t) &= [C_1 \quad C_2] \begin{Bmatrix} Z_r(t) \\ Z_l(t) \end{Bmatrix} + D_{b2} u(t) \\ &+ D_{b1} w(t),\end{aligned}\quad (11)$$

where  $A_1 = A_{br}(T^{-1})_{11} + A_{b12}(T^{-1})_{21}$ ,  $A_2 = A_{br}(T^{-1})_{12} + A_{b12}(T^{-1})_{22}$ ,  $A_3 = A_{b21}(T^{-1})_{11} + A_{b22}(T^{-1})_{21}$ ,  $A_4 = A_{b21}(T^{-1})_{12} + A_{b22}(T^{-1})_{22}$ ,  $C_1 = C_{br}(T^{-1})_{11} + C_{bl}(T^{-1})_{21}$ , and  $C_2 = C_{br}(T^{-1})_{12} + C_{bl}(T^{-1})_{22}$ .

The reduced-order model obtained by BT method retains the first few modes of the original structure that is continuous and with large modal mass participating ratio. Modal mass participation ratio is a coefficient to characterize the contribution of structural vibration mode to the structural response. Under an input excitation, the low-order modal mass participation ratio of a flexible structure is close to 1, and the high-order modal mass participation ratio is relatively small. Therefore, the contribution of high-order modes to the structural response can be ignored, in order to fulfill the requirement of engineering accuracy (e.g., the minimum retained modal mass participation ratio of a flexible building can be defined as 90% [33, 34]). According to (10),  $Z_{bl}$  is written as

$$Z_{bl}(t) = (T^{-1})_{21} \cdot Z_r(t) + (T^{-1})_{22} \cdot Z_l(t) = 0. \quad (12)$$

From (12),  $Z_l$  can be written as

$$Z_l(t) = -[(T^{-1})_{22}]^{-1} \cdot (T^{-1})_{21} \cdot Z_r(t). \quad (13)$$

Since some state messages of the balanced realization system in  $Z_l$  are directly discarded, this will result in the inaccuracy of this system.

Substituting (13) into (10) leads to

$$\begin{aligned}Z_{br}(t) &= [(T^{-1})_{11} - (T^{-1})_{12} \cdot ((T^{-1})_{22})^{-1} \cdot (T^{-1})_{21}] \\ &\cdot Z_r(t) = T_r Z_r(t).\end{aligned}\quad (14)$$

According to (14),  $\dot{Z}_{br}(t)$  that is the derivative of  $Z_{br}(t)$  with respect to time is expressed as

$$\dot{Z}_{br}(t) = T_r \dot{Z}_r(t). \quad (15)$$

Depending on (11),  $\dot{Z}_{bl}(t)$  can be expressed as

$$\begin{aligned}\dot{Z}_{bl}(t) &= A_3 \cdot Z_r(t) + A_4 \cdot Z_l(t) + B_{bl2} \cdot u(t) + B_{bl1} \\ &\cdot w(t) = 0.\end{aligned}\quad (16)$$

From (16),  $Z_l$  is

$$Z_l(t) = -A_4^{-1} [A_3 \cdot Z_r(t) + B_{bl2} \cdot u(t) + B_{bl1} \cdot w(t)]. \quad (17)$$

Substituting (15) and (17) into (11) leads to

$$\begin{aligned} \dot{Z}_r(t) &= T_r^{-1} (A_1 - A_2 A_4^{-1} A_3) Z_r(t) \\ &\quad + T_r^{-1} (B_{br2} - A_2 A_4^{-1} B_{bl2}) u(t) \\ &\quad + T_r^{-1} (B_{br1} - A_2 A_4^{-1} B_{bl1}) w(t), \end{aligned} \quad (18)$$

$$\begin{aligned} Y_r(t) &= (C_1 - C_2 A_4^{-1} A_3) Z_r(t) \\ &\quad + (D_{b2} - C_2 A_4^{-1} B_{bl2}) u(t) \\ &\quad + (D_{b1} - C_2 A_4^{-1} B_{bl1}) w(t), \end{aligned}$$

where  $A_r = T_r^{-1} (A_1 - A_2 A_4^{-1} A_3)$ ,  $B_{r2} = T_r^{-1} (B_{br2} - A_2 A_4^{-1} B_{bl2})$ ,  $B_{r1} = T_r^{-1} (B_{br1} - A_2 A_4^{-1} B_{bl1})$ ,  $C_r = C_1 - C_2 A_4^{-1} A_3$ ,  $D_{r2} = D_{b2} - C_2 A_4^{-1} B_{bl2}$ , and  $D_{r1} = D_{b1} - C_2 A_4^{-1} B_{bl1}$ .

Equation (18) displays a reduced-order model by improved BT method and can be simplified as

$$\begin{aligned} \dot{Z}_r(t) &= A_r Z_r(t) + B_{r2} u(t) + B_{r1} w(t), \\ Y_r(t) &= C_r Z_r(t) + D_{r2} u(t) + D_{r1} w(t). \end{aligned} \quad (19)$$

The truncation error of the reduced-order model shown as (19) can be defined as

$$\|e\|_\infty \leq 2(\sigma_{r+1} + \sigma_{r+2} + \dots + \sigma_n). \quad (20)$$

Depending on inequality (20), the model reduction accuracy of the reduced-order model is

$$\eta = 1 - \frac{\|e\|_\infty}{2 \sum_{i=1}^n \sigma_i} \geq \eta_{\min}, \quad (21)$$

where  $\eta_{\min} = 90\%$  is the minimum model reduction accuracy.

**2.2. Time-Delay Compensation Control Gain Design by GCC Algorithm.** Although the reduced-order controller design method in Section 2.1 can reduce the adverse effects of time-delay of control force calculation, the time-delay of the control system also includes other aspects. Therefore, it is necessary to design a compensation control gain to compensate other kinds of time-delays that includes the time of data acquisition and actuator response. The GCC algorithm is a suitable LQR controller design method. When the time-delay is considered, the control force of the reduced-order control system is

$$u_d(t) = -G_r Z_r(t-d), \quad (22)$$

where  $G_r$  is a closed-loop feedback gain matrix and  $d$  is a time-delay.

By substituting (22) into (19), the state equation of the system when input excitation is not considered temporarily is

$$\dot{Z}_r(t) = A_r Z_r(t) - B_{r2} G_r Z_r(t-d). \quad (23)$$

Defining  $\bar{A}_r = -B_{r2} G_r$ . If there exist symmetric positive-definite matrices  $P, S \in R^{n \times n}$ , then

$$\begin{bmatrix} A_r^T P + P A_r + S & P \bar{A}_r \\ \bar{A}_r^T P & -S \end{bmatrix} < 0. \quad (24)$$

Hence, system (23) is asymptotically stable. Lyapunov function is defined as follows:

$$V(Z_t) = Z_r^T(t) P Z_r(t) + \int_{t-d}^t Z_r^T(\tau) S Z_r(\tau) d\tau, \quad (25)$$

where  $Z_t = Z_r(t+\alpha)$ ,  $\alpha \in [-d, 0]$ ,  $V(Z_t)$  is a positive-definite matrix and  $\dot{V}(Z_t)$  is the derivative of  $V(Z_t)$  with respect to time. According to the algorithms of the transport matrix,

$$\begin{aligned} \dot{V}(Z_t) &= \dot{Z}_r^T(t) P Z_r(t) + Z_r^T(t) P \dot{Z}_r(t) + Z_r^T(t) \\ &\quad \cdot S Z_r(t) - Z_r^T(t-d) S Z_r(t-d) = \begin{bmatrix} Z_r(t) \\ Z_r(t-d) \end{bmatrix}^T \\ &\quad \cdot \begin{bmatrix} A_r^T P + P A_r + S & P \bar{A}_r \\ \bar{A}_r^T P & -S \end{bmatrix} \begin{bmatrix} Z_r(t) \\ Z_r(t-d) \end{bmatrix}. \end{aligned} \quad (26)$$

According to inequality (24),  $\dot{V}(Z_t)$  is a negative-definite function. Based on Lyapunov stability theory [35], it proves that the control system (23) is asymptotically stable.

When control force and input excitation are all considered, the reduced-order control system shown as (19) with time-delay can be described as

$$\begin{aligned} \dot{Z}_r(t) &= A_r Z_r(t) + \bar{A}_r Z_r(t-d) + B_{r1} w(t) \\ &\quad + B_{r2} u(t). \end{aligned} \quad (27)$$

If the control force  $u(t) = -G_r Z_r$ , the closed-loop system is

$$\begin{aligned} \dot{Z}_r(t) &= (A_r - B_{r2} G_r) Z_r(t) + \bar{A}_r Z_r(t-d) \\ &\quad + B_{r1} w(t). \end{aligned} \quad (28)$$

The performance index of system (28) can be defined as

$$\begin{aligned} J &= \int_0^\infty (Z_r^T Q Z_r + u_r^T R u_r) dt \\ &= \int_0^\infty \{Z_r^T [Q + (-G_r)^T R (-G_r)] Z_r\} dt, \end{aligned} \quad (29)$$

where weight matrices  $Q$  and  $R$  are the two important parameters in LQR algorithm and the selection of weight matrices reflects the importance of the security and economy in AMD control systems.

According to inequality (24), if there exist symmetric positive-definite matrices  $P, S \in R^{n \times n}$ , then

$$\begin{bmatrix} (A_r - B_{r2}G_r)^T P + P(A_r - B_{r2}G_r) + S + Q + (-G_r)^T R(-G_r) & P\bar{A}_r \\ \bar{A}_r^T P & -S \end{bmatrix} < 0. \quad (30)$$

System (28) is asymptotically stable. According to inequality (30),

$$\begin{bmatrix} (A_r - B_{r2}G_r)^T P + P(A_r - B_{r2}G_r) + S & P\bar{A}_r \\ \bar{A}_r^T P & -S \end{bmatrix} < \begin{bmatrix} -[Q + (-G_r)^T R(-G_r)] & 0 \\ 0 & 0 \end{bmatrix} < 0. \quad (31)$$

Depending on (26), inequality (31) is premultiplying  $[Z_r(t) \ Z_r(t-d)]$  and postmultiplying  $[Z_r(t) \ Z_r(t-d)]^T$ ; then

$$Z_r^T [Q + (-G_r)^T R(-G_r)] Z_r < -\dot{V}(Z_t). \quad (32)$$

By integrating inequality (32), the performance index of a system with time-delay satisfies

$$\begin{aligned} J &= \int_0^\infty \{Z_r^T [Q + (-G_r)^T R(-G_r)] Z_r\} dt \\ &\leq \left[ Z_0^T P Z_0 + \int_{-d}^0 \varphi^T(t) S \varphi(t) dt \right]. \end{aligned} \quad (33)$$

Inequality (30) is pre- and postmultiplying  $\text{diag}\{P^{-1}, I\}$ ; then

$$\begin{bmatrix} H_r & \bar{A}_r \\ \bar{A}_r^T & -S \end{bmatrix} < 0, \quad (34)$$

where  $X = P^{-1}$  and  $H_r = X(A_r - B_{r2}G_r)^T + (A_r - B_{r2}G_r)X + XSX + X[Q + (-G_r)^T R(-G_r)]X$ .

Variable substitution method can be used for solving this problem. Defining  $W = -G_r X$ . From Schur's complement [36], inequality (34) can be expressed as

$$\begin{bmatrix} \tilde{H}_r & \bar{A}_r & X & W^T & X \\ \bar{A}_r^T & -S & 0 & 0 & 0 \\ X & 0 & -Q^{-1} & 0 & 0 \\ W & 0 & 0 & -R^{-1} & 0 \\ X & 0 & 0 & 0 & -S^{-1} \end{bmatrix} < 0, \quad (35)$$

where  $\tilde{H}_r = A_r X + B_{r2} W + (A_r X + B_{r2} W)^T$ . Inequality (35) is pre- and postmultiplying  $\text{diag}\{I, S^{-1}, I, I, I\}$ , and  $V = S^{-1}$ . Inequality (35) can be expressed as

$$\begin{bmatrix} \tilde{H}_r & \bar{A}_r V & X & W^T & X \\ V \bar{A}_r^T & -V & 0 & 0 & 0 \\ X & 0 & -Q^{-1} & 0 & 0 \\ W & 0 & 0 & -R^{-1} & 0 \\ X & 0 & 0 & 0 & -V \end{bmatrix} < 0, \quad (36)$$

where the optimal solutions of  $X'$ ,  $W'$ , and  $V'$  are obtained through the LMI toolbox of MATLAB. The optimal feedback gain matrix of the controller is

$$G_r = -W' (X')^{-1}. \quad (37)$$

Then the state feedback control law is

$$u(t) = W' (X')^{-1} Z(t). \quad (38)$$

The reduced-order controller with GCC algorithm is shown in Figure 1. The state-space equation of the reduced-order system is depicted by the dashed box in the figure, and the symbol inside the solid box in the figure represents the time-delay compensation control gain obtained by GCC algorithm.

### 3. Numerical Verification

**3.1. Transfer Function Analysis of the Reduced-Order Model.** In this paper, a ten-storey frame shown in Figure 2 has been constructed for numerical analysis. The height and total mass of this structure are 33 m and 892.9 tons, respectively. The height of each floor is 3.3 m, and the height and the width of the beams along the minor-axis and the major-axis are 500 mm  $\times$  250 mm (Beam 1 and Beam 2). The height and the width of Beam 3 are 450 mm  $\times$  200 mm, and the dimensions of the columns are 500 mm  $\times$  500 mm.

The lumped mass method is used to build the mass matrix for the structure. A unit force is applied to each particle floor of the structure, and then the displacement at each floor is obtained and combined into the flexibility matrix. The stiffness matrix can be easily obtained, as the inverse of the flexibility matrix. The AMD control device is assumed to be installed on the 8th floor and is only used to control the horizontal vibration along the minor axis. Key parameters of AMD are listed in Table 1. Structural frequencies and modal

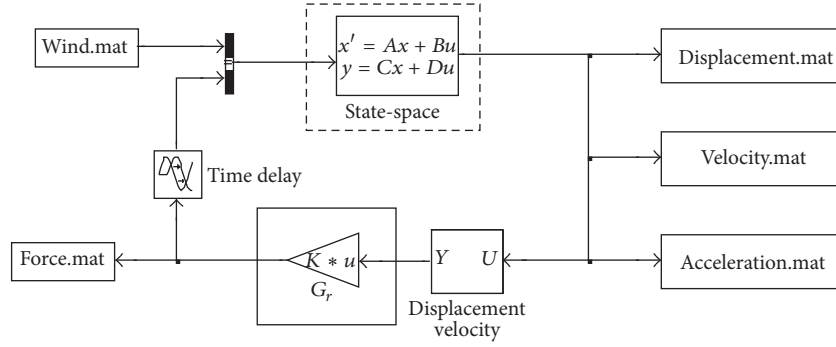


FIGURE 1: Simulink block diagram of the reduced-order controller with GCC algorithm.

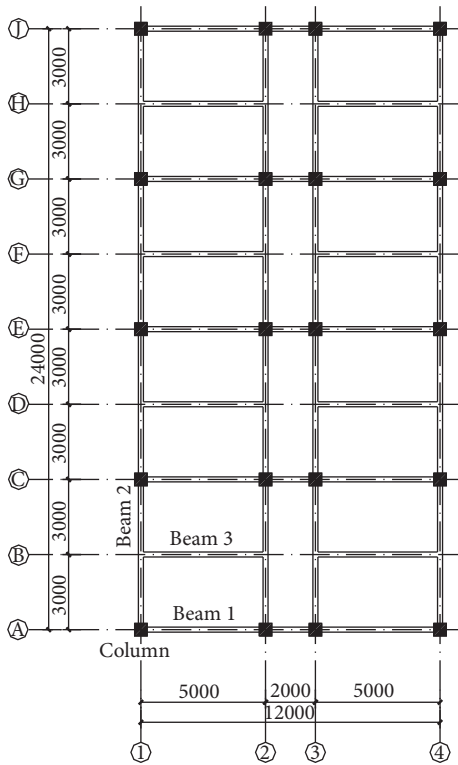


FIGURE 2: The plan of each floor.

TABLE 1: Key parameters of AMD.

Index	AMD
Auxiliary mass (kg)	4000
Effective stroke (m)	$\pm 1.1$
Maximum driving force (kN)	27.5

mass participation ratios [37] of the ten-storey frame are calculated using the model constructed in MATLAB and listed in Table 2.

The reduced-order controller can be designed by Simulink toolbox in MATLAB. In this paper, the improved BT method is used to reduce the orders of the original model, and its characteristics of the transfer functions are compared with

TABLE 2: Modal mass participation ratios and natural frequencies of the frame.

Vibration mode	Modal mass participation ratio	Sum	Frequency (Hz)
1	0.7940	0.7940	0.9009
2	0.0985	0.8925	2.8744
3	0.0410	0.9335	5.3248
4	0.0237	0.9572	8.4175
5	0.0156	0.9728	12.2549

the reduced-order model by classical BT method. Regarding the above ten-storey frame structure, its displacement and acceleration transfer functions of the top floor with different orders are shown in Figures 3 and 4. The input and output of these transfer functions are all top floor. In this figure, ORM means the structure retains the original model (20 orders), while  $r$  is retained orders of 4, 8, 12, and 16. Considering the structural frequency range, the part between 0.01 Hz and 100 Hz is shown in the figures.

Figures 3 and 4 show that, with the increase of the retained order, the difference between the original model and the reduced-order model by the above two BT methods will become smaller. From Figures 3(a) and 4(a), the displacement transfer functions of the two reduced-order models are basically consistent with the original model in low frequency. From Figures 3(b), 3(d), 4(b), and 4(d), since acceleration response is mainly affected by the higher modes and the reduced-order model by classical BT method discards some structural information of high-order modes, its acceleration transfer function is not well consistent with the original model in low frequency. Nevertheless, since the improved BT method presented in this paper can retain this discarded information, not only the displacement but also the acceleration transfer function of the improved model is basically consistent with the original model in low frequency, meaning that the reduced-order model by improved BT method can better reflect the dynamic characteristics of the original model in low frequency.

3.2. Mode Number Influence Analysis of the Reduced-Order Model. The necessity of the reduced-order controller by

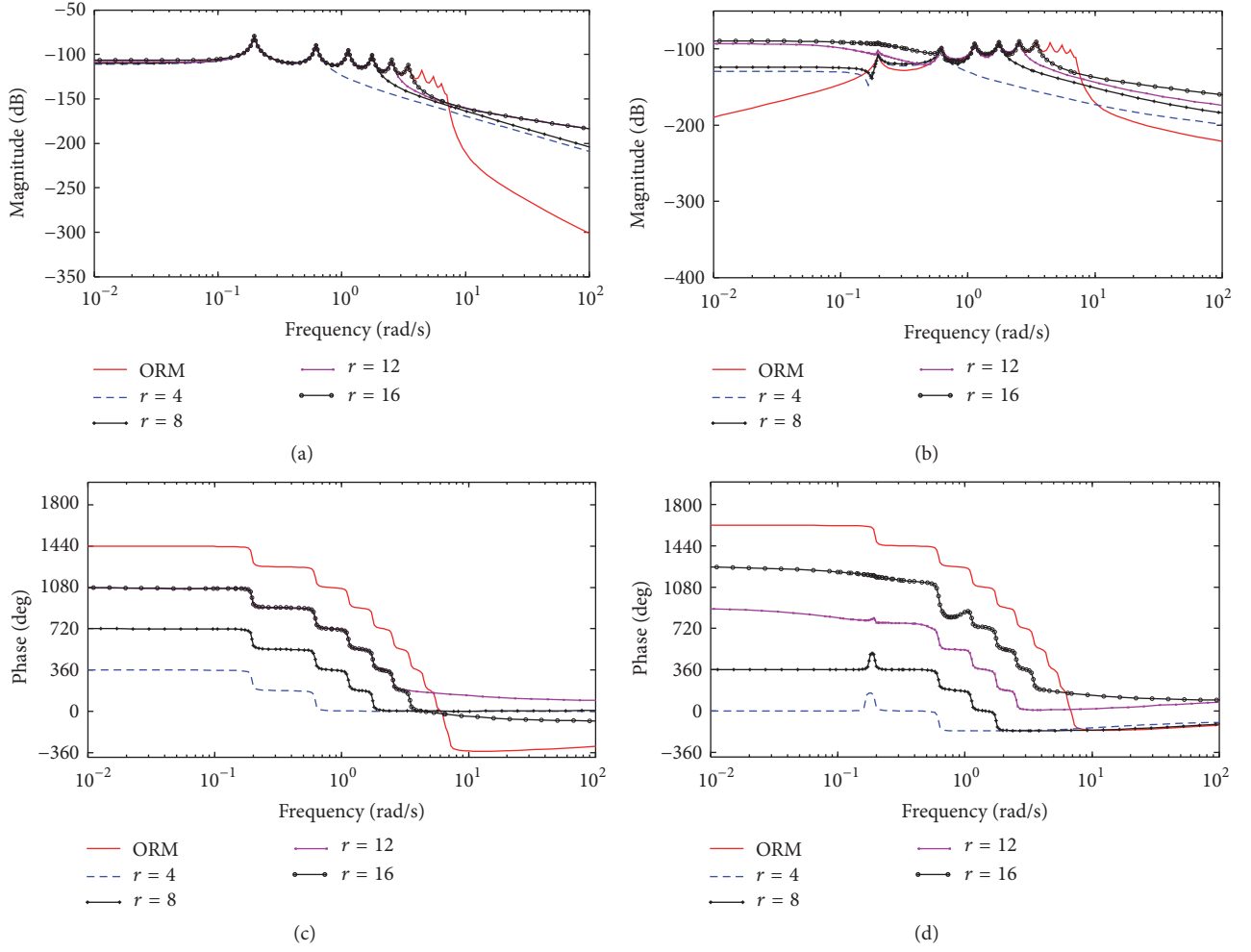


FIGURE 3: Comparison of transfer functions of the reduced-order model by *classical BT method*. (a) Magnitude and (c) phase of the displacement transfer functions. (b) Magnitude and (d) phase of the acceleration transfer functions.

improved BT method is verified by a numerical example of the above ten-storey frame. From Table 2, the first three orders of the modal mass participation ratios of the frame are 0.9335 which is greater than 90%, meaning that these orders contribute a large portion of the resultant structural dynamic response. The minimum order of the reduced-order model is defined as 6, and the maximum mode number is defined as 8, meaning that the maximum order is 16.

Fluctuating wind is caused by the irregularity of the wind, and its intensity is changed with time. Its short period and dynamic characteristics lead to the random vibration of the structure. In the paper, a ten-year return period fluctuating wind speed with Davenport spectrum will be generated, and mixed autoregressive-moving average (MARMA) model [38] is proposed to simulate the stochastic process. The wind load is applied to the ten-storey frame, and it can be calculated by the following equation:

$$P_i = \rho \bar{V}(z) u_i(z, t) \mu_s A, \quad (39)$$

where  $P_i$  is the fluctuating wind load at  $i$ th floor and  $\rho$  is the air density.  $\bar{V}(z)$  is the average wind speed at  $i$ th floor.  $u_i$  is

the fluctuating wind speed that is associated with height and time.  $\mu_s$  and  $A$  are the shape coefficient of a building and the area facing the wind, respectively.

Under the above wind load, the model reduction accuracy, the 8th floor's control effects (defined as the difference between controlled and uncontrolled responses), and the AMD parameters of different reduced-order models are listed in Table 3.

Table 3 shows that since the reduced-order model by improved BT method presented in this paper can effectively retain the structural high-order modal information, when the retained orders are a range from 6 to 16, the maximum variations of the displacement and acceleration control effects are 0.0049% and 0.0395%, and the maximum variations of the AMD parameters are only 0.0003 m and 0.0003 kN, meaning that the control effects and AMD parameters are all relatively stable. As a result, the order of the controlled structure can be reduced by the improved BT method in maximum extent.

The above ten-storey frame structure is recommended to retain 6 orders. The analysis whether the reduced-order system can effectively save the calculation time is given in

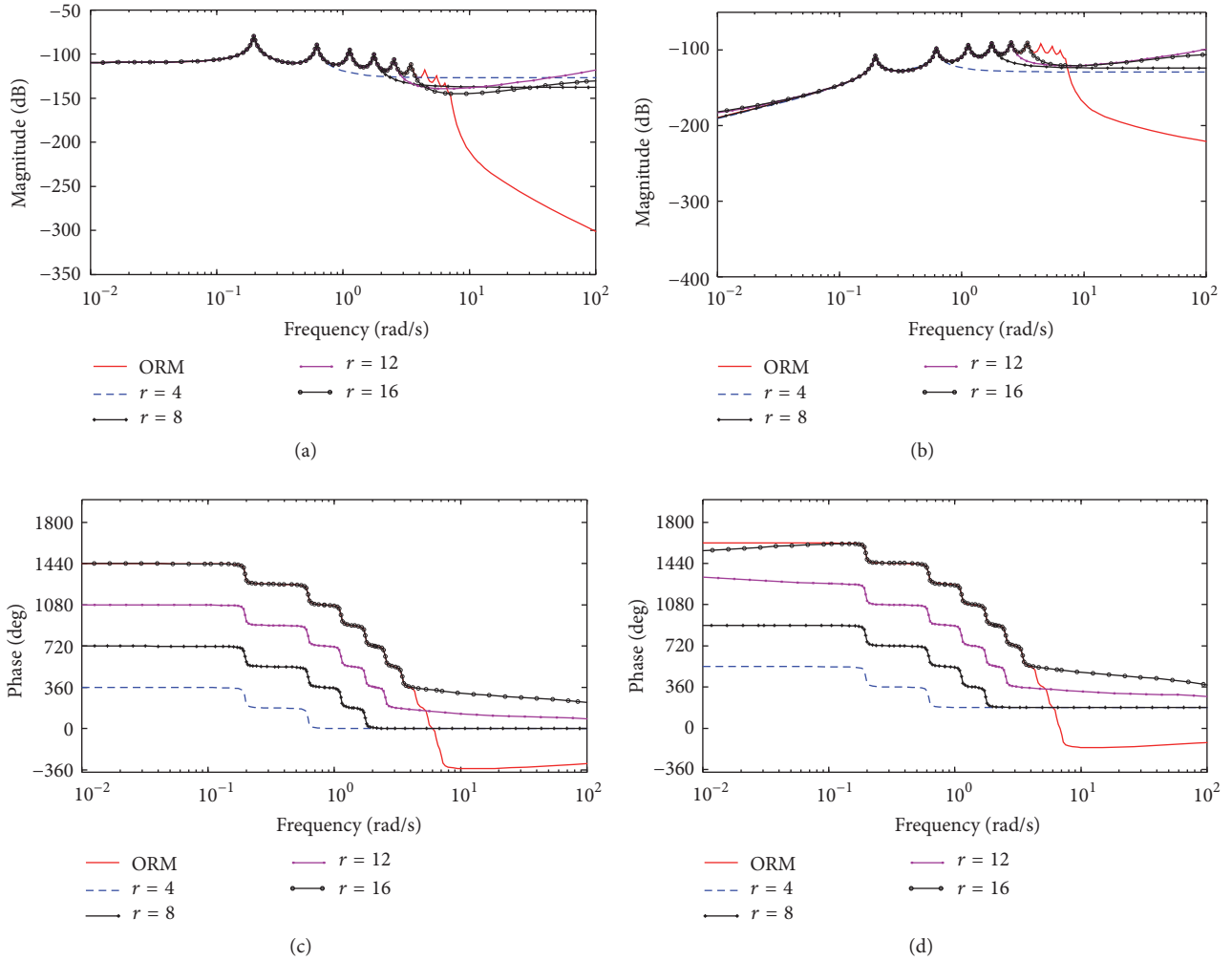


FIGURE 4: Comparison of transfer functions of the reduced-order model by *improved BT method*. (a) Magnitude and (c) phase of the displacement transfer functions. (b) Magnitude and (d) phase of the acceleration transfer functions.

TABLE 3: Comparison of the performances of control system under different orders.

Order	Model reduction accuracy (%)	Displacement control effect (%)	Acceleration control effect (%)	AMD strokes (m)	AMD control forces (kN)
6	80.94	34.4379	33.7841	0.0540	8.8061
8	84.02	34.4401	33.8022	0.0541	8.8062
10	86.82	34.4425	33.8152	0.0543	8.8064
12	89.54	34.4428	33.8073	0.0543	8.8064
14	92.21	34.4410	33.8201	0.0543	8.8063
16	94.86	34.4404	33.8236	0.0543	8.8063

this paper, and calculation times of the reduced-order system under different orders are shown in Table 4. The calculation time of the reduced-order system under 6 orders is regarded as the comparison target, and then the accelerated ratios of calculation time of the reduced-order system under different orders are obtained in the table.

Table 4 shows that, (1) with the increase of the retained order, the calculation time of control force will become larger. (2) The maximum retained order of the reduced-order system is 16, and its calculation time of control force is  $3.9583 \times 10^{-6}$  s. Nevertheless, the control force's calculation time of the reduced-order system with 6 retained orders is only

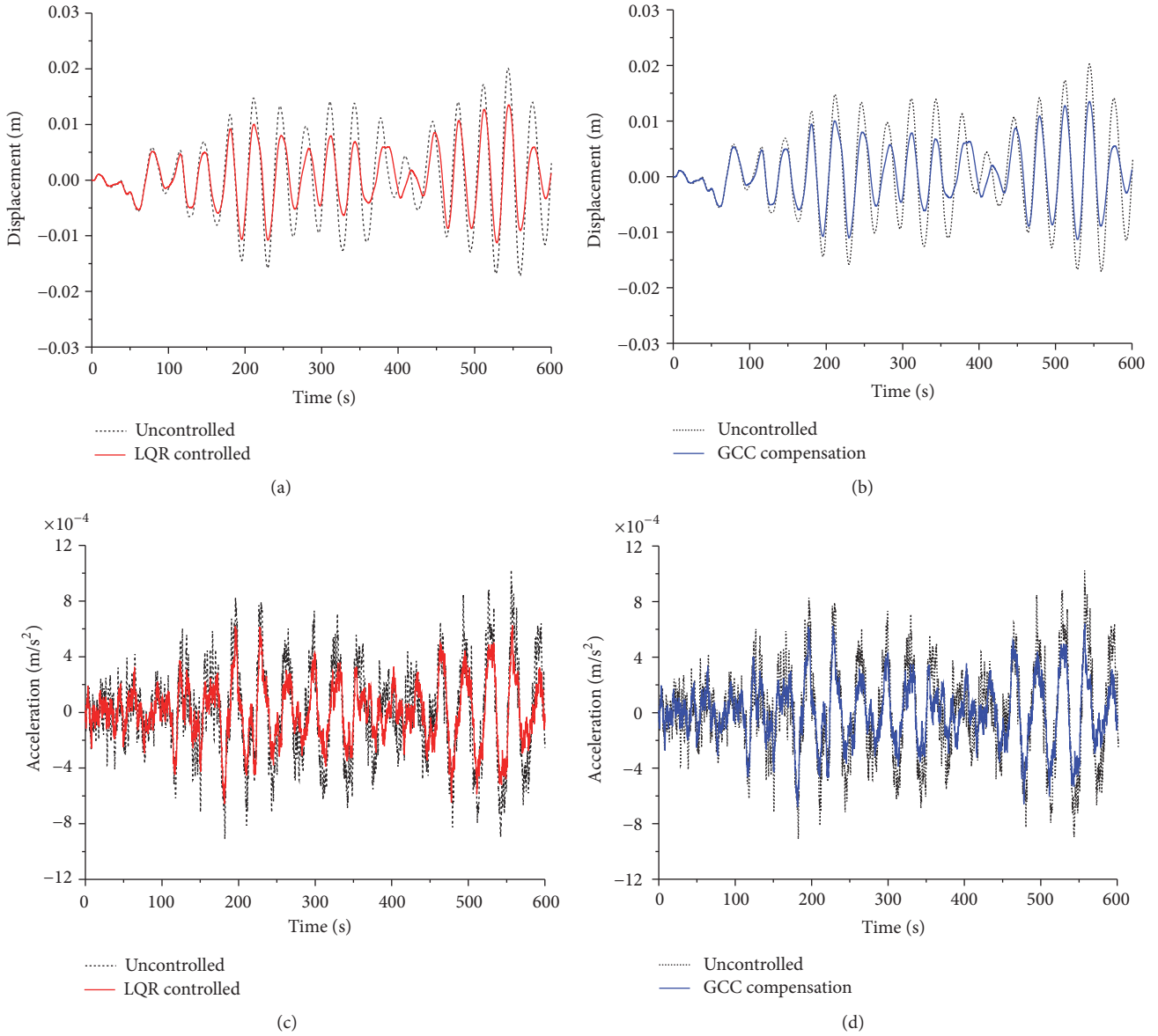


FIGURE 5: Comparison of structural responses to 8th floor. (a) and (c) Under uncontrolled and controlled by LQR algorithm without time-delay. (b) and (d) Under uncontrolled and controlled with GCC compensation.

TABLE 4: Comparison of the calculation time of control force under different orders

Order	Calculation time ( $\times 10^{-6}$ s)	Accelerated ratios (%)
6	2.9167	—
8	3.1250	6.6656
10	3.3750	13.5793
12	3.5833	18.6030
14	3.7917	23.0767
16	3.9583	26.3143

$2.9167 \times 10^{-6}$  s. The accelerated ratio between two reduced-order systems is 26.3143%. It is proved that the reduced-order controller can not only guarantee the performance of the

control system (from Table 3), but also effectively reduce the control force calculation time.

**3.3. Performance Analysis of the Reduced-Order Controller with GCC Algorithm.** A reduced-order controller with GCC algorithm for the ten-storey frame is designed to compare with the classical controller based on LQR algorithm, and *GCC compensation* stands for a system with time-delay and a designed reduced-order compensation controller with GCC algorithm. Under a ten-year return period wind load, the structural responses and the AMD parameters of different control systems with and without time-delay (time-delay in this paper is assumed as 0.5 s) are shown in Figures 5 and 6. The corresponding control effects and AMD parameters are listed in Table 5.

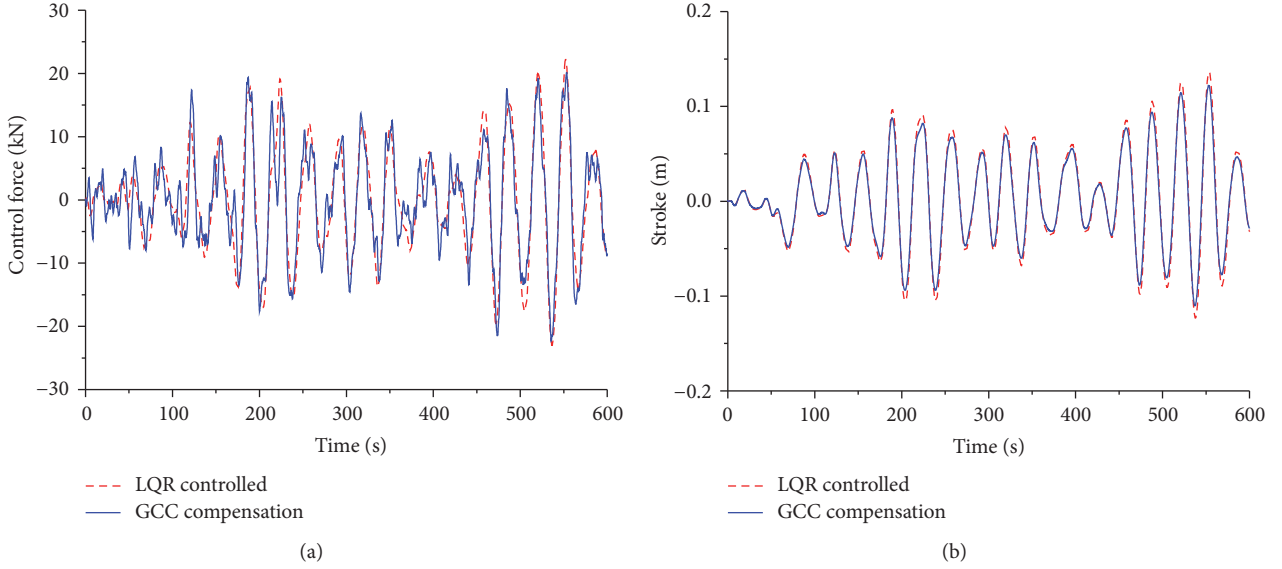


FIGURE 6: Comparison of AMD parameters, (a) AMD control forces, and (b) AMD strokes.

TABLE 5: Comparison of control effects (%) and AMD parameters of different control systems.

Floor	Index	Without time-delay and classical LQR algorithm (%)	With time-delay and classical LQR algorithm (%)	With time-delay and GCC compensation (%)
8th	Displacement (m)	34.8069	-14.4568	34.4633
	Velocity (m/s)	35.3560	-15.1235	34.8744
	Acceleration (m/s <sup>2</sup> )	34.5862	-14.1547	33.5514
9th	Displacement (m)	34.7768	-14.3658	34.4344
	Velocity (m/s)	34.7299	-14.1469	34.2723
	Acceleration (m/s <sup>2</sup> )	29.0512	-19.5269	28.1406
10th	Displacement (m)	34.7414	-14.4756	34.3974
	Velocity (m/s)	34.2854	-14.1975	33.8494
	Acceleration (m/s <sup>2</sup> )	29.4658	-19.3269	28.7185
Control force (kN)		8.4381	8.9587	8.1838
Stroke (m)		0.0524	0.0695	0.0464

From Figures 5 and 6 and Table 5, (1) the system with time-delay based on the classical LQR algorithm is divergent. (2) After GCC compensating the time-delay, the control effects and AMD parameters of the system with time-delay are close to the system without time-delays. In particular, the maximum variations of the displacement, velocity, and acceleration control effects are only 0.3440%, 0.4816%, and 1.0348%. Therefore, the reduced-order controller with GCC algorithm can effectively compensate the time-delay and decrease the structural response. (3) The reduced-order controller with GCC algorithm can maintain the stability of AMD parameters and are consistent with the system without time-delay. The AMD parameters of the system only change by 0.2543 N and 0.0060 m.

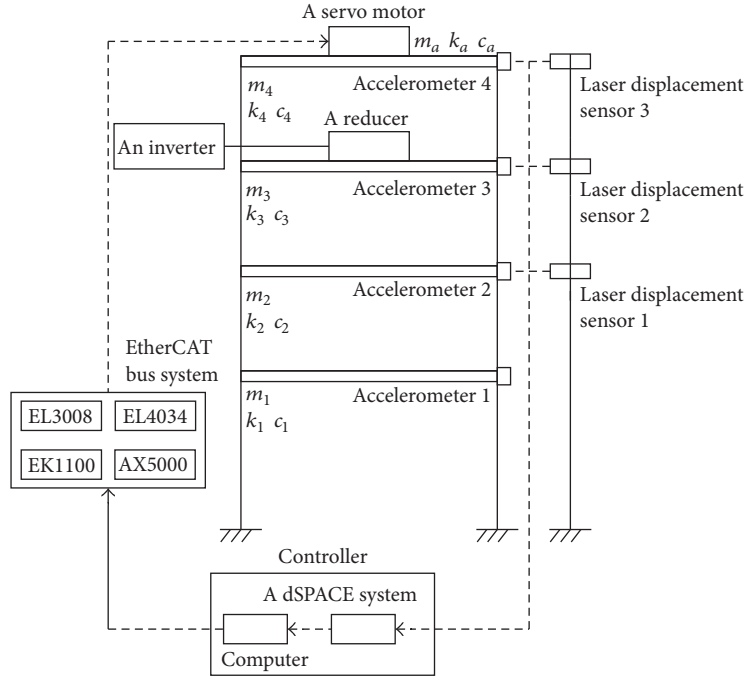
#### 4. Experimental Verification

Figure 7 shows an experimental system of a four-storey steel frame with an AMD control device installed on the fourth floor [39]. A servo motor can acquire the forces from an EtherCAT bus system and was used to add these forces to control the structure. The AMD system mainly consisted of a servo motor, servo controller, an EtherCAT bus system, a dSPACE system with a type of DS1103, and a computer.

To validate the efficiency of the developed method, the reduced-order controller by improved BT method is applied to the experimental system. The full-order model of the experimental system with AMD is 10, and the retained orders of the reduced-order model are recommended to be 4, 6,



(a)



(b)

FIGURE 7: Pictures of the steel frame structure. (a) Practicality. (b) Exhibition.

and 8, respectively. The loading frequency of the system is 1 Hz; that is, the peak value of the corresponding excitation force is 45.89 N, and the wave form of this force is sinusoidal. Under the above excitation load, the control effects and AMD parameters of different control systems are listed in Table 6, and the structural responses (includes displacement and acceleration) to 4th floor of different control systems are shown in Figures 8 and 9. AMD parameters of the 4-order system are shown in Figure 10.

From Figures 8–10 and Table 6, (1) as the retained orders of the experimental system are a range from 4 to 10, the displacement and acceleration control effects and AMD parameters are all relatively stable, meaning that the performance of the reduced-order controller is consistent with the full-order controller. Therefore, the retained order 4 of the controlled structure can be reduced by the improved BT method in maximum extent. (2) Because of the interaction between the AMD system and the structure as well as the coupling between the horizontal and vertical vibrations of the structure, the structural responses do not completely obey the change regulation of a sine-wave under a sinusoidal load. (3) The acceleration control needs high frequency control force that will stimulate the structural high-order modes, and AMD device is placed in the fourth floor of the structure. Due to above two reasons, the control effect of third floor is an opposite high-order phase with the fourth floor and significantly less than the control effects of second and fourth floors.

The retained order of the experimental can be determined as 4. Then, to validate the efficiency of the time-delay compensation control method, the compensation controller with

GCC algorithm is applied to the experimental system. The performance of the compensation controller is compared with the system without time-delay. Time-delay assumed as 0.5 s in the control system is introduced by a time-delay block in the program modules. Under the above excitation load, the structural responses of different systems are shown in Figure 11, and the corresponding control effects and AMD parameters are listed in Table 7.

Figure 11 and Table 7 show that (1) the displacement and acceleration control effects of the system without compensation are all minus numbers, meaning that AMD system may increase the structural response and play a negative role when time-delay exists. (2) The control effects and AMD parameters of the system with GCC compensation are close to the system without time-delay. In particular, the maximum variations of the displacement and acceleration control effects between two different systems are only 1.7453% and 2.8189%, and the AMD parameters of the controller with GCC compensation decrease by 1.8515 N and 0.0296 m. Therefore, the compensation controller based on GCC algorithm can effectively compensate the long time-delay (e.g., 0.5 s in this paper) and suppress the structural response.

## 5. Conclusions

Time-delay has a negative influence in AMD control system. To address this issue, this paper presents a new reduced-order controller by improved BT method that can retain the abandoned high-order modal information of the original structure to reduce calculation time-delay. Time-delay compensation control gain designed by GCC algorithm is also

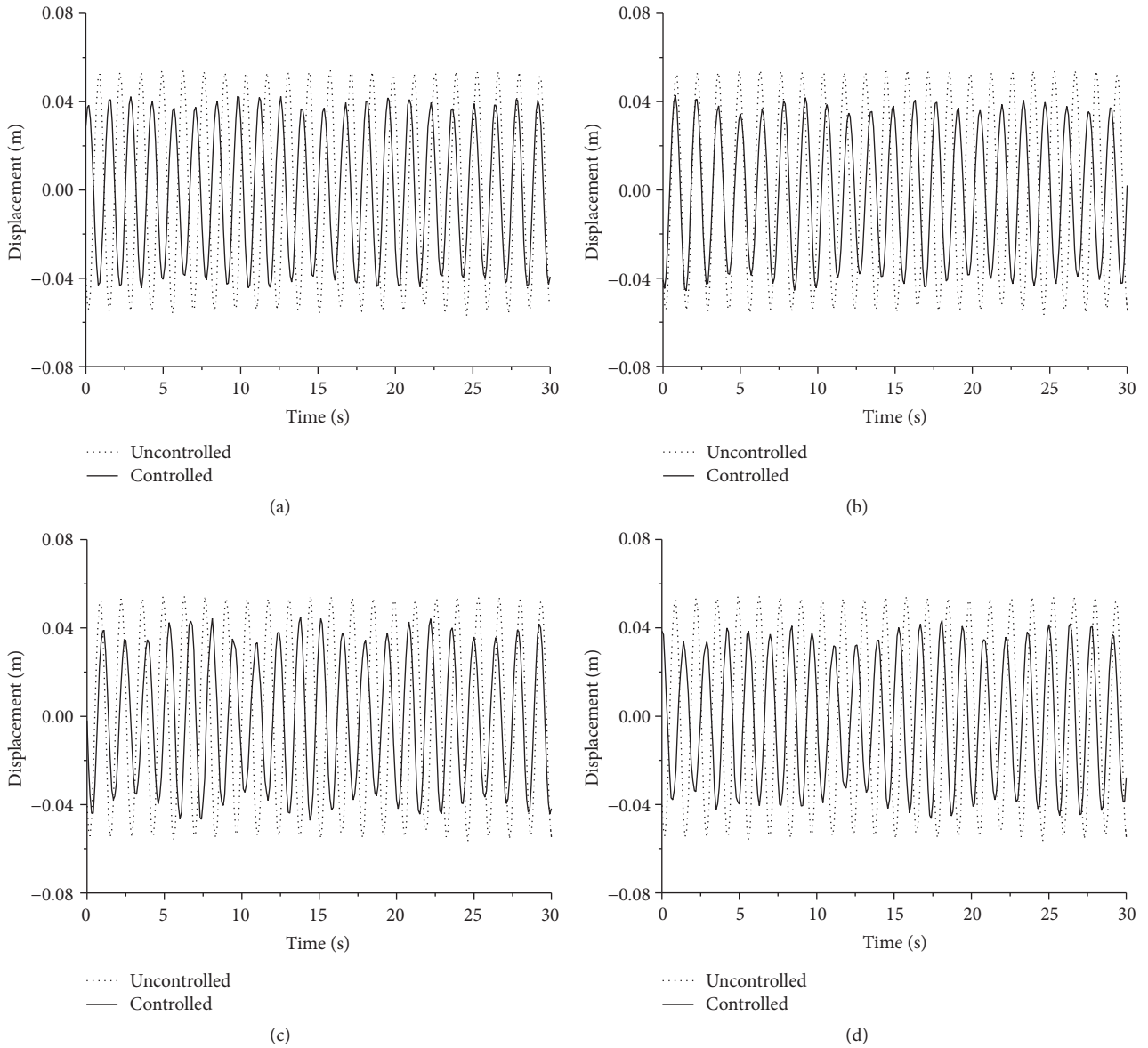


FIGURE 8: Comparison of displacement responses to 4th floor of the experimental system. (a) 4-order model, (b) 6-order model, (c) 8-order model, and (d) full-order model.

TABLE 6: Comparison of control effects of different control systems.

Index	Full-order model (%)	4-order model (%)	6-order model (%)	8-order model (%)
Displacement (m)				
2nd floor	24.8143	24.2223	24.4342	24.9452
3rd floor	25.5053	24.2089	24.8436	25.3991
4th floor	25.9376	24.5857	25.3514	25.8182
Acceleration ( $m/s^2$ )				
2nd floor	66.2392	67.0423	62.5976	66.4737
3rd floor	59.7265	51.1551	53.8394	54.2685
4th floor	72.4474	68.9787	71.4552	68.7089
AMD control forces (N)	35.1827	35.0064	34.7217	34.9065
AMD strokes (m)	0.1985	0.2167	0.2114	0.1975

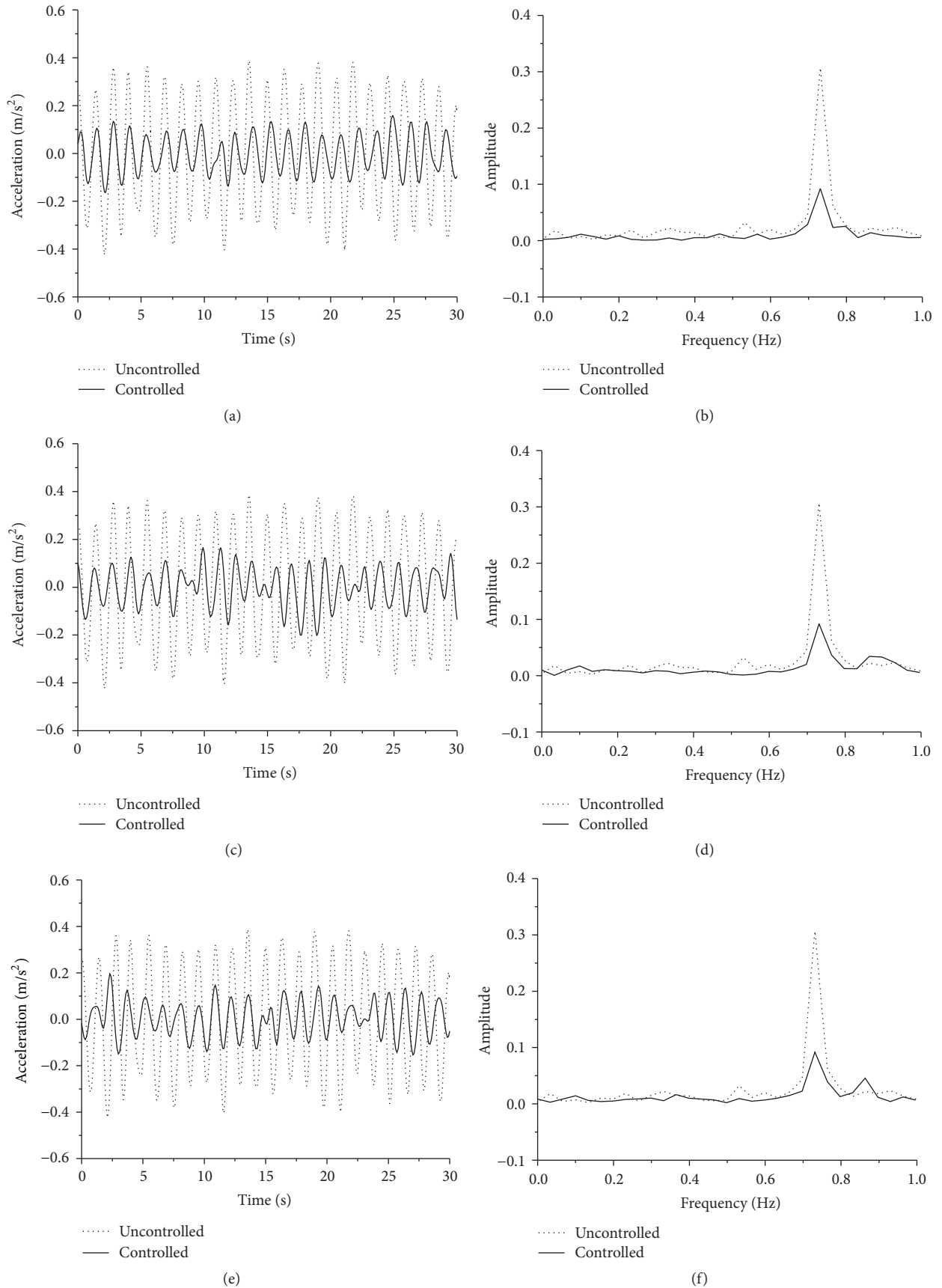


FIGURE 9: Continued.

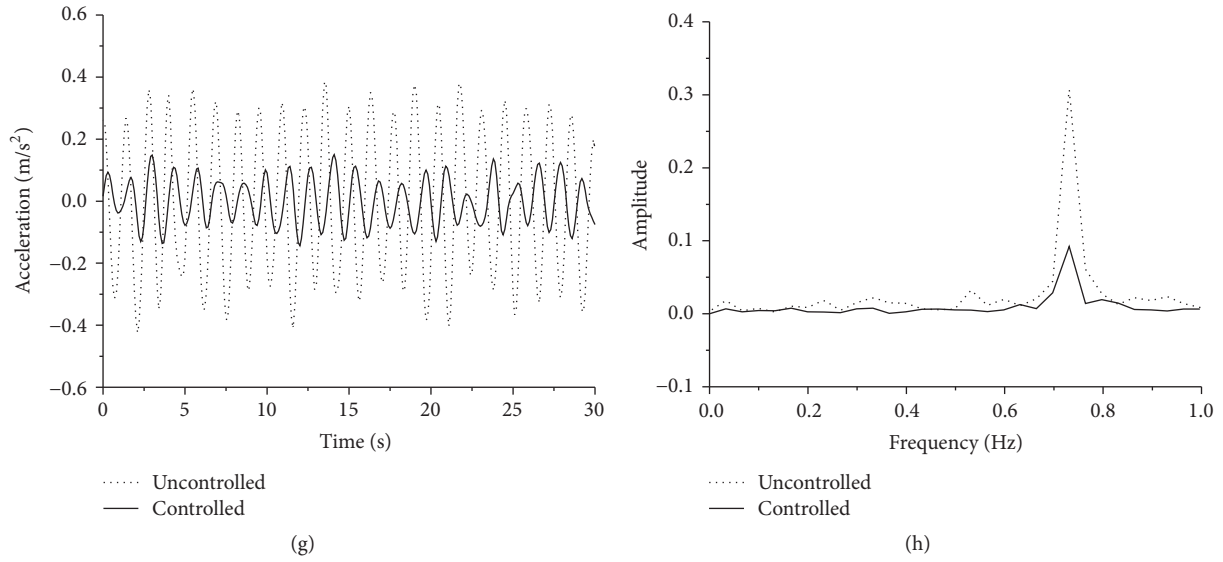


FIGURE 9: Comparison of acceleration responses to 4th floor of the experimental system. (a) and (b) 4-order model, (c) and (d) 6-order model, (e) and (f) 8-order model, and (g) and (h) full-order model.

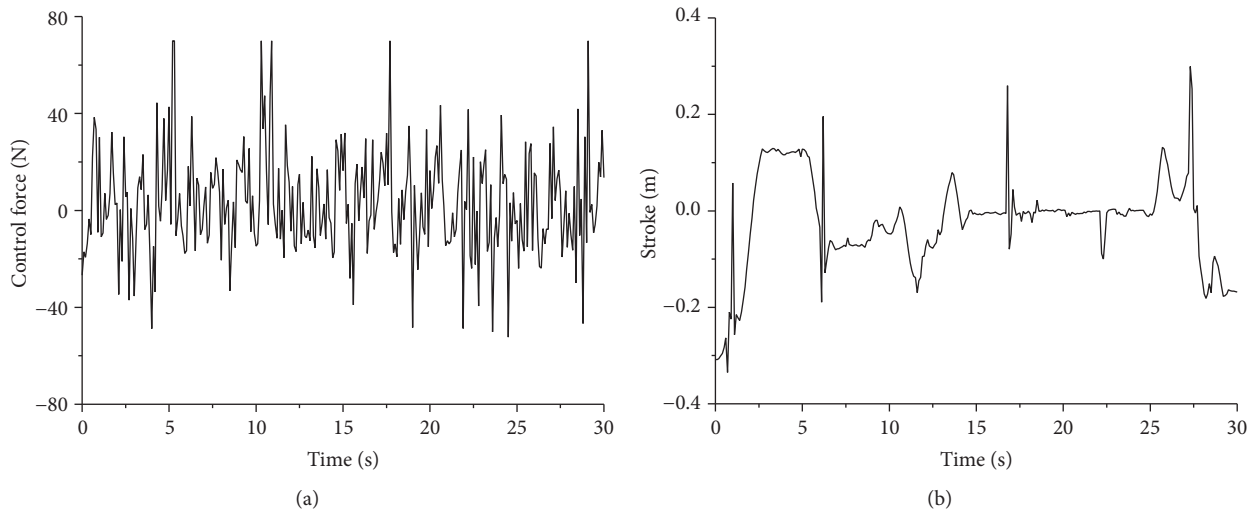


FIGURE 10: AMD parameters of the 4-order experimental system. (a) AMD control forces. (b) AMD strokes.

TABLE 7: Control effectiveness of structural responses (%).

Index	No control	No compensation		GCC compensation	
		Responses	Effect (%)	Responses	Effect (%)
Displacement (m)					
2nd floor	0.0181	0.0191	-5.5249	0.0136	24.8619
3rd floor	0.0262	0.0277	-5.7252	0.0194	25.9542
4th floor	0.0301	0.0318	-5.6478	0.0224	25.5814
Acceleration ( $m/s^2$ )					
2nd floor	0.2267	0.2486	-9.6603	0.0774	65.8580
3rd floor	0.2466	0.2656	-7.7048	0.1135	53.9740
4th floor	0.2478	0.2683	-8.2728	0.0700	71.7514
Peak control force (N)	—	33.7858	—	33.1549	—
Peak stroke (m)	—	0.1806	—	0.1871	—

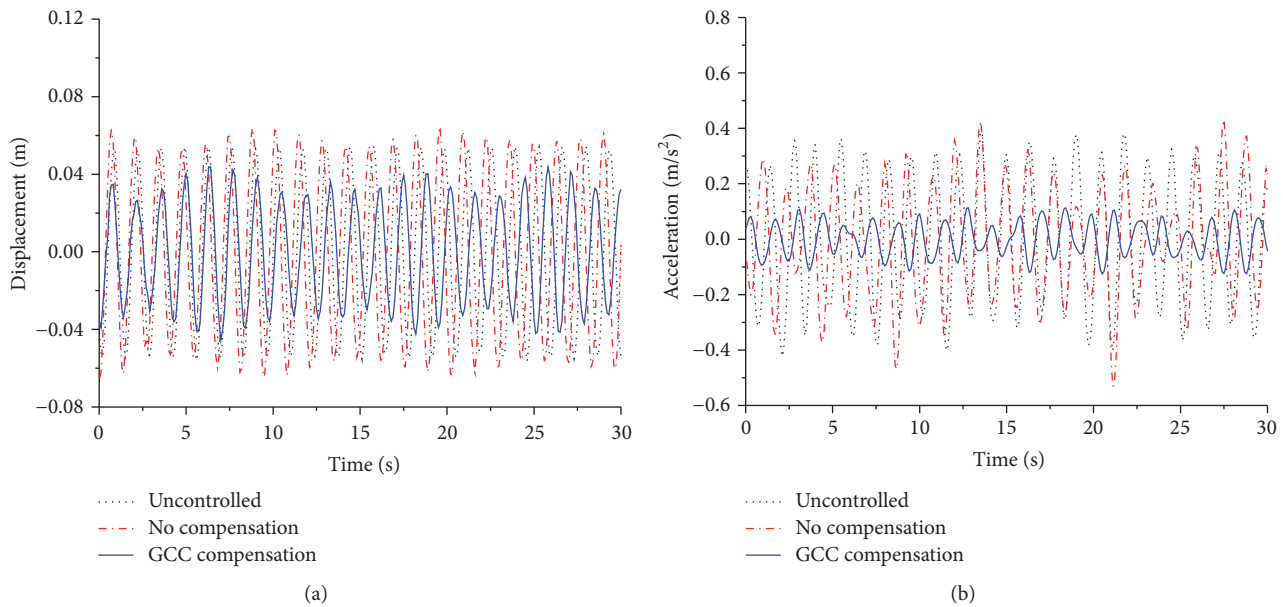


FIGURE 11: Comparison of structural responses to 4th floor of the experimental system under uncontrolled and controlled without compensation and with GCC compensation. (a) Displacement. (b) Acceleration.

presented to compensate data acquisition and actuator response time-delays. Finally, a numerical example and an experiment are presented to validate the effectiveness of the proposed method. Based on the results, the following conclusions can be drawn.

- (1) The improved BT method presented in this paper can retain the abandoned structural high-order modal information; the acceleration transfer function of the reduced-order model by improved BT method is more consistent with the original model in low frequency than the model by classical BT method.
- (2) As the modal mass participation ratio of a frame is larger than 90%, the minimum retained order of its reduced-order controller by improved BT method can be obtained. Although the model reduction accuracy cannot meet the requirements of 90%, this controller can still keep its control effects and AMD parameters stable.
- (3) This new reduced-order controller whose order is reduced in maximum extent not only guarantees the performance of the system, but also effectively reduces calculation time of control force.
- (4) The new reduced-order controller based on GCC algorithm in this paper can significantly improve the performance under the adverse influence of time-delay, and its performance is close to the classical control system without time-delay. As a result, it can effectively compensate time-delay and enhance the robustness of the control system.

## Competing Interests

The authors declare that there is no conflict of interests regarding the publication of this paper.

## Acknowledgments

The research described in this paper was financially supported by the National Key Research and Development Program of China (Grant no. 2016YFC0701102), the National Natural Science Foundations of China (Grants nos. 51378007 and 51538003), and the Shenzhen Technology Innovation Programs (Grants nos. JSGG20150330103937411 and JCYJ20150625142543473).

## References

- [1] H. Cao, A. M. Reinhorn, and T. T. Soong, "Design of an active mass damper for a tall TV tower in Nanjing, China," *Engineering Structures*, vol. 20, no. 3, pp. 134–143, 1998.
- [2] M. Yamamoto, S. Aizawa, M. Higashino, and K. Toyama, "Practical applications of active mass dampers with hydraulic actuator," *Earthquake Engineering and Structural Dynamics*, vol. 30, no. 11, pp. 1697–1717, 2001.
- [3] F. Ricciardelli, A. D. Pizzimenti, and M. Mattei, "Passive and active mass damper control of the response of tall buildings to wind gustiness," *Engineering Structures*, vol. 25, no. 9, pp. 1199–1209, 2003.
- [4] B. Basu, O. S. Bursi, F. Casciati et al., "A European association for the control of structures joint perspective. Recent studies in civil structural control across Europe," *Structural Control and Health Monitoring*, vol. 21, no. 12, pp. 1414–1436, 2014.

- [5] F. E. Udawadia and P. Phohomsiri, "Active control of structures using time delayed positive feedback proportional control designs," *Structural Control and Health Monitoring*, vol. 13, no. 1, pp. 536–552, 2006.
- [6] Y. Dong and F. Yang, "Stability analysis and observer design for a class of nonlinear systems with multiple time-delays," *Advances in Difference Equations*, vol. 2013, article no. 147, 2013.
- [7] H. Sandberg, "A case study in model reduction of linear time-varying systems," *Automatica*, vol. 42, no. 3, pp. 467–472, 2006.
- [8] G. Obinata and B. Anderson, *Model Reduction for Control System Design*, Springer, Vienna, Austria, 2001.
- [9] Z.-Q. Qu, Y. Shi, and H. Hua, "A reduced-order modeling technique for tall buildings with active tuned mass damper," *Earthquake Engineering and Structural Dynamics*, vol. 30, no. 3, pp. 360–362, 2001.
- [10] H. Du, J. Boffa, and N. Zhang, "Active seismic response control of tall Buildings based on reduced order model," in *Proceedings of the American Control Conference*, vol. 1–12, pp. 1132–1137, Minneapolis, Minn, USA, June 2006.
- [11] B. C. Moore, "Principal component analysis in linear-systems: controllability, observability, and model-reduction," *IEEE Transactions on Automatic Control*, vol. 26, no. 1, pp. 17–32, 1981.
- [12] S. Gugercin and A. C. Antoulas, "A survey of model reduction by balanced truncation and some new results," *International Journal of Control*, vol. 77, no. 8, pp. 748–766, 2004.
- [13] Q. S. Li, "Reduced order control for wind-induced vibrations of tall buildings," *Structural Design of Tall and Special Buildings*, vol. 12, no. 2, pp. 177–190, 2003.
- [14] J.-N. Yang, "Application of optimal control theory to civil engineering structures," *Journal of the Engineering Mechanics Division*, vol. 101, no. 6, pp. 819–838, 1975.
- [15] S. Boyd, L. E. Ghaoui, E. Feron, and V. Balakrishnan, *Linear Matrix Inequalities in System and Control Theory*, Society for Industrial and Applied Mathematics (SIAM), Philadelphia, Pa, USA, 1994.
- [16] X. R. Mao, N. Koroleva, and A. Rodkina, "Robust stability of uncertain stochastic differential delay equations," *Systems and Control Letters*, vol. 35, no. 5, pp. 325–336, 1998.
- [17] X. Mao, "Robustness of exponential stability of stochastic differential delay equations," *IEEE Transactions on Automatic Control*, vol. 41, no. 3, pp. 442–447, 1996.
- [18] Y. Chen and A.-K. Xue, "Improved stability criterion for uncertain stochastic delay systems with nonlinear uncertainties," *Electronics Letters*, vol. 44, no. 7, pp. 458–459, 2008.
- [19] W.-H. Chen, Z.-H. Guan, and X. Lu, "Delay-dependent exponential stability of uncertain stochastic systems with multiple delays: an LMI approach," *Systems & Control Letters*, vol. 54, no. 6, pp. 547–555, 2005.
- [20] S. Xu and T. Chen, "Robust  $H_\infty$  control for uncertain stochastic systems with state delay," *IEEE Transactions on Automatic Control*, vol. 47, no. 12, pp. 2089–2094, 2002.
- [21] S. Y. Xu and T. W. Chen, " $H_\infty$  output feedback control for uncertain stochastic systems with time-varying delays," *Automatica*, vol. 40, no. 12, pp. 2091–2098, 2004.
- [22] S. Xu, J. Lam, G.-H. Yang, and J. Wang, "Stabilization and  $H_\infty$  control for uncertain stochastic time-delay systems via non-fragile controllers," *Asian Journal of Control*, vol. 8, no. 2, pp. 197–200, 2006.
- [23] H. Liu, G. Duan, and L. Fan, "Delay-dependent passive control of stochastic differential system with time delay," in *Proceedings of the 8th World Congress on Intelligent Control and Automation (WCICA '10)*, pp. 963–968, Jinan, China, July 2010.
- [24] S. S. Chang and T. K. Peng, "Adaptive guaranteed cost control of systems with uncertain parameters," *IEEE Transactions on Automatic Control*, vol. 17, no. 4, pp. 474–483, 1972.
- [25] X.-P. Guan and C.-L. Chen, "Delay-dependent guaranteed cost control for T-S fuzzy systems with time delays," *IEEE Transactions on Fuzzy Systems*, vol. 12, no. 2, pp. 236–249, 2004.
- [26] B. Chen and X. P. Liu, "Fuzzy guaranteed cost control for nonlinear systems with time-varying delay," *IEEE Transactions on Fuzzy Systems*, vol. 13, no. 2, pp. 238–249, 2005.
- [27] M. Ikeda and T. Ashida, "Stabilization of linear system with time-varying delay," *IEEE Transactions on Automatic Control*, vol. 24, no. 2, pp. 369–370, 1979.
- [28] E. Cheres, Z. J. Palmor, and S. Gutman, "Quantitative measures of robustness for systems including delayed perturbations," *IEEE Transactions on Automatic Control*, vol. 34, no. 11, pp. 1203–1204, 1989.
- [29] H. S. Wu and K. Mizukami, "Robust stabilization of uncertain linear dynamical systems with time-varying delay," *Journal of Optimization Theory and Applications*, vol. 82, no. 3, pp. 593–606, 1994.
- [30] S. Moheimani and I. R. Petersen, "Optimal quadratic guaranteed cost control of a class of uncertain time-delay systems," *IEEE Proceedings-Control Theory and Applications*, vol. 144, no. 2, pp. 183–188, 1997.
- [31] C. Qu, L. Huo, and H. Li, "Fault tolerant control for civil structures based on LMI approach," *Mathematical Problems in Engineering*, vol. 2013, Article ID 762385, 8 pages, 2013.
- [32] A. J. Laub, M. T. Heath, C. C. Paige, and R. C. Ward, "Computation of system balancing transformations and other applications of simultaneous diagonalization algorithms," *IEEE Transactions on Automatic Control*, vol. 32, no. 2, pp. 115–122, 1987.
- [33] AASHTO, *AASHTO LRFD Bridge Design Specifications*, American Association of State Highway and Transportation Officials, Washington, DC, USA, 5th edition, 2012.
- [34] Caltrans, *Caltrans Seismic Design Criteria Version 1.7*, California Department of Transportation, Sacramento, Calif, USA, 2013.
- [35] S. Sastry, *Lyapunov Stability Theory*, Springer, New York, NY, USA, 1999.
- [36] F. Zhang, Ed., *The Schur Complement and its Applications*, vol. 4 of *Numerical Methods and Algorithms*, Springer-Verlag, 2005.
- [37] R. W. Clough and J. Penzien, *Dynamics of Structures*, McGraw-Hill, New York, NY, USA, 1975.
- [38] E. J. Hannan, "The identification of vector mixed autoregressive-moving average system," *Biometrika*, vol. 56, no. 1, pp. 223–225, 1969.
- [39] J. Teng, H. B. Xing, W. Lu, Z. H. Li, and C. J. Chen, "Influence analysis of time delay to active mass damper control system using pole assignment method," *Mechanical Systems and Signal Processing*, vol. 80, pp. 99–116, 2016.

## Research Article

# HOC Based Blind Identification of Hydroturbine Shaft Volterra System

Bing Bai<sup>1</sup> and Lixiang Zhang<sup>2</sup>

<sup>1</sup>*School of Civil Engineering and Communication, North China University of Water Resources & Electric Power, Beihuan Road No. 36, Zhengzhou, Henan 450045, China*

<sup>2</sup>*Department of Engineering Mechanics, Kunming University of Science and Technology, South Jingming Road No. 727, Kunming, Yunnan 650500, China*

Correspondence should be addressed to Bing Bai; [baibing7777@ncwu.edu.cn](mailto:baibing7777@ncwu.edu.cn)

Received 30 July 2016; Revised 9 November 2016; Accepted 5 December 2016; Published 10 January 2017

Academic Editor: Angelo M. Tusset

Copyright © 2017 B. Bai and L. Zhang. This is an open access article distributed under the Creative Commons Attribution License, which permits unrestricted use, distribution, and reproduction in any medium, provided the original work is properly cited.

In order to identify the quadratic Volterra system simplified from the hydroturbine shaft system, a blind identification method based on the third-order cumulants and a reversely recursive method are proposed. The input sequence of the system under consideration is an unobservable independent identically distributed (i.i.d.), zero-mean and non-Gaussian stationary signal, and the observed signals are the superposition of the system output signal and Gaussian noise. To calculate the third-order moment of the output signal, a computer loop judgment method is put forward to determine the coefficient. When using optimization method to identify the time domain kernels, we combined the traditional optimization algorithm (direct search method) with genetic algorithm (GA) and constituted the hybrid genetic algorithm (HGA). Finally, according to the prototype observation signal and the time domain kernel parameters obtained from identification, the input signal of the system can be gained recursively. To test the proposed method, three numerical experiments and engineering application have been carried out. The results show that the method is applicable to the blind identification of the hydroturbine shaft system and has strong universality; the input signal obtained by the reversely recursive method can be approximately taken as the random excitation acted on the runner of the hydroturbine shaft system.

## 1. Introduction

There are lots of nonlinear phenomena in engineering. Knowing of the coherent characteristics is of great importance to engineering safety. Thus exploring an appropriate method to describe an input-output relation defined by the nonlinear system has been a hot research topic. At present, Volterra series is a commonly used technique in researchers, and achievements are involved with plenty of engineering fields. Maheswaran and Khosa [1, 2] use a Volterra series model with wavelet functions to identify the nonlinearity of a natural stream flow and to forecast the water levels in groundwater system, respectively. In forensic investigation, a filter designed with Volterra series can well work when it is necessary to identify the latent fingerprints [3]. A nonlinear phenomenon that is produced by a distorted harmonic audible signal is recognized by estimating sound pressure level with

Volterra series [4]. In addition, the nonlinear structure response of a large container carrier in irregular seaway is calculated with a third-order Volterra model [5]. For a multiple input-multiple output (MIMO) system, a topological assemblage scheme is developed to make synthesis of Volterra system and applied to engineering, such as vibration analysis of wind-excited suspended cable [6].

The applications of Volterra series are mainly demonstrated in two aspects, that is, modeling and identification of an input-output system. Two important properties of Volterra series are (1) output of a Volterra system depends linearly on kernel parameters of this system; (2) nonlinearity of a signal can be represented throughout multidimensional operators on product of samples. Therefore, Volterra model is generally used to describe the input-output relationship of a nonlinear system in a long term. Nonlinear systems, such as system with additive white Gaussian noises [7], structure subjected to

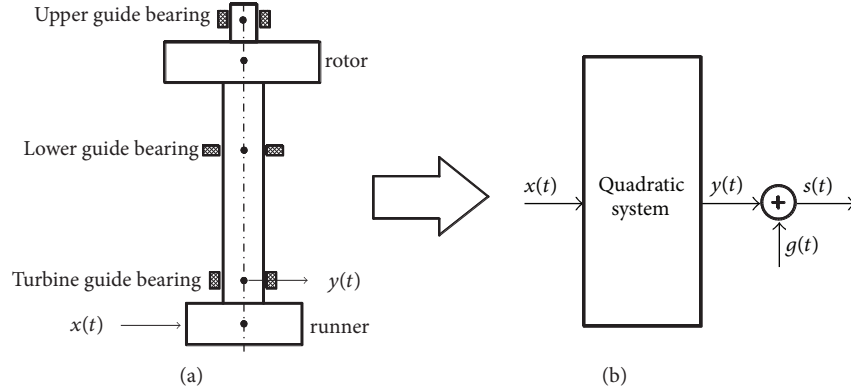


FIGURE 1: Hydroturbine shaft system and quadratic Volterra system.

impact load [8], and turbomachinery [9], can be represented by Volterra series. Systems with multispectral properties are also reported [10, 11].

Peng et al. make a lot of achievements on the modeling, identification, and prediction with Volterra series [12–14]. They discussed lots of problems, for instance, the influence on the force transmissibility of MDOF structures with cubic nonlinear damping device [12], a new method to detect the breathing fatigue crack in nonlinear beam [13] and the analytical expression of calculating the bispectrum with higher order cumulants for nonlinear systems subjected to zero-mean Gaussian excitation [14]. These works highly prove the advantages of Volterra series in describing a nonlinear system and the convenience for derivation of the subsequent formulae.

It is fundamental to use Volterra series method to identify a nonlinear system. Take Duffing oscillator as an example, its “jump” phenomenon can be recognized by the Volterra series method [15], which is expanded to identify a bilinear oscillator [16]. To deal with identification problems more effectively, Volterra series is usually combined with an optimization method [17]. However, the input signal of a nonlinear system is not always known. Thus the blind identification method without the input signal is developed. Le Caillec [18] blindly identified a second-order Wiener model driven by a Gaussian noise with corrupted output data. Ghandchi Tehrani et al. [19] compared the Volterra series method with the harmonic balance method, which proves the ability of blind identification by the Volterra series method.

Actually, when Volterra series is employed to model and blindly identify a nonlinear system, it needs to often meet the situation in which higher order cumulants are used. Antari et al. [20, 21] considered the third-order and fourth-order cumulants to blindly identify a Hammerstein system. However, the expression of higher cumulants sometimes seems to be quite complicated [22]. For a hydroturbine main shaft system in a hydropower station, the nonlinear input-output relation is very complicated. Especially for the input signals, such as the hydraulic excitation on the runner, its working mechanisms are not completely known so far. On the contrary, the corresponding output signals, such as the throw at turbine guide bearing, are always easy to be obtained.

Thus it is a mathematical problem which needs to be solved frequently in hydraulic engineering to identify the whole shaft system with the observed vibration response only.

This paper proposes a novel blind identification method based on higher order cumulants for a nonlinear system described by a hydroturbine shaft Volterra model. A computer loop judgment method is used to determine the coefficients  $\gamma_{ijk}$  when the third-order moment of the input signal is calculated. It greatly simplifies formula and algorithm. Finally, the Volterra kernel parameters of the nonlinear system under consideration are identified by the hybrid genetic algorithm (HGA).

## 2. Description of System

The shaft system of a certain hydroturbine generating set can be simplified as a quadratic Volterra model, as shown in Figure 1. The input sequence of the system is  $\{x(t)\}$ , representing the hydraulic excitation on the runner; the output sequence  $\{y(t)\}$  denotes the dynamic displacements at turbine guide bearing; the observed signal is  $\{s(t)\}$ , and Gaussian noise is  $\{g(t)\}$ .

The corresponding nonlinear system is described as

$$y(t) = \sum_{i=0}^q \sum_{j=0}^q h(i, j) x(t-i) x(t-j), \quad (1)$$

$$s(t) = y(t) + g(t), \quad (2)$$

where  $t$  stands for the discrete time,  $h(i, j)$  stands for the time domain kernels of the quadratic nonlinear system, and  $q$  represents the system memory length ( $q + 1$ ), and  $i, j$  are the time delay. The excitation sequence  $\{x(t)\}$  of the system is an unobservable, independent identically distributed (i.i.d.), zero-mean and non-Gaussian stationary signal. It is assumed that the following equations hold:

$$\begin{aligned} \gamma_{2x} &= E[x^2(t)] \neq 0, \\ \gamma_{3x} &= E[x^3(t)] \neq 0, \\ \gamma_{4x} &= E[x^4(t)] \neq 0, \\ \gamma_{6x} &= E[x^6(t)] \neq 0, \end{aligned} \quad (3)$$

where  $\gamma_{m,x}$  stands for the  $m^{\text{th}}$ -order moment at the origin of the input signal. It is proved that, when  $\{x(t)\}$  is a zero-mean sequence, the following properties [22] hold:

$$E\{x(t_1) \cdots x(t_6)\} = \begin{cases} \gamma_{6x} & \text{if } t_1 = t_2 = t_3 = t_4 = t_5 = t_6 \\ \gamma_{4x}\gamma_{2x} & \text{if } t_1 = t_2 \neq t_3 = t_4 = t_5 = t_6 \\ \gamma_{3x}^2 & \text{if } t_1 = t_2 = t_3 \neq t_4 = t_5 = t_6 \\ \gamma_{2x}^3 & \text{if } t_1 = t_2 \neq t_3 = t_4 \neq t_5 = t_6 \\ 0 & \text{otherwise.} \end{cases} \quad (4)$$

Letting  $C_{m,y}(\tau_1, \dots, \tau_{m-1})$  and  $C_{m,s}(\tau_1, \dots, \tau_{m-1})$  be cumulants of the output sequence and the observed sequence, respectively, a relationship between the higher order cumulants (HOC) and time domain kernels  $h(i, j)$  of the quadratic nonlinear system is established by calculation. In the present study, we try to establish a relationship between the third-order cumulants of the observed signal and time domain kernels  $h(i, j)$ . Because the third-order or higher order cumulants of the Gaussian noise are zero, we obtain from (2) the following:

$$C_{3s}(\tau_1, \tau_2) = C_{3y}(\tau_1, \tau_2) + C_{3g}(\tau_1, \tau_2) = C_{3y}(\tau_1, \tau_2). \quad (5)$$

Therefore, the third-order cumulants of the output sequence  $\{y(t)\}$  need to only be calculated. For a stationary random sequence  $\{y(t)\}$ , the third-order cumulants are defined as

$$\begin{aligned} C_{3y}(\tau_1, \tau_2) &= M_{3y}(\tau_1, \tau_2) \\ &\quad - M_{1y} [M_{2y}(\tau_1) + M_{2y}(\tau_2) + M_{2y}(\tau_2 - \tau_1)] \\ &\quad + 2(M_{1y})^3, \end{aligned} \quad (6)$$

where  $M_{1y}$ ,  $M_{2y}(\tau)$ , and  $M_{3y}(\tau_1, \tau_2)$  denote the first-order moment, second-order moment, and third-order moment of the sequence  $\{y(t)\}$ , respectively. The specific expression of  $M_{1y}$  is stated as

$$\begin{aligned} M_{1y} &= \sum_{i=0}^q \sum_{j=0}^q h(i, j) E\{x(t-i)x(t-j)\} \\ &= \gamma_{2x} \cdot \sum_{i=0}^q h(i, i). \end{aligned} \quad (7)$$

It implies that when  $i, j$  are not equal, the expectation value is zero; only the diagonal elements  $h(i, i)$  are left for the time domain kernels  $h(i, j)$ .  $M_{2y}(\tau)$  is as follows:

$$\begin{aligned} M_{2y}(\tau) &= E\{y(t)y(t+\tau)\} \\ &= \sum_{i_1, i_2, j_1, j_2=0}^q \gamma_{ij} \cdot h(i_1, i_2) h(j_1, j_2), \end{aligned} \quad (8)$$

where  $\gamma_{ij}$  is the coefficient, which consists of the second-order moment or the fourth-order moment of the input signal  $\{x(t)\}$ , and the value depends on the different time delay of the sequence  $\{x(t)\}$ . Among the four subscripts  $-i_1, -i_2, \tau - j_1$ , and  $\tau - j_2$ , if the value of one subscript (time) is different from the rest of the three, the expectation is zero, and  $\gamma_{ij} = 0$ . The values of  $\gamma_{ij}$  are yielded as

$$\gamma_{ij} = \begin{cases} \gamma_{4x} & \text{if } -i_1 = -i_2 = \tau - j_1 = \tau - j_2 \\ \gamma_{2x}^2 & \text{if } -i_1 = -i_2 \neq \tau - j_1 = \tau - j_2, \text{ or} \\ & \text{if } -i_1 = \tau - j_1 \neq -i_2 = \tau - j_2, \text{ or} \\ & \text{if } -i_1 = \tau - j_2 \neq -i_2 = \tau - j_1 \\ 0 & \text{otherwise.} \end{cases} \quad (9)$$

In order to calculate the three second-order cumulants in (6), we substitute  $\tau$ , respectively, by  $\tau_1$ ,  $\tau_2$ , and  $\tau_2 - \tau_1$  in (8). The expression of the last term  $M_{3y}(\tau_1, \tau_2)$  in (6) is written as

$$\begin{aligned} M_{3y}(\tau_1, \tau_2) &= E\{y(t)y(t+\tau_1)y(t+\tau_2)\} \\ &= \sum_{i_1, i_2, j_1, j_2, k_1, k_2=0}^q \gamma_{ijk} \cdot h(i_1, i_2) h(j_1, j_2) h(k_1, k_2) \end{aligned} \quad (10)$$

in which coefficient  $\gamma_{ijk}$  is composed of one or several certain order moments of the input signal sequence  $\{x(t)\}$ . According to the different time delay of the sequence  $\{x(t)\}$ , the different values are obtained as

$$\gamma_{ijk} = \begin{cases} \gamma_{6x} & \text{if } -i_1 = -i_2 = \tau_1 - j_1 = \tau_1 - j_2 = \tau_2 - k_1 = \tau_2 - k_2 \\ \gamma_{4x}\gamma_{2x} & \text{if } -i_1 = -i_2 \neq \tau_1 - j_1 = \tau_1 - j_2 = \tau_2 - k_1 = \tau_2 - k_2 \\ \gamma_{3x}^2 & \text{if } -i_1 = -i_2 = \tau_1 - j_1 \neq \tau_1 - j_2 = \tau_2 - k_1 = \tau_2 - k_2 \\ \gamma_{2x}^3 & \text{if } -i_1 = -i_2 \neq \tau_1 - j_1 = \tau_1 - j_2 \neq \tau_2 - k_1 = \tau_2 - k_2 \\ 0 & \text{otherwise.} \end{cases} \quad (11)$$

The judgment of the first line  $\gamma_{6x}$  is simple, and the judgments of the rest  $\gamma_{4x}\gamma_{2x}$ ,  $\gamma_{3x}^2$ , and  $\gamma_{2x}^3$  are relatively complicated since there exist a variety of different combinations, and all combinations need to compile a programming code to loop for judgment, which is called as a method on the computer loop judgment (details in the Appendix). With this method, it is possible to calculate the second-order moment and third-order moment of the output sequence  $\{y(t)\}$  and to have a great superiority in computing.

### 3. Hybrid Genetic Algorithm

**3.1. Consistent Estimate.** For a known observed signal  $\{s(t)\}$ , we need to have an expectation operation. Because the number of the observed signals is limited, it is difficult to precisely calculate the expectation required. So, an approximating

method is used to calculate this value by consistent estimate; namely,

$$\begin{aligned} \widehat{C}_{3s}(\tau_1, \tau_2) &= \widehat{M}_{3s}(\tau_1, \tau_2) \\ &\quad - \widehat{M}_{1s} \left[ \widehat{M}_{2s}(\tau_1) + \widehat{M}_{2s}(\tau_2) + \widehat{M}_{2s}(\tau_2 - \tau_1) \right] \\ &\quad + 2 \left( \widehat{M}_{1s} \right)^3, \end{aligned} \quad (12)$$

$$\widehat{M}_{3s}(\tau_1, \tau_2) = \frac{1}{N} \sum_{n=1}^N s(n) s(n + \tau_1) s(n + \tau_2), \quad (13)$$

$$\widehat{M}_{2s}(\tau) = \widehat{R}_s(\tau) = \frac{1}{N} \sum_{n=1}^N s(n) s(n + \tau), \quad (14)$$

$$\widehat{M}_{1s} = \widehat{\mu}_s = \frac{1}{N} \sum_{n=1}^N s(n). \quad (15)$$

In order to complete the consistent estimate of the third-order cumulants in (12), we replace  $\tau$  with  $\tau_1$ ,  $\tau_2$ , and  $\tau_2 - \tau_1$  in (14), respectively.

**3.2. Algorithm.** The hybrid genetic algorithm (HGA) is an intelligent optimization algorithm which combines the simple genetic algorithm (SGA) with the traditional optimization methods.

As we know, for a kind of optimization algorithm, the global search ability of the genetic algorithm (GA) is very strong. However, when the search process is close to a local optimal point, its local search ability starts to become poor. That is a shortcoming of the simple genetic algorithm. On the contrary, the traditional direct search method of discrete variables is lack of global search ability, although the local search ability is very strong. Therefore, the authors make a hybrid genetic algorithm by combining the traditional direct search method with the genetic algorithm. The hybrid genetic algorithm (HGA) improves the ability of the global and local searches in calculation.

The basic steps of HGA are sentenced in the process of GA. The local search is carried out in a certain probability  $p_h$  (for example 5%) to find out a local optimal point as soon as possible. Then it goes back to the genetic operation for the global search to complete the global search. The flow chart of HGA is as shown in Figure 2.

**3.3. Blind Identification of Time Domain Kernels.** Through the above derivation, we calculate the consistent estimates of the third-order cumulants of the observed signal  $\{s(t)\}$  by using (12) and (13)–(15). On the other hand, we obtain a relationship between time-domain kernels  $h(i, j)$  of the nonlinear system and the third-order cumulants by using (6) and (7)–(11). Thus, letting (6) equal (12), we obtain an equation as

$$\begin{aligned} \widehat{C}_{3s}(\tau_1, \tau_2) &= M_{3y}(\tau_1, \tau_2) \\ &\quad - M_{1y} \left[ M_{2y}(\tau_1) + M_{2y}(\tau_2) + M_{2y}(\tau_2 - \tau_1) \right] \\ &\quad + 2 \left( M_{1y} \right)^3. \end{aligned} \quad (16)$$

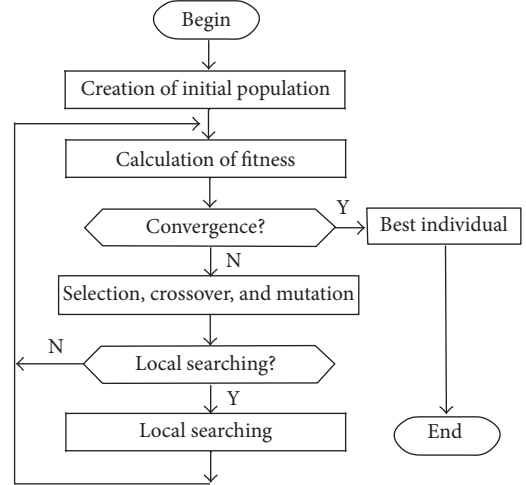


FIGURE 2: Flow chart of hybrid GA.

Obviously, this is a cubic nonlinear equation with unknown  $h(i, j)$ . By solving this equation,  $h(i, j)$  is obtained. It is noted that because the output signal of the system is only used in calculation, namely, no input signal  $\{x(t)\}$  is needed, so this identification method is called blind identification.

In actual application, the third-order cumulants of  $(q+1)^2$  have to be computed; that is,  $C_{3y}(\tau_1, \tau_2)$ ,  $0 \leq \tau_1, \tau_2 \leq q$ . Since it is not easy to directly solve a cubic nonlinear system, the above-mentioned HGA is proposed to solve (16). The objective function (the fitness value of an individual) of the optimization problem is as follows:

$$\min F(\mathbf{h}) = \sum_{\tau_1=0}^q \sum_{\tau_2=\tau_1}^q \left[ C_{3y}(\tau_1, \tau_2) - \widehat{C}_{3s}(\tau_1, \tau_2) \right]^2, \quad (17)$$

where  $\mathbf{h}$  is the unknown column matrix composed of the elements in time domain kernels  $h(i, j)$ . Due to the symmetry properties of the third-order cumulants, namely,  $C_{3y}(\tau_1, \tau_2) = C_{3y}(\tau_2, \tau_1)$ , the loop variable  $\tau_2$  in (17) increases from  $\tau_1$  to  $q$ .

For HGA, when the Gaussian noise is zero-mean i.i.d. signal, the following constraint condition can be used:

$$\left| M_{1y} - \widehat{M}_{1s} \right| \leq \varepsilon, \quad (18)$$

where  $\varepsilon$  denotes the admissible error of the constraint condition. Comparing (7) with (15), it is seen that the introduction of the constraint (18) can guarantee the small deviation of the diagonal elements  $h(i, i)$  in kernels  $h(i, j)$  to be identified.

TABLE 1: Identified results [EI: diagonal element  $h(i, i)$ ].

	True values	SNR = 0 dB	SNR = 20 dB	SNR = 40 dB	SNR = $\infty$
		Mean $\pm$ SD	Mean $\pm$ SD	Mean $\pm$ SD	Mean $\pm$ SD
$h(0, 0)$	1.00	0.9437 $\pm$ 0.1250	0.9877 $\pm$ 0.0913	0.9930 $\pm$ 0.0857	0.9962 $\pm$ 0.0685
$h(1, 1)$	-0.30	-0.2460 $\pm$ 0.1368	-0.3018 $\pm$ 0.1124	-0.2997 $\pm$ 0.1138	-0.3010 $\pm$ 0.1145
$h(2, 2)$	-0.85	-0.7958 $\pm$ 0.1394	-0.8328 $\pm$ 0.1003	-0.8377 $\pm$ 0.1001	-0.8390 $\pm$ 0.0872
$h(3, 3)$	0.66	0.6053 $\pm$ 0.1356	0.6557 $\pm$ 0.0981	0.6540 $\pm$ 0.0990	0.6534 $\pm$ 0.0953
$F$		0.751054E - 01	0.316731E - 02	0.314600E - 02	0.357726E - 02

TABLE 2: Identified results [EI: full element  $h(i, j)$ ].

	True values	SNR = 0 dB	SNR = 20 dB	SNR = 40 dB	SNR = $\infty$
		Mean $\pm$ SD	Mean $\pm$ SD	Mean $\pm$ SD	Mean $\pm$ SD
$h(0, 0)$	1.00	0.9568 $\pm$ 0.0631	0.9745 $\pm$ 0.0575	0.9783 $\pm$ 0.0610	0.9731 $\pm$ 0.0501
$h(0, 1)$	0	-0.0161 $\pm$ 0.0768	-0.0162 $\pm$ 0.0712	0.0001 $\pm$ 0.0712	-0.0071 $\pm$ 0.0717
$h(0, 2)$	0	0.0054 $\pm$ 0.0658	-0.0038 $\pm$ 0.0602	-0.0045 $\pm$ 0.0645	-0.0083 $\pm$ 0.0624
$h(0, 3)$	0	-0.0147 $\pm$ 0.0426	-0.0061 $\pm$ 0.0501	-0.0162 $\pm$ 0.0517	-0.0186 $\pm$ 0.0533
$h(1, 1)$	-0.30	-0.2752 $\pm$ 0.0687	-0.2928 $\pm$ 0.0706	-0.2935 $\pm$ 0.0733	-0.2948 $\pm$ 0.0668
$h(1, 2)$	0	-0.0484 $\pm$ 0.0785	-0.0212 $\pm$ 0.0693	-0.0405 $\pm$ 0.0600	-0.0294 $\pm$ 0.0635
$h(1, 3)$	0	0.0012 $\pm$ 0.0676	-0.0012 $\pm$ 0.0579	-0.0063 $\pm$ 0.0597	-0.0047 $\pm$ 0.0570
$h(2, 2)$	-0.85	-0.8289 $\pm$ 0.0668	-0.8324 $\pm$ 0.0678	-0.8348 $\pm$ 0.0713	-0.8328 $\pm$ 0.0598
$h(2, 3)$	0	-0.0096 $\pm$ 0.0782	-0.0191 $\pm$ 0.0627	-0.0143 $\pm$ 0.0579	-0.0044 $\pm$ 0.0632
$h(3, 3)$	0.66	0.6448 $\pm$ 0.0604	0.6543 $\pm$ 0.0627	0.6528 $\pm$ 0.0639	0.6534 $\pm$ 0.0516
$F$		0.693044E - 01	0.201256E - 02	0.184063E - 02	0.259258E - 02

#### 4. Numerical Experiment

To examine the proposed method, two quadratic nonlinear Volterra systems, E1 by (19) and E2 by (20), are herein considered as

$$y(n) = x^2(n) - 0.30x^2(n-1) - 0.85x^2(n-2) + 0.66x^3(n-3), \quad (19)$$

$$y(n) = x^2(n) - 0.3x(n)x(n-1) + 0.5x(n)x(n-2) - 0.26x(n)x(n-3) - 0.30x^2(n-1) + 0.36x(n-1)x(n-2) - 0.28x(n-1)x(n-3) - 0.85x^2(n-2) - 0.2x(n-2)x(n-3) + 0.66x^2(n-3). \quad (20)$$

In (19) and (20),  $n$  is used to replace time  $t$ , to denote discrete time.

Because (19) is of completely squared terms, the coefficients of each term are the true solutions. Therefore, the true solutions of E1 are

$$h(i, i) = [1.00 \quad -0.30 \quad -0.85 \quad 0.66]. \quad (21)$$

In (20), the coefficient of a squared term is the true solution; however, half of the coefficient of a cross term is the true solution. Hence the true values of E2 are

$$h(i, j) = \begin{bmatrix} 1.00 & -0.15 & 0.25 & -0.13 \\ & -0.30 & 0.18 & -0.14 \\ & & -0.85 & -0.10 \\ \text{sym} & & & 0.66 \end{bmatrix}. \quad (22)$$

The input signal  $x_0(n)$  is generated by RAND command in MATLAB. Their lengths are 1024 and 8192, and each has 50 groups. Then the generated uniform white noises are scaled as independent identically distributed (i.i.d.) signal with variance 1. Assuming that the memory length of the model is  $M = q + 1 = 4$ , the simulation is under the condition of 50 Monte-Carlo runs. At the same time, the different values of the signal-to-noise ratio (SNR) defined by (23) are considered [20]:

$$\text{SNR} = 10 \cdot \log_{10} \left[ \frac{E(y^2(t))}{E(g^2(t))} \right]. \quad (23)$$

Only the diagonal elements exist in the time domain kernels  $h(i, i)$  of EI; in other words, the system is a simplified Volterra Model: Hammerstein Model. The identification results are listed in Table 1 for four cases of SNR = 0, 20, 40,  $\infty$ . At the same time, to assess the universality of the method, the time domain  $h(i, i)$  is identified by treating it as a full matrix with element  $h(i, j)$ . The results are listed in Table 2. The time

TABLE 3: Identified results [E2: full element  $h(i, j)$ ].

	True values	SNR = 0 dB	SNR = 20 dB	SNR = 40 dB	SNR = $\infty$
		Mean $\pm$ SD	Mean $\pm$ SD	Mean $\pm$ SD	Mean $\pm$ SD
$h(0, 0)$	1.00	0.9793 $\pm$ 0.0689	1.0118 $\pm$ 0.0523	1.0138 $\pm$ 0.0546	1.0191 $\pm$ 0.0507
$h(0, 1)$	-0.15	-0.1713 $\pm$ 0.0945	-0.1395 $\pm$ 0.0593	-0.1364 $\pm$ 0.0543	-0.1319 $\pm$ 0.0518
$h(0, 2)$	0.25	0.2185 $\pm$ 0.1070	0.2273 $\pm$ 0.0789	0.2324 $\pm$ 0.0768	0.2282 $\pm$ 0.0773
$h(0, 3)$	-0.13	-0.0719 $\pm$ 0.0953	-0.0890 $\pm$ 0.0604	-0.0907 $\pm$ 0.0609	-0.0972 $\pm$ 0.0564
$h(1, 1)$	-0.30	-0.3062 $\pm$ 0.0699	-0.3024 $\pm$ 0.0604	-0.3071 $\pm$ 0.0620	-0.3167 $\pm$ 0.0599
$h(1, 2)$	0.18	0.2247 $\pm$ 0.0913	0.1723 $\pm$ 0.0654	0.1765 $\pm$ 0.0580	0.1812 $\pm$ 0.0529
$h(1, 3)$	-0.14	-0.0892 $\pm$ 0.1079	-0.1223 $\pm$ 0.0693	-0.1246 $\pm$ 0.0704	-0.1183 $\pm$ 0.0685
$h(2, 2)$	-0.85	-0.8162 $\pm$ 0.0606	-0.8569 $\pm$ 0.0660	-0.8494 $\pm$ 0.0662	-0.8467 $\pm$ 0.0603
$h(2, 3)$	-0.10	-0.0878 $\pm$ 0.0777	-0.1008 $\pm$ 0.0520	-0.1014 $\pm$ 0.0518	-0.1001 $\pm$ 0.0513
$h(3, 3)$	0.66	0.6423 $\pm$ 0.0722	0.6586 $\pm$ 0.0707	0.6558 $\pm$ 0.0635	0.6567 $\pm$ 0.0611
$F$		0.107841E + 00	0.351261E - 02	0.340253E - 02	0.384778E - 02

domain kernels  $h(i, j)$  of E2 are originally full matrix with the elements, and the E2's results are listed in Table 3.

It is seen from Tables 1–3 that the proposed method is suitable to well identify the quadratic nonlinear system under consideration. Table 1 shows that, when SNR = 0 dB, the relative errors of the four values of the time domain kernels  $h(i, i)$  are basically within 10%, and the standard deviation is between 0.12 and 0.14. With the increase of the signal-to-noise ratio, the relative errors are gradually reduced to less than 2%, and the standard deviation is to 0.06–0.11; the objective function value (sum of the square of the third-order cumulants errors) is also reduced. The identification error becomes large with the small SNR; this is due to the fact that there exists certain error between Gaussian noise signal generated by the numerical method and the real Gaussian distribution, which leads a direct effect of the identification results.

In Table 2, the same sequence to the signal data as Table 1 is used. The identified mean values of the nondiagonal elements are generally under 0.02 (the real value is 0), and the standard deviation is below 0.08. This is very important; when the blind identification method is used to identify a quadratic system, we do not know the length of the memory, or whether the time domain kernels  $h(i, j)$  have only the diagonal elements. By using different memory length to identify an identical system, we obtained very similar results, which show that this method has strong universality.

## 5. Blind Identification of Quadratic Volterra System of Number 4 Hydroturbine Shaft in a Certain Hydropower Station

The number 4 hydroturbine generating set shaft system in a certain hydropower station, as shown in Figure 1(a), can be simplified as a second-order Volterra system (shown in Figure 1(b)). The observed data of the lateral throw  $y_2(n)$  at the turbine guide bearing in the experiment is shown in Figure 3 (after filtration). These observed signals are taken as the output signals  $y(n)$ , and this engineering problem is identified according to the above proposed method. Note that, for the problem in which the input signals are unknown,

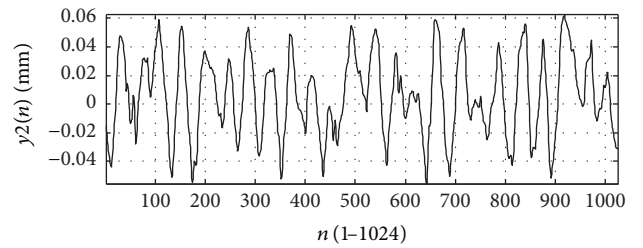


FIGURE 3: Transient wavelshape of the lateral throw at turbine guide bearing (filtered).

there is a precondition here: the input must be zero-mean, i.i.d., stationary signals, and their statistics are known.

According to the 50 groups of the zero-mean, i.i.d. stationary signals generated by MATLAB, the statistics of the input signals are chosen as follows:

$$\begin{aligned}
 \gamma_{2x} &= E[x^2(n)] = 1.000, \\
 \gamma_{3x} &= E[x^3(n)] = 2.645 \times 10^{-2}, \\
 \gamma_{4x} &= E[x^4(n)] = 1.800, \\
 \gamma_{6x} &= E[x^6(n)] = 3.900.
 \end{aligned} \tag{24}$$

The memory length of the system is taken as  $M_2 = q_2 + 1 = 6$ , so the time domain kernels parameters (optimization variables) to be identified are

$$h(i, j) = \begin{bmatrix} h(0, 0) & h(0, 1) & h(0, 2) & h(0, 3) & h(0, 4) & h(0, 5) \\ & h(1, 1) & h(1, 2) & h(1, 3) & h(1, 4) & h(1, 5) \\ & & h(2, 2) & h(2, 3) & h(2, 4) & h(2, 5) \\ & & & h(3, 3) & h(3, 4) & h(3, 5) \\ & & & & h(4, 4) & h(4, 5) \\ & & & & & h(5, 5) \end{bmatrix}. \tag{25}$$

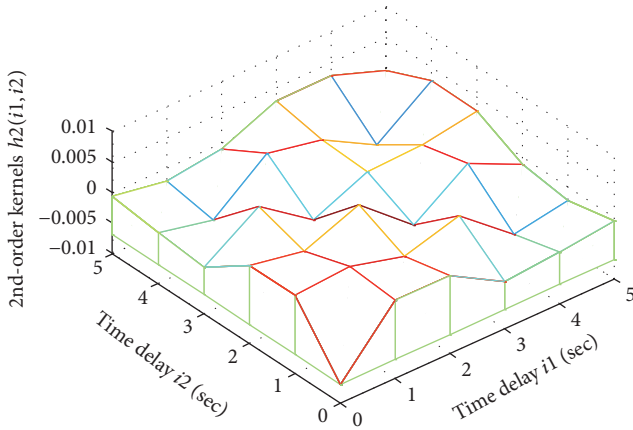


FIGURE 4: The second-order time domain kernels of the shaft system in overspeed test.

The system becomes an optimization problem with 21 design variables. When using HGA, we set the population as 50, crossover probability 50%, mutation probability 5%, and local search probability 5%. The lower and upper bounds of the variables are  $[-100, 100]$ , and the increment of the discrete variables is 0.01. The interval of each variable is narrowed down after some test run, and the increment of the discrete variables is ultimately decreased to 0.00001. The number of the evolution generations is one million.

After identification, the time domain kernels parameters  $h(i, j)$  of the Volterra system for this shaft system are obtained, as shown in Figure 4. The frequency domain kernels parameters (Generalized Frequency Response Function, GFRF) can be obtained by two-dimensional Fourier Transform, as shown in Figure 5.

So far, by use of the blind identification method proposed in this paper, the blind identification of the system was successfully carried out, based on the observed throw signals at the turbine guide bearing.

## 6. Reversely Recursive Solution to Hydraulic Excitation

**6.1. Reversely Recursive Algorithm.** The hydraulic excitation acted on the hydraulic turbine runner is very important in the design and calculation of shaft system in a hydroelectric generating set but difficult to be observed. A reversely recursive algorithm is proposed in the paper, which can be used to approximately find out the input signal of the system based on the following two sets of data: (1) the observed output signal  $y_0(n)$  of the system; (2) the system time domain kernels  $h(i, j)$  obtained through blind identification.

Expanding the second-order discretized time domain Volterra system (1), the specific expression of  $y(n)$  can be obtained. When  $n = 0$ , from the following expression:

$$y(0) = h(0, 0) x(0) x(0). \quad (26)$$

We can get

$$x(0) = \pm \sqrt{\frac{y_0(0)}{h(0, 0)}}, \quad (27)$$

where  $y_0(0)$  is the observed output signal of the system.  $x(0)$  thus obtained has two roots.

When  $n = 1$ ,

$$y(1) = h(0, 0) x(1) x(1) + h(0, 1) x(1) x(0) + h(1, 0) x(0) x(1) + h(1, 1) x(0) x(0) \quad (28)$$

in which  $x(0)$  is known and  $x(1)$  is unknown. Equation (28) becomes a quadratic equation of  $x(1)$ :

$$h(0, 0) x(1) x(1) + [h(0, 1) x(0) + h(1, 0) x(0)] x(1) + h(1, 1) x(0) x(0) - y(1) = 0. \quad (29)$$

Set  $a = h(0, 0)$ ,  $b = h(0, 1)x(0) + h(1, 0)x(0) = 2h(0, 1)x(0)$ , and  $c = h(1, 1)x(0)x(0) - y_0(1)$ ; then

$$a \cdot x(1) x(1) + b \cdot x(1) + c = 0. \quad (30)$$

So

$$x(1) = \frac{-b \pm \sqrt{b^2 - 4ac}}{2a}. \quad (31)$$

Because  $x(0)$  has two roots, substituting, respectively, the two roots into (31), we can obtain the four roots of  $x(1)$ . The question now is which roots should  $x(0)$  and  $x(1)$  take? The answer is obvious. First, calculate  $y(0)$  and  $y(1)$  through (26) and (28), then calculate the errors of  $y(0) - y_0(0)$  and  $y(1) - y_0(1)$ , and finally compare the errors. The roots with minimum error are the true solution. So we take

$$F = [y(1) - y_0(1)]^2 + [y(0) - y_0(0)]^2 \quad (32)$$

as the optimal objective function and find out the minimum value  $F_{\min}$  from several values of objective function  $F$ , and the corresponding  $x(0)$  and  $x(1)$  are taken as the true solution (input signal).

When the previous values of  $x(n-2)$  and the  $x(\cdot)$  have been confirmed, the general formulae for calculating  $x(n)$  are as follows:

$$y(n) = h(0, 0) x(n-0) x(n-0) + h(0, 1) x(n-0) x(n-1) + \dots + h(0, q) x(n-0) x(n-q) + h(1, 0) x(n-1) x(n-0) + h(1, 1) x(n-1) x(n-1) + \dots + h(1, q) x(n-1) x(n-q) + \dots + h(q, 0) x(n-q) x(n-0) + h(q, 1) x(n-q) x(n-1) + \dots + h(q, q) x(n-q) x(n-q). \quad (33)$$

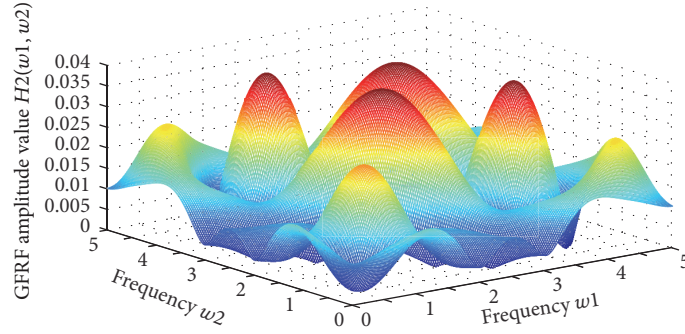


FIGURE 5: The frequency domain kernels of the shaft system in overspeed test.

Let  $a = h(0, 0)$ ,  $b = \sum_{i=1}^q 2 \cdot h(0, i)x(n - i)$ , and  $c = [\sum_{i=1}^q \sum_{j=1}^q h(i, j)x(n - i)x(n - j)] - y_0(n)$ ; thus

$$x(n) = \frac{-b \pm \sqrt{b^2 - 4ac}}{2a}. \quad (34)$$

Because  $x(n - 1)$  has two values, we can obtain the four roots of  $x(n)$ . In order to determine  $x(n - 1)$  and  $x(n)$ , we still use optimization method. The objective function for optimization is

$$F = \sum_{i=0}^q [y(n - i) - y_0(n - i)]^2. \quad (35)$$

Finding the minimum value  $F_{\min}$ , the corresponding  $x(n - 1)$  and  $x(n)$  can be taken as the input signal. Thus through recursive calculation, we can find out  $x(0) \sim x(N)$ ; here  $N + 1$  is the sampling length. The above method is the reversely recursive algorithm.

**6.2. Numerical Experiment E2.** For convenience, we still use the experimental data E2 in Section 4. According to the above method, the calculated input data  $x(n)$  can be obtained, as shown in Figure 6, where  $xx(n)$  is the calculated result and  $x0(n)$  is the original input signal.

To illustrate the correctness and feasibility of the calculation results, substituting in (1) the calculated results  $xx(n)$  and the original input signal  $x0(n)$ , respectively, we can find out the output signal  $y(n)$  and the original output signal  $y0(n)$  and their differences:

$$dy(n) = |y(n) - y_0(n)| \quad (36)$$

and draw in Figure 7. At the same time, the relative error of output signal energy is calculated by using the following formula:

$$R_E = \frac{\sum y^2(n) - \sum y_0^2(n)}{\sum y_0^2(n)} \times 100\%. \quad (37)$$

From Figures 6 and 7 we can see that, by the reversely recursive method proposed in this paper, we can approximately find out the input signal of the system based on the system output signal. The calculated input signal  $xx(n)$  is slightly

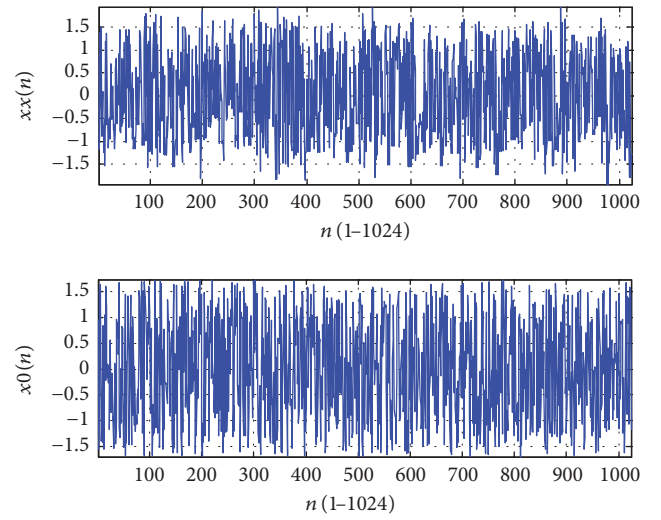


FIGURE 6: E2 numerical experiment results (input signals).

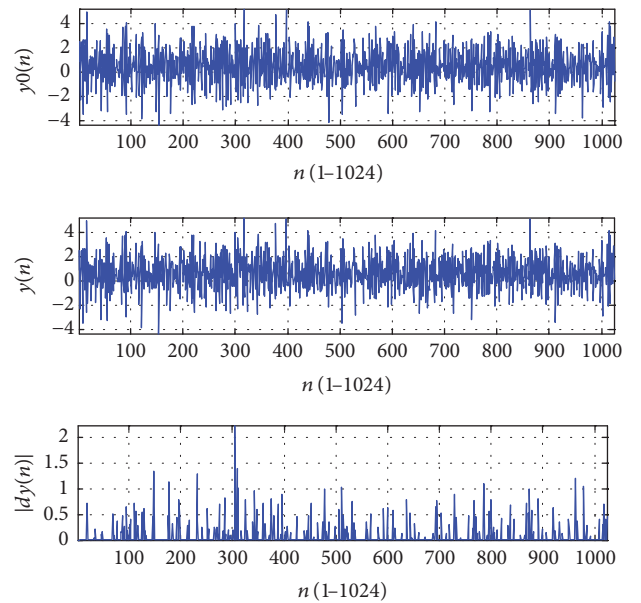


FIGURE 7: The comparison of the calculated output signals to the original observed signals.

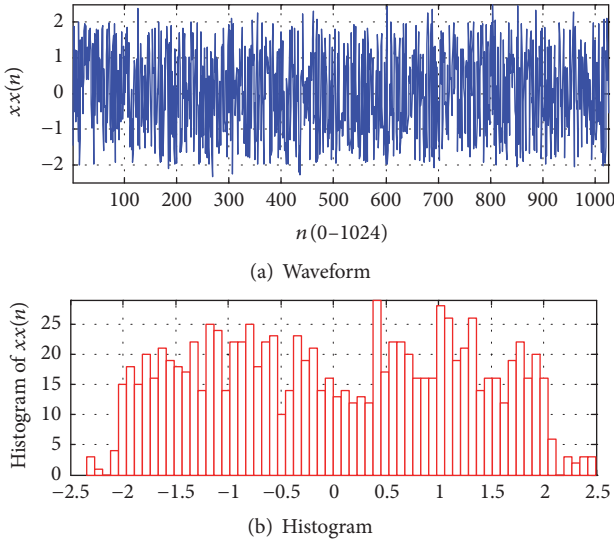


FIGURE 8: The input signals calculated by recursive method and their histogram.

different from the original input signal  $x_0(n)$ , which is mainly caused by the quadratic nonlinearity of the system. However, the errors  $dy(n)$  between the system output signal  $y(n)$  calculated through the input signal  $xx(n)$  and the original output signal  $y_0(n)$  are smaller (Figure 7). Only a few signal values have errors, and most output signal values are the same as the original value. The relative error of the output signal energy by (37) is only 3.96%. Therefore, the input data  $xx(n)$  thus calculated can be approximately used as the system input signal.

**6.3. Reversely Recursive Solution to Hydraulic Excitation on Turbine.** The hydraulic excitation (input signal)  $xx(n)$  on the turbine runner and its distribution can be calculated recursively using the proposed method in Section 6.1, as shown in Figure 8.

Since there is no real input signals that can be compared, we cannot tell the difference between the input signal  $xx(n)$  obtained with recursive method and the real input signals. However, we can compare the calculated output signal  $y(n)$  with the real output signal  $y_0(n)$ . Figure 9 shows the calculated output signal  $y(n)$  and the absolute errors with observed output signal  $y_0(n)$ . From the figure we can see that the error is not very big. Besides, the relative error of the output signal energy was calculated, whose value is 8.95%. This shows that the method is feasible; that is to say, the input signal  $xx(n)$  is acceptable and can be approximately taken as the hydraulic excitation on the turbine runner of a hydroelectric generating set shaft system.

## 7. Conclusions

A blind identification method based on the third-order cumulants is proposed for a quadratic Volterra nonlinear system. Through three numerical experiments and engineering application, the following conclusions are drawn.

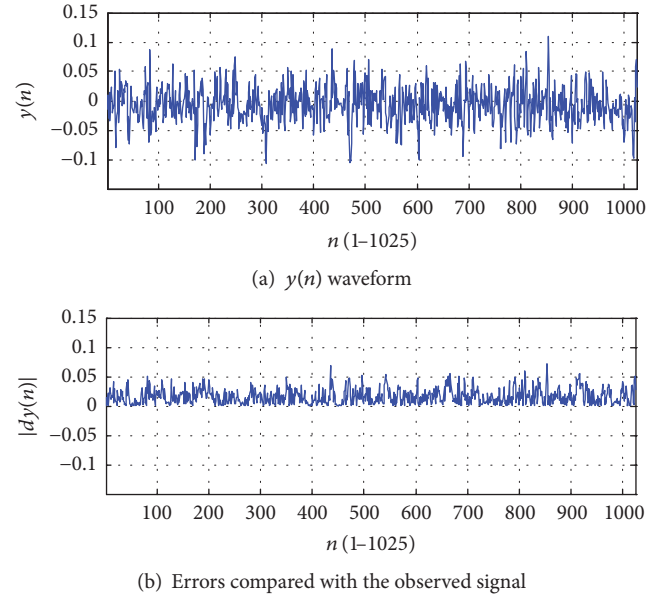


FIGURE 9: The output signals  $y(n)$  calculated by  $xx(n)$  and their errors.

- (1) Two different types of the memory length are used to identify the same sets of the signal data sequence of hydroturbine main shaft, and the error between the two groups of the time domain kernels  $h(i, j)$  is small. It shows that the proposed method is applicable to the blind identification of the hydroturbine main shaft system and has strong universality.
- (2) The proposed computer loop judgment method to determine the coefficient  $\gamma_{ijk}$  for calculating the third-order moment of the output signal greatly simplifies the formulae derivation and compiling of the programming code and is suitable for calculating the fourth- or higher order cumulants.
- (3) With the gradual increase of the signal-to-noise ratio, the relative error of the identified time domain kernels decreases, the standard deviation is reduced, and the objective function value is also reduced.
- (4) According to the observed signal of the shaft system of a certain hydroturbine generating set, the time domain kernels of the Volterra system can be blindly identified by the method proposed in this paper. Furthermore, according to these time domain kernels and the observed signal, the input signal of the system can be recursively calculated. The results show that the computed input signal can be approximately taken as the stochastic excitation acted on the turbine runner, and the error is not big (relative error of the output signal energy is acceptable). The proposed method is of enlightening significance for the form of hydraulic action.

## Appendix

### Loop Judgment Method for Determining Coefficient Value

In the expressions of the third-order moment (10), suppose the six subscripts of input sequence  $\{x(t)\}$  are, respectively,  $t_1 = -i_1$ ,  $t_2 = -i_2$ ,  $t_3 = \tau_1 - j_1$ ,  $t_4 = \tau_1 - j_2$ ,  $t_5 = \tau_2 - k_1$ , and  $t_6 = \tau_2 - k_2$ ; then the coefficient values  $\gamma_{ijk}$  can be determined by the loop judgment method from computer.

*Step 1.* If  $t_1 = t_2 = t_3 = t_4 = t_5 = t_6$ , obviously  $\gamma_{ijk} = \gamma_{6x}$ . If not satisfied, go to Step 2.

*Step 2.* If  $t_1 = t_2 = t_3 \neq t_4 = t_5 = t_6$ , then  $\gamma_{ijk} = \gamma_{3x}^2$ . In this condition, there are totally 10 kinds of combinations. These combinations can be expressed (only use subscripts) as 123 and 456; 124 and 356; 125 and 346; 126 and 345; 134 and 256; 135 and 246; 136 and 245; 145 and 236; 146 and 235; 156 and 234. If not satisfied, go to Step 3.

*Step 3.* If  $t_1 = t_2 \neq t_3 = t_4 \neq t_5 = t_6$ , then  $\gamma_{ijk} = \gamma_{2x}^3$ ; Furthermore, if  $t_1 = t_2 \neq t_3 = t_4 = t_5 = t_6$ , then  $\gamma_{ijk} = \gamma_{4x}\gamma_{2x}$ .

First, divide the six time  $t_i$  into two groups: 2 + 4. For example, when  $t_1 = t_2$ , then to judge whether  $t_3, t_4, t_5$ , and  $t_6$  are equal, there are three possibilities.

- (1) All four times  $t_3, t_4, t_5$ , and  $t_6$  equal each other; that is,  $t_3 = t_4 = t_5 = t_6$ ; then  $\gamma_{ijk} = \gamma_{4x}\gamma_{2x}$ .
- (2) Two times are equal; say  $t_3 = t_4$  and  $t_5 = t_6$ , and in the two groups there is one group equal to  $t_1$ ; then  $\gamma_{ijk} = \gamma_{4x}\gamma_{2x}$ .
- (3) Two times are equal; say  $t_3 = t_4, t_5 = t_6$ , and in the two groups there is no one group equal to  $t_1$ ; then  $\gamma_{ijk} = \gamma_{2x}^3$ .

This grouping can be distinguished by the following five kinds of combinations; that is, the 2 in 2 + 4 are  $t_1 = t_2, t_1 = t_3, t_1 = t_4, t_1 = t_5$ , and  $t_1 = t_6$ , and the rest is 4. In each combination, the previous comparison and judgment should be repeated.

If the previous conditions are not satisfied, go to Step 4.

*Step 4.* If Steps 1, 2, and 3 are not met,  $\gamma_{ijk} = 0$ .

### Competing Interests

The authors declare that there is no conflict of interests regarding the publication of this paper.

### Acknowledgments

The authors gratefully acknowledge the support from National Natural Science Foundation of China (no. 50839003, no. 51279071) and the Doctoral Foundation of Ministry of Education of China [Grant no. 20135314130002]. The paper is also supported by high-level personnel funds of North China University of Water Resources and Electric Power.

## References

- [1] R. Maheswaran and R. Khosa, "Wavelet-Volterra coupled model for monthly stream flow forecasting," *Journal of Hydrology*, vol. 450-451, pp. 320-335, 2012.
- [2] R. Maheswaran and R. Khosa, "Long term forecasting of groundwater levels with evidence of non-stationary and nonlinear characteristics," *Computers & Geosciences*, vol. 52, pp. 422-436, 2013.
- [3] V. S. Hari, V. P. Jagathy Raj, and R. Gopikakumari, "Unsharp masking using quadratic filter for the enhancement of fingerprints in noisy background," *Pattern Recognition*, vol. 46, no. 12, pp. 3198-3207, 2013.
- [4] W. Ji and W.-S. Gan, "Identification of a parametric loudspeaker system using an adaptive Volterra filter," *Applied Acoustics*, vol. 73, no. 12, pp. 1251-1262, 2012.
- [5] Y. Kim, J.-H. Kim, and Y. Kim, "Time series prediction of nonlinear ship structural responses in irregular seaways using a third-order Volterra model," *Journal of Fluids and Structures*, vol. 49, pp. 322-337, 2014.
- [6] L. Carassale and A. Kareem, "Synthesis of multi-variate Volterra systems by a topological assemblage scheme," *Probabilistic Engineering Mechanics*, vol. 37, pp. 109-122, 2014.
- [7] Z. Sigrist, E. Grivel, and B. Alcoverro, "Estimating second-order Volterra system parameters from noisy measurements based on an LMS variant or an errors-in-variables method," *Signal Processing*, vol. 92, no. 4, pp. 1010-1020, 2012.
- [8] J. Liu, Y. Zhang, and B. Yun, "A new method for predicting nonlinear structural vibrations induced by ground impact loading," *Journal of Sound and Vibration*, vol. 331, no. 9, pp. 2129-2140, 2012.
- [9] H. Tang, Y. H. Liao, J. Y. Cao, and H. Xie, "Fault diagnosis approach based on Volterra models," *Mechanical Systems and Signal Processing*, vol. 24, no. 4, pp. 1099-1113, 2010.
- [10] J. M. Nichols and K. D. Murphy, "Modeling and detection of delamination in a composite beam: a polyspectral approach," *Mechanical Systems and Signal Processing*, vol. 24, no. 2, pp. 365-378, 2010.
- [11] J. M. Nichols and C. C. Olson, "Optimal bispectral detection of weak, quadratic nonlinearities in structural systems," *Journal of Sound and Vibration*, vol. 329, no. 8, pp. 1165-1176, 2010.
- [12] Z. K. Peng, Z. Q. Lang, L. Zhao, S. A. Billings, G. R. Tomlinson, and P. F. Guo, "The force transmissibility of MDOF structures with a non-linear viscous damping device," *International Journal of Non-Linear Mechanics*, vol. 46, no. 10, pp. 1305-1314, 2011.
- [13] C. M. Cheng, Z. K. Peng, X. J. Dong, W. M. Zhang, and G. Meng, "A novel damage detection approach by using Volterra kernel functions based analysis," *Journal of the Franklin Institute*, vol. 352, no. 8, pp. 3098-3112, 2015.
- [14] Z. K. Peng, W. M. Zhang, B. T. Yang, G. Meng, and F. L. Chu, "The parametric characteristic of bispectrum for nonlinear systems subjected to Gaussian input," *Mechanical Systems and Signal Processing*, vol. 36, no. 2, pp. 456-470, 2013.
- [15] L. M. Li and S. A. Billings, "Analysis of nonlinear oscillators using Volterra series in the frequency domain," *Journal of Sound and Vibration*, vol. 330, no. 2, pp. 337-355, 2011.
- [16] A. Chatterjee, "Identification and parameter estimation of a bilinear oscillator using Volterra series with harmonic probing," *International Journal of Non-Linear Mechanics*, vol. 45, no. 1, pp. 12-20, 2010.

- [17] W.-D. Chang, "Volterra filter modeling of nonlinear discrete-time system using improved particle swarm optimization," *Digital Signal Processing*, vol. 22, no. 6, pp. 1056–1062, 2012.
- [18] J.-M. Le Caillec, "Spectral inversion of second order Volterra models based on the blind identification of Wiener models," *Signal Processing*, vol. 91, no. 11, pp. 2541–2555, 2011.
- [19] M. Ghandchi Tehrani, L. Wilmshurst, and S. J. Elliott, "Receptance method for active vibration control of a nonlinear system," *Journal of Sound and Vibration*, vol. 332, no. 19, pp. 4440–4449, 2013.
- [20] J. Antari, A. Zeroual, and S. Safi, "Blind identification of nonlinear quadratic systems using higher order cumulants and non-Gaussian input signals," *International Journal of General Systems*, vol. 37, no. 5, pp. 585–602, 2008.
- [21] J. Antari, S. Chabaa, R. Iqdour, A. Zeroual, and S. Safi, "Identification of quadratic systems using higher order cumulants and neural networks: application to model the delay of video-packets transmission," *Applied Soft Computing*, vol. 11, no. 1, pp. 1–10, 2011.
- [22] H.-Z. Tan and T. W. S. Chow, "Blind identification of quadratic nonlinear models using neural networks with higher order cumulants," *IEEE Transactions on Industrial Electronics*, vol. 47, no. 3, pp. 687–696, 2000.